Transactions of the ASME, Journal of Heat Transfer (ISSN 0022-1481) is published monthly by The American Society of Mechanical Engineers, Three Park Avenue, New York, NY 10016. Periodicals postage paid at New York, NY and additional mailing offices. POSTMASTER: Send address changes to Transactions of the ASME, Journal of Heat Transfer, c/o THE AMERICAN SOCIETY OF MECHANICAL ENGINEERS, 22 Law Drive, Box 2300, Fairfield, NJ 07007-2300. **CHANGES OF ADDRESS** must be received at Society headquarters seven weeks before they are to be effective. Please send old label and new address. **STATEMENT from By-Laws.** The Society shall not be responsible for statements or opinions advanced in papers or ... printed in its publications (B7.1, Para. 3).

Journal of Heat Transfer

Published Monthly by ASME

VOLUME 128 • NUMBER 3 • MARCH 2006

RESEARCH PAPERS

TECHNICAL BRIEFS

(Contents continued on inside back cover)

This journal is printed on acid-free paper, which exceeds the ANSI Z39.48-1992 specification for permanence of paper and library materials. ♾™
♻ 85% recycled content, including 10% post-consumer fibers.

Journal of Heat Transfer **Volume 128, Number 3** **MARCH 2006**

The ASME Journal of Heat Transfer is abstracted and indexed in the following:

Applied Science and Technology Index, Chemical Abstracts, Chemical Engineering and Biotechnology Abstracts (Electronic equivalent of Process and Chemical Engineering), Civil Engineering Abstracts, Compendex (The electronic equivalent of Engineering Index), Corrosion Abstracts, Current Contents, E & P Health, Safety, and Environment, Ei EncompassLit, Engineered Materials Abstracts, Engineering Index, Enviroline (The electronic equivalent of Environment Abstracts), Environment Abstracts, Environmental Engineering Abstracts, Environmental Science and Pollution Management, Fluidex, Fuel and Energy Abstracts, Index to Scientific Reviews, INSPEC, International Building Services Abstracts, Mechanical & Transportation Engineering Abstracts, Mechanical Engineering Abstracts, METADEX (The electronic equivalent of Metals Abstracts and Alloys Index), Petroleum Abstracts, Process and Chemical Engineering, Referativnyi Zhurnal, Science Citation Index, SciSearch (The electronic equivalent of Science Citation Index), Theoretical Chemical Engineering

Analysis of Hydrodynamics and Heat Transfer in a Thin Liquid Film Flowing Over a Rotating Disk by the Integral Method

S. Basu

B. M. Cetegen[1]
Fellow ASME

Mechanical Engineering Department,
University of Connecticut,
Storrs, CT 06269-3139

An integral analysis of hydrodynamics and heat transfer in a thin liquid film flowing over a rotating disk surface is presented for both constant temperature and constant heat flux boundary conditions. The model is found to capture the correct trends of the liquid film thickness variation over the disk surface and compare reasonably well with experimental results over the range of Reynolds and Rossby numbers covering both inertia and rotation dominated regimes. Nusselt number variation over the disk surface shows two types of behavior. At low rotation rates, the Nusselt number exhibits a radial decay with Nusselt number magnitudes increasing with higher inlet Reynolds number for both constant wall temperature and heat flux cases. At high rotation rates, the Nusselt number profiles exhibit a peak whose location advances radially outward with increasing film Reynolds number or inertia. The results also compare favorably with the full numerical simulation results from an earlier study as well as with the reported experimental results.
[DOI: 10.1115/1.2150836]

Keywords: liquid film cooling, rotation, heat transfer enhancement, integral analysis

Introduction

Many investigations have been performed in the past on flow and heat transfer characteristics in thin liquid films due to the fact that high heat transfer rates can be obtained in thin films as reviewed by Webb and Ma [1]. Hydrodynamic characteristics of thin liquid films flowing over stationary and rotating disk surfaces are important in understanding the major factors affecting the heat transfer performance. A better understanding of the fluid mechanics of the liquid film flow allows better design and optimization of high performance compact heat transfer systems such as those employed in space applications, where considerations on efficiency, size, and weight are of critical importance. The study of rotating thin-film fluid physics and heat transfer is also of fundamental interest in the development of compact vapor absorption systems.

Watson [2] was first to analyze a free-falling jet impinging on a horizontal stationary plate. The film flow was divided into four regions. The first region is the impingement zone, followed by a second region of a growing boundary layer in the liquid film which eventually reaches to the film surface. The third region is comprised of the transition to a fully developed film flow followed by a fully developed flow regime identified as the fourth region. For stationary and rotating liquid films at low flow rates and rotation speeds, a hydraulic jump could exist that has been studied both computationally and experimentally under normal and zero gravity conditions by Faghri and co-workers [3,4] and Avedisian and Zhao [5]. The hydraulic jump phenomenon was found to disappear at zero gravity conditions. Labus and Dewitt [6] conducted a combined numerical and experimental study to determine the free surface of a circular jet impinging on a flat plate in microgravity. The governing potential flow equations were solved numerically. The experimental study was performed using a drop-tower. The flow patterns of the free surface were examined experimentally, concluding that the surface tension and inertia were the dominant forces acting on the liquid. The experimental results were found to be in a good agreement with the numerical results. Thomas et al. [3] performed a useful one-dimensional analysis of the film thickness including the hydraulic jump phenomenon. They predicted significant thinning of the film with increased levels of rotation. They neglected inertia in their analysis.

Miyasaka [7] performed a similar theoretical and experimental study of the thickness of a thin viscous liquid film on a rotating disk. He obtained the film thickness by solving the governing equations of motion in the inviscid and viscous limits, with the latter utilizing the boundary layer approximation. Miyasaka also carried out experiments by using a liquid jet falling onto the center of a rotating disk. He deduced the film height from the electrical resistance of the liquid on the disk by comparing it to the electrical resistance of a standard thickness of the fluid. The computed values were found to agree with the experimental results. Rahman et al. [4] was the first to report a full numerical solution of the momentum equations using a finite difference scheme. The method utilized a boundary-fitted coordinate gridding scheme with a k-ε model for turbulence closure and an iterative technique to define the free surface. They predicted the liquid-film thickness in the vicinity of the hydraulic jump reasonably well and evaluated the effects at the outer edge of the disk. Rahman and Faghri [8] investigated the hydrodynamic behavior of a thin liquid film flowing over a rotating disk. They used a three-dimensional boundary-fitted coordinate system to perform the calculations. The computed film thickness agreed well with the existing experimental measurements. It was also concluded that the flow was dominated by inertia near the entrance and by centrifugal force near the outer edge the disk. The hydrodynamic characteristics of a radially spreading liquid jet on a horizontal plate were also predicted numerically by Buyevich and Ustinov [9]. However they reported no comparison with other studies.

Rao and Arakeri [10] performed an analytical study of free liquid jets on surfaces including circular plates, cones, and spheres. They used a boundary layer approximation and a third order polynomial for the velocity profile. The equations were

[1]Corresponding author; e-mail: cetegen@engr.uconn.edu
Contributed by the Heat Transfer Division of ASME for publication in the JOURNAL OF HEAT TRANSFER. Manuscript received April 18, 2005; final manuscript received September 12, 2005. Review conducted by Prof. Bengt Sunden.

solved by the integral method. Their work however did not include heat transfer in the film. Nevertheless, they were the first to use the integral approach to predict relevant parameters like film thickness. They also did not present any experimental validation of their data. Liu and Lienhard [11] performed an integral analysis of a liquid jet impingement heat transfer on a uniform heat flux surface without rotation. They reported Nusselt number correlations for a range of Prandtl numbers.

Azuma and Hoshino [12] examined the laminar-turbulent transition, liquid-film thickness, velocity profile, stability, and wall pressure fluctuations of thin liquid films on a stationary horizontal disk. The laminar-turbulent transition was determined as a function of the nozzle inside diameter, the gap height, and the volumetric flow rate. The liquid-film thickness measurements were performed using a needle probe. More recently, Ozar et al. [13] measured the liquid film thickness by a laser light reflection technique with which the spatial distributions of film thickness were captured including the hydraulic jump.

Heat transfer in liquid films was first analyzed by Chaudury [14] who incorporated Watson's results into the heat transfer analysis. Wang et al. [15] developed a two-domain solution in which the heat transfer at the liquid film and the solid disk were treated separately and matched at the liquid-disk interface. Rahman and Faghri [8] used mixed numerical and analytical methods to predict the heat transfer. For developing flow and heat transfer, a three-dimensional numerical model was utilized. Also, a two-dimensional analytical solution was formulated for developing heat transfer and fully developed flow assuming solid body rotation. For the case of fully developed heat transfer and fluid flow, a closed form solution was developed. This solution predicted that the Nusselt number, based on film thickness, approached a constant value in the fully developed regime. Carper et al. [16] evaluated the convective heat transfer from a jet of cooling oil to an approximately isothermal rotating disk. Correlations were presented for the average Nusselt number as influenced by rotational Reynolds number, jet Reynolds number and radius of impingement. Carper et al. [17] later extended their study to include the effect of Prandtl numbers. Vader et al. [18] studied the effects of jet velocity and temperature on the heat transfer between a planar water jet and a stationary heated plate. They concluded that the heat transfer performance was affected by the free stream turbulence intensity and the Prandtl number. A similar study was presented by Stevens and Webb [19] where the influence of jet Reynolds number, nozzle to plate spacing, and jet diameter were evaluated. Empirical correlations were developed for stagnation point, local and average Nusselt numbers. Faghri et al. [20] presented heat transfer results for a controlled liquid impinging jet on a stationary disk. They presented a numerical study showing good agreement between heat transfer predictions and experimental data. Auone and Ramshaw [21] performed heat and mass transfer experiments on a liquid flowing over a rotating disk. They predicted the heat transfer coefficients analytically by adapting the solution that Nusselt [22] used for the film condensation under the influence of gravity. Ozar et al. [23] published an experimental study of heat transfer and reported the local and disk surface averaged Nusselt number over a range of flow rates and rotation speeds for water. Recently, Rice et al. [24] published full numerical computation of heat transfer in a thin liquid film over a rotating disk simulating the experimental conditions of Ozar et al. [23].

Review of the literature indicates that the analysis of the problem has progressed along two main themes. One theme has been numerical solution of the full problem taking into account its salient features. The other is of analytical nature utilizing simplifying assumptions to obtain simple analytical results. In between lies the studies that utilize the Karman-Pohlhausen-type integral analyses. This type of analysis is capable of capturing sufficient details of the solution while avoiding oversimplifications needed in analytical studies. For example, many of the analytical analyses had not considered the liquid film inertia effects in the presence of rotation. It was thus the objective of this study to present a comprehensive integral analysis of the thin liquid film flowing radially outward on a circular disk including effects of inertia and rotation. Capability of the integral method to predict the flow and heat transfer is demonstrated by comparisons with experimental and numerical results for the same problem.

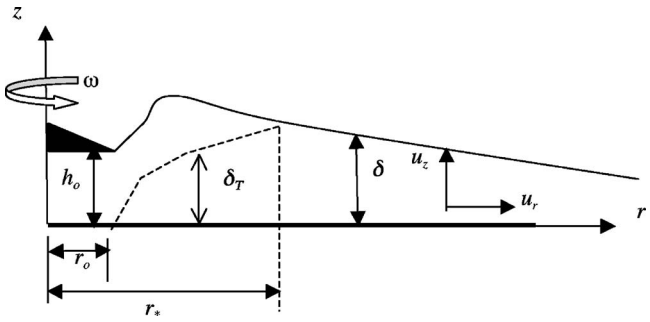

Fig. 1 Schematics of the thin film over a rotating disk

Problem Formulation

The rotating disk is schematically shown in Fig. 1 which resembles the experimental set-up that has been utilized by Thomas et al. [3] and Ozar et al. [13,23] in a series of experimental studies. In the experiments, the flow is introduced from a central collar that directs the liquid radially outward over a gap height of h_o. The liquid flows over the rotating disk while being heated from underneath by an electric resistance heater. In these experimental studies, the liquid film thickness and heat transfer coefficients were measured. Liquid film thickness measurements were made by either a capacitance probe [3] or an optical technique [13]. The heat transfer coefficients were determined from the difference between the measured disk surface temperature and the liquid inlet temperatures and the constant heat flux supplied to the disk.

The problem is considered in the radial (r) and axial (z) coordinates assuming azimuthal symmetry. For this situation, the governing equations in cylindrical coordinate system over a rotating circular disk are:

Continuity:

$$\frac{1}{r}\frac{\partial}{\partial r}(ru_r)+\frac{\partial u_z}{\partial z}=0 \tag{1}$$

r-momentum:

$$\frac{1}{r}\frac{\partial}{\partial r}(ru_ru_r)+\frac{\partial(u_ru_z)}{\partial z}=r\omega^2+\nu\left[\frac{\partial^2 u_r}{\partial z^2}-\frac{u_r}{r^2}+\frac{1}{r}\frac{\partial}{\partial r}\left(r\frac{\partial u_r}{\partial r}\right)\right] \tag{2}$$

Energy:

$$\frac{1}{r}\frac{\partial}{\partial r}[ru_rT]+\frac{\partial}{\partial z}[u_zT]=\alpha\left[\frac{1}{r}\frac{\partial}{\partial r}\left(r\frac{\partial T}{\partial r}\right)+\frac{\partial^2 T}{\partial z^2}\right] \tag{3}$$

Defining nondimensional parameters as,

$$\tilde{r}\equiv\frac{r}{r_0},\quad \tilde{u}_r\equiv\frac{u_r}{u_o},\quad \tilde{z}\equiv\frac{z}{h_o},\quad \tilde{u}_z\equiv\frac{u_z}{u_o},$$

$$\theta_T\equiv\frac{T-T_o}{T_o-T_i},\quad \theta_q\equiv\left(\frac{k}{q_oh_o}\right)(T-T_i),$$

where r_0 is the inlet radius of the disk, u_0 is the inlet velocity of the liquid jet, h_0 is the collar height, θ_T is the nondimensional temperature for the constant wall temperature, and θ_q is its counterpart for constant wall heat flux. T_0 is the temperature of the disk surface for constant wall temperature case, T_i is the inlet temperature of the liquid jet, q_0 is the heat flux supplied to the disk for the constant wall heat flux case. Nondimensionalizing the governing equations we obtain,

$$\frac{1}{\tilde{r}}\frac{\partial}{\partial \tilde{r}}(\tilde{r}\tilde{u}_r)+\left(\frac{r_o}{h_o}\right)\frac{\partial \tilde{u}_z}{\partial \tilde{z}}=0 \tag{4}$$

$$\frac{1}{\tilde{r}}\frac{\partial}{\partial \tilde{r}}[\tilde{r}\tilde{u}_r^2]+\left(\frac{r_o}{h_o}\right)\frac{\partial}{\partial \tilde{z}}[\tilde{u}_r\tilde{u}_z]=\frac{\tilde{r}}{\mathrm{Ro}}+\frac{1}{\mathrm{Re}}\left[\frac{1}{\tilde{r}}\frac{\partial}{\partial \tilde{r}}\left(\tilde{r}\frac{\partial \tilde{u}_r}{\partial \tilde{r}}\right)+\left(\frac{r_o}{h_o}\right)^2\frac{\partial^2 \tilde{u}_r}{\partial \tilde{z}^2}-\frac{\tilde{u}_r}{\tilde{r}^2}\right] \tag{5}$$

$$\frac{1}{\tilde{r}}\frac{\partial}{\partial \tilde{r}}[\tilde{r}\tilde{u}_r\theta]+\left(\frac{r_o}{h_o}\right)\frac{\partial}{\partial \tilde{z}}[\tilde{u}_z\theta]=\frac{1}{\mathrm{Pe}}\left[\frac{1}{\tilde{r}}\frac{\partial}{\partial \tilde{r}}\left(\tilde{r}\frac{\partial \theta}{\partial \tilde{r}}\right)+\left(\frac{r_o}{h_o}\right)^2\frac{\partial^2 \theta}{\partial \tilde{z}^2}\right] \tag{6}$$

where Reynolds, Rossby, and Peclet numbers are defined as

$$\mathrm{Re}\equiv\frac{u_o r_o}{\nu},\quad \mathrm{Ro}\equiv\frac{u_o^2}{\omega^2 r_o^2},\quad \mathrm{Pe}\equiv\frac{u_o r_o}{\alpha}$$

where ν is the kinematic viscosity and α is the thermal diffusivity, both of which are assumed to be constant in the context of this analysis.

Since $r_o > h_o$, then, $r_o^2/h_o^2 \gg 1$, we can infer that

$$\left(\frac{r_o}{h_o}\right)^2\frac{\partial^2 \tilde{u}_r}{\partial \tilde{z}^2}\gg\frac{1}{\tilde{r}}\frac{\partial}{\partial \tilde{r}}\left(\tilde{r}\frac{\partial \tilde{u}_r}{\partial \tilde{r}}\right)\ \text{and}\ \left(\frac{r_o}{h_o}\right)^2\frac{\partial^2 \tilde{u}_r}{\partial \tilde{z}^2}\gg\frac{\tilde{u}_r}{\tilde{r}^2}\ \text{and}\ \left(\frac{r_o}{h_o}\right)^2\frac{\partial^2 \theta}{\partial \tilde{z}^2}\gg\frac{1}{\tilde{r}}\frac{\partial}{\partial \tilde{r}}\left(\tilde{r}\frac{\partial \theta}{\partial \tilde{r}}\right)$$

Hence the momentum and energy equations take the form

$$\frac{1}{\tilde{r}}\frac{\partial}{\partial \tilde{r}}[\tilde{r}\tilde{u}_r^2]+\left(\frac{r_o}{h_o}\right)\frac{\partial}{\partial \tilde{z}}[\tilde{u}_r\tilde{u}_z]=\frac{\tilde{r}}{\mathrm{Ro}}+\frac{1}{\mathrm{Re}}\left[\left(\frac{r_o}{h_o}\right)^2\frac{\partial^2 \tilde{u}_r}{\partial \tilde{z}^2}\right] \tag{7}$$

$$\frac{1}{\tilde{r}}\frac{\partial}{\partial \tilde{r}}[\tilde{r}\tilde{u}_r\theta]+\left(\frac{r_o}{h_o}\right)\frac{\partial}{\partial \tilde{z}}[\tilde{u}_z\theta]=\frac{1}{\mathrm{Pe}}\left(\frac{r_o}{h_o}\right)^2\frac{\partial^2 \theta}{\partial \tilde{z}^2} \tag{8}$$

Liquid Film Hydrodynamics

Integrating the momentum equation with respect to $\tilde{z}$ from 0 to $\tilde{\delta}=\delta/h_o$, we get,

$$\frac{1}{\tilde{r}}\frac{\partial}{\partial \tilde{r}}\int_0^{\tilde{\delta}}\tilde{r}\tilde{u}_r^2 d\tilde{z}+\frac{r_o}{h_o}[\tilde{u}_r\tilde{u}_z]_{\tilde{\delta}}=\frac{\tilde{r}\tilde{\delta}}{\mathrm{Ro}}-\frac{1}{\mathrm{Re}}\left[\left(\frac{r_o}{h_o}\right)^2\left.\frac{\partial \tilde{u}_r}{\partial \tilde{z}}\right|_0\right] \tag{9}$$

From the continuity equation, we can write

$$\tilde{u}_z(\tilde{\delta})=-\frac{h_o}{r_o\tilde{r}}\frac{\partial}{\partial \tilde{r}}\int_0^{\tilde{\delta}}\tilde{r}\tilde{u}_r d\tilde{z} \tag{10}$$

A parabolic radial velocity profile is assumed as,

$$\tilde{u}_r=a_0+a_1\tilde{z}+a_2\tilde{z}^2 \tag{11}$$

subject to the boundary conditions of no slip at the wall $\tilde{u}_r(\tilde{z}=0)=0$ and no shear at the free surface $(\partial \tilde{u}_r/\partial \tilde{z})=0$ at $\tilde{z}=\tilde{\delta}$. In addition, the total volume flow at any cross section perpendicular to r has to be equal to the inlet flow rate for the case of no vaporization or mass loss, these conditions allow determination of coefficients in the velocity profile leading to,

$$\tilde{u}_r=3\left(\frac{\tilde{z}}{\tilde{r}\tilde{\delta}^2}\right)-\frac{3}{2}\left(\frac{\tilde{z}^2}{\tilde{r}\tilde{\delta}^3}\right) \tag{12}$$

Substituting this profile into the integral momentum equation and integrating with respect to z, one gets

$$\frac{d\tilde{\delta}}{d\tilde{r}}+\frac{\tilde{\delta}}{\tilde{r}}+\frac{5}{6\,\mathrm{Ro}}\tilde{r}^3\tilde{\delta}^3=\frac{5}{2\,\mathrm{Re}}\left(\frac{r_o}{h_o}\right)^2\tilde{r} \tag{13}$$

In this equation, the first two terms are due to advection, the third term is a result of rotation and the term on the right-hand side represents the viscous shear. Equation (13), subject to the initial condition $\tilde{\delta}(\tilde{r}=1)=1$, was numerically integrated to determine the film thickness over the disk surface. Equation (13) becomes an algebraic equation for the case of negligible inertia in which case the first two terms disappear. The film thickness can be written in exact form as,

$$\tilde{\delta}=\left[\frac{3\,\mathrm{Ro}}{\mathrm{Re}}\left(\frac{r_o}{h_o}\right)^2\right]^{1/3}\frac{1}{\tilde{r}^{2/3}} \tag{14}$$

This result is identical to that obtained based on the falling film analysis with gravity being replaced by the centrifugal force. Having the liquid film hydrodynamics established, we now proceed with the heat transfer analysis in the film.

Heat Transfer in the Liquid Film

The heat transfer in the liquid film is analyzed by considering the two cases of constant disk surface temperature and constant disk surface heat flux. In either case, there is a thermal entry region where the thermal boundary layer lies below the film surface as shown in Fig. 1. As it is shown in Appendix A for constant disk surface temperature case, the thermal entry region length scales as,

$$\tilde{r}_*=\left[1+\frac{\mathrm{Pe}}{6}\left(\frac{h_o}{r_o}\right)^2\right]^{1/2} \tag{15}$$

For moderate Peclet numbers, $\tilde{r}_*\approx 1$ (or $r_*\approx r_o$) since $h_o \ll r_o$, thus allowing us to neglect the entry length.

Constant Disk Surface Temperature Case. For this case, the temperature profile can be constructed as a second order polynomial given by,

$$\theta=a_0+a_1\left(\frac{z}{\delta_T}\right)+a_2\left(\frac{z}{\delta_T}\right)^2 \tag{16}$$

which has to satisfy the boundary conditions: $\theta=0$ at $z=0$, $d\theta/dz=0$ at $z=\delta_T$. The profile satisfying these conditions is,

$$\theta=\theta_\infty\left[\left(\frac{z}{\delta_T}\right)^2-2\left(\frac{z}{\delta_T}\right)\right]\ \text{where}\ \begin{matrix}\delta_T<\delta\Rightarrow\theta_\infty=1\\ \delta_T=\delta\Rightarrow\theta_\infty=\dfrac{T_\delta(r)-T_o}{T_o-T_i}\end{matrix} \tag{17}$$

Substituting this profile along with the velocity profile into the integral energy equation, one obtains,

$$\frac{d\theta_\infty}{d\tilde{r}}=-\theta_\infty\left[\frac{5}{2\,\mathrm{Pe}}\left(\frac{r_o}{h_o}\right)^2\frac{\tilde{r}}{\tilde{\delta}}-\frac{5}{4}\frac{d\tilde{\delta}}{d\tilde{r}}\right] \tag{18}$$

Integrating and applying the condition that $\theta_\infty(\tilde{r}=\tilde{r}_*)=1$, we get

$$\theta_\infty=\exp\left[-\frac{5}{2}\left(\frac{r_o}{h_o}\right)^2\frac{1}{\mathrm{Pe}}\int_{r_*}^{\tilde{r}}\frac{\tilde{r}d\tilde{r}}{\tilde{\delta}}+\frac{5}{4}(\tilde{\delta}-\tilde{\delta}_*)\right] \tag{19}$$

Defining the Nusselt number as,

$$\mathrm{Nu}_T\equiv\frac{hr_0}{k}=-\frac{r_o}{\tilde{\delta}}\left.\frac{d\theta}{d\tilde{z}}\right|_{\tilde{z}=0}$$

$$\mathrm{Nu}_T=2\frac{r_o}{h_o\tilde{\delta}}\exp\left[-\frac{5}{2}\left(\frac{r_0}{h_0}\right)^2\frac{1}{\mathrm{Pe}}\int_{r_*}^{\tilde{r}}\frac{\tilde{r}d\tilde{r}}{\tilde{\delta}}+\frac{5}{4}(\tilde{\delta}-\tilde{\delta}_*)\right] \tag{20}$$

The area-averaged Nusselt number can be defined as

$$\mathrm{Nu}_{\mathrm{avg}} = \frac{1}{\pi(\tilde{r}^2 - 1)} \int_1^{\tilde{r}} \mathrm{Nu}_T \, 2\pi \tilde{r} d\tilde{r} \tag{21}$$

Constant Heat Flux Case. The temperature profile for the constant heat flux case is subject to

$$\left. \frac{d\theta_q}{d\tilde{z}} \right|_{\tilde{z}=0} = -1$$

and

$$\left. \frac{d\theta_q}{d\tilde{z}} \right|_{\tilde{z}=\tilde{\delta}} = 0,$$

i.e., prescribed heat flux at the wall, q_o and adiabatic free surface. With these conditions, the temperature profile becomes,

$$\theta = a_o + \tilde{\delta}\left(\frac{\hat{z}^2}{2} - \hat{z}\right) \tag{22}$$

where a_0 is a parameter which is a function of r. Substituting this temperature profile into the integral form of the energy equation and integrating, one gets,

$$\frac{da_0}{d\tilde{r}} + a_0 \frac{d\tilde{\delta}}{d\tilde{r}} = \frac{\tilde{r}}{\mathrm{Pe}} \left(\frac{r_0}{h_0}\right)^2 + \frac{2}{5} \frac{d\tilde{\delta}}{d\tilde{r}} + \frac{\tilde{\delta}}{2} \frac{d\tilde{\delta}}{d\tilde{r}} \tag{23}$$

subject to the initial value of $a_0(\tilde{r}=1)$. While this value can be taken as $a_o(\tilde{r})=0$ based on $\theta_q(\tilde{r}=1)=0$ in Eq. (22), a better estimate is provided by integrating the energy flux at $\tilde{r}=1$,

$$\int_0^1 \left[\frac{q_o h_o \theta_q}{kT_i} + 1 \right] d\tilde{z} = 1,$$

yielding $a_o(\tilde{r}=1)=1/3$. For the case of negligible inertia, an analytical solution for a_o can be obtained as described in Appendix B,

$$a_o = \left(\frac{r_o}{h_o}\right)^2 \frac{\tilde{r}-1}{\mathrm{Re\,Pr}} - \frac{7}{20}\left(\frac{r_o}{h_o}\right)^{2/3} \left(\frac{3\,\mathrm{Ro}}{\mathrm{Re}}\right)^{1/3} (\tilde{r}^{-2/3} - 1) + \frac{1}{3} \tag{24}$$

The Nusselt number for the case of constant disk surface heat flux can be found from,

$$\mathrm{Nu}_q \equiv \frac{hr_o}{k} = \frac{q_o r_o}{k[T(\tilde{z}=0) - T_i]} = \frac{r_o}{a_o h_o} \tag{25}$$

For the case of negligible inertia,

$$\mathrm{Nu}_q = \left[\left(\frac{r_o}{h_o}\right) \frac{\tilde{r}-1}{\mathrm{Re\,Pr}} - \frac{3^{1/3}7}{20} \left(\frac{r_o}{h_o}\right)^{-1/3} \left(\frac{\mathrm{Ro}}{\mathrm{Re}}\right)^{1/3} (\tilde{r}^{-2/3} - 1) + \frac{1}{3}\left(\frac{h_o}{r_o}\right) \right]^{-1} \tag{26}$$

The averaged Nusselt number is obtained by integrating the local Nusselt number over the disk surface based on Eq. (21). In the following, the results obtained from this analysis are presented and discussed.

Results and Discussion

The calculation of the liquid film thickness and Nusselt numbers for constant wall temperature and constant heat flux cases were performed for a range of inlet Reynolds numbers $\mathrm{Re} \equiv u_o r_o/\nu$ and Rossby numbers $\mathrm{Ro} \equiv u_o^2/\omega^2 r_o^2$. The range of parameters were chosen to cover those reported in the experiments of Ozar et al. [13,23] and the recent numerical simulations of Rice et al. [24]. The value of the geometric parameter r_o/h_o was taken to be same as in the experiments with a value of 200. In the following, the computed results are presented and compared with numerical and experimental results mentioned above.

Figure 2 shows the variation of the film thickness over the disk surface with Reynolds number for two values of Rossby number.

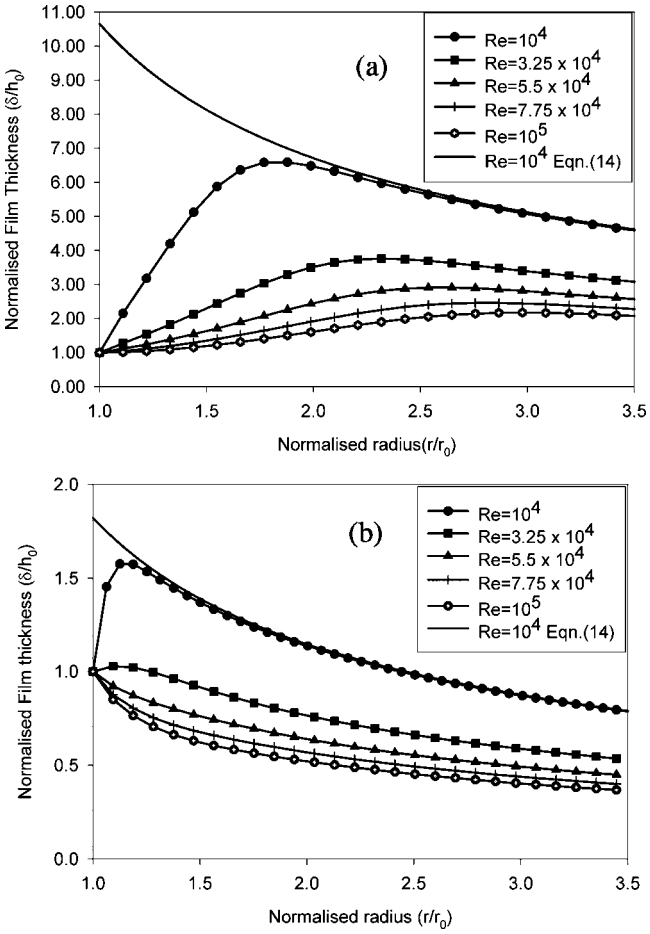

Fig. 2 Variation of normalized film thickness as a function of Reynolds number for (*a*) Ro=1000 and (*b*) Ro=0.5

At low rotation speeds (Ro=1000), the film thickness initially increases along the disk radius and then begins to thin out at outer radii due to effect of rotation as seen in Fig. 2(*a*). The film thickness decreases with increasing inlet velocity or Reynolds number and the peak film thickness location shifts to larger radii with increasing Re. The analytical result given by Eq. (14) is also shown in Fig. 2(*a*) for $\mathrm{Re}=10^4$. It is seen that the two results agree at large radii where the inertial effects are diminished and the negligible inertia result agrees with the full solution. At high rotation rates (Ro=0.5), film thickness exhibits a radial decay with the film thickness still decreasing with increasing inertia as shown in Fig. 2(*b*). The variation of the film thickness for high levels of rotation is well represented by Eq. (14) as seen by the agreement at $\mathrm{Re}=10^4$. The effect of varying the rotation speed on the film thickness at a constant value of inlet velocity or Reynolds number is depicted in Fig. 3. With increasing rotation speed (i.e., decreasing Ro), the film thickness decreases. The trend at high Ro, which exhibits a maximum in the film thickness, gradually changes to a radially decaying film thickness at high rotation speeds (i.e., low Ro). This change appears to happen at around Ro=10 for this case. The computed results are in reasonably good agreement with the experimental results reported by Ozar et al. [13] as shown in Fig. 4. The integral model captures the trend of liquid film thickness variation at different Reynolds and Rossby numbers. Due to the uncertainties in the experimentally measured film thickness, a closer agreement can not be expected.

Figure 5 shows the variation of the Nusselt number over the disk surface for the case of constant wall temperature. At low rotation rates (Ro=1000), shown in Fig. 5(*a*), the Nusselt number

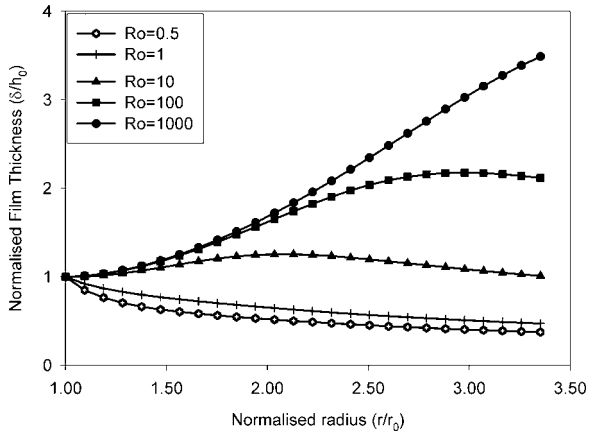

Fig. 3 Normalized film thickness variation over the disk surface for different Rossby numbers for medium flow rate Re $=10^5$

decreases continuously with increasing radial distance. The magnitude of Nusselt number is highest at the entrance since the temperature gradient, and heat flux is the highest there at the liquid-disk interface. With increasing radial distance, the liquid film temperature increases and consequently the heat flux diminishes leading to a decrease in the heat transfer coefficient and Nusselt number. The value of the Nusselt number approaches a constant value at large radii. The Nusselt number increases with increasing inlet velocity or Reynolds number as expected. At high rotation speeds, shown in Fig. 5(*b*), the trend of Nusselt number is quite different in that it increases from the inlet to a maximum value and decreases from that point on. The magnitude of Nusselt number increases with increasing Reynolds number with the peak Nusselt number location shifting radially outward. This pronounced increase in Nusselt number is due to the thinning of the liquid film due to inertia and rotation. The decrease at larger radii is due to the effect of heating of the liquid film reducing the temperature gradient and heat flux. At high rotation rates, the Nusselt number increases significantly above the values for low rotation rates suggesting the strong enhancement of heat transfer due to rotation.

To better visualize the effects of rotation at a fixed value of inlet velocity or Reynolds number, Fig. 6 shows the effect of Rossby number on Nusselt number variation. At low rotation speeds (i.e., high Ro), the Nusselt number is highest at the entrance and decreases with increasing radial distance. At about Ro=1, the trend exhibits an increase of Nusselt number from the inlet reaching a maximum value followed by a decay. At higher rotation rates (Ro=0.5), this trend of Nusselt number becomes more pronounced with the maximum values of Nusselt number being an

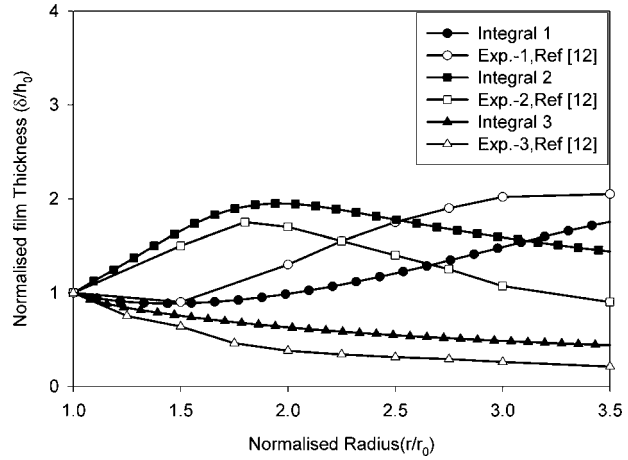

Fig. 4 Comparison of film thickness for experimental and theoretical data for several Reynolds number and Rossby numbers. Case 1: Re=2.4×10^5, Ro=361; Case 2: Re=4.8×10^4, Ro=361; Case 3: Re=4.8×10^4, Ro=0.4

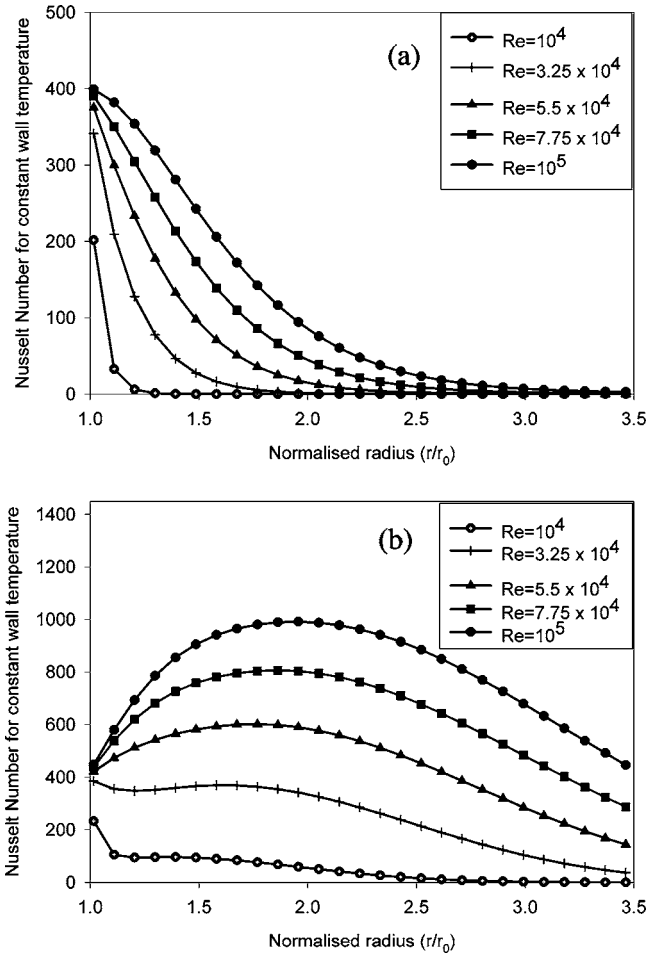

Fig. 5 Constant wall temperature Nusselt number variation over the disk surface for different Reynolds numbers for (*a*) low rotation Ro=1000 and (*b*) high rotation Ro=0.5 cases

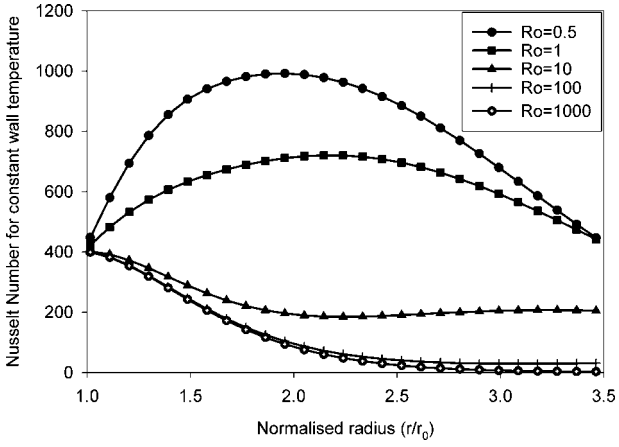

Fig. 6 Nusselt number variation for different Rossby numbers for Re=10^5

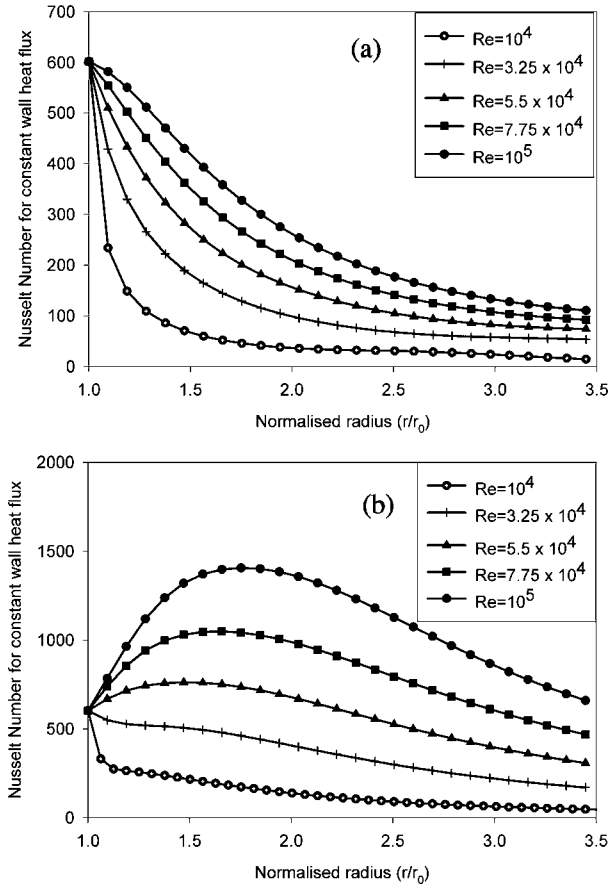

Fig. 7 Constant wall heat flux Nusselt number variation over the disk surface for different Reynolds numbers for (*a*) low rotation Ro=1000 and (*b*) high rotation Ro=0.5 cases

order of magnitude higher. The peak Nusselt number location shifts to smaller radii indicating that the rotational effects are felt at smaller radii with increasing rotation speed.

In Fig. 7, the results are shown for the constant heat flux case at two values of Rossby number. At low rotation rates (i.e., high Ro), the Nusselt number variation is similar to that of constant wall temperature case [shown in Fig. 5(*a*)] except that the Nusselt number magnitude is higher than that for the constant wall temperature. The increase in Nusselt number is expected since the heat flux at the disk surface is maintained in this case. For the high rotation speed (Ro=0.5), Nusselt number exhibits a decay with increasing radial distance at low Reynolds number as the temperature of the liquid at the disk surface increases with increasing radial distance, similar to the constant wall temperature case. With increasing Reynolds number, the Nusselt number magnitude increases and it exhibits a maximum.

Figure 8 illustrates the influence of rotation on the Nusselt number variation with at a fixed value of inlet velocity or Reynolds number. It is found that rotation enhances the heat transfer into the liquid film very significantly. As the rotation rate reduces, the maximum in the Nusselt number variation disappears and it decays continuously with increasing radial distance. The location of the peak shifts to smaller radii with increasing rotation rate (i.e., decreasing Ro) since the effects of rotation are felt closer to the center with increasing rotation.

Figure 9 shows the comparison of the integral method results with the full numerical simulation results of Rice et al. [24]. The comparisons are shown for $Re=1.42\times10^4$ and 2.84×10^4 for two rotation speeds of 50 and 100 rpm. The agreement between the integral model and numerical simulations appears to be good with

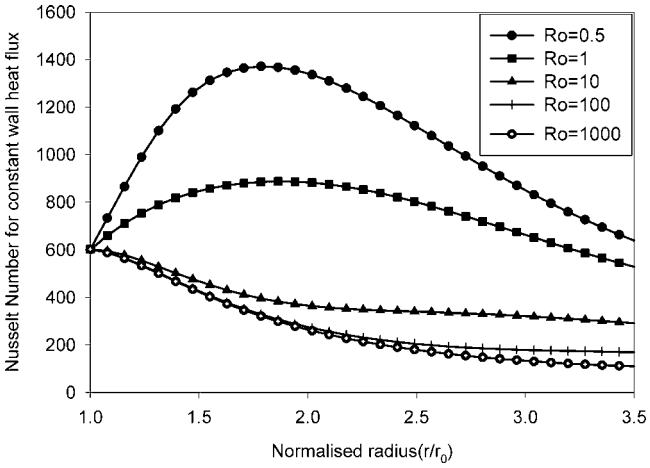

Fig. 8 Nusselt number variation for different Rossby numbers for $Re=10^5$

maximum deviations of about 20%. It is conceivable that the differences are due to the more detailed treatment afforded in the numerical model and other effects not captured by the integral model. Figure 10 displays the comparison of experimental results with the integral model for two cases. It is found that the experimental results are in good agreement with the model for these two

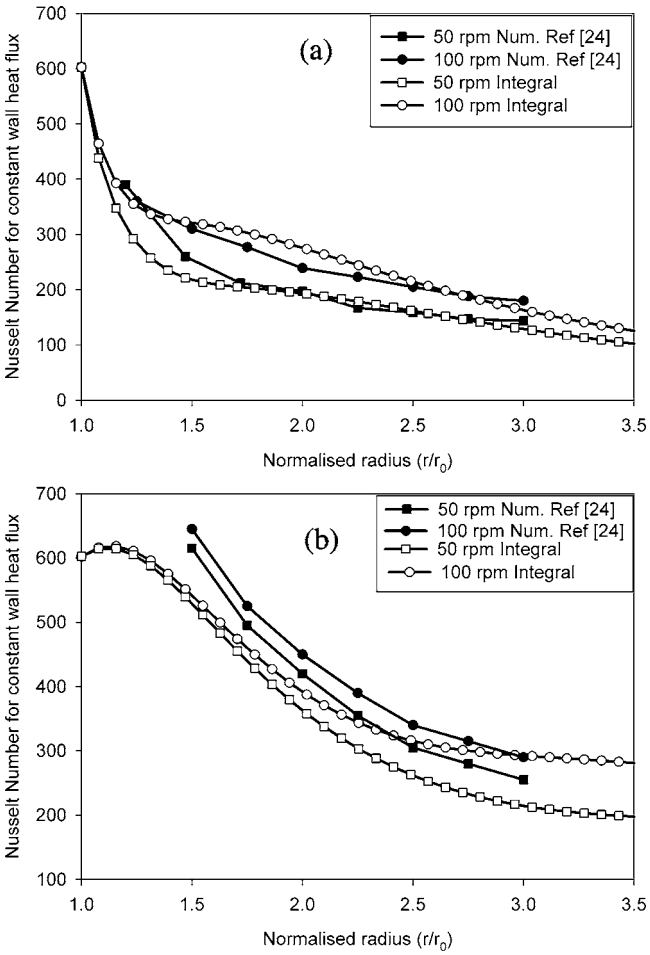

Fig. 9 Comparison of calculated Nusselt Number with numerical data of Rice et al. [24] for (*a*) $Re=2.84\times10^4$; (*b*) $Re=1.42\times10^5$ and rotation speeds of 50, 100 rpm

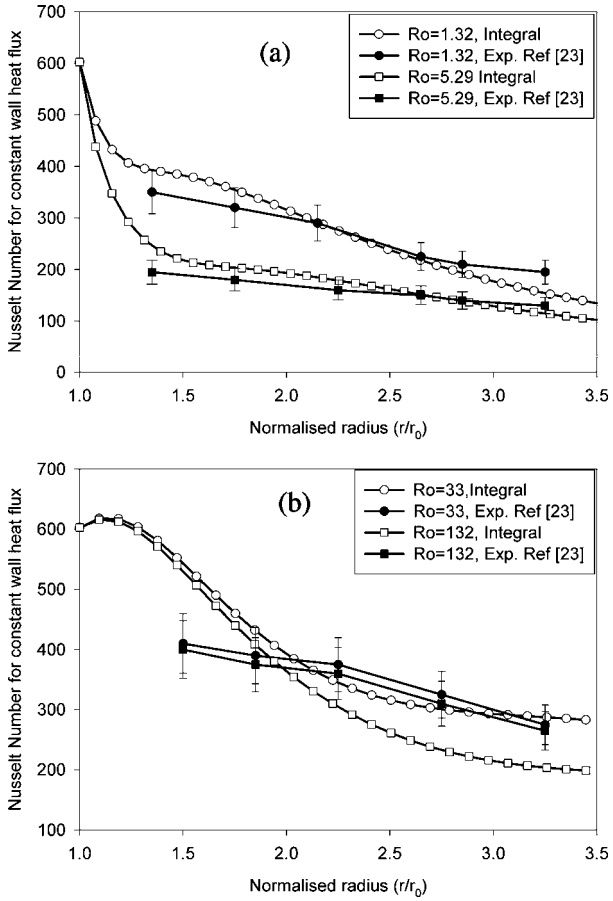

Fig. 10 Comparison of Nusselt Number from the integral analysis and the experimental data of Ozar et al. [23] for (*a*) $Re=2.85\times10^4$ and (*b*) $Re=1.42\times10^5$

cases with the radial variation of experimental Nusselt number being slightly less. Considering the uncertainty of the experimental data and the simplifications employed in the model, the level of agreement is remarkable.

The area averaged Nusselt numbers over the disk surface are shown in Figs. 11 and 12, respectively, for the cases of constant wall temperature and constant heat flux. The trend of average

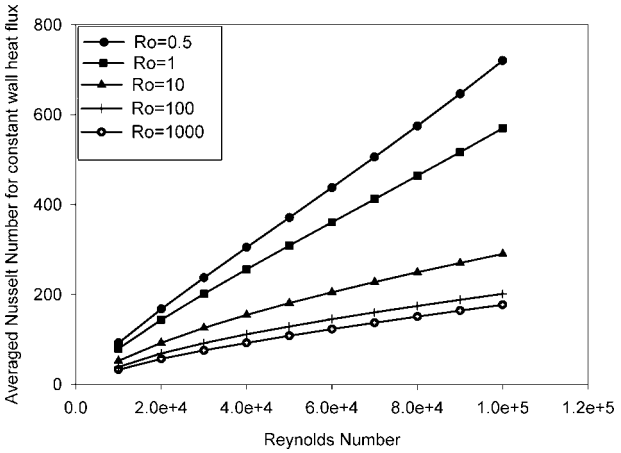

Fig. 12 Variation of average Nusselt number (based on area) with Reynolds number for different rotation rates corresponding to the constant wall heat flux case

Nusselt number is approximately linear for both cases with slightly decreasing curvature for the constant wall heat flux at low rotation rates (i.e., high Ro). The Nusselt numbers for constant heat flux are always higher than those for the constant wall temperature. The influence of Rossby number appears to be nonlinear and the average Nusselt number is found to scale as $\overline{Nu}\propto Ro^{-m}$, where $m\approx0.55$ for constant wall temperature and $m\approx0.18$ for constant heat flux. The stronger dependence for constant wall temperature can be rationalized based on the fact the thinning of the liquid film has a stronger effect on the temperature gradient at the wall for the constant wall temperature case than that for the constant heat flux. The Reynolds number dependence of the average Nusselt number was found scale as $\overline{Nu}\propto Re^{1.2}$.

Finally, Fig. 13 shows the comparison of the analytical solution given by Eq. (26) for the negligible inertia case with the full solution for $Re=10^4$ and $Ro=0.5$. It is seen that the two solutions differ substantially near the entrance region with similar trends of Nusselt number.

Concluding Remarks

A detailed integral analysis of flow and heat transfer in a thin liquid film flowing over a rotating disk was formulated to determine the liquid film thickness and Nusselt numbers for both constant wall temperature and heat flux cases. The results are pre-

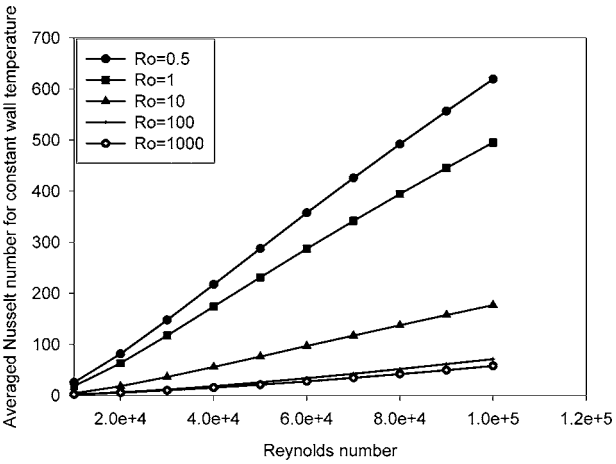

Fig. 11 Variation of average Nusselt number (based on area) with Reynolds number for different rotation rates corresponding to the constant wall temperature

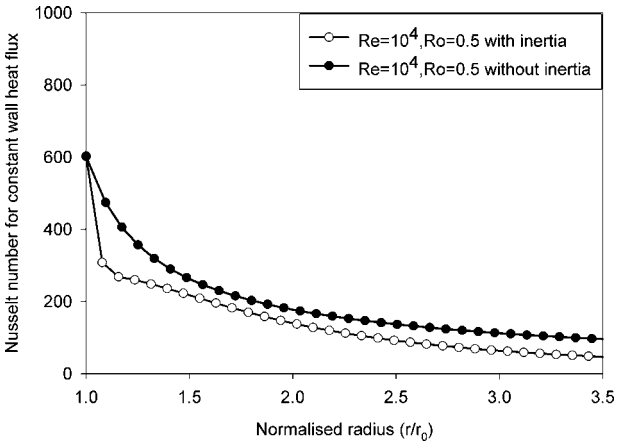

Fig. 13 The comparison of the Nusselt number for constant heat flux obtained from full solution and the approximation of negligible inertia

sented for a range of inlet liquid flow rates or Reynolds numbers and Rossby numbers. It is found that the integral model captures the variation of film thickness over the disk radius for a range of parameters representing both inertia and rotation dominated regimes. At low rotation rates corresponding to high Rossby numbers, the film thickness grows radially until the centrifugal effect becomes sufficiently strong at large radii. For high inlet flow rates or Reynolds numbers, the film thickness decreases radially with decay being stronger with increasing inertia. For low inertia, the film thickness increases radially due to significant retardation of the film flow by viscosity. In cases where both inertial and rotational effects come into play, the film thickness first increases reaching a maximum followed by radial decay. The location of maximum film thickness changes based on the values of Reynolds and Rossby numbers. For cases dominated either by high rotation or low inertia, the film thickness is well represented by the analytical expression obtained for negligible inertia.

The analysis of the heat transfer in the liquid film indicate that the Nusselt number exhibits a radial decay at low rotation rates (i.e., high Ro) for both cases of constant wall temperature and constant heat flux. The dependence of Nusselt number is slightly stronger than linear on inlet Reynolds number for both cases. However, the Nusselt number values for constant wall heat flux are uniformly greater than those for the constant wall temperature. At high rotation speeds and inlet Reynolds numbers, the Nusselt number first increases, reaches a peak and then displays a radial decay. The radial location of the peak Nusselt number shifts to larger radii with increasing Reynolds number and this is due to the competing effects of inertia and rotation on the film thickness and heat transfer characteristics. The effect of Rossby number appears to be significantly nonlinear and high rotation rates can produce significant enhancement in heat transfer for both cases of constant wall temperature and heat flux. In addition to local Nusselt number variation, the disk surface area averaged Nusselt numbers were computed for both cases. They also show an approximately linear variation with respect to inlet flow rate or Reynolds number and inverse power law dependence on Rossby number. Rossby number dependence is stronger for the constant wall temperature case.

The results obtained from this integral analysis were compared with those from a recent numerical study of Rice et al. [24] as well as the experiments of Ozar et al. [13,23]. Both comparisons indicate good agreement with the integral model. Finally, the integral analysis provided analytical and semianalytical expressions for the local Nusselt number in the limit of negligible inertia for the cases of constant wall heat flux and constant wall temperature, respectively.

Acknowledgment

The work presented in this article was funded by NASA Microgravity Fluid Physics Program under Grant No. NCC3-789 with Dr. S. Sankaran as the grant monitor.

Nomenclature

a_o = constant in Eq. (22)
C = heat capacity (J/kg K)
h_o = collar height (m)
h = convective heat transfer coefficient (W/m^2 K)
k = thermal conductivity (W/m K)
Nu = Nusselt number (hr_o/k)
Pe = Peclet number ($u_o r_o/\alpha$)
q_o = Constant wall heat flux (W/m^2)
r = radial coordinate (m)
$\tilde{r}$ = normalized radial coordinate (r/r_o)
r_o = collar radius (m)
Re = Reynolds number ($u_o r_o/\nu$)
Ro = Rossby number ($u_o^2/\omega^2 r_o^2$)
T = temperature (K)
T_o = temperature of the disk surface (K)
T_i = inlet temperature of the liquid (K)
u_o = liquid inlet velocity at the collar exit (m/s)
u_r = velocity component in the radial direction (m/s)
u_z = velocity component in the direction normal to disk surface (m/s)
$\tilde{u}$ = nondimensional velocity (u/u_o)
z = coordinate normal to disk surface
$\tilde{z}$ = normalized coordinate (z/h_o)
$\hat{z}$ = normalized coordinate with respect to thermal boundary thickness

Greek

α = thermal diffusivity, $k/\rho C$ (m^2/s)
β = ratio of thermal to hydrodynamic boundary layer thickness (δ/δ_T)
δ = hydrodynamic boundary layer or film thickness (m)
δ_T = thermal boundary layer thickness (m)
$\tilde{\delta}$ = normalized film thickness (δ/h_o)
$\tilde{\delta}_T$ = normalized film thickness (δ_T/h_o)
θ_T = nondimensional temperature for constant wall temperature, $(T-T_o)/(T_o-T_i)$
θ_q = nondimensional temperature for constant wall heat flux, $k(T_o-T_i)/(q_o h_o)$
ω = rotational speed (rev/s)

Appendix A

For determining the thermal entry length for the constant disk surface temperature case, the temperature profile in this region is taken as,

$$\theta = \left[\left(\frac{z}{\delta_T}\right)^2 - 2\left(\frac{z}{\delta_T}\right)\right] \tag{A1}$$

Introducing, $\hat{z} \equiv \tilde{z}/\tilde{\delta}_T$ and $\beta \equiv \delta_T/\delta$, the previously determined velocity profile and the nondimensional temperature profiles become,

$$\tilde{u}_r = 3\frac{\hat{z}}{\tilde{r}\tilde{\delta}_T^2}\beta^2 - \frac{3}{2}\frac{\hat{z}^2}{\tilde{r}\tilde{\delta}_T^3}\beta^3 \quad \theta = \hat{z}^2 - 2\hat{z} \tag{A2}$$

substituting into the integral energy equation and integrating to $\hat{z}=1$, one gets

$$\beta\frac{d}{d\tilde{r}}\left[\frac{\beta^2}{4} - \frac{\beta^3}{20}\right] = \frac{2}{\mathrm{Pe}}\left(\frac{r_o}{h_o}\right)^2\frac{\tilde{r}}{\tilde{\delta}} \tag{A3}$$

which can be integrated subject to the condition $\beta(\tilde{r}=1)=0$ as,

$$\beta^3\left[1 - \frac{18}{80}\beta\right] = \frac{12}{\mathrm{Pe}}\left(\frac{r_o}{h_o}\right)^2\int_1^{\tilde{r}_*}\frac{\tilde{r}d\tilde{r}}{\tilde{\delta}} \tag{A4}$$

It seen that the second term in the bracket on the left is small for liquids with high Prandtl numbers. For example, water with a Prandtl number 5–9 leads to a value of β around 0.5. Upon neglecting this second term, one obtains

$$\beta = \left[\frac{12}{\mathrm{Pe}}\left(\frac{r_o}{h_o}\right)^2\int_1^{\tilde{r}_*}\frac{\tilde{r}d\tilde{r}}{\tilde{\delta}}\right]^{1/3} \tag{A5}$$

If we assume that $\tilde{\delta} \approx 1$ near the entrance, then the integral can be evaluated and the result becomes,

$$\tilde{r}_* = \left[1 + \frac{\mathrm{Pe}}{6}\left(\frac{h_0}{r_0}\right)^2\right]^{1/2} \tag{A6}$$

Since $h_o \ll r_o$, then, $\tilde{r}_* \approx 1$ or $r_* \approx r_o$. The smallness of the entry region length is utilized in the heat transfer analysis presented in the main body of the paper.

Appendix B

Considering the integral momentum equation given by Eq. (9), neglecting the inertial terms on the left-hand side allows the direct integration between $\tilde{z}=0$ and $\tilde{z}=\tilde{\delta}$ to yield the velocity profile,

$$\tilde{u}_r = \frac{\mathrm{Re}}{\mathrm{Ro}}\left(\frac{h_o}{r_o}\right)^2 \tilde{r}\left[\tilde{\delta}\tilde{z} - \frac{\tilde{z}^2}{2}\right] \tag{B1}$$

The corresponding film thickness can be obtained upon integration for the total volumetric flow rate of liquid at any radius leading to the expression for $\tilde{\delta}$ given by Eq. (14). Substitution of this velocity profile into the energy integral equation leads to the following differential equation for a_o,

$$\frac{da_0}{d\tilde{r}} = \frac{1}{\mathrm{Re\,Pr}}\left(\frac{r_o}{h_o}\right)^2 + \frac{3^{1/3}7}{30}\left(\frac{\mathrm{Ro}}{\mathrm{Re}}\right)^{1/3}\left(\frac{r_o}{h_o}\right)^{2/3}\tilde{r}^{-5/3} - \frac{2}{3^{2/3}}\left(\frac{h_o}{r_o}\right)^{1/3}\left(\frac{\mathrm{Ro}}{\mathrm{Re}}\right)^{1/3} a_o \tilde{r}^{-8/3} \tag{B2}$$

Since $r_o > h_o$, the last term on the right-hand side is small compared to the others. If neglected, Eq. (B2), becomes directly integrable. Applying the condition $a_o(\tilde{r}=1)=1/3$, we get,

$$a_o = \left(\frac{r_o}{h_o}\right)^2 \frac{\tilde{r}-1}{\mathrm{Re\,Pr}} - \frac{3^{1/3}7}{20}\left(\frac{r_o}{h_o}\right)^{2/3}\left(\frac{\mathrm{Ro}}{\mathrm{Re}}\right)^{1/3}(\tilde{r}^{-2/3}-1) + \frac{1}{3} \tag{B3}$$

References

[1] Webb, B. W., and Ma, C. F., 1995, "Single Phase Liquid Impingement Heat Transfer," Adv. Heat Transfer, **26**, pp. 105–217.

[2] Watson, E. J., 1964, "The Radial Spread of a Liquid Jet Over a Horizontal Plane," J. Fluid Mech., **20**, pp. 481–499.

[3] Thomas, S., Hankey, W., Faghri, A., and Swanson, T., 1990, "One-Dimensional Analysis of the Hydrodynamic and Thermal Characteristics of Thin Film Flows Including Hydraulic Jump and Rotation," ASME J. Heat Transfer, **112**, pp. 728–735.

[4] Rahman, M. M., Faghri, A., and Hankey, W., 1991, "Computation of Turbulent Flow in a Thin Liquid Layer of Fluid Involving a Hydraulic Jump," J. Fluids Eng., **113**, pp. 411–418.

[5] Avedisian, C. T., and Zhao, Z., 2000, "The Circular Hydraulic Jump in Low Gravity," Proc. R. Soc. London, Ser. A, **456**, pp. 2127–2151.

[6] Labus, T. L., and DeWitt, K. J., 1978, "Liquid Jet Impingement Normal to a Disk in Zero Gravity," J. Fluids Eng., **100**, pp. 204–209.

[7] Miyasaka, Y., 1974, "On the Flow of a Viscous Free Boundary Jet on a Rotating Disk," Bull. JSME, **17**, pp. 1469–1475.

[8] Rahman, M. M., and Faghri, A., 1992, "Numerical Simulation of Fluid Flow and Heat Transfer in a Thin Liquid Film Over a Rotating Disk," Int. J. Heat Mass Transfer, **35**, pp. 1441–1453.

[9] Buyevich, Y. A., and Ustinov, V. A., 1994, "Hydrodynamic Conditions of Transfer Processes Through a Radial Jet Spreading Over a Flat Surface," Int. J. Heat Mass Transfer, **37**, pp. 165–173.

[10] Rao, A., and Arakeri, J. H., 1998, "Integral Analysis Applied to Radial Film Flows," Int. J. Heat Mass Transfer, **41**, pp. 2757–2767.

[11] Liu, X., and Lienhard, J. H., 1989, "Liquid Jet Impingement Heat Transfer on a Uniform Flux Surface," *Heat Transfer Phenomena in Radiation, Combustion and Fires*, ASME HTD, 106, pp. 523–530.

[12] Azuma, T., and Hoshino, T., 1984, "The Radial Flow of a Thin Liquid Film, 1st–4th Reports," Bull. JSME, **27**, pp. 2739–2770.

[13] Ozar, B., Cetegen, B. M., and Faghri, A., 2003, "Experiments on the Flow of a Thin Liquid Film Over a Horizontal Stationary and Rotating Disk Surface," Exp. Fluids, **34**, pp. 556–565.

[14] Chadhury, Z. H., 1964, "Heat Transfer in a Radial Liquid Jet," J. Fluid Mech., **20**, pp. 501–511.

[15] Wang, X. S., Dagan, Z., and Jiji, L. M., 1989, "Heat Transfer Between a Circular Free Impinging Jet and a Solid Surface with Non-Uniform Wall Temperature of Wall Heat Flux: 1: Solution for the Stagnation Region," Int. J. Heat Mass Transfer, **32**, pp. 1351–1360.

[16] Carper, H. J., and Defenbaugh, D. M., 1978, "Heat Transfer from a Rotating Disk with Liquid Jet Impingement," Proceedings of the 6th International Heat Transfer Conference, Toronto, pp. 113–118.

[17] Carper, Jr., H. J., Saavedra, J. J., and Suwanprateep, T., 1986, "Liquid Jet Impingement Cooling of a Rotating Disk," ASME J. Heat Transfer, **108**, pp. 540–546.

[18] Vader, D. T., Incropera, F. P., and Viskanta, R., 1991, "Local Convective Heat Transfer From a Heated Surface to an Impinging, Planar Jet of Water," Int. J. Heat Mass Transfer, **34**, pp. 611–623.

[19] Stevens, J., and Webb, B. W., 1991, "Local Heat Transfer Coefficients Under and Axisymmetric, Single-Phase Liquid Jet," ASME J. Heat Transfer, **113**, pp. 71–78.

[20] Faghri, A., Thomas, S., and Rahman, M. M., 1993, "Conjugate Heat Transfer from a Heated Disk to a Thin Liquid Film Formed by a Controlled Impinging Jet," ASME J. Heat Transfer, **115**, pp. 116–123.

[21] Aoune, A., and Ramshaw, C., 1999, "Process Intensification: Heat and Mass Transfer Characteristics of Liquid Films on Rotating Discs," Int. J. Heat Mass Transfer, **42**, pp. 2543–2556.

[22] Nusselt, W. Z., 1916, "Die Oberflachenkondensation des Wasserdampfes," Z. Ver Deut. Ing., **60**, pp. 541–546.

[23] Ozar, B., Cetegen, B. M., and Faghri, A., 2004, "Experiments on Heat Transfer in a Thin Liquid Film Flowing Over a Rotating Disk," ASME J. Heat Transfer, **126**, pp. 184–192.

[24] Rice, J., Faghri, A., and Cetegen, B. M., 2005, "Analysis of a Free Surface Film From a Controlled Liquid Impingement Jet Over a Rotating Disk Including Conjugate Effects With and Without Evaporation," Int. J. Heat Mass Transfer, **48**, pp. 5192–5204.

Heat Transfer Enhancement of a Circular Cylinder

Takayuki Tsutsui
e-mail: tsutsui@nda.ac.jp

Tamotsu Igarashi

Department of Mechanical Engineering,
The National Defense Academy,
1-10-20 Hashirimizu, Yokosuka,
Kanagawa 239-8686, Japan

A rod was positioned upstream of a circular cylinder to enhance its heat transfer in an air stream. The diameter of the cylinder was 40 mm *and the diameter of the rod ranged from* 1 to 12 mm. *The distance between the axes of the cylinder and the rod was varied between 40 and* 120 mm *and the Reynolds number ranged from* 1.5×10^4 *to* 6.2×10^4. *In the optimum configuration, the heat transfer on the front face of the cylinder increases remarkably relative to a single circular cylinder, and results in a 40% overall increase in heat transfer.* [DOI: 10.1115/1.2150832]

Keywords: forced convection heat transfer, heat transfer enhancement, flow control, circular cylinder

1 Introduction

Circular cylinders are employed by many practical applications, including multitube heat exchangers. The shape, size, and spacing of the heat exchanger tubes affect the flow pattern and the separated flow characteristics. In a heat exchanger, the lower the resistance and the higher the heat transfer, the better. In general, the flow patterns around in-line and staggered tube banks have their own characteristics, but many characteristics are based on those for a single isolated cylinder in an infinite fluid. Therefore, the flow control method for a single cylinder can be applied to several kinds of cylinder arrangements such as tandem, parallel and stagger with a little improvement.

Lesage and Gartshore [1] proposed a simple method for controlling the flow around bluff bodies. The surface flow around the bluff bodies was controlled by placing a small rod on the stagnation line upstream of a flat plate, a square cylinder, and a circular cylinder. This method resulted in a reduction in the drag and the fluctuating side force. Further investigation of this method produced several important conclusions, including the existence of a two-flow pattern and the optimum conditions for drag reduction [2]. Igarashi [3] applied a similar method for the flow control of a square prism. In this case, total drag with the small rod decreased by about 75% relative to the square prism without the small rod. This method has recently been applied in a staggered arrangement [4] for square prisms with various incidence angles [5].

Prasad and Williamson [6] used a small flat plate for drag reduction of a circular cylinder. The plate was placed upstream and parallel to the cylinder, and resulted in a system drag reduction of 62%.

Eckert et al. [7] reported up to 25% heat transfer improvements for free stream turbulence levels up to 7%. When the previously mentioned flow control method is applied to a circular cylinder, the cylinder's front face is exposed to the rod's wake, thereby enhancing the heat transfer.

The small rod was applied to the heat transfer enhancement of a square prism [8,9]. This flow control method enhanced overall heat transfer by 34% (0 deg angle to the flow) and 23% (45 deg angle to the flow) compared to a square prism without a small rod.

The present study investigates the potential for heat transfer enhancement when a rod is positioned upstream of a circular cylinder. The local and overall heat transfer for the cylinder are measured for varying rod sizes, distances between the rod and the cylinder, and Reynolds numbers, which were changed systematically. The relationship between the flow pattern and the heat transfer behavior was rediscovered and the optimum heat transfer conditions were established.

2 Experimental Device and Method

The configuration around the circular cylinder is shown in Fig. 1. Experiments were performed in a low speed wind tunnel with a 400 mm high, 150 mm wide, and 800 mm long working section. The circular cylinder diameter D was 40 mm, and the rod diameter d ranged from 1 to 12 mm. The longitudinal distance between the axes of the rod and the cylinder L was varied between 40 and 120 mm. The blockage ratio is 10% and the aspect ratio of the cylinder is 3.75. The free stream velocity U was varied between 4 and 24 m/s and the turbulent intensity was about 0.4% in this range. The Reynolds number based on D ranged from 1.5×10^4 to 6.2×10^4. A smoke tunnel was used to visualize the flow around the rod and the cylinder and a manometer was employed to measure the pressure distribution around the cylinder.

Figures 2(a) and 2(b) display a constant heat flux model and a constant temperature model. These two models have the same outer diameters sizes (40 mm) and were used for the local and average heat transfer measurements. The constant heat flux model was fabricated from a 5 mm thick acrylic resin pipe. The pipe was covered with two 0.02 mm thick stainless steel sheets. The sheets were connected in series electrically and heated by applying an alternating current to produce a constant heat flux condition. The temperature difference between the heated face and the free-stream was approximately 10°C. 0.1 mm diameter copper-constantan (C-C) thermocouples were attached to the underside of the stainless steel sheets at 10 deg intervals. The local heat transfer measurements for the constant heat flux condition were verified by comparing the overall heat transfer value with the value measured by the constant temperature model.

Figure 2(b) shows the constant temperature model. The diameter D is 40 mm. The model was fabricated from copper and a heater buried in the model was used to heat the cylinder. Six C-C thermocouples were attached near the model's surface. The surface temperature was held constant at approximately 6°C higher than the free-stream temperature, within ±0.05°C.

The effects of the blockage and aspect ratio on heat transfer are well known from Perkins et al. [10] and Chang et al. [11]. The overall and local Nusselt numbers increase with increasing blockage ratios and decreasing aspect ratios [10,11]. According to Refs. [10,11], the overall and local Nusselt numbers subjected to a 10% blockage and a 3.75 aspect ratio can be evaluated as 2% and above 14%, respectively. The effects of the blockage and aspect ratios were checked in advance and the results are shown in Fig. 3. These results include the combined effects of the blockage and

Contributed by the Heat Transfer Division of ASME for publication in the JOURNAL OF HEAT TRANSFER. Manuscript received November 17, 2004; final manuscript received September 15, 2005. Review conducted by Jay M. Khodadadi.

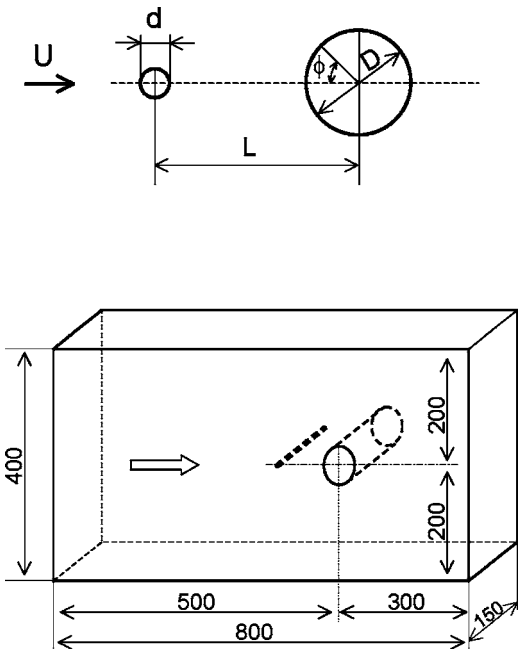

Fig. 1 Coordinate system and symbols

aspect ratio. In the present study, the overall Nusselt number of single cylinder is at most 6% higher than the previous overall Nusselt numbers reported by Igarashi and Hirata [12] and Zukauskas [13]. The reason for this difference between the estimated value (2% and above 14%) and the result (6%) seems to be due to the model being positioned too close to the outlet of the working section. Therefore, the effect of the distance between the center of the circular cylinder and the outlet of the working section is also investigated. The results are shown in Figs. 4(*a*) and 4(*b*). The effect of the distance, *x*, appears on rear face of the cylinder. The pressure coefficient on the rear face decreases and local Nusselt number on the rear face increases with increasing *x*. The upper and lower walls affect vortex shedding from the circular cylinder. The heat transfer data in present study accounts for the effects of the blockage, aspect ratio and distance from the outlet of the working section.

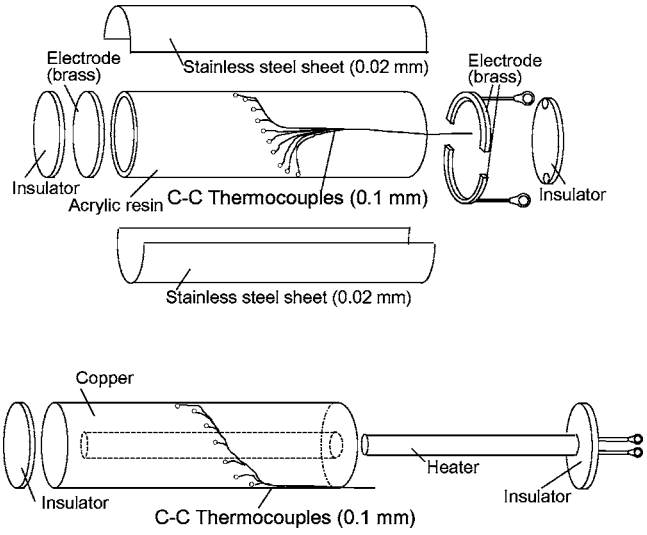

Fig. 2 Experimental models: (*a*) constant heat flux model and (*b*) constant temperature model

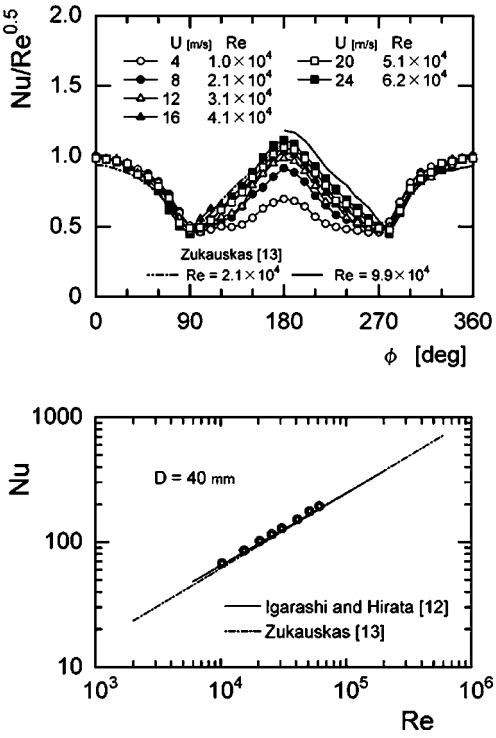

Fig. 3 Local and overall Nusselt number of a circular cylinder: (*a*) local Nusselt number and (*b*) overall Nusselt number

The experimental uncertainties were calculated using standard uncertainty analysis methods proposed by Kline [14]. The total uncertainty for the heat transfer coefficient $\Delta h/h$ is obtained by using the following equation:

$$\frac{\Delta h}{h} = \sqrt{\left(\frac{\Delta t}{t}\right)^2 + \left(\frac{\Delta q_{\text{in}}}{q_{\text{in}}}\right)^2 + \left(\frac{\Delta q_{\text{loss}}}{q_{\text{loss}}}\right)^2} \tag{1}$$

where $\Delta t/t$, $\Delta q_{\text{in}}/q_{\text{in}}$, and $\Delta q_{\text{loss}}/q_{\text{loss}}$ are the uncertainties of the measured temperature, the heat input, and the heat loss, respectively. The constant heat flux model produced the following values: $\Delta t/t=2\%$, $\Delta q_{\text{in}}/q_{\text{in}}=1\%$ and $\Delta q_{\text{loss}}/q_{\text{loss}}=5\%$. Therefore, the total uncertainty for the heat transfer coefficient is within 5.5%. The constant temperature model generated the following values: $\Delta t/t=0.8\%$, $\Delta q_{\text{in}}/q_{\text{in}}=0.2\%$, and $\Delta q_{\text{loss}}/q_{\text{loss}}=0.6\%$. For this case, the total uncertainty for the heat transfer coefficient is within 1.1%.

3 Flow Characteristics for a Circular Cylinder with a Rod

3.1 Flow Pattern. Figures 5(*a*)–5(*c*) display typical examples of the flow visualization around the circular cylinder. Figure 5(*a*) shows the flow around a single cylinder. Two flow patterns exist between the rod and cylinder, one with vortex shedding from the rod and one without. Figure 5(*b*) shows pattern A, the flow with vortex shedding from the rod. In this case, the front face of the circular cylinder is exposed to the rod's vortices. Figure 5(*c*) shows pattern B. In this case, the shear layer that separated from the rod attaches on the front face of the cylinder and a quasistatic vortex is formed between the rod and the cylinder. A previous paper [2] reported that the flow patterns depend upon the rod diameter d/D, the longitudinal distance between the axes of the circular cylinder and the rod L/D and the Reynolds number Re.

The existence of patterns A and B are classified on the L/D-d/D map presented in Fig. 6. Figures 6(*a*) and 6(*b*) are for $\text{Re}=1.5\times10^4$ and $\text{Re}=6.2\times10^4$, which are the minimum and maximum Reynolds numbers in this experiment. The open and

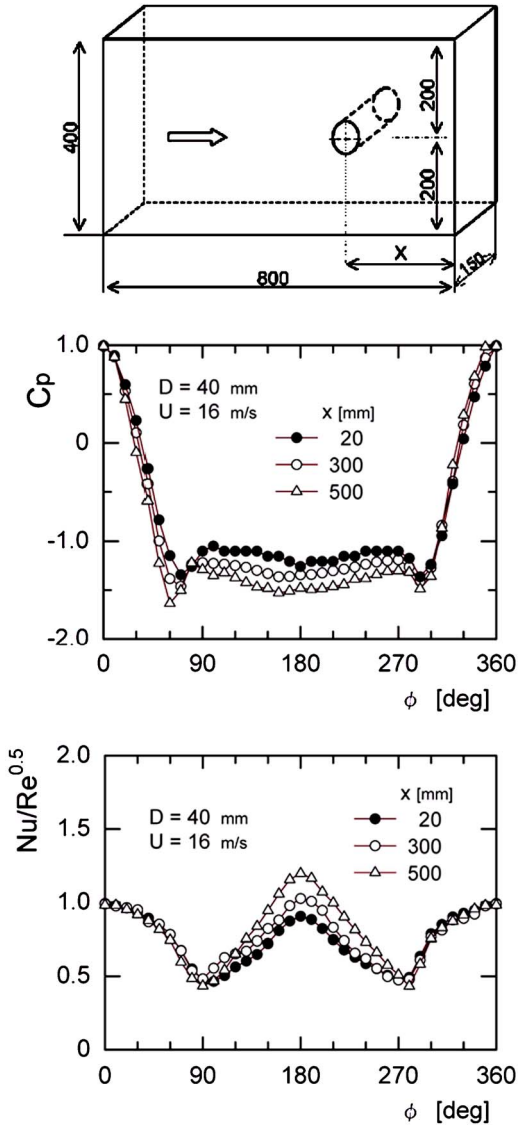

Fig. 4 Effect of distance *x* on a circular cylinder: (*a*) pressure distribution and (*b*) local Nusselt number

closed circles correspond to patterns A and B, respectively. A dash-dotted line separates pattern A from pattern B. Pattern A occurs on the right-hand side of the line and pattern B occurs on the left-hand side. According to the previous paper [2], the change in flow pattern depends on the rod diameter d/D, distance between the axes of the rod and circular cylinder L/D, and the Reynolds number Re. The demarcation line can be calculated using the following equation [2]:

$$d/D = 0.02(L/D)^n, \quad n = 2.8 + 2 \times 10^{-5}\ \mathrm{Re}$$

$$(0.025 \leqq d/D \leqq 0.25, 1.0 \leqq L/D \leqq 3.0) \qquad (2)$$

3.2 Flow Characteristics. The distributions of the pressure coefficient *Cp* around the cylinder for patterns A and B are shown in Fig. 7. The figure reveals remarkable differences between the two patterns on the front and rear faces of the cylinder. For pattern A, the pressure coefficient on the front face decreases to 0.7. This can be attributed to a decreasing velocity toward the front stagnation point on the cylinder. For pattern B, the pressure coefficient on the front region ($\phi = -25$ deg to 25 deg) is negative because a quasistatic vortex has formed between the rod and cylinder. *Cp* reaches a maximum at the attachment region ($\phi = \pm 35$ deg) of the

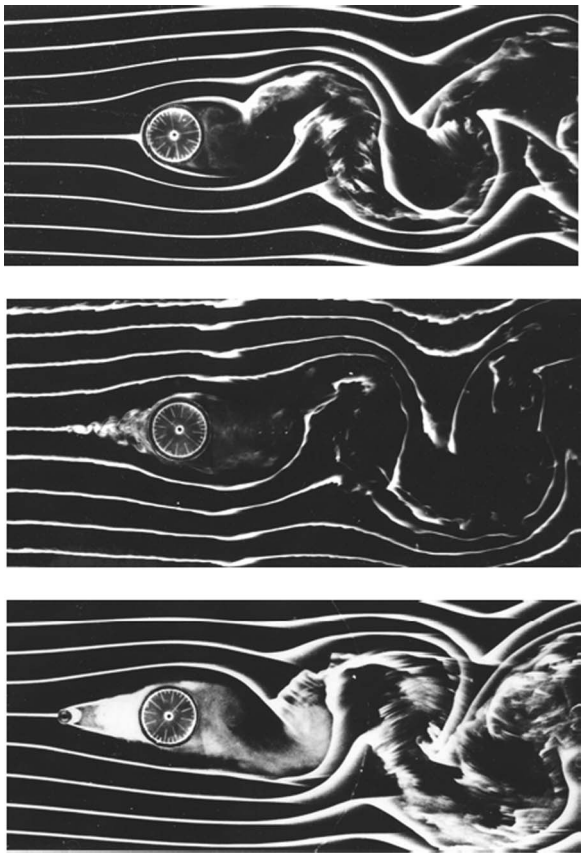

Fig. 5 Flow visualizations around the cylinder ($Re = 2.1 \times 10^4$): (*a*) without rod; (*b*) pattern A ($L/D = 1.75$, $d/D = 0.05$); and (*c*) pattern B ($L/D = 1.75$, $d/D = 0.25$)

shear layer that separated from the rod. The base pressure coefficient Cp_b for pattern B is considerably higher than the one for pattern A because the vortex formation region for pattern B is longer.

A flow visualization using the oil-film method was conducted to measure the separation point on the cylinder. Figures 8(*a*)–8(*d*) display photographs of the surface oil pattern for $L/D = 1.75$ and $d/D = 0.25$, which produces pattern B. When the Reynolds number increases to 3.1×10^4, 4.1×10^4, and 6.2×10^4, a separation

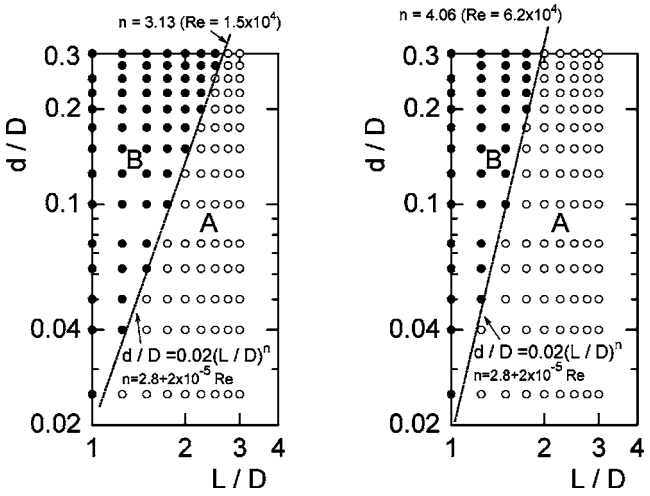

Fig. 6 Classification of the flow patterns: (*a*) $Re = 1.5 \times 10^4$ and (*b*) $Re = 6.2 \times 10^4$

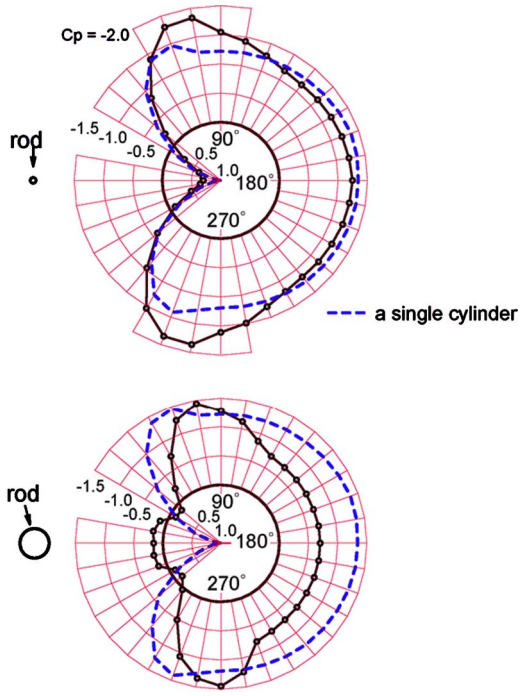

Fig. 7 Pressure coefficient distributions around the cylinder (Re=4.1×10⁴): (*a*) pattern A (*L*/*D*=1.75, *d*/*D*=0.05) and (*b*) pattern B (*L*/*D*=1.75, *d*/*D*=0.25)

bubble is evident over Re=3.1×10⁴. When the separation bubble is formed, the flow separates in front of the separation bubble, attaches behind the separation bubble and finally separates. The separation point moves downstream from 87 deg to 114 deg, 116 deg, and 118 deg, respectively.

Figure 9 represents the effect of the Reynolds number as a combination of three diagrams. The diagrams show the final separation point, the Strouhal number and the drag coefficient [15].

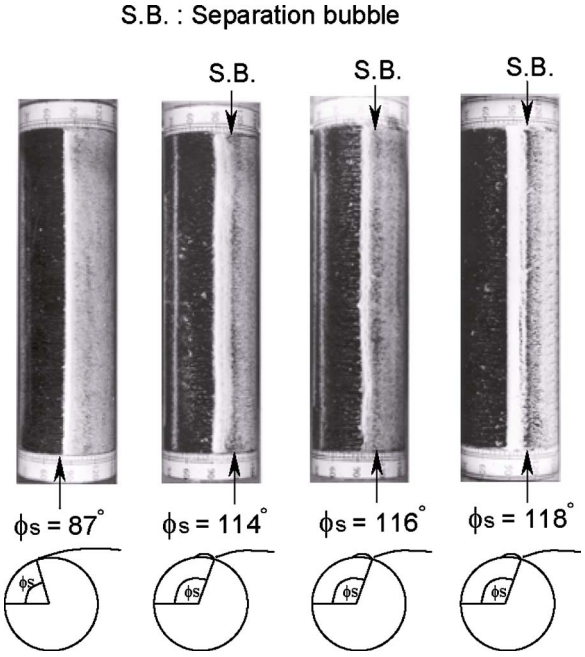

Fig. 8 Surface oil flow patterns (*d*/*D*=0.25, *L*/*D*=1.75, pattern B): (*a*) Re=1.5×10⁴; (*b*) Re=3.1×10⁴; (*c*) Re=4.1×10⁴; and (*d*) Re=6.2×10⁴

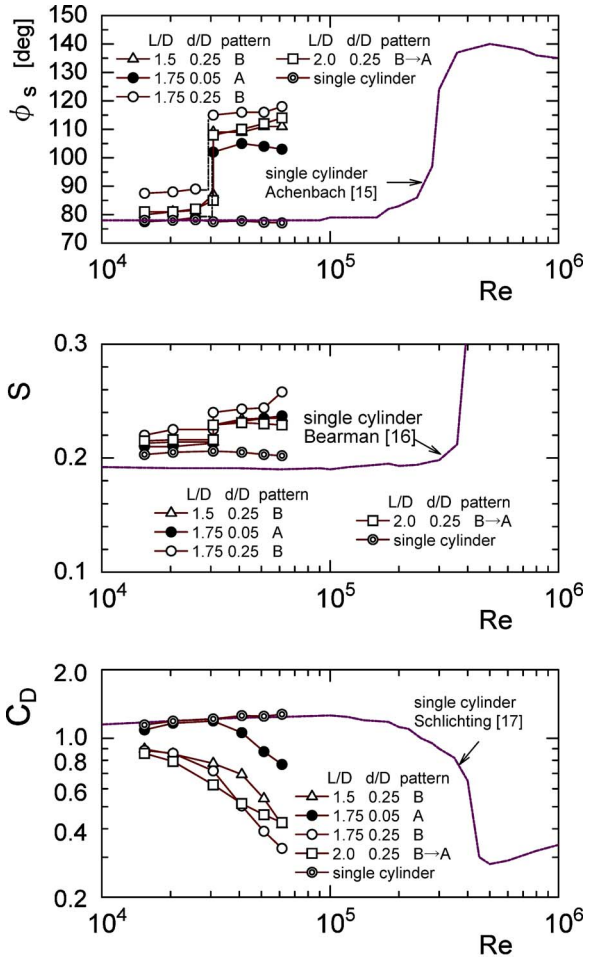

Fig. 9 Flow characteristics: (*a*) separation point; (*b*) Strouhal number; and (*c*) drag coefficient

Figure 9(*a*) displays the separation point ϕ_s on the cylinder. The dotted line represents the separation point on a single cylinder. When the rod is introduced, the separation point suddenly shifted downstream at about Re=3×10⁴. This can be attributed to the formation of a separation bubble. Bearman [16] previously reported that the separation bubble forms at Re=3.4×10⁵, the critical Reynolds number [17]. The same phenomenon occurs at about Re=3×10⁴ in the current experiments because of the turbulent transition. For pattern A, the front surface of the cylinder is exposed the wake of the rod, so that the front surface flow is turbulent. For pattern B, the attachment flow on the cylinder surface, which is the separated shear layer from the rod, is also turbulent.

Figure 9(*b*) shows the Strouhal number *S* calculated from the vortex shedding frequency behind the cylinder. The vortex shedding frequency is determined primarily by the width between the shear layers, which depends upon the separation point. The dotted line in the figure represents the Strouhal number for the single cylinder. When the rod is introduced, the Strouhal number increases dramatically at Re=3×10⁴, which corresponds to the sudden shift of the separation point downstream, decreasing the width between the separated shear layers.

The pressure drag coefficient C_D of the circular cylinder is shown in Fig. 9(*c*). The dotted line represents the C_D values for the single cylinder. In general, the drag coefficient decreases with an increasing Reynolds number in Re=3.5×10⁴–4.5×10⁴ (critical and supercritical region). This relationship is particularly distinct around Re=3×10⁴ due to the same reasons as the drag reduction of a single cylinder in the critical and super critical

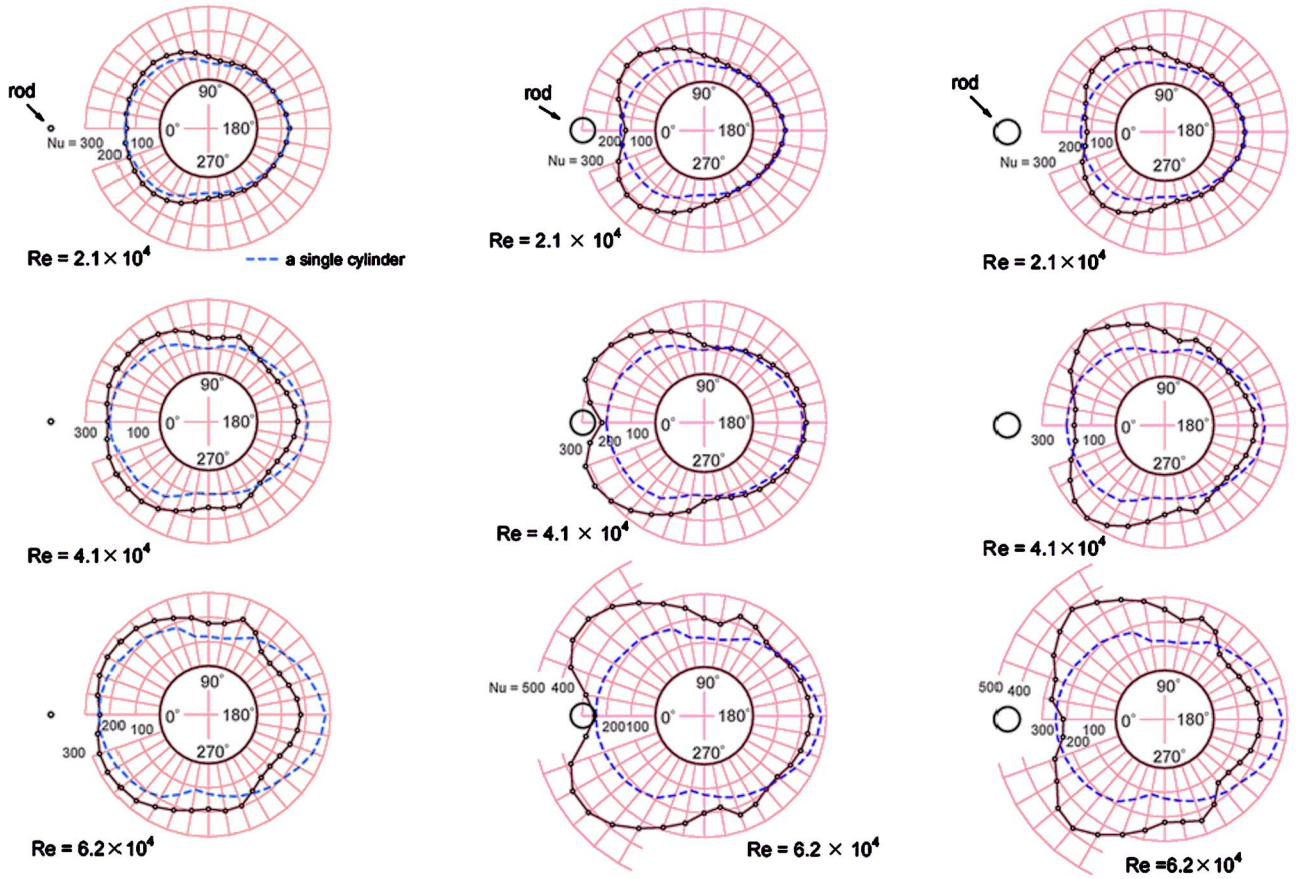

Fig. 10 Local Nusselt number distributions around the cylinder: (*a*) pattern A ($L/D=1.75$, $d/D=0.05$); (*b*) pattern B ($L/D=1.25$, $d/D=0.25$); and (*c*) pattern B ($L/D=1.75$, $d/D=0.25$)

Reynolds number region. The pressure drag reduction is due to the decreasing pressure on the front face of the cylinder and the displacement of the separation point. Therefore, pattern B is more effective in reducing drag than pattern A.

4 Heat Transfer Characteristics around a Circular Cylinder with a Rod

4.1 Local Heat Transfer. Figures 10(*a*)–10(*c*) show the local Nusselt number distributions around the cylinder for three cases. Figure 10(*a*) depicts a typical case for pattern A, while Figs. 10(*b*) and 10(*c*) are for pattern B. Figure 10(*b*) shows the optimum conditions for overall heat transfer enhancement (described later) and Fig. 10(*c*) shows the optimum conditions for drag reduction [2].

In pattern A, the Reynolds number increases to over 2.1×10^4 and the heat transfer coefficients in the area in front of the cylinder, between $\phi=-130$ deg and 130 deg, are higher than for a single cylinder. However, in the area behind the cylinder, between $\phi=130$ deg and -130 deg, the heat transfer coefficient is lower than for a single cylinder. As the Reynolds number increases, these characteristics become even more distinct.

The heat transfer coefficients for Pattern B are considerably higher at about $\phi=\pm30$ deg$\sim\pm50$ deg, which correspond to the separated shear layer attachment points. The values and positions of these maximum Nusselt numbers for $L/D=1.25$, $d/D=0.25$ are higher and at smaller angles of ϕ than those for $L/D=1.75$, $d/D=0.25$. The heat transfer coefficients in the frontal stagnation area ($\phi=-10$ deg to 10 deg), though, are lower than those for a single cylinder due to the quasistatic vortex. The heat transfer coefficient characteristics on the rear area between $\phi=130$ deg and -130 deg are same as those for pattern A. This is expected because the separation point on the cylinder shifts downstream with an increasing Reynolds number, causing the vortex formation region to also be short. As a result, the most effective heat transfer region for the circular cylinder is on the front face for both flow patterns.

The effect of L/D and d/D on the cylinder's Nusselt number is shown in Figs. 11(*a*)–11(*d*). Figure 11(*a*) displays the local Nusselt number distributions for $L/D=1.0$, $d/D=0.25$ for pattern B, where most of the front face is buried in the rod's wake. Therefore, the local Nusselt number distribution on the front face of the cylinder for $L/D=1.0$ is lower than that for $L/D=1.25$ in Fig. 10(*b*). Decreasing the rod diameter d/D from 0.25 to 0.15 [Fig. 10(*c*) and Fig. 11(*c*)] results in a conversion from pattern B to pattern A. In addition, a couple of the peaks vanish and very little heat transfer enhancement is gained. The effect of L/D is evident by comparing Figs. 10(*b*) and 10(*c*) and Figs. 11(*a*) and 11(*d*). The flow pattern changes from B to B to B to A when L/D is increased from 1.0 to 1.25 to 1.75 to 2.5. For pattern A, the local Nusselt numbers on most of the cylinder surface areas except for the rear area for $L/D=1.75$, $d/D=0.15$ in Fig. 11(*c*) are higher than that for $L/D=1.75$, $d/D=0.05$ in Fig. 10(*a*). Because of the bigger rod, a larger scale wake from the rod for pattern A is generated. Figures 10(*b*) and 11(*b*) indicate that a rod that is too large cannot effectively enhance heat transfer because the majority of the front face is buried in the rod's wake, for the same reason as when the rod is positioned to close to the cylinder. For pattern B, the attachment on the front surface of the cylinder is the decisive factor for heat transfer enhancement, requiring the optimum conditions for L/D and d/D.

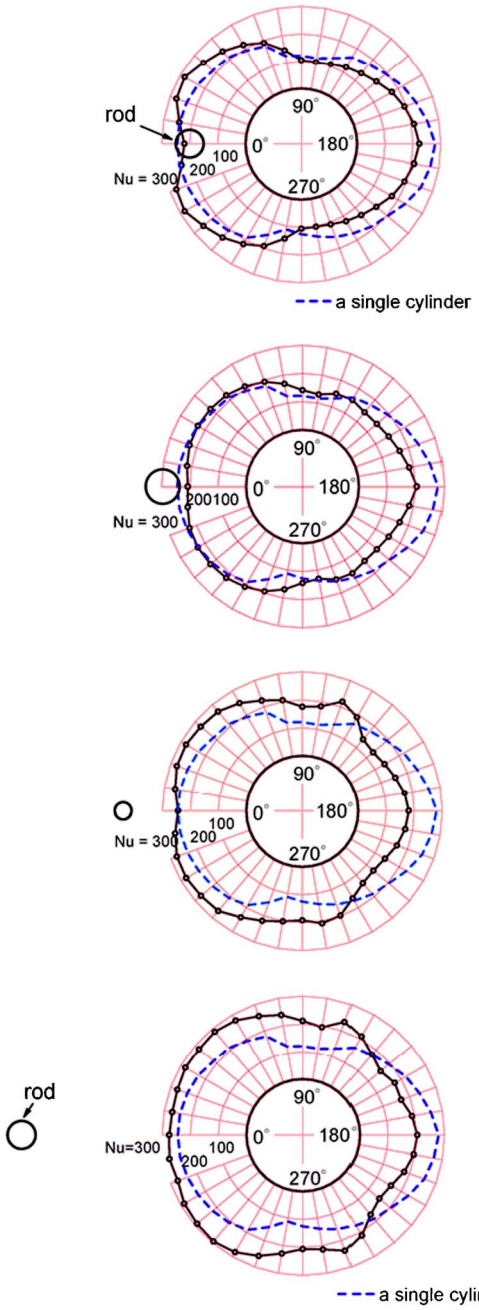

Fig. 11 Local Nusselt number distributions around the cylinder Re=6.2×10⁴: (*a*) *L*/*D*=1.0, *d*/*D*=0.25, pattern B; (*b*) *L*/*D*=1.25, *d*/*D*=0.3, pattern B; (*c*) *L*/*D*=1.75, *d*/*D*=0.15, pattern A; and (*d*) *L*/*D*=2.5, *d*/*D*=0.25, pattern A

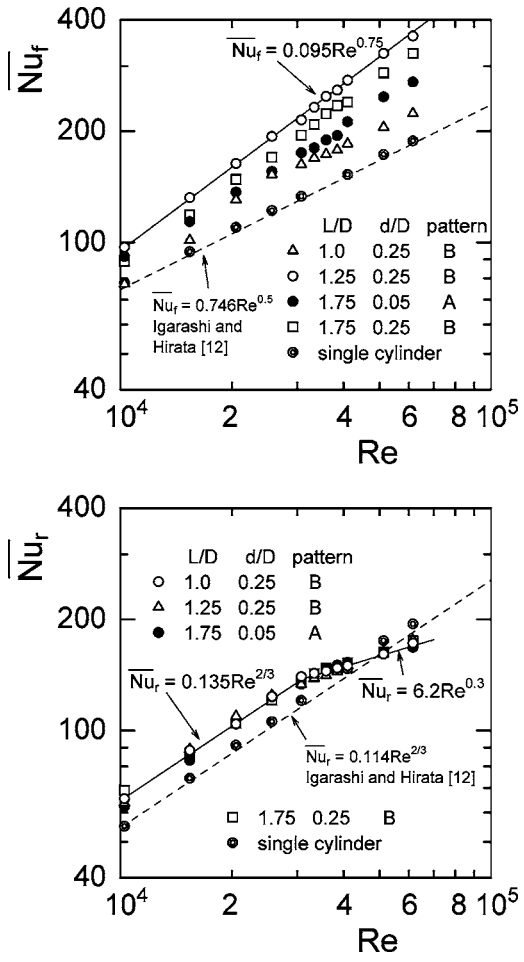

Fig. 12 Average Nusselt number: (*a*) front face and (*b*) rear face

4.2 Average Heat Transfer. Figure 12 displays the variations in the average Nusselt numbers on the front face ($-90\ \text{deg} \leqslant \varphi \leqslant 90\ \text{deg}$), the rear face ($90\ \text{deg} < \phi < -90\ \text{deg}$) and the overall values as a function of the Reynolds number.

Figure 12(*a*) shows the average Nusselt number on the front face $\overline{Nu}_f$. For $L/D=1.25$, $d/D=0.25$ and pattern B, the Nusselt number increases with a slope of 0.75. This value is greater than the 0.5 "laminar slope" value. In fact, the Nusselt number at Re $=6.2\times10^4$ is almost double of that for a single cylinder. The heat transfer from the front surface of the cylinder is enhanced by the higher level of rod wake turbulence in the pattern A case, but this enhancement is less than for the pattern B case in which the two peaks in the Nusselt number distributions appear at the reattachment points of the rod shear layers.

Figure 12(*b*) shows the average Nusselt number on the rear face $\overline{Nu}_r$. The average Nusselt number trends for patterns A and B are nearly the same. That is, the average Nusselt number increases with $Re^{0.67}$ when $Re \leqq 3.2\times10^4$ and with $Re^{0.3}$ when $Re > 3.2\times10^4$. According to Fig. 9, the flow around the cylinder drastically changes above $Re=3\times10^4$. The separation points shift aft rapidly, the width of the wake decreases and, consequently, the Strouhal number increases. When the Reynolds number increases over $Re=4.8\times10^4$, $\overline{Nu}_r$ is less than the single cylinder value. For $L/D=1.25$, $d/D=0.25$, the value of the Nusselt number at Re $=6.2\times10^4$ is 10% smaller than the single cylinder value.

The cylinder's overall Nusselt number values, Nu_m, are shown in Fig. 13. The overall Nusselt numbers for the single cylinder and the $L/D=1.25$, $d/D=0.25$ case were both obtained using the constant heat flux model and the constant temperature model shown in Fig. 13(*a*). Both Nusselt numbers agree within ±2%. Nu_m was calculated using the local heat transfer model as $(\overline{Nu}_f+\overline{Nu}_r)/2$. This figure describes the optimum conditions for the $L/D=1.25$, $d/D=0.25$ case. Here, Nu_m increases with a slope of 0.66, which is greater than the 0.6 single cylinder value reported by Zukauskas [13]. This Nu_m value at $Re=6.2\times10^4$ is over 40% higher than the single cylinder value. Figure 13(*b*) shows a comparison of square prisms controlled by a small rod. The L/D and d/D conditions in the figure are the optimum conditions for heat transfer enhancement. By using a small control rod, the heat transfer of a circular cylinder is enhanced to values even higher than that of a square prism.

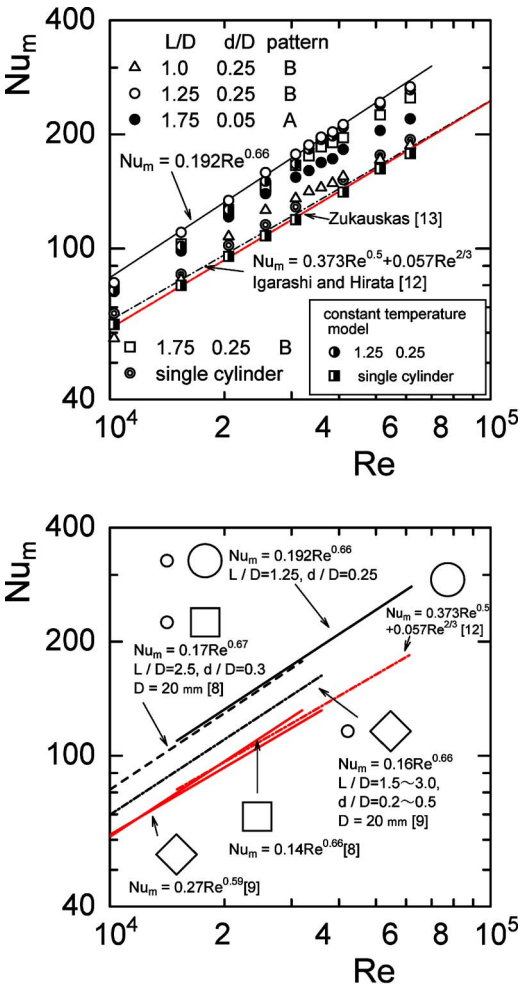

Fig. 13 Overall Nusselt number: (*a*) variation with *L*/*D* and *d*/*D* and (*b*) comparison of the present study with square prisms

The heat transfer enhancement rates for the cylinder, Nu_m/Nu_{m0}, are shown in Figs. 14(*a*)–14(*c*). Nu_{m0} is the overall Nusselt number of the single cylinder. According to Eq. (2), the demarcation lines for patterns A and B for $Re=2.1\times10^4$, $Re=4.2\times10^4$, and $Re=6.2\times10^4$ are $d/D=0.02(L/D)^{3.22}$, $d/D=0.02(L/D)^{3.62}$, and $d/D=0.02(L/D)^{4.06}$, respectively. Further, pattern B always enhances the heat transfer more effectively than pattern A. The optimum condition was found to be approximately $L/D=1.25$ and $d/D=0.25$. Heat transfer enhancement declines when the rod is larger or the distance is shorter than the optimum values.

5 Conclusions

Experimental studies were performed on the fluid flow around a circular cylinder whose flow was controlled by a rod. The local and average heat transfers were also investigated. The Reynolds number for these experiments was based on D and ranged from 1.5×10^4 to 6.2×10^4. The diameter ratio between the cylinder and the rod, d/D, ranged from 0.025 to 0.3 and the distance ratio between the axes of the circular cylinder and the rod, L/D, was varied between 1.0 and 3.0.

The results indicated that the most effective heat transfer region for the circular cylinder was the front face for both the flow patterns. However, pattern B enhanced the heat transfer more effectively than pattern A for all Reynolds numbers. The optimum conditions for overall heat transfer enhancement was found to be at $L/D=1.25$ and $d/D=0.25$. The resulting overall Nusselt number value at $Re=6.2\times10^4$ is over 40% higher than the single cylinder value.

Nomenclature

C_D = pressure drag coefficient of circular cylinder
C_p = pressure coefficient $=(p-po)/0.5\ \rho\ U^2$
D,d = diameters of circular cylinder and rod
f = vortex shedding frequency from circular cylinder
h = local heat transfer coefficient
$\overline{h_f}$ = average heat transfer coefficient on the front face
$\overline{h_r}$ = average heat transfer coefficient on the rear face
h_m = overall heat transfer coefficient
L = longitudinal distance between the axes of circular cylinder and rod
Nu = local Nusselt number $=hD/\lambda$
$\overline{Nu}_f$ = average Nusselt numbers on the front face $=\overline{h_f}D/\lambda$

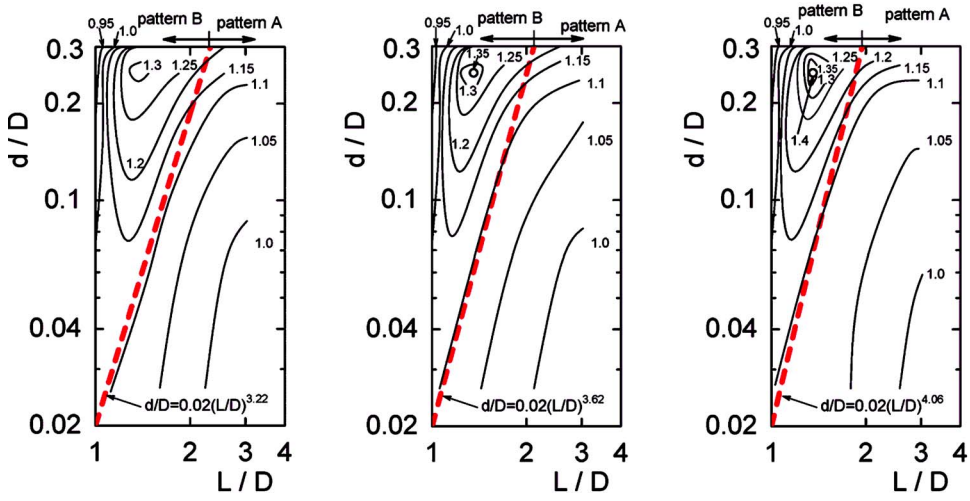

Fig. 14 Contour map of the rate of heat transfer enhancement of the cylinder: (*a*) Re=2.1 $\times10^4$; (*b*) Re=4.1$\times10^4$; and (*c*) Re=6.2$\times10^4$

$\overline{\mathrm{Nu}_r}$ = average Nusselt numbers on the rear face $=\overline{h}_r D/\lambda$

Nu_m = overall Nusselt number $= h_m D/\lambda$

p, po = static pressure and free stream static pressure

Re = Reynolds number $= UD/v$

S = Strouhal number $= fD/U$

U, u, u' = free stream velocity, time mean velocity, fluctuating velocity

λ, v, ρ = thermal conductivity, kinematic viscosity, and density of fluid

Subscript

o = without rod

References

[1] Lesage, F., and Gartshore, L. S., 1987, "A Method of Reducing Drag and Fluctuating Side Force on Bluff Bodies," J. Wind. Eng. Ind. Aerodyn., **25**, pp. 229–245.

[2] Tsutsui, T., and Igarashi, T., 2002, "Drag Reduction of a Circular Cylinder in an Air-Stream," J. Wind. Eng. Ind. Aerodyn., **90**, pp. 527–541.

[3] Igarashi, T., 1997, "Drag Reduction of a Square Prism by Flow Control Using a Small Rod," J. Wind. Eng. Ind. Aerodyn., **69–71**, pp. 141–153.

[4] Zhang, P. F., Wang, J. J., Lu, S. F., and Mi, J., 2005, "Aerodynamic Characteristics of a Square Cylinder With a Rod in a Staggered Arrangement," Exp. Fluids, **35-4**, pp. 494–502.

[5] Sarioglu, M., Akansu, Y. E., and Yavuz, T., 2005, "Control of Around Square Cylinders at Incidence by Using a Rod," AIAA J., **43–7**, pp. 1419–1426.

[6] Prasad, A., and Williamson, C. H. K., 1997, "A Method for the Reduction of Bluff Body Drag," J. Wind. Eng. Ind. Aerodyn., **69–71**, pp. 155–167.

[7] Eckert, E. G. G., and Drake, Jr., R. M., *Heat and Mass Transfer*, 2nd ed., McGraw-Hill, New York, p. 242.

[8] Tsutsui, T., Igarashi, T., and Nakamura, H., 2001, "Drag Reduction and Heat Transfer Enhancement of a Square Prism," JSME Int. J., Ser. B, **44–4**, pp. 575–583.

[9] Igarashi, T., and Tsutsui, T., 1998, "Enhancement of Heat Transfer and Reduction of Drag of a Square Prism Arranged Diamond-Shape in an Air Stream," in *Proceedings of the 11th IHTC*, Kyongju, Korea, Vol. 5, pp. 261–266.

[10] Perkins, Jr., H. C., and Leppert, G., 1964, "Local Heat-Transfer Coefficients on a Uniformly Heated Cylinder," Int. J. Heat Mass Transfer, **7**, pp. 143–158.

[11] Chang, B. H., and Mills, A. F., 2004, "Effect of Aspect Ratio on Forced Convection Heat Transfer From Cylinders," Int. J. Heat Mass Transfer, **47**, pp. 1289–1296.

[12] Igarashi, T., and Hirata, M., 1977, "Heat Transfer in Separated Flows, Part 2: Theoretical Analysis," Heat Transfer-Jpn. Res., **6**(3), pp. 60–78.

[13] Zukauskas, A., 1972, "Heat Transfer From Tube in Crossflow," *Advances in Heat Transfer*, Academic, New York, Vol. 8, pp. 93–160.

[14] Kline, S. J., 1985, "The Purposes of Uncertainty Analysis," ASME J. Fluids Eng., **107**, pp. 153–160.

[15] Achenbach, E., 1968, "Distribution of Local Pressure and Skin Friction Around a Circular Cylinder in Cross-Flow up to $\mathrm{Re} = 5 \times 10^6$," J. Fluid Mech., **34**, part 4, pp. 625–639.

[16] Bearman, P. W., 1969, "On Vortex Shedding From a Circular Cylinder in the Critical Reynolds Number Regime," J. Fluid Mech., **37**, part 3, pp. 577–585.

[17] Schlichting, H., 1968, *Boundary Layer Theory*, 6th ed., McGraw-Hill, New York, p. 17.

Choongho Yu[1]
Sanjoy Saha
Jianhua Zhou
Li Shi[2]

Department of Mechanical Engineering
and Center for Nano and Molecular Science and Technology,
Texas Materials Institute,
The University of Texas at Austin,
Austin, Texas 78712

Alan M. Cassell
Brett A. Cruden
Quoc Ngo
Jun Li

Center for Nanotechnology,
NASA Ames Research Center,
Moffett Field, CA 94035

Thermal Contact Resistance and Thermal Conductivity of a Carbon Nanofiber

We have measured the thermal resistance of a 152-nm-diameter carbon nanofiber before and after a platinum layer was deposited on the contacts between the nanofiber and the measurement device. The contact resistance was reduced by the platinum coating for about 9–13% of the total thermal resistance of the nanofiber sample before the platinum coating. At a temperature of 300 K, the axial thermal conductivity of the carbon nanofiber is about three times smaller than that of graphite fibers grown by pyrolysis of natural gas prior to high-temperature heat treatment, and increases with temperature in the temperature range between 150 K and 310 K. The phonon mean free path was found to be about 1.5 nm and approximately temperature-independent. This feature and the absence of a peak in the thermal conductivity curve indicate that phonon-boundary and phonon-defect scattering dominate over phonon-phonon Umklapp scattering for the temperature range. [DOI: 10.1115/1.2150833]

Keywords: contact resistance, nanofiber, thermal conductivity, uncertainty analysis, platinum coating, nanoscale contact, thermal constriction resistance, phonon scattering

Introduction

Diamond, graphite, and graphite fibers have been known as excellent heat conductors with a high thermal conductivity up to 3000 W/m-K [1–3]. Recently, the axial thermal conductivity of individual multiwalled carbon nanotubes (CNTs) [4] has been found to be higher than 3000 W/m-K at a temperature of 300 K [5]. It was also found that the effective thermal conductivity of CNT mats [6] and CNT bundles [7] was one or two orders of magnitude lower than that of individual defect-free CNTs due to the large thermal contact resistance between adjacent CNTs in the bundles.

It has been suggested that CNTs and carbon nanofibers (CNFs) can be used as thermal interface materials to enhance contact thermal conductance for electronic packaging applications. Several groups have reported mixed experimental results from no improvements to large improvements in the thermal contact conductance due to the CNTs and CNFs [8–12]. These mixed results can be caused by the difference in surface coverage and perpendicular alignment of the CNTs or CNFs. Moreover, the results can be affected by two other factors. First, the CNTs and CNFs grown using different methods possess different defect densities and different intrinsic thermal conductivities. Secondly, the contact thermal resistance of the nanometer scale point and line contacts between a CNT or CNF and a planar surface can be high due to enhanced phonon-boundary scattering at the nanocontacts.

We have used a microfabricated device to measure the thermal resistance of an individual CNF from a vertically aligned CNF film for applications as thermal interface materials. The measurement was conducted before and after a platinum (Pt) layer was deposited on the contacts between the CNF and the microdevice so as to investigate the thermal contact resistance between the CNF and a planar surface. The contact resistance was reduced by the platinum coating for about 9–13% of the total thermal resistance of the nanofiber sample before the Pt coating. At temperature 300 K, the obtained axial thermal conductivity of the carbon nanofibers was about three times smaller than that of graphite fibers grown by pyrolysis of natural gas prior to high-temperature heat treatment.

Experimental Methods

Nanostructure Growth. CNFs were grown using a plasma enhanced chemical vapor deposition (PECVD) method as described previously [13]. Briefly, silicon substrates with a predeposited 30-nm-thick Ti barrier layer and a 30-nm-thick Ni catalyst layer were subjected to a glow discharge at a dc bias of 585 V, 500 W, and 0.85 A under a total flow of 100 standard cubic centimeter per minute (sccm) of 4:1 NH_3:C_2H_2 process gas mixture at 4 Torr for 45 min. CNF growth rate under these conditions was approximately 500 nm/min. Cross-sectional transmission electron micrographs (Fig. 1) were obtained to investigate the CNF quality and graphitic microstructure. The CNFs possessed cone angles between 5°–20° with typical cone angles around 10° (Fig. 1(*c*)).

Measurement Procedure. The measurement was conducted with the use of a previously reported method based on a microdevice. A detailed description of the measurement method can be found in Ref. [7]. In brief, the microdevice consists of two symmetric silicon nitride (SiN_x) membranes suspended by long SiN_x beams, as shown in Fig. 2(*a*). A Pt serpentine line was patterned on each membrane and used as a heater and resistance thermometer (RT). A nanofiber deposited from a suspension was trapped between the two membranes. When a dc current (I) was supplied

[1]Current address: Materials Sciences Division, Lawrence Berkeley National Laboratory, Berkeley, CA 94720.

[2]Author to whom correspondence should be addressed; e-mail: lishi@mail.utexas.edu

Contributed by the Heat Transfer Division of ASME for publication in the JOURNAL OF HEAT TRANSFER. Manuscript received December 20, 2004; final manuscript received September 18, 2005. Review conducted by C. P. Grigoropoulos.

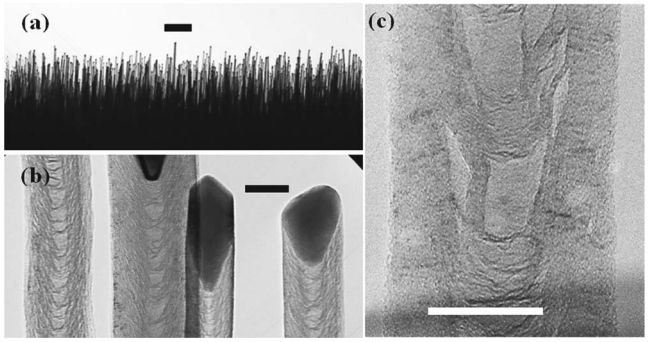

Fig. 1 Cross-sectional transmission electron micrographs of the as grown carbon nanofibers obtained from PECVD. Panel (*a*) shows a low magnification image depicting the vertical orientation and alignment of the carbon nanofibers. Panel (*b*) shows a higher magnification image which reveals the microstructural arrangement of the graphitic sheets in the fibers and panel (*c*) details the disordered crystalline morphology that reveals nanofiber cone angles around 10 deg. Scale bars are 2 μm, 50 nm, and 20 nm, respectively, for (*a*), (*b*), and (*c*).

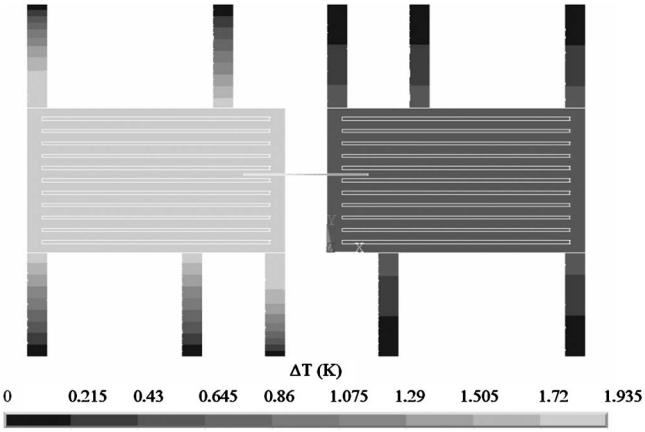

Fig. 3 Calculated temperature distribution in the measurement device. Each membrane is 25 μm long, 14 μm wide, and 0.5 μm thick. Each of the ten supporting beams of the actual device was 210 μm long and 2 μm wide. In the calculation, the beam length was scaled down to 10 μm with the thermal resistance of the beams kept the same by rescaling the thermal conductivity of the beams. The edges of the RTs and the nanowire are highlighted in white. The contact resistance per unit length between the nanofiber and the membrane was taken to be 0.03 Km/W.

to one Pt RT to raise the temperature of one membrane, part of the Joule heat generated in the heating membrane was conducted through the carbon nanofiber to the other (sensing) membrane.

The temperature distribution in each membrane can be assumed to be uniform compared to the average temperature rise in the membrane because the internal thermal resistance of the membrane is on the order of 10^5 K/W, which is two orders of magnitude smaller than either the sample thermal resistance or the thermal resistance of the five SiN_x beams. To verify the temperature uniformity, we have used a commercial finite element package (ANSYS) to calculate the three-dimensional (3D) temperature distribution in the measurement device. The top view of the calculated temperature distribution is shown in Fig. 3. For a device with ten supporting beams of the length $L=210$ μm, the maximum temperature difference in the heating (or sensing) membrane is 1.5% (or 6.5%) of the temperature rise in the membrane. For another design with $L=420$ μm, the maximum temperature difference in the heating (or sensing) membrane is 1.8% (or 3.1%) of the temperature rise in the membrane.

The two Pt RTs were used to measure the temperature rises on the heating and sensing membranes at different I values, i.e., $\Delta T_h(I) \equiv T_h(I) - T_h(I=0)$ and $\Delta T_s(I) \equiv T_s(I) - T_s(I=0)$, respectively. The thermal conductance (G_b) of the five beams supporting each membrane and the thermal conductance (G_m) of the sample were obtained as

$$G_b = \frac{Q_h + Q_L}{\Delta T_h + \Delta T_s} \tag{1a}$$

and

$$G_m = G_b \frac{\Delta T_s}{\Delta T_h - \Delta T_s} \tag{1b}$$

where Q_h is the Joule heat dissipation in the Pt RT on the heating membrane, and Q_L is the Joule heat dissipation in one of the two identical Pt leads supplying the dc heating current to the heating RT.

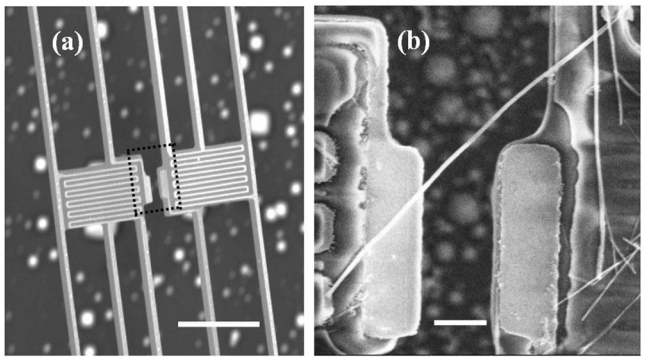

Fig. 2 (*a*) A scanning electron microscopy (SEM) image of the microdevice before the nanofiber was deposited. (*b*) A SEM image of a rectangular portion in (*a*) showing a carbon nanofiber bridging two membranes. The scale bars correspond to 20 μm and 2 μm, respectively, in (*a*) and (*b*).

Data Processing and Uncertainty Analysis. The measurement uncertainty of this method was discussed previously for the case of a single point measurement at a fixed I value [7]. To improve the measurement uncertainty, we ramped I from zero to a negative maximum ($-I_{\max}$), from $-I_{\max}$ back to zero, from zero to a positive maximum ($I_{\max}$), and from $I_{\max}$ back to zero. One ramping cycle took about 11 min. During each ramping cycle, a total number of $N=203$ sets of measurements were taken. G_b was obtained as the slope of a least-square linear curve fit of $Q \equiv (Q_h + Q_L)$ as a function of $(\Delta T_h + \Delta T_s)$ according to Eq. (1*a*), as illustrated in Fig. 4(*a*). The ratio G_m/G_b was then obtained as the slope of a linear curve fit of the measured ΔT_s as a function of the measured $(\Delta T_h - \Delta T_s)$ according to Eq. (1*b*), as shown in Fig. 4(*b*). G_m is then obtained as $G_m = G_b(G_m/G_b)$.

The uncertainty in each G_m measurement, i.e., U_{G_m}, was calculated from the uncertainties in G_b and G_m/G_b, i.e., U_{G_b} and U_{G_m/G_b}, according to

$$\frac{U_{G_m}}{G_m} = \sqrt{\left(\frac{U_{G_b}}{G_b}\right)^2 + \left(\frac{U_{G_m/G_b}}{G_m/G_b}\right)^2} \tag{2}$$

U_{G_b} and U_{G_m/G_b} were calculated as the uncertainties in the slope of the corresponding least-square linear fitting according to the error propagation method of Coleman and Steele [14]. Both random and systematic errors in individual (X_i, Y_i) data set were

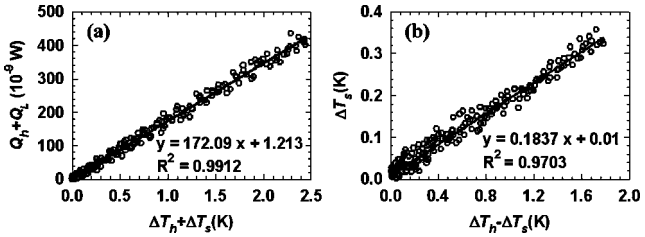

Fig. 4 (*a*) Measurement results of Q_h+Q_L plotted as a function of $\Delta T_h+\Delta T_s$; (*b*) Measurement results of ΔT_s plotted as a function of $\Delta T_h-\Delta T_s$. Also shown in each figure are the equation and the square of the Pearson product moment correlation coefficient (R^2) of the linear curve fitting.

accounted for by this method.

During each ramping cycle of the measurement, four (X_i, Y_i) data sets were measured at the same I magnitude. The random uncertainties in Y_i and X_i are calculated as $P_{Y_i}=t_{\upsilon,95}S_{Y_i}$ and $P_{X_i}=t_{\upsilon,95}S_{X_i}$, where $t_{\upsilon,95}=3.182$ is the t distribution for a $\upsilon=3$ degrees of freedom corresponding to a sample size of four at a confidence level of 95%, and S_{Y_i} (or S_{X_i}) is the sample standard deviation of the four Y_i (or X_i) measurement results at the same I magnitude.

As discussed by Brown et al. [15], systematic errors that are a fixed value or "percent of full scale" have no influence on the uncertainty of the slope and thus do not need to be accounted for. On the other hand, a systematic error of a second type that is a function of the magnitude of the variables, such as those of a "percent of reading" nature, can cause a nonzero systematic uncertainty in the slope of the linear curve fit. This second type of systematic errors in the measurement results of ΔT_h, ΔT_s, Q_L, and Q_h were identified and calculated as following.

First, the Pt RT was calibrated with one of the two factory-calibrated silicon diodes in the cryostat serving as the reference temperature (T_r). The specified uncertainty of T_r is $U_{T_r}=0.01\%T_r$ including both random and systematic errors. Due to a small temperature gradient in the cryostat, there was a less than 0.2% difference between the temperature readings of the two diodes that were located 4.5 cm apart from each other. The RT on the microdevice was located between the two diodes and the diode right next to the RT was used as the reference in the temperature calibration. The difference between T_r and the actual temperature of the RT should be less than 0.2% because the distance between the RT and the reference diode was much shorter than that between the two diodes. Thus, the systematic error in the calibration of the RT was calculated to be $B_T\leqslant 0.2\%T$. Because $B_{T_{h(I)}}$ and $B_{T_{h(I=0)}}$ arise from the same calibration error and are thus perfectly correlated, the propagation of $B_{T_{h(I)}}\leqslant 0.2\%T_h(I)$ and $B_{T_{h(I=0)}}\leqslant 0.2\%T_h(I=0)$ results in $B_{\Delta T_{h(I)}}\leqslant 0.2\%\Delta T_h(I)$ [14]. In other words, because $T_h(I)$ and $T_h(I=0)$ were distorted by the same percent of the reading due to the same calibration error, $\Delta T_h(I)$ was distorted by the same percent of the reading. Similarly, $B_{\Delta T_s(I)}\leqslant 0.2\%\Delta T_s(I)$. Because T_h and T_s were calibrated using the same T_r and thus B_{T_h} and B_{T_s} arise from the same calibration error, B_{T_h} and B_{T_s} are also perfectly correlated and propagate into $B_{(\Delta T_h-\Delta T_s)}\leqslant 0.2\%(\Delta T_h-\Delta T_s)$ and $B_{(\Delta T_h+\Delta T_s)}\leqslant 0.2\%(\Delta T_h+\Delta T_s)$.

The Joule heat Q was obtained as a product of the measured voltage (V) and current (I). The systematic error of the second type in the V measurement, i.e., B_V, was specified in the instrument manual to be less than 0.05% of the reading, and this error (B_I) in the I measurement was less than 0.1% of the reading. Hence, the same type of error in Q was calculated as $B_Q=(B_I^2/I^2+B_V^2/V^2)^{1/2}Q=0.125\%Q$.

The dominant uncertainty source is the random fluctuation in the temperature measurement. This fluctuation was observed to be about 40×10^{-3} K, as evident in Fig. 4(*b*). The random fluctuation was caused by the temperature fluctuation of the evaluated cryostat where the sample was located as well as the random uncertainty of the lock-in amplifier that was used to measure the differential electrical resistance of the RT. The uncertainty calculation shows that the random uncertainty accounts for more than 95% of U_{G_m}.

To reduce the uncertainty, for each measurement we often needed to spend a few hours to reduce the temperature fluctuation of the cryostat and used a sufficiently large ΔT_h value of about 2 K to obtain U_{G_m}/G_m between 4% and 15%. In addition, we obtained three to seven measurement results with $U_{G_m}/G_m\leqslant 15\%$ at one temperature, and the averaged value ($\overline{G_m}$) of the several G_m results is reported because the random uncertainty is reduced with increasing number (n) of measurements. The total uncertainty in $\overline{G_m}$ is calculated as

$$U_{\overline{G_m}}=(P_{\overline{G_m}}^2+B_{\overline{G_m}}^2)^{1/2} \tag{3}$$

where the random uncertainty in $\overline{G_m}$ is calculated as

$$P_{\overline{G_m}}=t_{n-1,95}S_{G_m}/\sqrt{n} \tag{4}$$

where S_{G_m} is the sample standard deviation of the n measurements of G_m, and $t_{n-1,95}$ is the t distribution for $n-1$ degree of freedom and a confidence level of 95%.

In Eq. (3), $B_{\overline{G_m}}$ is the systematic error of the second type in $\overline{G_m}$. Because B_{G_m}/G_m is the same for each measurement, $B_{\overline{G_m}}/\overline{G_m}=B_{G_m}/G_m$. In the fitting to obtain G_m/G_b, $B_{(\Delta T_h-\Delta T_s)}$ and $B_{\Delta T_s}$ are perfectly correlated because they share the same error source. In other words, the obtained X and Y variables in Fig. 4(*b*) were distorted by the same percent of the reading, or $B_{(\Delta T_h-\Delta T_s)}/(\Delta T_h-\Delta T_s)=B_{\Delta T_s}/\Delta T_s$. Consequently, the slope G_m/G_b is not affected by this perfectly correlated error, resulting in $B_{G_m/G_b}=0$. Therefore, $B_{G_m}/G_m=\sqrt{(B_{G_b}/G_b)^2+(B_{G_m/G_b}/(G_m/G_b))^2}=B_{G_b}/G_b$. In the fitting step for obtaining G_b, $B_{(\Delta T_h+\Delta T_s)}$ and B_Q are not correlated. Thus

$$\frac{B_{\overline{G_m}}}{\overline{G_m}}=\frac{B_{G_m}}{G_m}=\frac{B_{G_b}}{G_b}=\sqrt{\left(\frac{B_{(\Delta T_h+\Delta T_s)}}{\Delta T_h+\Delta T_s}\right)^2+\left(\frac{B_Q}{Q}\right)^2}\leqslant 0.24\% \tag{5}$$

Reduction of the Thermal Contact Resistance. The measured thermal resistance of the sample ($R_m=G_m^{-1}$) consists of the intrinsic thermal resistance of the nanofiber (R_n) and the total contact thermal resistance between the nanofiber and the two membranes (R_c), i.e.,

$$R_m=R_n+R_c \tag{6}$$

To reduce R_c, we used a focused electron beam deposition method to deposit a thin Pt layer locally on the contacts from precursor gases in a dual beam focused ion beam (FIB) tool. The deposited Pt layer is shown in Figs. 5(*a*) and 5(*b*). The effective contact area between the nanofiber and the membranes was increased by the Pt layer.

Measurement Results and Discussions

Figure 6 shows the measured thermal resistance (R_m) before and after the Pt coating on the contacts. The difference in R_m is caused by the reduction in the thermal contact resistance by the Pt layer, and the reduction of the contact resistance (R_c), i.e., ΔR_c, is shown in the inset of Fig. 6. The uncertainty in ΔR_c is calculated as the root-sum-square of the uncertainty in R_m before the Pt coating and that after the Pt coating. The contact resistance was reduced by the Pt coating for about 9–13% of the R_m value obtained before the Pt coating.

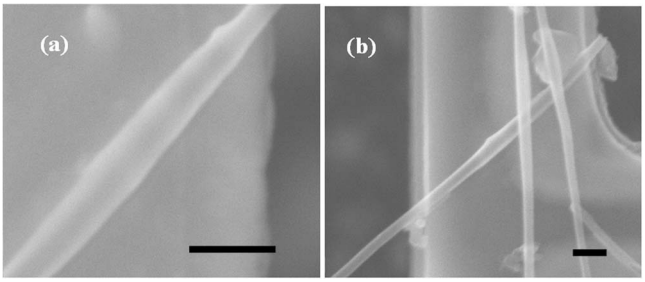

Fig. 5 SEM images of the two contacts between the nanofiber and the two membranes after a thin Pt layer was deposited on the contacts. The scale bars in the two images are 500 nm.

We have calculated the contact resistance using an approach based in part on a recent work by Bahadur et al. [16], who have extended McGee et al.'s model [17] of the thermal resistance of cylinder-flat contacts to analyze the constriction thermal resistance (R_c') of unit contact length between a nanowire and a flat surface. The contact width ($2b$) between the cylinder and the surface can be calculated from the contact force.

Bahadur et al. calculated the contact force between a nanowire and a substrate to be the van der Waals force. The calculation requires the knowledge of the Hamaker constant (A) that can be calculated from Lifshitz-van der Waals coefficient [18]. For the contact between Pt and carbon (C) in vacuum, the Hamaker constant can be estimated from those of Pt–Pt and C–C interfaces to be $A_{\mathrm{Pt-C}} \approx \sqrt{A_{\mathrm{Pt-Pt}} A_{\mathrm{C-C}}}$ [18,19]. We could not find the Hamaker constant for Pt–Pt and graphite-graphite interfaces in the literature, and have used the values for Au-Au and diamond-diamond interfaces to approximate $A_{\mathrm{Pt-Pt}}$ and $A_{\mathrm{C-C}}$ and obtained $A_{\mathrm{Pt-C}} \approx 4 \times 10^{-19}$ J for the contact between the nanofiber and the membrane. In the calculation, we have used Van der Waals radii for Pt and carbon found in Ref. [20]. Based on these alternative properties, we calculated that the contact width ($2b$) between the 152-nm-diameter nanofiber and the Pt surface was approximately 10 nm.

Because the temperature of the nanofiber segment in contact with the membrane varies along the nanofiber as a result of heat transfer to the membrane, the portion of the nanofiber in contact with the membrane should be treated as a fin. The thermal contact resistance between the nanofiber and the sensing membrane is thus the fin resistance. Assuming adiabatic boundary condition at

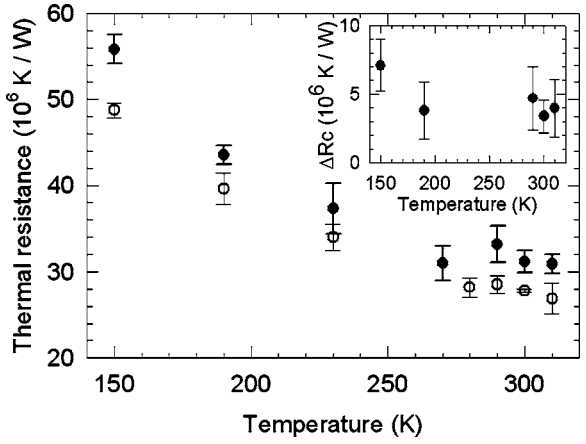

Fig. 6 Measured thermal resistance of the nanofiber sample before a Pt layer was deposited (solid black circles) and after a Pt layer was deposited with the use of the electron beam (open circles). The inset shows the reduction in contact resistance, ΔR_c, after the Pt coating.

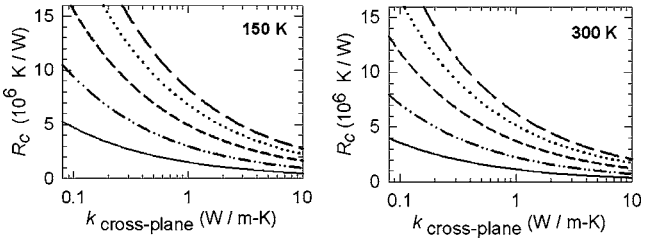

Fig. 7 Calculation results of thermal contact resistance (R_c) at 150 K and 300 K as a function of the cross-plane thermal conductivity ($k_\perp$ or $k_{\mathrm{cross\text{-}plane}}$) of the nanofiber. The five lines in each figure correspond to a contact width of $2b$=0.1 nm (long dashed line), $2b$=1 nm (dotted line), $2b$=10 nm (short dashed line), $2b$=50 nm (double dotted line), and $2b$=100 nm (solid line).

the end of the nanofiber fin, the total thermal contact resistance of the two contacts between the nanofiber and the two membranes can be calculated as [2]

$$R_c = \frac{2}{\sqrt{\dfrac{k_\parallel \pi D^2}{4R_c'}} \tanh\left(l\sqrt{\dfrac{4}{k_\parallel \pi D^2 R_c'}}\right)} \tag{7}$$

where $k_\parallel$ is the axial thermal conductivity of the nanofiber, and l_c is the contact length in the axial direction. The radial or cross-plane thermal conductivity of the nanofiber, i.e., $k_\perp$, is needed for the calculation of R_c'. Although the cross-plane thermal conductivity of graphite is given in the literature to be $k_\perp = 5.7$ W/m-K at 300 K [2], the value for the nanofiber can be different because of different crystalline structure and quality. More importantly, the effective thermal conductivity at a point contact of a Knudsen number (K) of the order of unity or larger, where K is the ratio between the phonon mean free path and the contact width, can be substantially reduced [21]. This reduction needs to be taken into account in the calculation of the contact resistance based on the continuum model when the contact width is comparable to or smaller than the mean free path. On the other hand, the axial or in-plane thermal conductivity $k_\parallel$ can be calculated from the measured thermal resistance of the nanofiber after the Pt coating. Using the obtained $k_\parallel$ values at 150 K and 300 K, we have calculated the contact thermal resistance as a function of $k_\perp$ for different contact widths of $2b$=0.1 nm, 1 nm, 10 nm, 50 nm, and 100 nm. The results are shown in Fig. 7.

Without the Pt coating, a contact width of $2b$=50 and 100 nm is rather unlikely because the diameter of the nanofiber is only 152 nm. With the Pt coating, on the other hand, a contact width of $2b \geqslant 50$ nm is possible. If $2b \geqslant 50$ nm with the Pt coating and $2b \approx 10$ nm without the Pt coating, the calculated ΔR_c can match the measurement value when $k_\perp < 0.6$ W/m-K for 150 K and $k_\perp < 2$ W/m-K for 300 K. For this case, the residual R_c after the Pt coating is comparable to the measure ΔR_c shown in the inset of Fig. 6.

We have used the thermal resistance results measured after the Pt coating to calculate the axial thermal conductivity of the nanofiber. The results are shown in Fig. 8. As a comparison, Fig. 8 also shows the measured thermal conductivity of a graphite fiber grown by pyrolysis prior to heat treatment. The thermal conductivity of the PECVD nanofiber increases nearly linearly with the temperature in the temperature range between 150 K and 310 K and the value at 300 K is about three times smaller than that of the graphite fiber. Note that the thermal conductivity of the graphite fiber and the specific heat (C) of graphite [22] increase nearly linearly with temperature in the temperature range between 150 K and 310 K. Using the specific heat of graphite and a sound velocity of v=10000 m/s, we have calculated the phonon mean free path (l) according to the thermal conductivity formula, i.e., k

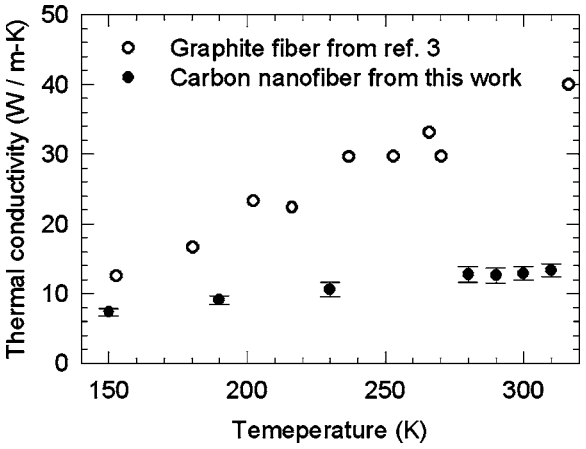

Fig. 8 Thermal conductivity of the nanofiber (solid circles) calculated from the measured thermal resistance of the sample after the Pt coating. The uncertainty error bars do not include the residual contact resistance after the Pt coatings. The thermal conductivity of a graphite fiber (open circles) from Ref. [3] is shown for comparison.

$=Cvl/3$. The obtained mean free path of $l \approx 1.5$ nm is almost independent of temperature between 150 K and 310 K. This feature and the absence of a peak in the thermal conductivity curve indicates that phonon-boundary and phonon-defect scattering with a short mean free path dominates over phonon-phonon Umklapp scattering for the temperature range. The short mean free path indicates that there is a high density of defects in the nanofiber.

Conclusion

We have measured the thermal resistance of a 152-nm-diameter carbon nanofiber grown by using PECVD before and after a platinum layer was deposited on the contacts between the nanofiber and the measurement device. The contact resistance was reduced by the Pt coating for about 9–13% of the total thermal resistance before the Pt coating. The in-plane thermal conductivity of the carbon nanofiber increases with temperature in the temperature range between 150 K and 310 K, and the value at 300 K was about three times smaller than that of graphite fibers grown by pyrolysis of natural gas prior to high-temperature heat treatment. The phonon mean free path in the nanofiber was found to be about 1.5 nm and is independent of temperature. This feature and the absence of a peak in the thermal conductivity curve indicate that phonon-boundary and phonon-defect scattering dominates over phonon-phonon Umklapp scattering for the temperature range. To develop thermal interface materials using CNT or CNF films, it is necessary to reduce the defect density and increase the intrinsic thermal conductivity of the carbon nanostructures. Additionally, the contact thermal resistance at the nanoscale point or line contacts between CNTs and the surrounding should not be underestimated.

Acknowledgment

Four of the authors (C.Y., S.S., J.Z., L.S.) were supported by the Chemical and Transport System Division of the National Science Foundation and by SEMATECH through the Advanced Materials Research Center (AMRC).

Nomenclature

A = Hamaker constant (N/m)
b = half width of the contact line between the nanofiber and the substrate (m)
B_x = systematic or bias uncertainty for the x variable
D = diameter of the nanofiber (m)
G_m = measured thermal conductance of the sample (W/K)
G_b = thermal conductance of the five beams of one membrane (W/K)
I = dc current (A)
k_n = thermal conductivity of the nanofiber (W/m-K)
k_s = thermal conductivity of the substrate (W/m-K)
$k_\parallel$ = in-plane or axial thermal conductivity (W/m-K)
$k_\perp$ = cross-plane or radial thermal conductivity (W/m-K)
l_c = contact length along the axis of the nanofiber (m)
l_i = length of the Pt layer deposited on the nanofiber along the axis of the nanofiber (m)
L = length of a SiN_x beam of the measurement device (m)
P_x = random or precision uncertainty for the x variable
Q_h = Joule heat dissipation in the Platinum resistance thermometer (W)
Q_L = Joule heat dissipation in one of the two Pt leads supplying the dc current (I) to the heating Pt RT (W)
R = thermal resistance (K/W)
R_c = thermal contact resistance between the nanofiber and the two membranes (K/W)
R_c' = constriction thermal resistance of unit axial length of the nanofiber (K m/W)
R_m = measured thermal resistance (K/W)
R_n = intrinsic thermal resistance of the nanofiber (K/W)
T = temperature (K)
T_h = temperature of the heating membrane (K)
T_s = temperature of the sensing membrane (K)
T_r = reference temperature in temperature calibration (K)
U_x = uncertainty for the x variable

References

[1] Touloukian, Y. S., Powell, R. W., Ho, C. Y., and Klemens, P. G., 1970, *Thermal Conductivity: Nonmetallic Solid, Thermophysical Properties of Matter*, Plenum, NY, Vol. 2.
[2] Incropera, F. P., and Dewitt, D. P., 1996, *Fundamentals of Heat and Mass Transfer*, Wiley, NY.
[3] Heremans, J., and Beetz, C. P. Jr., 1985, "Thermal Conductivity and Thermopower of Vapor-grown Graphite Fibers," Phys. Rev. B, **32**, pp. 1981–1986.
[4] Dresselhaus, M. S., Dresselhaus, G., and Eklund, P. C., 1996, *Science of Fullerenes and Carbon Nanotubes*, Academic, New York.
[5] Kim, P., Shi, L., Majumdar, A., and McEuen, P. L., 2001, "Thermal Transport Measurements of Individual Multiwalled Carbon Nanotubes," Phys. Rev. Lett., **87**, pp. 215502(1-4).
[6] Hone, J., Llaguno, M. C., Nemes, N. M., and Johnson, A. T., Fischer, J. E., Walters, D. A., Casavant, M. J., Schmidt, J., and Smalley, R. E., 2000, "Electrical and Thermal Transport Properties of Magnetically Aligned Single Wall Carbon Nanotube Films," Appl. Phys. Lett., **77**(5), pp. 666–668.
[7] Shi, L., Li, D., Yu, C., Jang, W., Yao, Z., Kim, P., and Majumdar, A., 2003, "Measuring Thermal and Thermoelectric Properties of One-Dimensional Nanostructures Using a Microfabricated Device," J. Heat Transfer, **125**, pp. 881–888.
[8] Chuang, H. F., Cooper, S. M., Meyyappan, M., and Cruden, B. A., 2004, "Improvement of Thermal Contact Resistance by Carbon Nanotubes and Nanofibers," J. Nanosci. Nanotechnol., **4**(8), pp. 964–967.
[9] Ngo, Q., Cruden, B. A., Cassell, A. M., Walker, M. D., Ye, Q., Koehne, J. E., Meyyappan, M., Li, J., and Yang, C. Y., 2004, "Thermal Conductivity of Carbon Nanotube Composite Films," Mater. Res. Soc. Symp. Proc., **812**, F3.18.1–6.
[10] Ngo, Q., Cruden, B. A., Cassell, A. M., Sims, G., Meyyappan, M., Li, J., and Yang, C. Y., 2004, "Thermal Interface Properties of Cu-filled Vertically Aligned Carbon Nanofiber Arrays," Nano Lett., **4**(12), pp. 2403–2407.
[11] Xu, J., and Fisher, T. S., 2004, "Enhanced Thermal Contact Conductance using Carbon Nanotube Arrays," The Ninth Intersociety Conference on Thermal and Thermomechanical Phenomena in Electronic Systems, ITHERM'04, **2**, pp. 549–555.
[12] Xu, J., and Fisher, T. S., 2004, "Thermal Contact Conductance Using Carbon

Nanotube Arrays," in Proceedings of the 2004 ASME International Mechanical Engineering Congress and Exposition, Anaheim, CA, IMECE2004–60185, pp. 1–5.
[13] Cruden, B. A., Cassell, A. M., Ye, Q., and Meyyappan, M., 2003, "Reactor Design Consideration in the Hot Filament/Direct Current Plasma Synthesis of Carbon Nanofibers," J. Appl. Phys., **94**, pp. 4070–4078.
[14] Coleman, H. W., and Steele, W. G., 1999, *Experimentation and Uncertainty Analysis for Engineers*, Wiley, NY.
[15] Brown, K. K., Coleman, H. W., and Steele, W. Gl., 1998, "A Methodology for Determining Experimental Uncertainties in Regressions," J. Fluids Eng., **120**, pp. 445–456.
[16] Bahadur, V., Xu, J., Liu, Y., and Fisher, T. S., 2005, "Thermal Resistance of Nanowire-Plane Interfaces," J. Heat Transfer, **127**, pp. 664–668.
[17] McGee, G. R., Schankula, M. H., and Yovanovich, M. M., 1985, "Thermal Resistance of Cylinder-Flat Contacts: Theoretical Analysis and Experimental Verification of a Line-Contact Model," Nucl. Eng. Des., **86**, pp. 369–381.
[18] Visser, J., 1989, "van der Waals and Other Cohesive Forces Affecting Powder Fluidization," Powder Technol., **58**, pp. 1–10.
[19] Israelachvili, J. N., 1992, *Intermolecular and Surface Forces*, Academic, London, UK.
[20] Bondi, A., 1964, "van der Waals and Other Cohesive Forces Affecting Powder Fluidization," Powder Technol., **58**, pp. 1–10.
[21] Wexler, G., 1966, "The Size Effect and the Non-local Boltzmann Transport Equation in Orifice and Disk Geometry," Proc. Phys. Soc. London, **89**, 927 (1966).
[22] Touloukian, Y. S., and Buyco, E. H., 1970, *Thermophysical Properties of Matter*, Plenum, NY, Vol. 5.

Convective Transport in Nanofluids

J. Buongiorno[1]
Nuclear Science and Engineering Department,
Massachusetts Institute of Technology,
77 Massachusetts Avenue,
Cambridge, MA 02139-4307

Nanofluids are engineered colloids made of a base fluid and nanoparticles (1–100 *nm*). *Nanofluids have higher thermal conductivity and single-phase heat transfer coefficients than their base fluids. In particular, the heat transfer coefficient increases appear to go beyond the mere thermal-conductivity effect, and cannot be predicted by traditional pure-fluid correlations such as Dittus-Boelter's. In the nanofluid literature this behavior is generally attributed to thermal dispersion and intensified turbulence, brought about by nanoparticle motion. To test the validity of this assumption, we have considered seven slip mechanisms that can produce a relative velocity between the nanoparticles and the base fluid. These are inertia, Brownian diffusion, thermophoresis, diffusiophoresis, Magnus effect, fluid drainage, and gravity. We concluded that, of these seven, only Brownian diffusion and thermophoresis are important slip mechanisms in nanofluids. Based on this finding, we developed a two-component four-equation nonhomogeneous equilibrium model for mass, momentum, and heat transport in nanofluids. A nondimensional analysis of the equations suggests that energy transfer by nanoparticle dispersion is negligible, and thus cannot explain the abnormal heat transfer coefficient increases. Furthermore, a comparison of the nanoparticle and turbulent eddy time and length scales clearly indicates that the nanoparticles move homogeneously with the fluid in the presence of turbulent eddies, so an effect on turbulence intensity is also doubtful. Thus, we propose an alternative explanation for the abnormal heat transfer coefficient increases: the nanofluid properties may vary significantly within the boundary layer because of the effect of the temperature gradient and thermophoresis. For a heated fluid, these effects can result in a significant decrease of viscosity within the boundary layer, thus leading to heat transfer enhancement. A correlation structure that captures these effects is proposed.*
[DOI: 10.1115/1.2150834]

Keywords: nanofluid, heat transfer, thermophoresis

1 Introduction

The earliest observations of thermal conductivity enhancement in liquid dispersions of submicronic solid particles (i.e., nanoparticles) were reported in 1993 by Masuda et al. [1]. The term "nanofluid" was first proposed by Choi about a decade ago [2], to indicate engineered colloids composed of nanoparticles dispersed in a base fluid. However, only recently have nanoparticles become sufficiently inexpensive and widely available to warrant their consideration for practical applications. For example, at the Massachusetts Institute of Technology (MIT) we are exploring the possibility of using nanofluids as coolants for advanced nuclear systems [3]. Contrary to the milli- and microsized particle slurries explored in the past, nanoparticles are relatively close in size to the molecules of the base fluid, and thus can realize very stable suspensions with little gravitational settling over long periods of time. Materials commonly used for nanoparticles include oxides such as alumina, silica, titania and copper oxide, and metals such as copper and gold. Carbon nanotubes and diamond nanoparticles have also been used to realize nanofluids. Popular base fluids include water and organic fluids such as ethanol and ethylene glycol. The volumetric fraction of the nanoparticles, ϕ, is usually below 5%.

The following nanofluid behavior has been observed consistently by different researchers at different organizations and with different nanofluids:

(1) Abnormal thermal conductivity increase relative to the base fluid. Eastman et al. [4] reported a 40% increase in the thermal conductivity of ethylene-glycol with 0.3 vol % copper nanoparticles of 10 nm diameter. Das et al. [5] have observed increases of 10–25% in water with 1–4 vol % alumina nanoparticles. Also, it appears that thermal conductivity of nanofluids is a strongly increasing function of temperature, much more so than that of pure liquids [5,6].

(2) Abnormal viscosity increase relative to the base fluid. Pak and Cho [7] measured the viscosity of alumina/water and titania/water nanofluids at 1–10 vol %, and found it to be much higher than that of pure water, well beyond the prediction of traditional viscosity models such as Brikman-Einstein's [8] or Batchelor's [9]. The same conclusion was reached by Maïga et al. [10] while correlating the viscosity data of Lee et al. [11] and Wang et al. [12].

(3) Abnormal single-phase convective heat-transfer coefficient increase relative to the base fluid. Pak and Cho [7] reported heat transfer data for turbulent flow of alumina/water and titania/water nanofluids in circular tubes. Their data show Nusselt numbers up to about 30% higher than predicted by the pure fluid correlation (Dittus-Boelter), even though the measured nanofluid properties were used in defining the dimensionless groups in the correlation (Fig. 1(*a*)). Nusselt numbers over 30% higher than the Dittus-Boelter correlation were also reported by Xuan and Li [13] for turbulent flow of copper/water nanofluids (Fig. 1(*b*)).

Despite several attempts, a satisfactory explanation for the abnormal increase of the thermal conductivity and viscosity in nanofluids is yet to be found, as emphasized by Eastman et al. [14] in their recent comprehensive review of the nanofluid literature. However, in this paper we do not intend to develop an ex-

[1]e-mail: jacopo@mit.edu
Contributed by the Heat Transfer Division of ASME for publication in the JOURNAL OF HEAT TRANSFER. Manuscript received March 7, 2005; final manuscript received August 15, 2005. Review conducted by Jay M. Khodadadi.

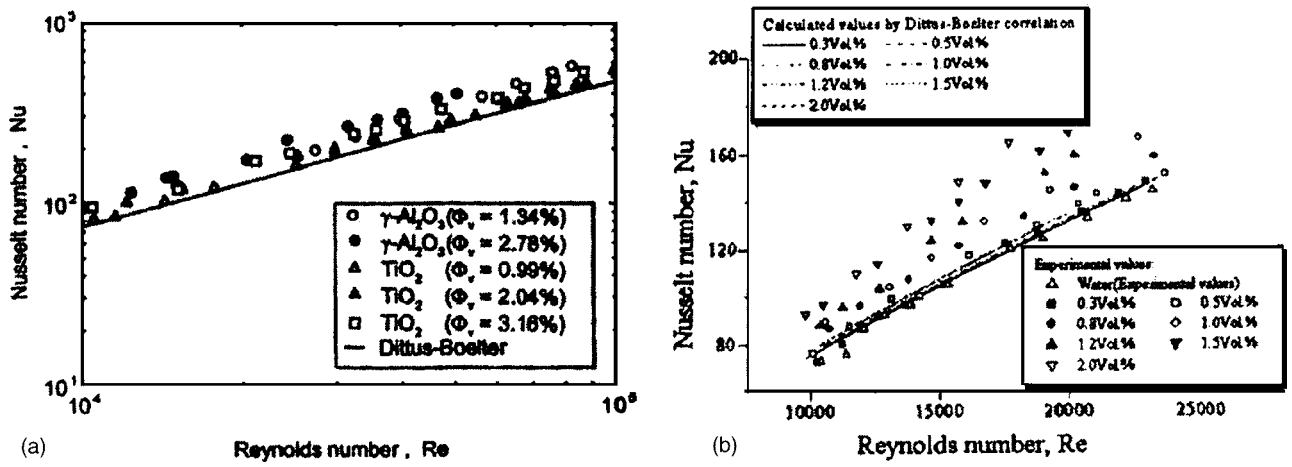

Fig. 1 Heat transfer data for water-based nanofluids with oxide nanoparticles [7] and metal nanoparticles [13]. Note the deviation from the Dittus-Boelter correlation, despite the fact that the nanofluid properties were used in defining Nu, Re, and Pr in both studies: (*a*) alumina and titania nanoparticles; and (*b*) copper nanoparticles.

planation for the effect of the nanoparticles on the thermophysical properties. Hereafter the thermophysical properties of nanofluids will be considered as given functions of the nanoparticle volumetric fraction (see Appendix A). Instead, we want to focus on explaining the further heat transfer enhancement observed in convective situations.

Pak and Cho [7], Xuan and Roetzel [15], and Xuan and Li [13] assumed that convective heat transfer enhancement is due mainly to dispersion of the suspended nanoparticles. However, our mechanistic description of particle dispersion suggests that this effect is very small in nanofluids, and thus cannot explain the observed heat transfer enhancement (see Secs. 3 and 4 below).

Xuan and Li [13] proposed that the enhancement could also come from intensification of turbulence due to the presence of the nanoparticles. However, pressure drop measurements by Xuan and Li [13] and Pak and Cho [7] clearly show that turbulent friction factors in their nanofluids can be very well predicted by the traditional friction factor correlations for pure fluids, if the measured nanofluid viscosity is used. This suggests that, beyond the obvious viscosity effect, turbulence is not affected by the presence of the nanoparticles. This conclusion is corroborated by a comparison of the time and length scales for the nanoparticles and the turbulent eddies (see Sec. 2.1 and Appendix B).

In his experiments with micro-sized particles (40–100 μm) suspended in water and glycerine, Ahuja [16] demonstrated that heat transfer enhancement may occur from particle rotation. That is, under the effect of the shear stress, the suspended particles rotate about an axis perpendicular to the main flow direction, creating a three-dimensional hydrodynamic boundary layer which increases the fluid flow towards the wall. To evaluate the importance of this effect with respect to heat conduction, Ahuja [16] proposed the use of a "rotational" Peclet number, Pe_r:

$$\mathrm{Pe}_r \equiv (\tau_w/\mu)\cdot(d_p^2/\alpha) \tag{1}$$

where τ_w is the shear stress at the wall, d_p is the particle diameter, μ is the fluid viscosity, and $\alpha = k/\rho c$ is the fluid thermal diffusivity. In Eq. (1) the term (d_p^2/α) represents the time constant for conduction heat transfer, while the term (τ_w/μ) represents the angular velocity of the particle, which Ahuja recommends assuming to be of the same order of magnitude of the shear rate at the wall. So, if Pe_r is large, heat transfer enhancement by particle rotation is possible. Using the definition of the Darcy's friction factor, f, the shear stress can be expanded as follows:

$$\tau_w \equiv \frac{f}{8}\rho\overline{V}^2 = \frac{C}{8}\frac{\mu^2}{\rho D^2}\mathrm{Re}^{2-n} \tag{2}$$

In Eq. (2), $\overline{V}$ is the mean axial velocity in the channel, ρ is the fluid density, D is the channel diameter, $\mathrm{Re} = (\rho\overline{V}D)/\mu$ is the Reynolds number, and $f = C/\mathrm{Re}^n$ is the friction factor correlation. For conditions typical of alumina/water nanofluids at room temperature ($\mu \sim 1$ mPa s, $\rho \sim 1$ g/cm^3, $\alpha \sim 2\times10^{-7}$ m^2/s, $\mathrm{Re} \sim 50{,}000$, $D \sim 1$ cm, $C = 0.184$, $n = 0.2$), and for nanoparticles with $d_p < 100$ nm, one gets $\mathrm{Pe}_r < 3\times10^{-4}$; thus nanoparticle rotation can also be discarded as a heat transfer enhancement mechanism in nanofluids.

Several authors have attempted to develop convective transport models for nanofluids. The models proposed so far are of the following two types:

(1) Homogeneous flow models. The conventional transport equations for pure fluids are directly extended to the nanofluids. This means that all traditional heat transfer correlations (e.g., Dittus-Boelter) could be used also for a nanofluid, provided that the nanofluid thermophysical properties were used in the calculations. Therefore, heat transfer enhancement is assumed to come only from the higher thermal conductivity. This approach was initially adopted by Choi [2] and more recently by Maïga et al. [10].

(2) Dispersion models. This approach is based on the assumption that the convective heat transfer enhancement in nanofluids comes from two factors, (i) the higher thermal conductivity, and (ii) the dispersion of the nanoparticles. In this approach, first proposed for nanofluids by Xuan and Roetzel [15], the effect of the nanoparticle/base fluid relative velocity is treated as a perturbation of the energy equation, and an empirical dispersion coefficient is introduced to describe the heat transfer enhancement.

The homogeneous flow models are in conflict with the experimental observation that pure-fluid correlations (such as Dittus-Boelter's) tend to underpredict the nanofluid heat transfer coefficient systematically, e.g., see Fig. 1 or the comparison of analytical predictions and experimental results in Maïga et al. [10]. As far as the dispersion models are concerned, we will show in Sec. 4 that heat transfer enhancement from nanoparticle dispersion is completely negligible in nanofluids. Therefore, in this paper we develop an alternative model that eliminates the shortcom-

ings of the homogeneous and dispersion models. In this new model the effect of the nanoparticle/base-fluid relative velocity is described more mechanistically than in the dispersion models.

2 Nanoparticle/Fluid Slip

The nanoparticle absolute velocity can be viewed as the sum of the base fluid velocity and a relative (slip) velocity. In order to develop a realistic two-component model for transport phenomena in nanofluids, it is important to understand the mechanisms by which the nanoparticles can develop a slip velocity with respect to the base fluid. The slip mechanisms mentioned in the literature [15,17–19] and analyzed here are seven: inertia, Brownian diffusion, thermophoresis, diffusiophoresis, Magnus effect, fluid drainage, and gravity settling.

For the purpose of our studies, we will assume that the fluid around the nanoparticles can be regarded as a continuum. To assess the accuracy of this assumption, we need to calculate the Knudsen number, Kn, which is defined as the ratio of the water molecule mean free path, λ, to the nanoparticle diameter, d_p:

$$\mathrm{Kn} = \frac{\lambda}{d_p} \tag{3}$$

The water molecule effective size and mean free path in liquid water are both of the order of 3 Å (0.3 nm). Therefore, for the nanoparticle range of interest (1–100 nm), the Knudsen number is relatively small ($\mathrm{Kn} < 0.3$), and the continuum assumption is reasonable.

2.1 Inertia. Due to its inertia, a particle suspended in a fluid could develop a slip velocity in the presence of turbulent eddies. The nanoparticle/fluid slip velocity due to the turbulent eddies, V_e, can be obtained from the equation of motion:

$$\frac{\pi}{6} d_p^3 \rho_p \frac{dV_e}{dt} = -3\pi d_p \mu V_e \Rightarrow V_e = V_{eo} e^{-t/\tau_p} \text{ with } \tau_p = \frac{\rho_p d_p^2}{18\mu} \tag{4}$$

where Stokes Law was used for the viscous resistance, and its use is justified by the continuum assumption. In Eq. (4), ρ_p is the mass density of the nanoparticles, μ is the viscosity of the fluid, V_{eo} is the velocity of the turbulent eddies, and τ_p is the so-called "relaxation time" of the nanoparticles. Assuming typical values for water/alumina nanofluids ($\mu \sim 1$ mPa s, $\rho_p \sim 4$ g/cm^3) and $d_p < 100$ nm, the relaxation time is <2 ns, which is negligible compared with the typical fluctuation time scale of the turbulent eddies (see Appendix B). Therefore, the nanoparticles are readily entrained by the fluid turbulent eddies, and the slip velocity is negligible. This is a direct consequence of the very small size and inertia of the nanoparticles.

The nanoparticle stopping distance, S_p, is defined as the distance a nanoparticle travels by inertia after the turbulent eddy that was carrying it comes to a complete stop. The stopping distance can be obtained by integrating Eq. (4)

$$S_p = \frac{\rho_p d_p^2}{18\mu} V_{eo} \tag{5}$$

where V_{eo} is of the order of the "shear velocity:"

$$V_{eo} \sim \sqrt{\tau_w/\rho} = \overline{V}\sqrt{f/8} = \frac{\mu}{\rho D}\sqrt{C/8}\,\mathrm{Re}^{1-n/2} \tag{6}$$

Assuming the same conditions of Eq. (2), V_{eo} is about 0.3 m/s, and $S_p < 1$ nm. Therefore, S_p is much smaller than the length scale of the eddies (see Appendix B). This result is important, because it ensures that the nanoparticles move homogeneously with the fluid in the presence of turbulent eddies.

Note also that the nanoparticles cannot penetrate the laminar sublayer near the wall by virtue of their inertia. The thickness of the laminar sublayer near the wall, δ_v, is of the order of 5 in dimensionless units:

$$\delta_v \sim 5\frac{\mu/\rho}{\sqrt{\tau_w/\rho}} \tag{7}$$

which is about 20 μm for the flow conditions assumed. Thus, $S_p \ll \delta_v$.

2.2 Brownian Diffusion. The random motion of nanoparticles within the base fluid is called Brownian motion, and results from continuous collisions between the nanoparticles and the molecules of the base fluid. The nanoparticles themselves can be viewed effectively as large molecules, with an average kinetic energy equal to that of the fluid molecules $\left(\frac{1}{2}k_B T\right)$, and thus with a considerable lower velocity. Here k_B is the Boltzmann's constant and T is the nanofluid temperature. Brownian motion is described by the Brownian diffusion coefficient, D_B, which is given by the Einstein-Stokes's equation:

$$D_B = \frac{k_B T}{3\pi\mu d_p} \tag{8}$$

For water nanofluids at room temperature with nanoparticles of 1–100 nm diameter, the Brownian diffusion coefficient ranges from 4×10^{-10} to 4×10^{-12} m^2/s. We will show in Sec. 2.8 that Brownian diffusion may become important as a slip mechanism in the absence of turbulent eddies. The nanoparticle mass flux due to Brownian diffusion, $\mathbf{j}_{p,B}$(kg/m^2 s) can be calculated as:

$$\mathbf{j}_{p,B} = -\rho_p D_B \nabla \phi \tag{9}$$

We will use this flux in developing the general transport model for nanofluids (see Sec. 3).

2.3 Thermophoresis. Particles can diffuse under the effect of a temperature gradient. This phenomenon is called thermophoresis, and is the "particle" equivalent of the well-known Soret effect for gaseous or liquid mixtures. The thermophoretic velocity, $\mathbf{V}_T$, can be found as:

$$\mathbf{V}_T = -\beta\frac{\mu}{\rho}\cdot\frac{\nabla T}{T}, \tag{10}$$

where an expression for the proportionality factor, β, is given by McNab and Meisen [20]:

$$\beta = 0.26\frac{k}{2k + k_p} \tag{11}$$

In Eq. (11), k and k_p are the thermal conductivity of the fluid and particle materials, respectively. Equation (11) is based on data for relatively large particles (1 μm) in water and *n*-hexane, and is recommended also by Lister [18] and, more recently, by Müller-Steinhagen [21]. Unfortunately, thermophoretic data for nanoparticles are not available at this time, so in the interim Eq. (11) will be used for the nanoparticles as well. The negative sign in Eq. (10) means that the particles move down the temperature gradient, i.e., from hot to cold. For alumina nanoparticles in water at room temperature, $k \sim 1$ W/m K, $k_p \sim 40$ W/m K, and assuming a temperature gradient of 10^5 K/m (corresponding to 100 kW/m^2 heat flux), one gets $V_T \sim 2\times10^{-6}$ m/s. We will show in Sec. 2.8 that thermophoresis may become important as a slip mechanism in the absence of turbulent eddies.

The nanoparticle mass flux due to thermophoretic effects, $\mathbf{j}_{p,T}$, can be calculated as

$$\mathbf{j}_{p,T} = \rho_p \phi \mathbf{V}_T = -\rho_p D_T \frac{\nabla T}{T} \text{ with } D_T \equiv \beta\frac{\mu}{\rho}\phi \tag{12}$$

The coefficient D_T is sometimes referred to as the "thermal diffusion" coefficient. We will use Eq. (12) in developing the general transport model for nanofluids (see Sec. 3).

2.4 Diffusiophoresis. A particle suspended in a solution in which a concentration gradient exists, is subjected to a net force acting in the direction opposite to that gradient. This phenomenon

is known as diffusiophoresis, and is caused by the impact of the particle with the diffusing species. However, the base fluid of nanofluids is usually a one-component substance with no concentration gradients, thus nanoparticle diffusiophoresis does not occur.

2.5 Magnus Effect. Under the effect of the shear stress, a particle rotates about an axis perpendicular to the main flow direction. If a relative axial velocity exists between the particle and the fluid, a force perpendicular to the main flow direction will arise. This is known as the Magnus effect, or lift force, and is due to the pressure gradient around the particle, created by its rotation. For large particles (>1 μm) moving in the laminar sublayer of a turbulent flow, it is commonly assumed that the relative axial velocity is significant and of the order of the turbulent eddy velocity [18]. This is based on the assumption that the particles are carried by turbulent eddies to the edge of the laminar sublayer and injected into the sublayer by inertia. However, we have shown in Sec. 2.1 that the nanoparticles cannot be injected into the laminar sublayer because their inertia is extremely low, and thus also the relative axial velocity is expected to be very low. Then it can be concluded that for nanoparticles the Magnus effect should be negligible.

2.6 Fluid Drainage. As a particle approaches the wall, there is a resistance caused by the pressure in the draining fluid film between the two approaching surfaces. This effect becomes important when the distance between the particle and the wall is of the order of the particle diameter. Therefore, for nanoparticles of 1–100 nm diameter, this effect is relevant only over a very small fraction of the laminar sublayer near the wall, and can be safely neglected.

2.7 Gravity. The nanoparticle settling velocity due to gravity, V_g, can be calculated from a balance of the buoyancy and viscous forces:

$$\frac{\pi}{6}d_p^3(\rho_p-\rho)g = 3\pi d_p \mu V_g \Rightarrow V_g = \frac{d_p^2(\rho_p-\rho)g}{18\mu} \tag{13}$$

where again Stokes Law was used for the viscous resistance. In the nanoparticle size range of interest (<100 nm), V_g is then $<1.6\times10^{-8}$ m/s.

2.8 Relative Importance of the Nanoparticle Transport Mechanisms. To estimate the relative importance of a certain nanoparticle transport mechanism, we compute the time a nanoparticle takes to diffuse a length equal to its diameter under the effect of that mechanism. So, with reference to a nanoparticle of 100 nm diameter, one has $d_p/V_{eo}\sim3\times10^{-7}$ s for turbulent transport, $d_p^2/D_B\sim0.002$ s for Brownian diffusion, $d_p/V_T\sim0.05$ s for thermophoresis, and $d_p/V_g\sim6$ s for gravity. Therefore, in the presence of turbulent eddies, turbulent transport of the nanoparticles dominates, i.e., the nanoparticles are carried by the turbulent eddies and other diffusion mechanisms are negligible. Note that turbulent transport occurs without slip, as per the discussion in Sec. 2.1. When turbulent effects are not important (e.g., in the laminar sublayer near the wall), Brownian diffusion and thermophoresis may become important as slip mechanisms. Gravity settling is negligible. These conclusions hold well for nanoparticles of any material and size.

3 Conservation Equations for Nanofluids

Now that the slip mechanisms for the nanoparticles have been clarified, we can develop a complete transport model for the nanofluids. We will treat the nanofluid as a two-component mixture (base fluid+nanoparticles) with the following assumptions:

(1) incompressible flow,
(2) no chemical reactions,
(3) negligible external forces,
(4) dilute mixture ($\phi\ll1$),
(5) negligible viscous dissipation,
(6) negligible radiative heat transfer,
(7) nanoparticles and base fluid locally in thermal equilibrium.

Assumptions (1) and (6) are accurate for liquid nanofluids. Assumption (2) is accurate because nanoparticle materials are chosen for their chemical inertness with the base fluid. Assumption (3) is justified in light of the discussion in Sec. 2.8. Assumption (4) is valid for most nanofluid studies published so far, in which $\phi<0.05$. Assumption (5) is often made in heat transfer problems, in which the heat flux at the surface is the dominant energy source in the system. To justify assumption (7), one has to calculate the heat transfer time constants for heat conduction within the nanoparticles, and within the base fluid in the vicinity of the nanoparticles. These time constants can be estimated as d_p^2/α_p and d_p^2/α_{bf}, respectively, where $\alpha_p=\mathrm{k}_p/\rho_p c_p$ and $\alpha_{bf}=\mathrm{k}_{bf}/\rho_{bf}c_{bf}$ are the thermal diffusivity of the nanoparticle material and base fluid, respectively. For alumina nanoparticles of 100 nm diameter in water, α_p and α_{bf} are about 10^{-5} m^2/s and 10^{-7} m^2/s, respectively, and the heat transfer time constants are about 1 ns and 100 ns, respectively, which are much smaller than the time constants calculated in Sec. 2.8 for Brownian diffusion and thermophoresis, and also smaller than the turbulent eddy time scale calculated in Appendix B. Therefore, as the nanoparticles move in the surrounding fluid, they achieve thermal equilibrium with it very rapidly, which justifies assumption (7).

The conservation equations for a two-component mixture can be found in most transport phenomena books. For our nanofluid application we will adopt the formalism of Bird, Stewart, and Lightfoot's classic textbook [22], which is referred to as BSL in the following discussion. To capture the effect of the nanoparticle/base fluid slip, we will use a four-equation approach (two mass equations, one momentum equation, and one energy equation).

From Assumption (1), the continuity equation for the nanofluid is (BSL, Eq. (18.1-9)):

$$\boldsymbol{\nabla}\cdot\mathbf{v}=0 \tag{14}$$

where $\mathbf{v}$ is the nanofluid velocity. Equation (14) is identical to the continuity equation for a pure incompressible fluid. The continuity equation for the nanoparticles in the absence of chemical reactions (Assumption 2) is (BSL, Eq. (18.3-4)):

$$\frac{\partial\phi}{\partial t}+\mathbf{v}\cdot\nabla\phi=-\frac{1}{\rho_p}\boldsymbol{\nabla}\cdot\mathbf{j}_p \tag{15}$$

where t is time, $\mathbf{j}_p$ is the diffusion mass flux for the nanoparticles (kg/m^2 s), and represents the nanoparticle flux relative to the nanofluid velocity $\mathbf{v}$. If the external forces are negligible (assumption (3)), $\mathbf{j}_p$ can be written as the sum of only two diffusion terms, i.e., Brownian diffusion and thermophoresis:

$$\mathbf{j}_p=\mathbf{j}_{p,B}+\mathbf{j}_{p,T}=-\rho_p D_B\nabla\phi-\rho_p D_T\frac{\nabla T}{T} \tag{16}$$

The diffusion coefficients D_B and D_T can be calculated from Eqs. (8) and (12), respectively. Substituting Eq. (16) in Eq. (15), one gets:

$$\frac{\partial\phi}{\partial t}+\mathbf{v}\cdot\nabla\phi=\nabla\cdot\left[D_B\nabla\phi+D_T\frac{\nabla T}{T}\right] \tag{17}$$

Equation (17) states that the nanoparticles can move homogeneously with the fluid (second term of the left-hand side), but they also possess a slip velocity relatively to the fluid (right-hand side), which is due to Brownian diffusion and thermophoresis.

The momentum equation for the nanofluid with negligible external forces is (BSL, Eq. (18.3-2)):

$$\rho\left[\frac{\partial \mathbf{v}}{\partial t}+\mathbf{v}\cdot\nabla\mathbf{v}\right]=-\nabla P-\nabla\cdot\boldsymbol{\tau} \tag{18}$$

where P is pressure. Note that Eq. (18) is identical to the momentum equation for a pure fluid. The stress tensor, $\boldsymbol{\tau}$, can be expanded assuming Newtonian behavior and incompressible flow:

$$\boldsymbol{\tau}=-\mu[\nabla\mathbf{v}+(\nabla\mathbf{v})^t] \tag{19}$$

where the superscript t indicates the transpose of $\nabla\mathbf{v}$. If the viscosity μ is constant, Eq. (18) becomes the usual Navier-Stokes equation. However, μ strongly depends on ϕ for a nanofluid. Therefore, Eqs. (18) and (17) are coupled.

The energy equation for the nanofluid can be written as (BSL, Table 18.3-1, Eq. (F)):

$$\rho c\left[\frac{\partial T}{\partial t}+\mathbf{v}\cdot\nabla T\right]=-\nabla\cdot\mathbf{q}+h_p\nabla\cdot\mathbf{j}_p \tag{20}$$

where assumptions (1), (2), (3), (4), and (5) were used. In Eq. (20), c is the nanofluid specific heat, T is the nanofluid temperature, h_p is the specific enthalpy of the nanoparticle material (J/kg), and $\mathbf{q}$ is the energy flux relative to the nanofluid velocity $\mathbf{v}$. Neglecting radiative heat transfer (assumption (6)), $\mathbf{q}$ can be calculated as the sum of the conduction heat flux and the heat flux due to nanoparticle diffusion (BSL, Eq. (18.4-2)):

$$\mathbf{q}=-k\nabla T+h_p\mathbf{j}_p \tag{21}$$

where k is the nanofluid thermal conductivity. Substituting Eq. (21) in Eq. (20), recognizing that $\nabla\cdot(h_p\mathbf{j}_p)\equiv h_p\nabla\cdot\mathbf{j}_p+\mathbf{j}_p\cdot\nabla h_p$, and indicating the nanoparticle specific heat with c_p, one gets:

$$\rho c\left[\frac{\partial T}{\partial t}+\mathbf{v}\cdot\nabla T\right]=\nabla\cdot k\nabla T-c_p\mathbf{j}_p\cdot\nabla T \tag{22}$$

where ∇h_p has been set equal to $c_p\nabla T$, which follows from assumption (7). Note that if $\mathbf{j}_p$ is zero, Eq. (22) becomes the familiar energy equation for a pure fluid. Substituting Eq. (16) in Eq. (22), the final form of the energy equation for the nanofluid is found:

$$\rho c\left[\frac{\partial T}{\partial t}+\mathbf{v}\cdot\nabla T\right]=\nabla\cdot k\nabla T+\rho_p c_p\left[D_B\nabla\phi\cdot\nabla T+D_T\frac{\nabla T\cdot\nabla T}{T}\right] \tag{23}$$

Equation (23) states that heat can be transported in a nanofluid by convection (second term on the left-hand side), by conduction (first term on the right-hand side), and also by virtue of nanoparticle diffusion (second and third terms on the right-hand side). It is important to emphasize that ρc is the heat capacity of the nanofluid, and thus already accounts for the sensible heat of the nanoparticles as they move homogeneously with the fluid. Therefore, the last two terms on the right-hand side truly account for the additional contribution associated with the nanoparticle motion *relative* to the fluid.

In summary, Eq. (14) (nanofluid continuity), Eq. (17) (nanoparticle continuity), Eq. (18) (nanofluid momentum), and Eq. (23) (nanofluid energy) constitute a complete set of equations from which $\mathbf{v}(\mathbf{r},t)$, $P(\mathbf{r},t)$, $\phi(\mathbf{r},t)$, and $T(\mathbf{r},t)$ can be calculated, once the boundary and initial conditions are known, and the nanofluid transport coefficients (ρ,c,μ,k,D_B,D_T) are known as functions of ϕ and temperature. To draw from the terminology of two-phase flow analysis, the nanofluid model we developed can be characterized as a two-"fluid" (nanoparticles+base fluid), four-equation (2 mass+1 momentum+1 energy), nonhomogeneous (nanoparticle/fluid slip velocity allowed) equilibrium (nanoparticle/fluid temperature differences not allowed) model.

Note that the conservation equations are strongly coupled. That is, $\mathbf{v}$ depends on ϕ via viscosity; ϕ depends on T mostly because of thermophoresis; T depends on ϕ via thermal conductivity and also via the Brownian and thermophoretic terms in the energy equation; ϕ and T obviously depend on $\mathbf{v}$ because of the convection terms in the nanoparticle continuity and energy equations, respectively.

4 Discussion

To assess the relative importance of the various transport mechanisms in nanofluids, it is useful to make the conservation equations nondimensional. For this purpose, we make use of the following transformations:

$$\mathbf{V}\equiv\frac{\mathbf{v}}{\bar{V}};\quad \Phi\equiv\frac{\phi}{\phi_b};\quad \theta\equiv\frac{T-T_b}{\Delta T};$$
$$\wp\equiv\frac{P}{\rho\bar{V}^2};\quad \mathbf{R}\equiv\frac{\mathbf{r}}{D};\quad \xi\equiv\frac{t}{(D/\bar{V})} \tag{24}$$

where $\bar{V}$, ϕ_b, T_b, ΔT, and D are the reference velocity, nanoparticle volumetric fraction, temperature, temperature difference, and length, respectively. For example, for a heat transfer problem with internal flow in a round tube, $\bar{V}$, ϕ_b, T_b, ΔT, and D would be the mean axial velocity of the nanofluid, the nominal nanoparticle volumetric fraction, the bulk temperature, the film temperature drop, and the tube diameter, respectively. Introducing the above transformations into the conservation equations, assuming constant properties (which is appropriate for order-of-magnitude estimates), and recognizing that $\Delta T/T_b\ll 1$, Eqs. (14), (17), (18), and (23) become, respectively:

$$\nabla\cdot\mathbf{V}=0 \tag{25}$$

$$\frac{\partial\Phi}{\partial\xi}+\mathbf{V}\cdot\nabla\Phi=\frac{1}{\mathrm{Re}\cdot\mathrm{Sc}}\left[\nabla^2\Phi+\frac{\nabla^2\theta}{N_{BT}}\right] \tag{26}$$

$$\frac{\partial\mathbf{V}}{\partial\xi}+\mathbf{V}\cdot\nabla\mathbf{V}=-\nabla\wp+\frac{\nabla^2\mathbf{V}}{\mathrm{Re}} \tag{27}$$

$$\left[\frac{\partial\theta}{\partial\xi}+\mathbf{V}\cdot\nabla\theta\right]=\frac{1}{\mathrm{Re}\cdot\mathrm{Pr}}\left[\nabla^2\theta+\frac{\nabla\Phi\cdot\nabla\theta}{\mathrm{Le}}+\frac{\nabla\theta\cdot\nabla\theta}{\mathrm{Le}\cdot N_{BT}}\right] \tag{28}$$

In Eqs. (25)–(28), the following dimensionless groups have been used:

$$\mathrm{Re}\equiv\frac{\rho\bar{V}D}{\mu}\ (\text{Reynolds number = inertial forces/viscous forces}) \tag{29}$$

$$\mathrm{Sc}\equiv\frac{\mu}{\rho D_B}\ (\text{Schmidt number = momentum diffusivity/Brownian diffusivity}) \tag{30}$$

$$N_{BT}\equiv\frac{\phi_b D_B T_b}{D_T\Delta T}=\frac{D_B T_b\rho}{\beta\mu\Delta T}\ (\text{=Brownian diffusivity/thermophoretic diffusivity}) \tag{31}$$

$$\mathrm{Pr}\equiv\frac{c\mu}{k}\ (\text{Prandtl = momentum diffusivity/thermal diffusivity}) \tag{32}$$

$$\mathrm{Le}\equiv\frac{k}{\rho_p c_p D_B\phi_b}\ (\text{Lewis = thermal diffusivity/Brownian diffusivity}) \tag{33}$$

and Eq. (12) was used to simplify the expression for N_{BT}.

Let us consider the following conditions, which are typical of the alumina/water (copper/water) nanofluid studies published in

the literature: $\phi_b \sim 0.01$, $T_b \sim 300$ K, $\Delta T \sim 10$ K, $\mu \sim 1$ mPa s, $\rho \sim 1$ g/cm^3, $k \sim 1$ W/m K, $\rho_p c_p \sim 3.1$ MJ/m^3 (~ 3.4 MJ/m^3 for copper nanoparticles), $\beta \sim 0.006$ (~ 0.0006 for copper nanoparticles), $D_B \sim 4 \times 10^{-11}$ m^2/s (calculated from Eq. (8) for $d_p = 10$ nm). With these values, $\mathrm{Le} \sim 8 \times 10^5$, $N_{BT} \sim 0.2$ and $\mathrm{Le} \cdot N_{BT} \sim 1.6 \times 10^5$ for alumina nanoparticles, and $\mathrm{Le} \sim 7 \times 10^5$, $N_{BT} \sim 2$ and $\mathrm{Le} \cdot N_{BT} \sim 1.4 \times 10^6$ for copper nanoparticles. Because $\mathrm{Le} \gg 1$ and $\mathrm{Le} \cdot N_{BT} \gg 1$, Eq. (28) suggests that heat transfer associated with nanoparticle dispersion is negligible compared with heat conduction and convection. It follows that, in solving nanofluid heat transfer problems, the second and third terms on the right-hand side of Eq. (23) can be neglected, which makes the energy equation for a nanofluid formally identical to that of a pure fluid. This also implies that, contrary to what is commonly stated in the literature, the nanoparticles indeed affect convective heat transfer in nanofluids only via the thermophysical properties. However, it is important to recognize that a spatial distribution of the nanofluid thermophysical properties (especially viscosity and thermal conductivity) is expected, because such properties do depend on the nanoparticle distribution within the channel (i.e., they strongly depend on ϕ), as well as temperature. Therefore, the nanoparticle continuity equation (Eq. (17)) must always be solved in conjunction with the energy equation, which explains why pure-fluid correlations fail to reproduce the heat transfer data. The importance of coupling a nanoparticle continuity equation with the energy equation was also emphasized by Wen and Ding [23]. About Eq. (17), one should also notice that for $d_p = 1-100$ nm, N_{BT} ranges from 2 to 0.02 for alumina nanoparticles, and from 20 to 0.2 for copper nanoparticles, which suggests that thermophoretic effects are of the same order or more important than Brownian diffusion effects for alumina nanoparticles over the whole nanoparticle range, but in general less important for copper nanoparticles, especially at the lower end of the size range. This stems from the higher thermal conductivity of copper, which makes the thermal diffusion coefficient, D_T, lower (see Eq. (11)).

5 Nanofluid Heat Transfer in Turbulent Flow

In the presence of turbulence the conservation equations have to be modified to include the effect of the momentum, energy and particle eddy diffusivities. If we focus on the region near the wall of a round tube at steady state, Eqs. (17), (18), and (23) can be rewritten, respectively, as:

$$\frac{d}{dy}\left[(D_B + \varepsilon_p)\frac{d\phi}{dy} + \frac{D_T}{T}\frac{dT}{dy}\right] = 0 \tag{34}$$

$$\frac{d}{dy}\left[(\mu + \rho\varepsilon_M)\frac{dv}{dy}\right] = 0 \tag{35}$$

$$\frac{d}{dy}\left[(k + \rho c\varepsilon_H)\frac{dT}{dy}\right] = 0 \tag{36}$$

where y is the radial coordinate measuring the distance from the wall, v is the axial component of the velocity, and ε_M, ε_H, and ε_p are the momentum, energy, and particle eddy diffusivities, respectively. In Eqs. (34)–(36) the typical boundary-layer approximations for fully-developed internal flow were made, i.e.:

(a) curvature effects are negligible,
(b) axial transport terms are small compared with radial transport terms.

Integration of the above equations yields:

$$(D_B + \varepsilon_p)\frac{d\phi}{dy} + \frac{D_T}{T}\frac{dT}{dy} = 0 \tag{37}$$

$$(\mu + \rho\varepsilon_M)\frac{dv}{dy} = \tau_w \tag{38}$$

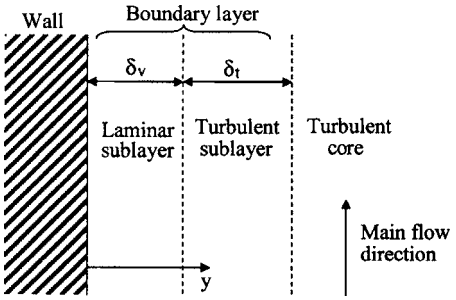

Fig. 2 Flow structure near the wall

$$(k + \rho c\varepsilon_H)\frac{dT}{dy} = -q_w \tag{39}$$

where τ_w is the wall shear stress, q_w is the wall heat flux, and also it was assumed that the net nanoparticle flux at the wall is zero, i.e., the nanoparticles neither deposit on nor are created at the wall.

Let us now assume that the wall layer is composed of two regions (Fig. 2): a laminar sublayer in which $D_B \gg \varepsilon_p$, $\mu \gg \varepsilon_M$, and $k \gg \varepsilon_H$, and a turbulent sublayer, in which $D_B \ll \varepsilon_p$, $\mu \ll \varepsilon_M$, $k \ll \varepsilon_H$. This approach was first proposed by Prandtl [24]. We can then solve Eqs. (37)–(39) with the boundary conditions: $\phi = \phi_b$, $v = \overline{V}$, $T = T_b$ at $y = \delta_v + \delta_t$, and $v = 0$, $T = T_w$ at $y = 0$, where the subscript b refers to bulk and w to wall.

5.1 Turbulent Sublayer. Because the nanoparticles move homogeneously with the turbulent eddies, it is reasonable to assume that $\varepsilon_p \sim \varepsilon_M$. In Sec. 2.8 we demonstrated that turbulent transport is the dominant nanoparticle transport mechanism in the presence of turbulent eddies, thus we can assume that $\phi \sim \phi_b$ in the turbulent sublayer. This conclusion is also corroborated by order-of-magnitude estimates of the eddy diffusivity and thermophoresis terms in Eq. (37). Integrating the momentum and energy equations in the turbulent sublayer, taking the ratio q_w/τ_w and using the Reynolds analogy ($\varepsilon_H \sim \varepsilon_M$), one gets:

$$\frac{q_w}{\tau_w} = c\frac{T_i - T_b}{\overline{V} - V_i} \tag{40}$$

where c is the nanofluid specific heat, and T_i and V_i are temperature and velocity at the interface of the laminar and turbulent sublayers.

5.2 Laminar Sublayer. Using Eq. (39), the temperature gradient can be eliminated from Eq. (37). Thus:

$$D_B\frac{d\phi}{dy} - \frac{D_T}{T}\frac{q_w}{k} = 0 \tag{41}$$

Equation (41) suggests that for a heated fluid ($q_w > 0$), the effect of thermophoresis is to reduce ϕ in the laminar sublayer. Using the definition of D_T (Eq. (12)) and neglecting the temperature dependencies, Eq. (41) can be readily integrated to yield:

$$\phi = \phi_b e^{(1/N_{BT})(1-y/\delta_v)} \tag{42}$$

with the following definition of the N_{BT} number:

$$N_{BT} \equiv \frac{D_B T_b \rho}{\beta\mu\left[\dfrac{q_w \delta_v}{k}\right]} \tag{43}$$

Equation (42) is plotted in Fig. 3 with N_{BT} as a parameter. Thus,

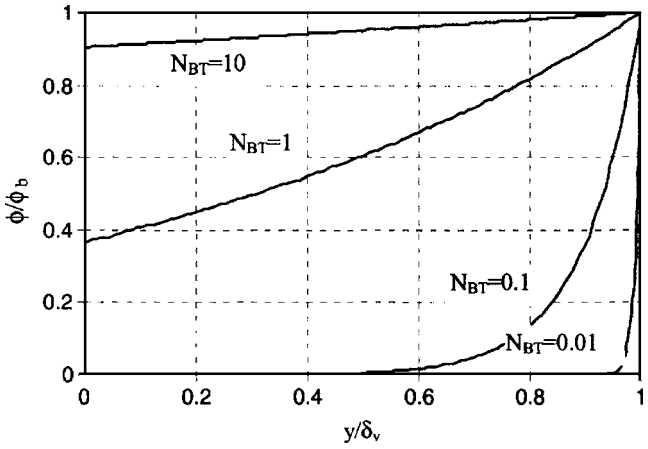

Fig. 3 Variation of the nanoparticle volumetric fraction within the laminar sublayer

for relatively low values of N_{BT} (e.g., large nanoparticles, high heat fluxes), the nanoparticle volumetric fraction near the wall can be significantly lower than in the bulk.

The average nanoparticle volumetric fraction in the laminar sublayer, $\phi_v(\equiv 1/\delta_v \int_0^{\delta_v} \phi dy)$, can be obtained from Eq. (42):

$$\frac{\phi_v}{\phi_b} = N_{BT}(1 - e^{-(1/N_{BT})}) \tag{44}$$

The momentum and energy equations in the laminar sublayer can be readily integrated to yield:

$$\frac{q_w}{\tau_w} \approx \frac{k_v}{\mu_v} \frac{T_w - T_i}{V_i} \tag{45}$$

where k_v and μ_v are the nanofluid thermal conductivity and viscosity corresponding to ϕ_v, respectively. Equation (45) is approximate because in reality both thermal conductivity and viscosity vary within the laminar sublayer, due to the variation of ϕ.

5.3 Heat Transfer Coefficient. Eliminating T_i from Eqs. (40) and (45), and introducing the definition of heat transfer coefficient, $h \equiv q_w/(T_w\text{-}T_b)$, one gets:

$$h = \frac{\tau_w}{\dfrac{\mu_v V_i}{k_v} + \dfrac{\overline{V} - V_i}{c}} \tag{46}$$

Using the definition of friction factor (Eq. (2)) and rearranging the terms, Eq. (46) can be rewritten as:

$$\mathrm{Nu}_b = \frac{\dfrac{f}{8}\mathrm{Re}_b \mathrm{Pr}_b}{1 + \dfrac{V_i}{\overline{V}}(\mathrm{Pr}_v - 1)} \tag{47}$$

where the subscript b indicates the use of properties corresponding to ϕ_b, while the subscript v indicates the use of properties corresponding to ϕ_v. In the derivation of Eq. (47), it was assumed that the ratio $c_b/c_v \sim 1$, which is true at low nanoparticle concentrations. Assuming that velocity varies linearly within the laminar sublayer, the ratio $V_i/\overline{V}$ becomes equal to $\delta_v^+\sqrt{f/8}$, where δ_v^+ is the thickness of the laminar sublayer in dimensionless units. In Prandtl's original derivation δ_v^+ was assumed to be 8.7 [24]. Thus, Eq. (47) becomes:

$$\mathrm{Nu}_b = \frac{\dfrac{f}{8}\mathrm{Re}_b \mathrm{Pr}_b}{1 + 8.7\sqrt{\dfrac{f}{8}}(\mathrm{Pr}_v - 1)} \tag{48}$$

which is the well-known Prandtl correlation for a pure fluid, except that the Prandtl number at the denominator is not evaluated with the bulk properties, but with the laminar sublayer properties. Equation (48) can be used to explain the convective heat transfer enhancements in nanofluids and their deviation from a pure-fluid correlation, as follows. For a heated fluid ($T_w > T_b$), one has $\mathrm{Pr}_v < \mathrm{Pr}_b$ because of two effects:

(1) $\mu_v < \mu_b$ and $k_v > k_b$. While this effect is present also in pure liquids, it is more pronounced for nanofluids, because viscosity and especially thermal conductivity are much stronger functions of temperature for nanofluids than for pure liquids [5,25].
(2) $\phi_v < \phi_b$. Both μ and k increase with ϕ. However, the μ dependence on ϕ is stronger [7,10,13] (see also Appendix A). Therefore, the net effect of a ϕ reduction is a reduction of the Prandtl number in the boundary layer.

With reference to Eq. (48), the ratio

$$\frac{1 + 8.7\sqrt{\dfrac{f}{8}}(\mathrm{Pr}_b - 1)}{1 + 8.7\sqrt{\dfrac{f}{8}}(\mathrm{Pr}_v - 1)}$$

is a measurement of the nanofluid heat transfer deviation from the predictions of a pure-fluid correlation. Clearly, if $\mathrm{Pr}_v < \mathrm{Pr}_b$, this ratio is greater than unity. We will demonstrate this conclusion quantitatively in Sec. 5.4. In the meantime, it should be noted that the Prandtl correlation is known to be valid only for Prandtl numbers around unity, which is consistent with the use of the Reynolds analogy in its derivation. However, nanofluids can have Prandtl numbers significantly higher than unity (>10). A correlation that has a physical basis similar to Eq. (48), but is valid within a much broader range of the parameters ($0.5 < \mathrm{Pr} < 2000$, $2300 < \mathrm{Re} < 5 \times 10^6$) is that of Gnielinski [26], recommended in most heat transfer handbooks [27,28]:

$$\mathrm{Nu} = \frac{\dfrac{f}{8}(\mathrm{Re} - 1000)\mathrm{Pr}}{1 + 12.7\sqrt{\dfrac{f}{8}}(\mathrm{Pr}^{2/3} - 1)} \tag{49}$$

Thus, we adopt the following correlation structure for nanofluid heat transfer in turbulent flow:

$$\mathrm{Nu}_b = \frac{\dfrac{f}{8}(\mathrm{Re}_b - 1000)\mathrm{Pr}_b}{1 + \delta_v^+\sqrt{\dfrac{f}{8}}(\mathrm{Pr}_v^{2/3} - 1)} \tag{50}$$

where δ_v^+ is now a constant to be determined empirically. Once δ_v^+ is given, Eq. (50) can be used as follows:

(i) Calculate the friction factor (and the shear stress) from a traditional friction factor correlation for turbulent flow, e.g., McAdams' or Karman-Nikuradse's.
(ii) Guess a value for ϕ_v.
(iii) Calculate the thickness of the laminar sublayer, $\delta_v \sim \delta_v^+(\mu_v/\rho/\sqrt{\tau_w/\rho})$

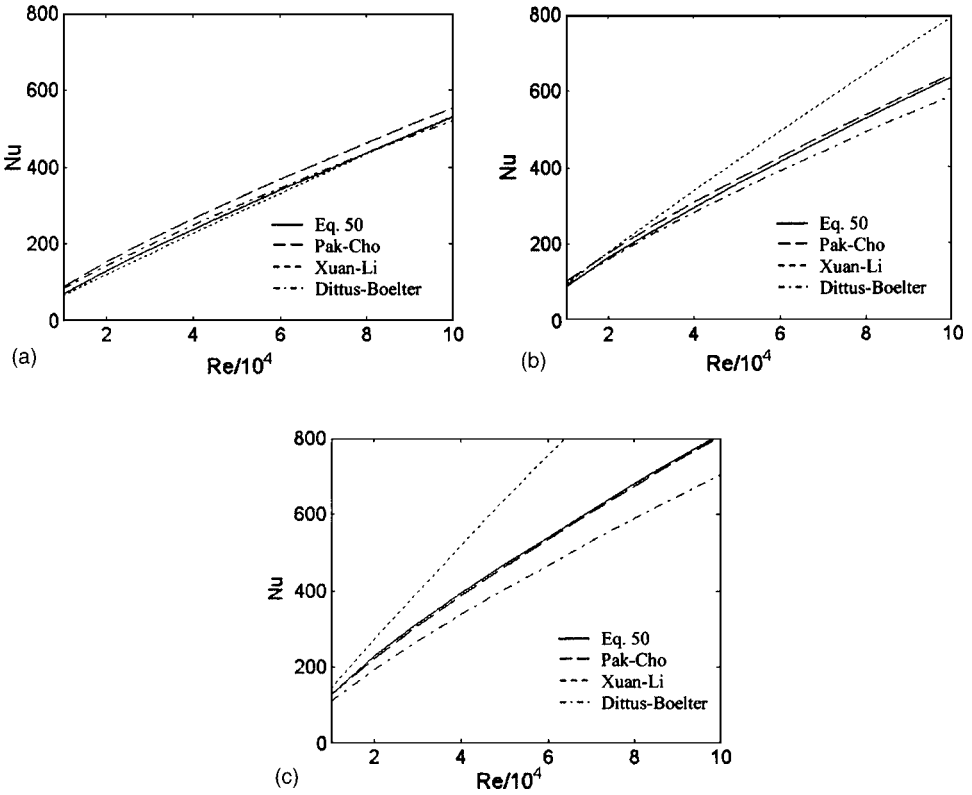

Fig. 4 Heat transfer in alumina/water nanofluids: (*a*) $\phi_b=0$; (*b*) $\phi_b=0.01$; and (*c*) $\phi_b=0.03$

(iv) Calculate N_{BT} from Eq. (43).
(v) Calculate ϕ_v from Eq. (44).
(vi) Repeat steps (iii)–(v) until ϕ_v converges.
(vii) Calculate Pr_v for $\phi=\phi_v$ and $T=(T_w+T_b)/2$.
(viii) Calculate the heat transfer coefficient from Eq. (50).
(ix) Calculate T_w from Newton's law of cooling.

For a problem with fixed q_w, these steps need to be repeated until T_w converges.

5.4 Performance of the New Heat Transfer Correlation for Nanofluids. The two most comprehensive sets of data for single-phase turbulent heat transfer in nanofluids are those of Pak and Cho [7] and Xuan and Li [13]. These databases are reproduced well by the following two correlations, respectively:

$$\mathrm{Nu}_b = 0.021 \cdot \mathrm{Re}_b^{0.8}\,\mathrm{Pr}_b^{0.5} \tag{51}$$

$$\mathrm{Nu}_b = 0.0059 \cdot \left[1 + 7.6286 \cdot \phi_b^{0.6886}\left(\mathrm{Re}_b\,\mathrm{Pr}_b\frac{d_p}{D}\right)^{0.001}\right]\mathrm{Re}_b^{0.9238}\,\mathrm{Pr}_b^{0.4} \tag{52}$$

To test the performance of our correlation, we use Pak and Cho's data [7], represented by Eq. (51). The Nusselt number for their water-based nanofluids with three different loadings of alumina nanoparticles (13 nm) is plotted in Fig. 4, as a function of the Reynolds number. There are four curves in this figure: the data (Pak and Cho's correlation, Eq. (51)) and three different correlations, i.e., Eq. (50), Xuan-Li (Eq. (52)) and Dittus-Boelter. It can be seen that all correlations are in good agreement for $\phi_b=0$ (pure water), while for $\phi_b>0$ Dittus-Boelter and Xuan-Li tend to significantly under- and overestimate the Nusselt number, respectively. On the other hand, Eq. (50) is in good agreement with the data. The Nusselt number for water-based nanofluids with titania nanoparticles (27 nm) is plotted in Fig. 5, and the same qualitative behavior is seen. Thus, we conclude that our correlation is reasonable. In generating the curves of Figs. 4 and 5, the following assumptions were made: $\delta_v^+\sim 15.5$, $T_b=20°\mathrm{C}$, and $q_w=50\ \mathrm{kW/m^2}$. The values of the bulk temperature and wall heat flux are consistent with Pak and Cho's experimental conditions.

Unfortunately, Xuan and Li's copper/water nanofluid data cannot be used to test the performance of our correlation further, because the size of their nanoparticles is not reported in [13]. Moreover, Xuan and Li did not measure the temperature dependence of the thermophysical properties, but this dependence is expected to be very strong especially for copper and copper-oxide nanoparticles [5,25]. From the rated power of Xuan and Li's power supply and the values they report for the heat transfer coefficient, we estimate that in their experiments the temperature drop across the boundary layer could have been as high as 15°C, which according to Jang and Choi's model [25] could result in a thermal conductivity enhancement of about 30% at the wall. The combination of this effect and the effect of reduced viscosity in the boundary layer would explain the very significant deviation from the Dittus-Boelter correlation in their experiments.

Note that Pak and Cho's correlation is completely empirical, while Xuan and Li's is based on the dispersion model, but needed five empirical coefficients to match the data. In comparison, Eq. (50) is physically based, has only one empirical coefficient (i.e., δ_v^+), and has the following two desirable features:

(1) It accounts for the effect of thermophoresis and temperature on the thermophysical properties of the nanofluid.
(2) It reduces to a reliable pure-fluid correlation for $\phi_b=0$.

Note that the new correlation implies that the heat transfer coefficient in nanofluids depends on the wall heat flux (via the N_{BT} number and the dependence of Pr_v on T_w). Moreover, if our explanation of the heat transfer enhancement in flowing nanofluids is correct, the Nusselt number measured in a cooling experiment ($T_w<T_b$) should be lower than that predicted by a pure-fluid correlation. To test our conclusions, we will soon measure the heat

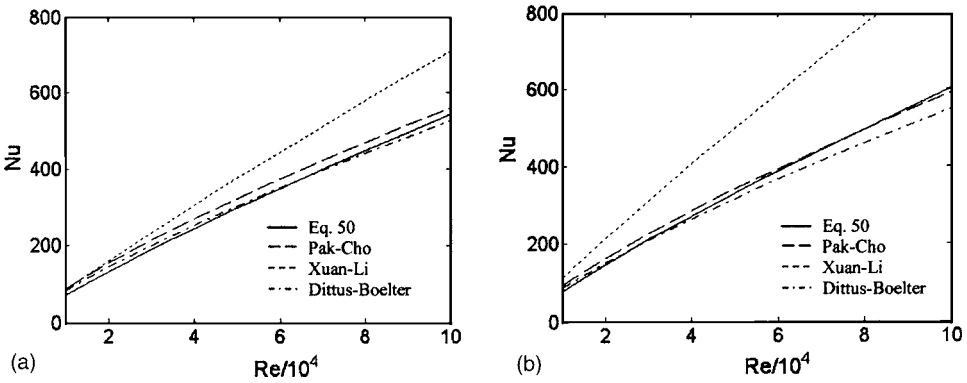

Fig. 5 Heat transfer in titania/water nanofluids: (*a*) ϕ_b=0.01; and (*b*) ϕ_b=0.03

transfer coefficient for various nanofluids and for both heating and cooling situations, in a flow loop under construction at MIT.

6 Conclusions

The objective of this work was to develop an explanation for the abnormal convective heat transfer enhancement observed in nanofluids. The major findings contained in this paper are as follows:

(a) Brownian diffusion and thermophoresis have been identified as the two most important nanoparticle/base-fluid slip mechanisms.

(b) A general two-component nonhomogeneous equilibrium model for transport phenomena in nanofluids has been developed, incorporating the effects of Brownian diffusion and thermophoresis.

(c) Order-of-magnitude estimates for the various terms of the energy equation suggest that energy transfer by nanoparticle dispersion is negligible, contrary to what is commonly stated in the literature.

(d) Application of our model to nanofluid heat transfer in the turbulent regime has highlighted the role of nanoparticle diffusion effects in the boundary layer near the wall. In particular, this paper represents the first attempt to describe the effect of thermophoresis in nanofluids mechanistically.

(e) Convective heat transfer enhancement can be explained mainly with a reduction of viscosity within and consequent thinning of the laminar sublayer.

(f) We have developed a new correlation structure (based on this explanation of the heat transfer enhancement) that can reproduce published nanofluid heat transfer data reasonably well. The correlation is given by Eq. (50).

Nomenclature

c = nanofluid specific heat (J/kg K)
c_{bf} = base fluid specific heat (J/kg K)
c_p = Nanoparticle specific heat (J/kg K)
C = friction factor correlation coefficient
d_p = nanoparticle diameter (m)
D = channel diameter (m)
D_B = Brownian diffusion coefficient (m^2/s)
D_T = thermal diffusion coefficient (m^2/s)
f = friction factor
g = acceleration of gravity (m/s^2)
h = heat transfer coefficient (W/m^2 K)
h_p = nanoparticle specific enthalpy (J/kg)
$\mathbf{j}_p$ = total nanoparticle mass flux (kg/m^2 s)
$\mathbf{j}_{p,B}$ = nanoparticle mass flux due to Brownian diffusion (kg/m^2 s)
$\mathbf{j}_{p,T}$ = nanoparticle mass flux to thermophoresis (kg/m^2 s)
k = nanofluid thermal conductivity (W/m K)
k_B = Boltzmann constant (J/K)
k_p = nanoparticle thermal conductivity (W/m K)
Kn = Knudsen number
ℓ_o = large eddy length scale (m)
ℓ_s = small eddy length scale (m)
Le = Lewis number
n = friction factor correlation exponent
N_{BT} = ratio of Brownian and thermophoretic diffusivities
P = pressure (Pa)
$\wp$ = dimensionless pressure
Pe_r = rotational Peclet number
Pr = prandtl number
$\mathbf{q}$ = energy flux (W/m^2)
q_w = heat flux at the wall (W/m^2)
$\mathbf{r}$ = position vector (m)
$\mathbf{R}$ = dimensionless position vector
Re = Reynolds number
S_p = nanoparticle stopping distance (m)
Sc = Schmidt number
t = time (s)
T = nanofluid temperature (K)
T_i = temperature at the laminar/turbulent sublayer interface (K)
$\mathbf{v}$ = nanofluid velocity (m/s)
$\mathbf{V}$ = dimensionless nanofluid velocity
$\overline{V}$ = mean axial velocity (m/s)
V_e = nanoparticle slip velocity due to turbulent eddies (m/s)
V_{eo} = turbulent eddy velocity (m/s)
V_g = settling velocity due to gravity (m/s)
V_T = thermophoretic velocity (m/s)
V_i = velocity at the laminar/turbulent sublayer interface (m/s)
y = radial coordinate (m)

Greek

α = thermal diffusivity (m^2/s)
β = thermophoretic coefficient
δ_v = thickness of the laminar sublayer (m)
δ_v^+ = dimensionless thickness of the laminar sublayer
δ_t = thickness of the turbulent sublayer (m)
ΔT = film temperature drop (K)
ε_H = eddy diffusivity for heat (m^2/s)

ε_M = eddy diffusivity for momentum (m^2/s)
ε_p = eddy diffusivity for nanoparticles (m^2/s)
ϕ = nanoparticle volumetric fraction
Φ = normalized nanoparticle volumetric fraction
λ = water molecules mean free path (m)
μ = viscosity (Pa s)
θ = dimensionless temperature
ρ = nanofluid density (kg/m^3)
ρ_{bf} = base fluid density (kg/m^3)
ρ_p = nanoparticle density (kg/m^3)
τ = stress tensor (Pa)
τ_o = large eddy time scale (s)
τ_p = nanoparticle relaxation time (s)
τ_s = small eddy time scale (s)
τ_w = shear stress at the wall (Pa)
ξ = dimensionless time

Subscript

b = bulk
bf = base fluid
i = interface
p = nanoparticle
v = laminar sublayer
w = wall

Appendix A: Thermophysical Properties of Nanofluids

A.1 Density. The nanofluid density, ρ, is the average of the nanoparticle and base fluid densities:

$$\rho = \phi\rho_p + (1-\phi)\rho_{bf} \tag{A1}$$

where the subscripts p and bf refer to the nanoparticles and base fluid, respectively.

A.2 Specific Heat. Assuming that the nanoparticles and the base fluid are in thermal equilibrium, the nanofluid specific heat, c(J/kg K), should be calculated as follows:

$$c = \frac{\phi\rho_p c_p + (1-\phi)\rho_{bf}c_{bf}}{\rho} \tag{A2}$$

However, some authors [7,10,29] prefer to use a simpler (albeit incorrect) approach:

$$c = \phi c_p + (1-\phi)c_{bf} \tag{A3}$$

Note that Pak and Cho correlated their data with Eq. (A3). Therefore, to be consistent with them, we also made use of this equation in generating the curves of Fig. 4 and 5 in Sec. 5.4.

A.2.1 Viscosity. General and accurate models for prediction of the viscosity of a nanofluid, μ, are not available at this time. However, the room-temperature viscosity measured by Pak and Cho [7] can be correlated by means of the following equations:

$$\mu = \mu_{bf}(1 + 39.11\phi + 533.9\phi^2) \quad \text{(alumina nanoparticles)} \tag{A4}$$

$$\mu = \mu_{bf}(1 + 5.45\phi + 108.2\phi^2) \quad \text{(titania nanoparticles)} \tag{A5}$$

A.2.2 Thermal Conductivity. Models for prediction of the nanofluid thermal conductivity, k, are not available either. The thermal conductivity data used by Pak and Cho [7] can be correlated as follows:

$$k = k_{bf}(1 + 7.47\phi) \quad \text{(alumina nanoparticles)} \tag{A6}$$

$$k = k_{bf}(1 + 2.92\phi - 11.99\phi^2) \quad \text{(titania nanoparticles)} \tag{A7}$$

Appendix B: Turbulent Scales

An important concept in turbulent flow is that of energy cascade. That is, the kinetic energy fed to turbulence goes primarily into large eddies, from which it is transferred to smaller eddies, then to still smaller ones, until is dissipated (converted to heat) by viscous forces. Therefore, within a turbulent flow there exists a spectrum of turbulent eddies. The large eddies have length and time scales comparable with those of the flow itself [30]. For example, with reference to turbulent flow inside a round tube of diameter D and mean velocity $\overline{V}$, the length scale of the large eddies, ℓ_o, would be of the order of D, and their time scale, τ_o, of the order of $D/\overline{V}$. On the other hand, the smallest (dissipative) eddies have a length scale, ℓ_s, and a time scale, τ_s, that can be found by the Kolmogorov's scaling laws [30]:

$$\ell_s/\ell_o \sim \mathrm{Re}^{-3/4} \tag{B1}$$

$$\tau_s/\tau_o \sim \mathrm{Re}^{-1/2} \tag{B2}$$

Assuming typical flow conditions ($\mathrm{Re}\sim 50{,}000$, $D\sim 1$ cm, $\overline{V}\sim 5$ m/s), one gets $\ell_o\sim 1$ cm, $\ell_s\sim 3$ μm, $\tau_o\sim 2$ ms, and $\tau_s\sim 10$ μs. Therefore, the length and time scales of the turbulent eddies are much larger than the nanoparticle size and relaxation time, respectively (see Sec. 2.1). This means that the nanoparticles are transported by the turbulent eddies very effectively.

References

[1] Masuda, H., Ebata, A., Teramae, K., and Hishinuma, N., 1993, "Alteration of Thermal Conductivity and Viscosity of Liquid by Dispersing Ultra-Fine Particles," Netsu Bussei, **7**, No. 4, pp. 227–233.
[2] Choi, S., 1995, "Enhancing Thermal Conductivity of Fluids With Nanoparticles," in *Developments and Applications of Non-Newtonian Flows*, D. A. Siginer, and H. P. Wang, eds., ASME, FED-Vol. 231/MD-Vol. 66, pp. 99–105.
[3] Buongiorno, J., and Hu, L.-W., 2005, "Nanofluid Coolants for Advanced Nuclear Power Plants," Paper No. 5705, *Proceedings of ICAPP '05*, Seoul, May 15–19.
[4] Eastman, J., et al., 2001, "Anomalously Increased Effective Thermal Conductivities of Ethylene-Glycol-Based Nanofluids Containing Copper Nanoparticles," Appl. Phys. Lett., **78**(6), pp. 718–720.
[5] Das, S., et al., 2003, "Temperature Dependence of Thermal Conductivity Enhancement for Nanofluids," J. Heat Transfer, **125**, pp. 567–574.
[6] Bhattacharya, P., et al., 2004, "Evaluation of the Temperature Oscillation Technique to Calculate Thermal Conductivity of Water and Systematic Measurement of the Thermal Conductivity of Aluminum Oxide-Water Nanofluid," *Proceedings of the 2004 ASME International Mechanical Engineering Congress and Exposition*, Anaheim, California, November 13–20.
[7] Pak, B. C., and Cho, Y., 1998, "Hydrodynamic and Heat Transfer Study of Dispersed Fluids With Submicron Metallic Oxide Particles," Exp. Heat Transfer, **11**, pp. 151–170.
[8] Brinkman, H. C., 1952, "The Viscosity of Concentrated Suspensions and Solutions," J. Chem. Phys., **20**, pp. 571–581.
[9] Batchelor, G. K., 1977, "The Effect of Brownian Motion on the Bulk Stress in a Suspension of Spherical Particles," J. Fluid Mech., **83**(1), pp. 97–117.
[10] Maïga, S., et al., 2004, "Heat Transfer Behaviors of Nanofluids in a Uniformly Heated Tube," Superlattices Microstruct., **35**, pp. 543–557.
[11] Lee, S., et al., 1999, "Measuring Thermal Conductivity of Fluids Containing Oxide Nanoparticles," J. Heat Transfer, **121**, pp. 280–289.
[12] Wang, X., et al., 1999, "Thermal Conductivity of Nanoparticle-Fluid Mixture," J. Thermophys. Heat Transfer, **13**(4), pp. 474–480.
[13] Xuan, Y., and Li, Q., 2003, "Investigation on Convective Heat Transfer and Flow Features of Nanofluids," J. Heat Transfer, **125**, pp. 151–155.
[14] Eastman, J., et al., 2004, "Thermal Transport in Nanofluids," Annu. Rev. Mater. Res., **34**, pp. 219–246.
[15] Xuan, Y., and Roetzel, W., 2000, "Conceptions for Heat Transfer Correlation of Nanofluids," Int. J. Heat Mass Transfer, **43**, pp. 3701–3707.
[16] Ahuja, A., 1975, "Augmentation of Heat Transport in Laminar Flow of Polystyrene Suspensions," J. Appl. Phys., **46**(8), pp. 3408–3425.
[17] Bott, T. R., 1995, *Fouling of Heat Exchangers*, Elsevier, New York.
[18] Lister, D. H., 1980, Corrosion Products in Power Generating Systems, AECL-6877, June.
[19] Whitmore, P. J., and Meisen, A., 1977, "Estimation of Thermo- and Diffusiophoretic Particle Deposition," Can. J. Chem. Eng., **55**, pp. 279–285.
[20] McNab, G. S., and Meisen, A., 1973, "Thermophoresis in Liquids," J. Colloid Interface Sci., **44**(2), pp. 339.
[21] Müller-Steinhagen, H., 1999, "Cooling-Water Fouling in Heat Exchangers," Adv. Heat Transfer, **33**, pp. 415–496.
[22] Bird, R. B., et al., 1960, *Transport Phenomena*, Wiley, New York.
[23] Wen, D., and Ding, Y., 2004, "Effect on Heat Transfer of Particle Migration in Suspensions of Nanoparticles Flowing Through Minichannels," *Proceedings of*

the 2nd International Conference on Microchannels and Minichannels, Paper No. 2434, Rochester, New York, June 17–19.
[24] Prandtl, L., 1944, *Füehrer Durch die Ströemungslehre*, Vieweg, Braunschweig, p. 359.
[25] Jang, S. P., and Choi, S. U., 2004, "Role of Brownian Motion in the Enhanced Thermal Conductivity of Nanofluids," Appl. Phys. Lett., **84**(21), pp. 4316–4318.
[26] Gnielinski, V., 1976, "New Equations for Heat and Mass Transfer in Turbulent Pipe and Channel Flow," Ind. Eng. Chem., **16**, pp. 359–368.
[27] Rohsenow, W. M., et al., 1998, *Handbook of Heat Transfer*, 3rd ed., McGraw-Hill, New York.
[28] Kakac, S., et al., 1987, *Handbook of Single-Phase Convective Heat Transfer*, Wiley, New York.
[29] Jang, S. P., and Choi, S. U., 2004, "Free Convection in a Rectangular Cavity (Benard Convection) With Nanofluids," Proceedings of the 2004 ASME International Mechanical Engineering Congress and Exposition, Anaheim, California, November 13–20.
[30] Pope, S. B., 2000, *Turbulent Flows*, Cambridge University Press, Cambridge.

Suppression of Boiling Flow Oscillations in Parallel Microchannels by Inlet Restrictors

Ali Koşar

Chih-Jung Kuo

Yoav Peles
e-mail: pelesy@rpi.edu

Department of Mechanical, Aerospace and Nuclear Engineering,
Rensselaer Polytechnic Institute,
Troy, NY 12180

Geometrical effects of MEMS-based microfabricated inlet orifices on the suppression of parallel channel and upstream compressible volume instabilities commonly exhibited during flow boiling in parallel microchannels have been investigated. The heat fluxes at the onset of unstable boiling have been obtained over effective heat fluxes ranging from 9 to 614 W/cm^2 *and mass fluxes from* 115 *to* 389 kg/m^2 s. *A dimensionless parameter M, which accounts for the pressure drop increase imposed by the inlet restrictors, has been used to correlate the extent of flow instability suppression. It has been shown that the onset of unstable boiling asymptotically increases with M. At sufficiently high M values, parallel channels and upstream compressible volume instabilities are completely eradicated although it gives way to another instability to develop, namely, the critical heat flux conditions. A correlation has been developed in terms of M to predict the conditions leading to unstable boiling.* [DOI: 10.1115/1.2150837]

Keywords: flow instabilities, microchannels, inlet restrictor, onset of unstable boiling, boiling

1 Introduction

Boiling two-phase flow in microsystems has attracted considerable attention in recent years, and copious investigations have been devoted to unveil the thermal, hydrodynamic, and morphological characteristics of boiling in channels whose length scale resides near 100 μm. Two-phase heat transfer coefficients [1–7], onset of nucleate boiling [8–10], flow patterns [11–13], and flow instabilities [13–20] pertaining to microsystems were investigated and compared to conventional scale systems. One very important flow characteristic that stands out in channels with hydraulic diameter below ~200 μm is significant flow and pressure oscillations often observed in parallel microchannel arrangements [16–26]. Flow oscillations are commonly related with upstream compressible volume [19,25,26] and parallel channel instabilities [19,25,26] instigated by a unique flow pattern frequently referred to as *rapid bubble growth* [2,16,18,27]. In the initial stage of the ebullition cycle, i.e., during the *rapid bubble growth*, a spherical bubble grows until it attains a size comparable to the channel hydraulic diameter. Constrained by the channel walls, the bubble cannot expand radially, and thus grows rapidly in the longitudinal direction (downstream as well as upstream) causing flow reversal. As noted by several investigators [3,19], instabilities of this magnitude will certainly precipitate critical heat flux conditions (CHF) [28–31], especially at low flow rates.

Macroscale flow instabilities have been a topic of extensive study since the mid 1960s, and a thorough characterization of flow instability modes are provided by Bouré et al. [32]. As discussed by Daleas and Bergles [33] and Maulbetsch and Griffith [34] and echoed in [19], upstream compressible flow is caused by an entrained air bubble or flexible hose, while in microchannels a large volume of degassed liquid is sufficient to cause instability [19]. *Parallel channel* instability is closely connected with another instability mode commonly known as Ledinegg or excursive instability [35], which is instigated when the pressure drop demand-flow rate curve becomes algebraically smaller than the loop supply pressure drop-flow rate curve. Although the mechanisms responsible for the *upstream compressible flow* instability are intrinsically different from *parallel channel* instability, a common remedy in the form of an inlet throttle valve is frequently employed in conventional channels to contain these instabilities. However, for *upstream compressible flow* instability a single common valve is sufficient to isolate the boiling channels from the compressible volume, while suppression of *parallel channels* require individual valves for each channel.

The majority of archival publications delineating boiling flow instabilities in microchannels fall short of discussing the origin of these deleterious manifestations or suggesting means to suppress its occurrence. Koşar et al. [5,7,12] placed 20 μm wide 400 μm long restrictors in the inlet of 200 μm wide microchannels to successfully eradicate flow oscillations. Qu and Mudawar [3] placed a throttling valve upstream of the test module and increased the overall pressure drop by ~500% to eliminate *upstream compressible flow* instability. Although, these studies confirm the effectiveness of inlet throttling to eliminate flow instabilities in microchannels, no design criteria have been discussed in selecting these regulators. Bergles and Kandlikar [19] are perhaps the first to comprehensively discuss apparent flow instabilities in microchannels and suggest various means for suppression. In a later study, Kandlikar et al. [36] experimentally investigated several methods to reduce the occurrence of flow instabilities in channels having hydraulic diameter of 333 μm by throttling valves and artificially drilled nucleation sites.

The current investigation parametrically studies geometrical effect of MEMS-based microfabricated inlet orifices on the suppression of boiling flow instabilities in parallel microchannels. The projected work involves an in-depth evaluation of flow oscillation, premature CHF conditions induced by flow oscillations, and pressure drop associated with 20 μm orifices of varying length placed inside 200 μm wide microchannels. The microchannel devices' overview is presented in Sec. 2. The design, fabrication, experimental setup description, and the experimental procedure are pro-

Contributed by the Heat Transfer Division of ASME for publication in the JOURNAL OF HEAT TRANSFER. Manuscript received May 12, 2005; final manuscript received: September 27, 2005. Review conducted by Yogendra Joshi.

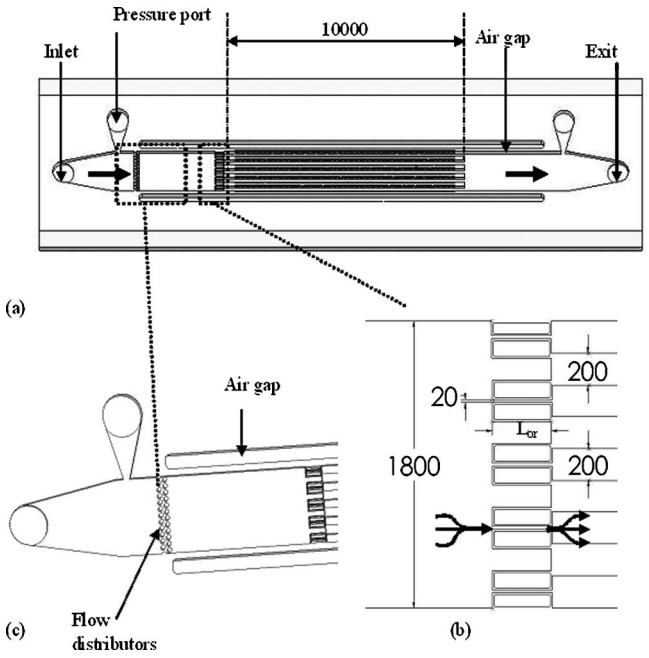

Fig. 1 (*a*) CAD model of the microchannel device, (*b*) Geometry of a sample orifice configuration, (*c*) Flow distributive pillars (units in μm)

vided in Sec. 3. Section 4 presents data reduction and uncertainty analysis, and Sec. 5 is devoted to the discussion of the experimental results. Finally, Sec. 6 presents the conclusions of this investigation.

2 Experimental Devices

Figure 1(*a*) schematically displays the microchannel devices consisting of five 1-cm long, 200-μm wide, and 264-μm deep, parallel microchannels, spaced 200 μm apart. In order to minimize ambient heat losses, an air gap is formed on the two ends of the side walls, and an inlet and exit plenum are etched on the thin silicon substrate ($\sim$150 μm). A heater is deposited on the backside to deliver the heating power and also to serve as a thermistor for temperature measurements. A pyrex substrate seals the device from the top and allows flow visualization. Five 20-μm wide orifices with different lengths (L_{or}) are installed (Fig. 1(*b*)) at the entrance of each channel to study their effect on suppressing flow instabilities. Flow distributive pillars have been employed to provide homogeneous distribution of flow in the inlet (Fig. 1(*c*)). They are arranged in 2 columns of 12 circular pillars having a diameter of 100 μm. The transverse pitch between the pillars is 150 μm and equal to the longitudinal pitch. Four devices with different inlet conditions, listed in Table 1, are tested in this study.

Table 1 Microchannel devices in the current study

Device	L (mm)	d_h (μm)	L_{or} (μm)	w_{or} (μm)	$d_{h,or}$ (μm)
1NR	10	227	0	20	37
2*R*50	10	227	50	20	37
3*R*200	10	227	100	20	37
4*R*400	10	227	400	20	37

3 Device Fabrication, Experimental Setup, and Experimental Procedure

3.1 Microchannel Fabrication Method. The MicroElectroMechanical Systems (MEMS) device is micromachined on a polished double-sided *n*-type $\langle 100 \rangle$ single crystal silicon wafer employing techniques adapted from IC manufacturing.

A 1-μm thick high quality oxide film is deposited on both sides of the silicon wafer to protect the bare wafer surface during processing, and serves as an electrical insulator. The heater and the vias are formed on the backside of the wafer (on top of the thermistors) by CVC sputtering. A 70 Å thick layer of titanium is initially deposited to improve adhesion characteristics, which is followed by sputtering a 1 μm thick layer of aluminum containing 1% silicon and 4% copper. Subsequent photolithography and concomitant wet bench processing create the heater on the backside of the wafer. A 1-μm thick plasma enhanced chemical vapor deposition (PECVD) oxide is deposited to protect the heater during further processing.

Next, the microchannels are formed on the top side of the wafer. The wafer undergoes a photolithography step and an oxide removal process (reactive ion etching) to mask certain areas on the wafer which are not to be etched during the deep reactive ion etching (DRIE) process. The wafer is subsequently etched in a DRIE process, and silicon is removed from places not protected by the photoresist/oxide mask. The DRIE process forms deep vertical trenches on the silicon wafer with a characteristic scalloped sidewall possessing a peak-to-peak roughness of $\sim$0.3 μm. A profilometer and SEM are employed to measure and record various dimensions of the device.

The wafer is flipped and the backside is then processed to create an inlet, outlet, side air gap, and pressure port taps for the transducers. Photolithography followed by a buffer oxide etching (BOE) (6:1) oxide removal process is carried out to create a pattern mask. The wafer is then etched-through in a DRIE process to create the fluidic ports. Thereafter, electrical contacts/pads are opened on the backside of the wafer by performing another round of photolithography and RIE processing. Finally, the processed wafer is stripped of any remaining resist or oxide layers and anodically bonded to a 1-mm thick polished Pyrex (glass) wafer to form a sealed device. After the successful completion of the bonding process, the processed stack is die-sawed to separate the devices from the parent wafer.

The MEMS device is packaged by sandwiching it between two plates. The fluidic seals are forged using miniature "O-rings," while the external electrical connections to the heater are achieved from beneath through spring-loaded pins, which connect the heater and thermistors to electrical pads residing away from the main microchannel body.

3.2 Experimental Test Setup and Procedure. The setup, shown in Fig. 2, consists of the flow loop section, instrumentation, and a data acquisition system. The test section includes the MEMS based microchannel devices and its fluidic and thermal packaging module. The microchannel device is installed on the fluidic packaging module through O-rings to ensure a leak proof system. The fluidic packaging delivers the working fluid to the microchannels and allows access to the pressure transducers.

The main flow loop contains the microchannel device, a pulseless gear pump, a reservoir which consists of a deaerator unit and a heating element to control the inlet temperature, flow meter, and dissolved oxygen meter (for use with water). The micro heater is connected to a power supply with an adjustable DC current to provide power to the device. The temperature sensor's output signals are recorded by the data acquisition system through the Labview® interface. While the inlet pressure and test section pressure drop are collected, the boiling process in the microchannels is recorded by a Phantom V4.2 high-speed camera (maximum frame rate of 90,000 frames/s, and 2-μs exposure time) mounted over a

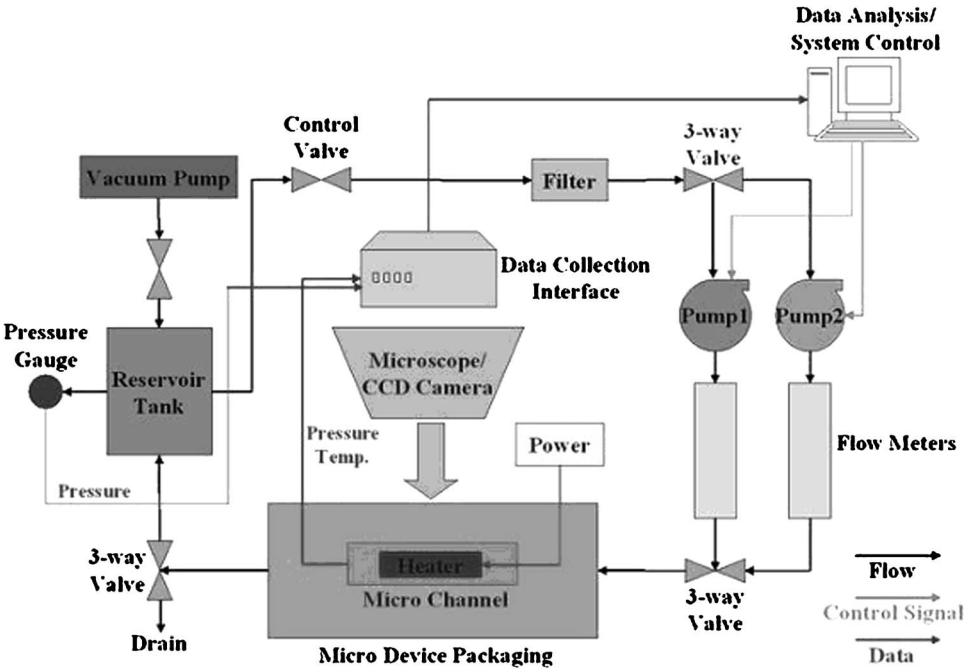

Fig. 2 Experimental setup

Leica DMLM microscope. Prior to the experiments, calibration of the temperature sensors is done by placing the device in an oven and establishing the resistance-temperature curve for each individual sensor.

The deionized water flow rate was fixed at the desired value, and experiments were conducted after steady flow conditions were reached at the atmospheric exit pressure and ambient room temperature. First, the electrical resistance of the device was measured at room temperature. Thereafter, voltage was applied in 0.5 V increments to the heater, and the current/voltage data were recorded once steady state was reached. At impeding unstable boiling conditions, a meager increase in the applied power causes severe temperature fluctuations and in some cases (in device 1NR and 2*R*50) flow reversal. Once this condition is attained, the power was switched off to prevent potential burnout. Flow visualization through the high-speed camera and microscope complements the measured data. The procedure is repeated for different flow rates for each device.

To estimate heat losses, electrical power was applied to the test section after evacuating the water from the test loop. Once the temperature of the test section became steady, the temperature difference between the ambient and test section was recorded with the corresponding power, so that the plot of power versus temperature difference was generated to calculate the heat loss ($\dot{Q}_{\text{loss}}$) associated with each experimental data point, and the heat losses were found accordingly.

4 Data Reduction and Uncertainties

Data obtained from the voltage, current, and pressure measurements were used to calculate the average surface temperature, friction factors, and pressure drops across the microchannels and orifices. The electrical input power and heater resistance, respectively, were determined with

$$P = V \times I \tag{1}$$

and

$$R = V/I \tag{2}$$

The heater electrical resistance-temperature calibration curve is used for determining the heater temperature. The surface temperature at the base of the microchannels is then calculated as:

$$\overline{T} = \overline{T}_{\text{heater}} - \frac{(P - \dot{Q}_{\text{loss}})t}{k_s A_p} \tag{3}$$

The pressure drop across the microchannels is approximated as the difference between the measured pressure drop across device 1NR and the measured pressure losses:

$$\Delta p_{\text{microchannels}} = \Delta p_{\text{exp,1NR}} - \Delta p_{\text{losses}} \tag{4}$$

Pressure losses can be calculated using one dimensional momentum and mechanical conservation equations as:

$$\Delta p_{\text{losses}} = \Delta p_i + \Delta p_e + \Delta p_{i,\text{plenum}} + \Delta p_{e,\text{plenum}} + \Delta p_{i,\text{distributor}} \tag{5}$$

where [40]:

$$\Delta p_i = \rho \frac{\overline{u}^2}{2} \frac{1 - \beta\tau^2 C_C^2 - 2C_C + 2C_C^2 k_d}{C_C}$$

$$\Delta p_e = \rho \frac{\overline{u}^2}{2} \left[\frac{1 - 2k_d\tau + \tau^2(k_d - 1)}{2} - (1 - \tau^2) \right]$$

$$C_C = 1 - \frac{1 - \tau}{2.08(1 - \tau) + 0.5371} \text{ given by Geiger [37]}$$

$$k_d = \frac{\overline{u^2}}{\overline{u}^2}\beta = \frac{\overline{u^3}}{\overline{u}^3}$$

$$\Delta p_{i,\text{plenum}} = f_{\text{plenum}} \rho \frac{L_{i,\text{plenum}}}{d_{h,\text{plenum}}} \frac{\overline{u}^2_{\text{plenum}}}{2}$$

$$\Delta p_{e,\text{plenum}} = f_{\text{plenum}} \rho \frac{L_{e,\text{plenum}}}{d_{h,\text{plenum}}} \frac{\overline{u}^2_{\text{plenum}}}{2}$$

$$f_{\text{plenum}} = \frac{K_1}{\text{Re}_{\text{plenum}}}; \quad K_1 \text{ is given in Shah and London [38]}$$

$$\Delta p_{i,\text{distributor}} = N f_{\text{cross}} \rho \left(\frac{S_T}{S_T - D} \right)^2 \frac{\overline{u}^2_{\text{plenum}}}{2};$$

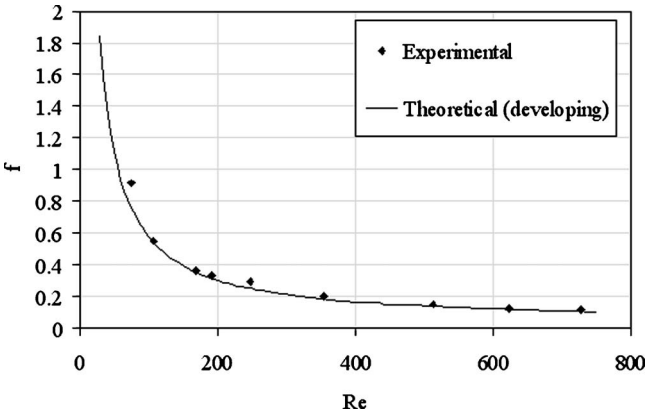

Fig. 3 Dependence of friction factor on the Reynolds number

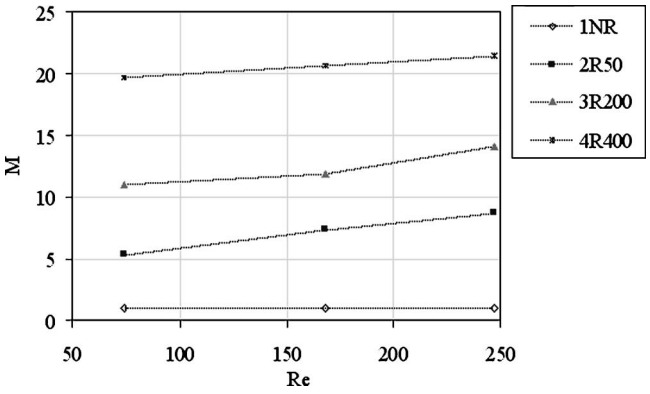

Fig. 4 Dependence of *M* on the Reynolds number

f_{cross} is given by Gunther and Shaw [39]

Friction factors are obtained using the following expression:

$$f = \frac{2\Delta p_{\text{microchannels}} d_h}{\rho \bar{u}^2 L} \tag{6}$$

Pressure drop across the orifices is:

$$\Delta p_{\text{tot,or}} = \Delta p_{\text{exp}} - \Delta p_{\text{exp,1NR}} \tag{7}$$

Similar analysis performed for the losses at the inlet and exit of the microchannels has been executed to calculate the losses for the orifices using Eq. (6). Finally, the exit quality can be calculated with the known mass flow rate and net power supplied to the device as:

$$x_e = \frac{(P - \dot{Q}_{\text{loss}}) - \dot{m} c_p (T_{\text{sat}} - T_i)}{\dot{m} h_{FG}} \tag{8}$$

Mean absolute error (MAE) is used to compare the experimental results with theory:

$$\text{MAE} = \frac{1}{m} \sum_{j=1}^{m} \frac{|U_{\text{exp}} - U_{\text{theoretical}}|}{U_{\text{exp}}} \times 100\% \tag{9}$$

Uncertainties in the measured values were obtained from the manufacturer's specification sheets, while the uncertainties of the derived parameters are calculated using the method developed by Kline and McClintock [41]. Uncertainties in the surface temperature, heat flux, and friction factor are estimated to be ±1°C, ±0.7%, and ±7.5%, respectively.

5 Results and Discussion

5.1 Pressure Drop Across Inlet Restrictors. The method used in the current study to suppress hydrodynamic instabilities involves effectively increasing the ratio between the inlet losses (via inlet orifices) to the major microchannel pressure losses (Moody-type losses). Therefore, any discussion delineating the extent of flow instability suppression using inlet restrictors should entail a comprehensive discussion on the pressure drop magnitude that is imposed by the orifices at the channel entrance (in comparison to the main channel pressure drop).

To differentiate between the unrestricted channel losses and the losses imposed by the inlet restrictors, pressure drop measurements have been performed on the device without inlet restrictors (device 1NR). The pressure losses at the inlet and exit of the microchannels due to sudden contraction and expansion, as well as the losses in the inlet and outlet plenums, and flow distributors, have been subtracted from the measured pressure drops to obtain the net pressure drop across the microchannels, and the corresponding friction factors have been obtained. Figure 3 shows the dependence of the friction factor on the Reynolds number alongside the prediction of London and Shah [38] correlation recommended for developing laminar flow in rectangular channels which is given by the following expression:

$$f_{\text{developing}} = \frac{\left(13.76(x^+)^{-0.5} + \dfrac{K_2/(4x^+) + f\,\text{Re} - 13.76(x^+)^{-0.5}}{1 + K_1(x^+)^{-0.2}}\right)}{\text{Re}} \tag{10}$$

where

$$f = \frac{C}{\text{Re}}(1 - 1.355\beta + 1.947\beta^2 - 1.701\beta^3 + 0.953\beta^4 - 0.254\beta^5)$$

$$x^+ = \frac{L_{\text{ent}}}{\text{Re}\, d_h}$$

As is clear, the developing flow correlation predicted the trend as well as the values of the experimental data well with a MAE of 7.55%. Following the developing flow approach performed on device 1NR, pressure drops have been experimentally obtained for the three devices with inlet restrictors. An experimental pressure drop multiplier parameter, *M*, given by:

$$M = \frac{\Delta p_{\text{microchannel}} + \Delta p_{\text{orifice}}}{\Delta p_{\text{microchannel}}} \tag{11}$$

is then used to deduce the pressure drop magnification imposed by the inlet orifices. Experimental measurements of the magnification *M* at adiabatic single-phase flow are shown for all devices in Fig. 4.

In Fig. 5, friction factors are displayed for the three different orifice configurations along with London and Shah correlations for fully developed and developing flows. As expected, the entrance effects are significant for flow in shorter orifices ($L_{\text{or}} < 100\ \mu$m) as shown in Fig. 5(*a*), and gradually diminishes with the increase in orifice length (Figs. 5(*b*) and 5(*c*)). With the increase in the Reynolds number, the experimental data gradually diverges from the fully developed prediction and tends to shift toward the developing flow model for device 2*R*50.

Figure 6 depicts the pressure drop magnification as a function of the exit mass quality. Since the inlet liquid temperature is fixed, the pressure drop across the inlet orifices is assumed to be constant regardless of heat flux. At low heat fluxes, while liquid single-phase flow prevails, *M* monotonically increases due to a reduction of the liquid viscosity downstream with the increase in flow temperature. With a sufficient increase in heat flux, boiling incepts and a maximum is reached. Thereafter, *M* monotonically declines due to the increase in two-phase pressure drop with the increase in void fraction. Therefore, designers should be aware that the effectiveness of the inlet restrictors gradually erodes with

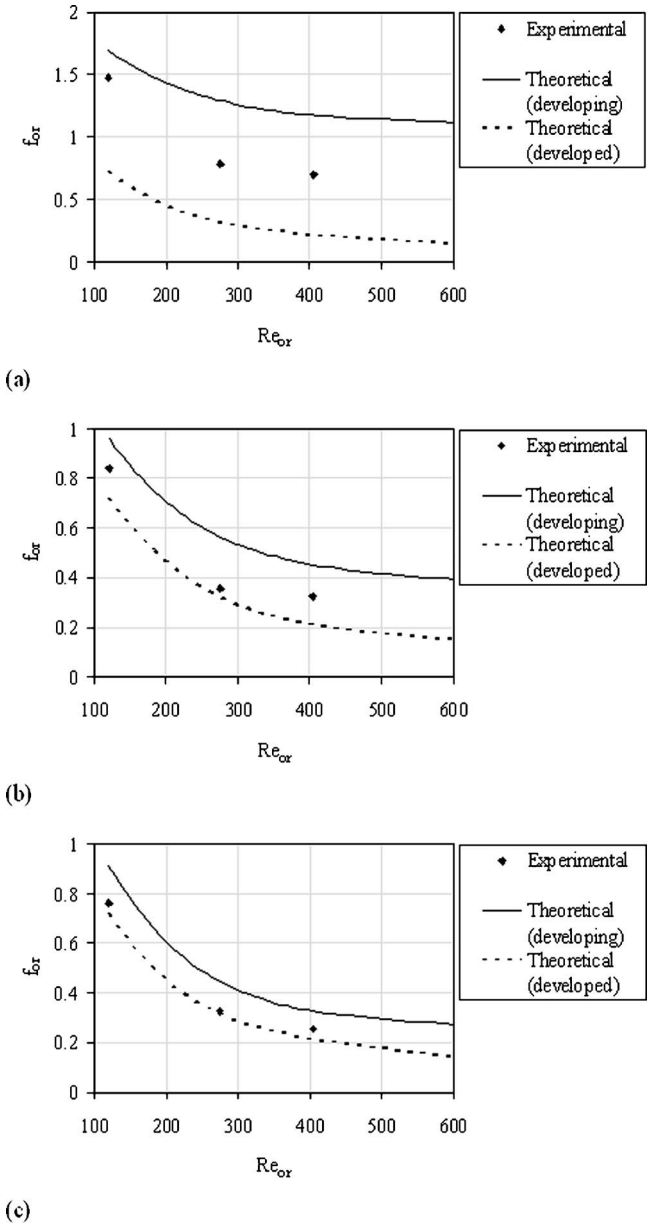

Fig. 5 Experimental and theoretical [38] friction factors across orifices: (*a*) Device 2*R*50, (*b*) Device 3*R*200, (*c*) Device 4*R*400

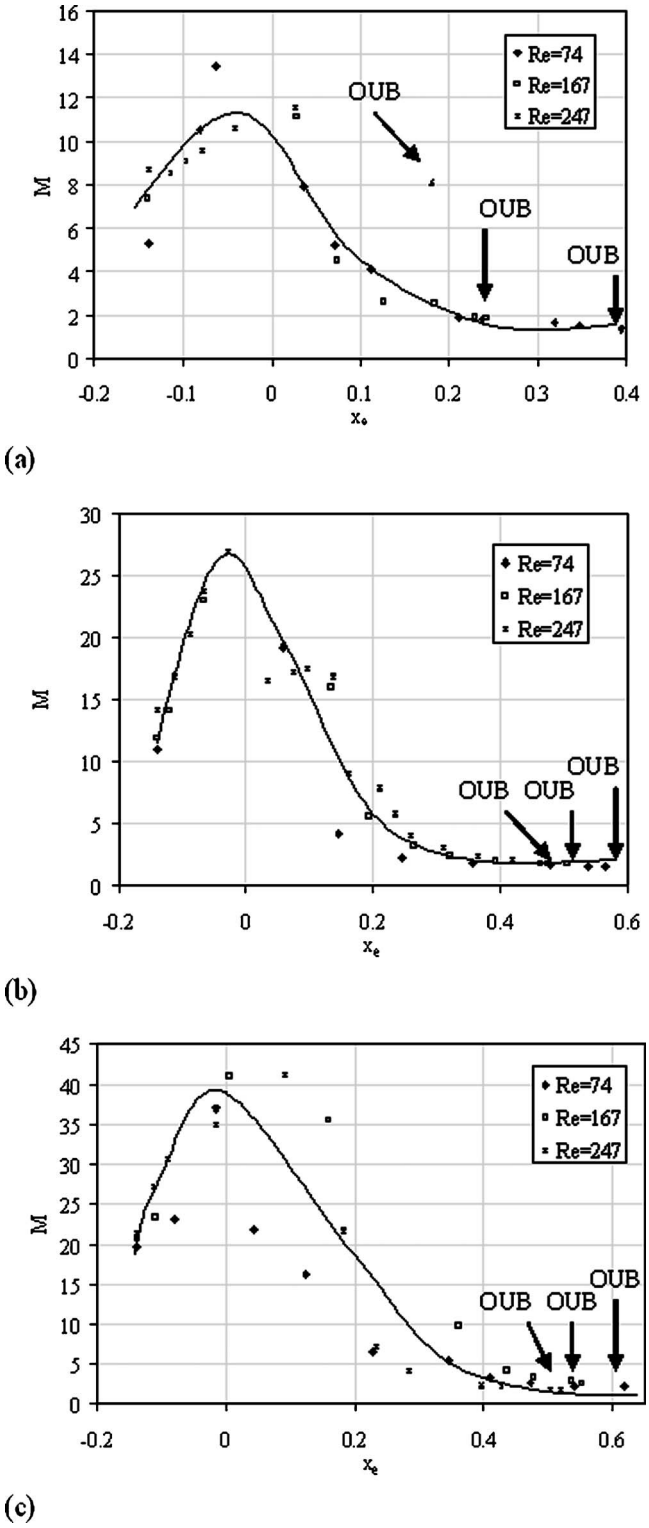

Fig. 6 Pressure multiplier as a function of x_e: (*a*) Device 2*R*50, (*b*) Device 3*R*200, (*c*) Device 4*R*400

an increase in the intensity of the two-phase flow. Continuing to increase the heat flux a condition associated with flow oscillations is reached, which is depicted as the data point corresponding to the largest exit quality attained, and is termed the onset of unstable boiling (OUB). For the unrestricted device (1NR) severe flow fluctuations causing large oscillations in pressure drop are apparent once boiling occurs. Figure 7 portrays the pressure drop profile for $G=389$ kg/m^2 s with time for device 1NR at adiabatic condition (Fig. 7(*a*)), at impeding OUB (Fig. 7(*b*)), and following OUB (Fig. 7(*c*)). At adiabatic condition, the flow is stable and pressure fluctuations are small (<0.5 kPa). As the power is increased, the pressure drop decreases, until OUB condition (for this device OUB is closely connected with the onset of nucleate boiling) is reached, which in turn instigate severe pressure drop fluctuations as evident from Fig. 7(*c*). These fluctuations are an indicator of flow reversals and instabilities, which are dominant in the unrestricted device. Contrary to device 1NR no significant pressure fluctuation under any working condition in device 4*R*400 has been registered. Even during the OUB condition, pressure fluctuations are insignificant (<1 kPa) compared to the time averaged pressure drop.

5.2 Effect of Inlet Restrictors on Flow Instability and Critical Heat Flux Conditions. The effect of the inlet restrictor on the heat flux-temperature curve is evident from Fig. 8. During single-phase flow, the temperature difference between all devices

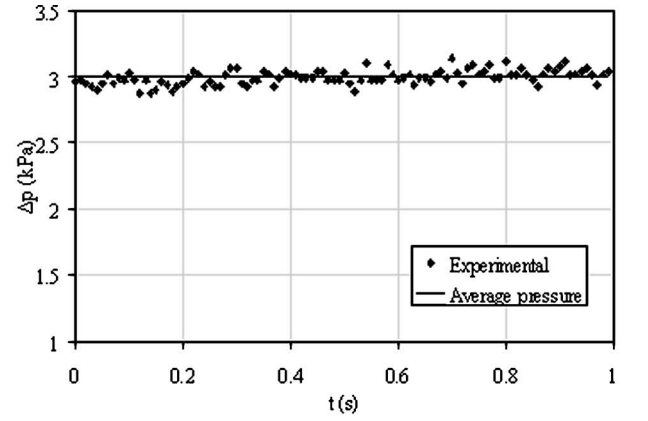

(a)

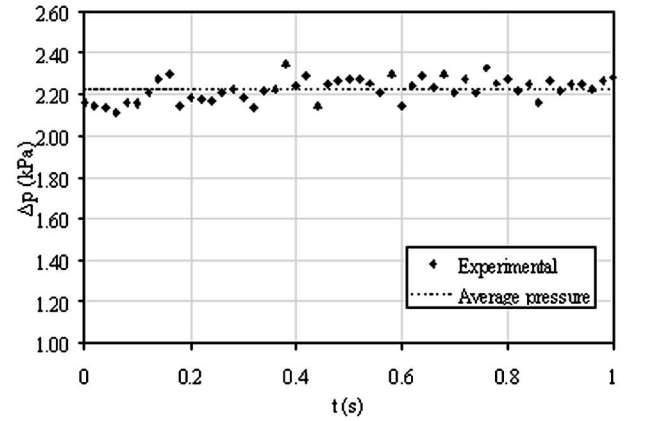

(b)

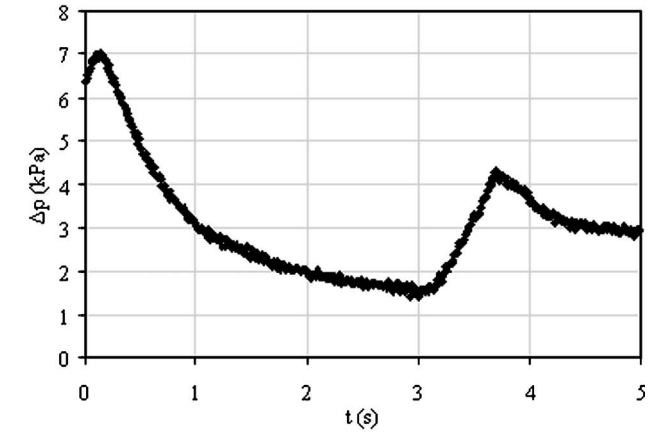

(c)

Fig. 7 Pressure drop fluctuations in device 1NR at $G = 389$ kg/m^2 s: (*a*) Adiabatic condition, (*b*) Impeding OUB, (*c*) At OUB

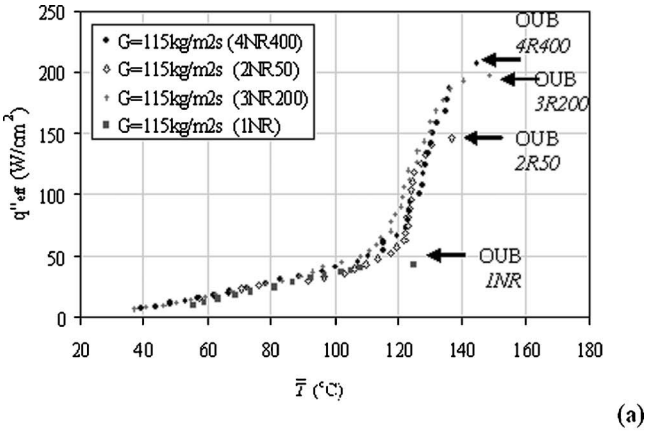

(a)

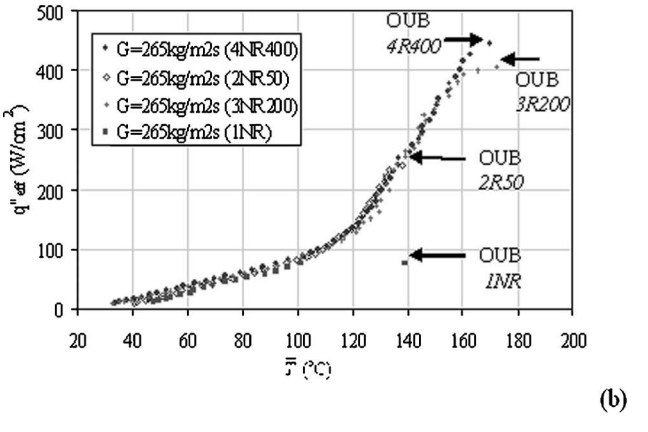

(b)

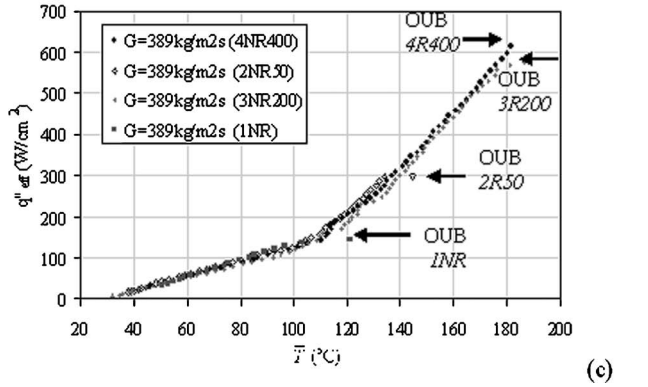

(c)

Fig. 8 Average surface temperatures of the devices: (*a*) $G = 115$ kg/m^2 s; (*b*) $G = 265$ kg/m^2 s; (*c*) $G = 389$ kg/m^2 s

is small. However, severe flow oscillations were observed in the device without the restrictors (1NR) once boiling occurs. These flow oscillations dominated all boiling flow conditions to a degree that accurate temperature measurements could not be obtained due to severe temperature fluctuations. Figure 9 shows a time sequence of images taken by the high-speed camera depicting the extent of the flow oscillations and the associated flow reversal typical of boiling in unrestricted microchannels. These flow instabilities are well documented in various reports [13–20] and the present results show no anomalies to previous microchannel boiling studies. Although realization of steady flow significantly beyond ONB was achieved in device 2*R*50, the increased inlet pressure drop of devices 3*R*200 and 4*R*400 notably elevated the stability of the boiling flow as shown in Fig. 8. For example, at $G = 265$ kg/m^2 s (Fig. 8(*b*)) the heat fluxes at the onset of unstable boiling are 75.5, 241, 407.5, and 445.9 W/cm^2 for devices 1NR, 2*R*50, 3*R*200, and 4*R*400, respectively. As the inlet restrictor lengthens, the increase in the heat fluxes corresponding to the onset of unstable boiling diminishes. Since devices 3*R*200 and 4*R*400 exhibit almost identical q''_{oub}, it can be inferred that the hydrodynamic instabilities (e.g., *parallel channel* and *upstream compressible volume*) are eradicated in these devices, and the abrupt increase in the surface temperature at high heat fluxes is the corresponding critical heat flux condition. Moreover, flow vi-

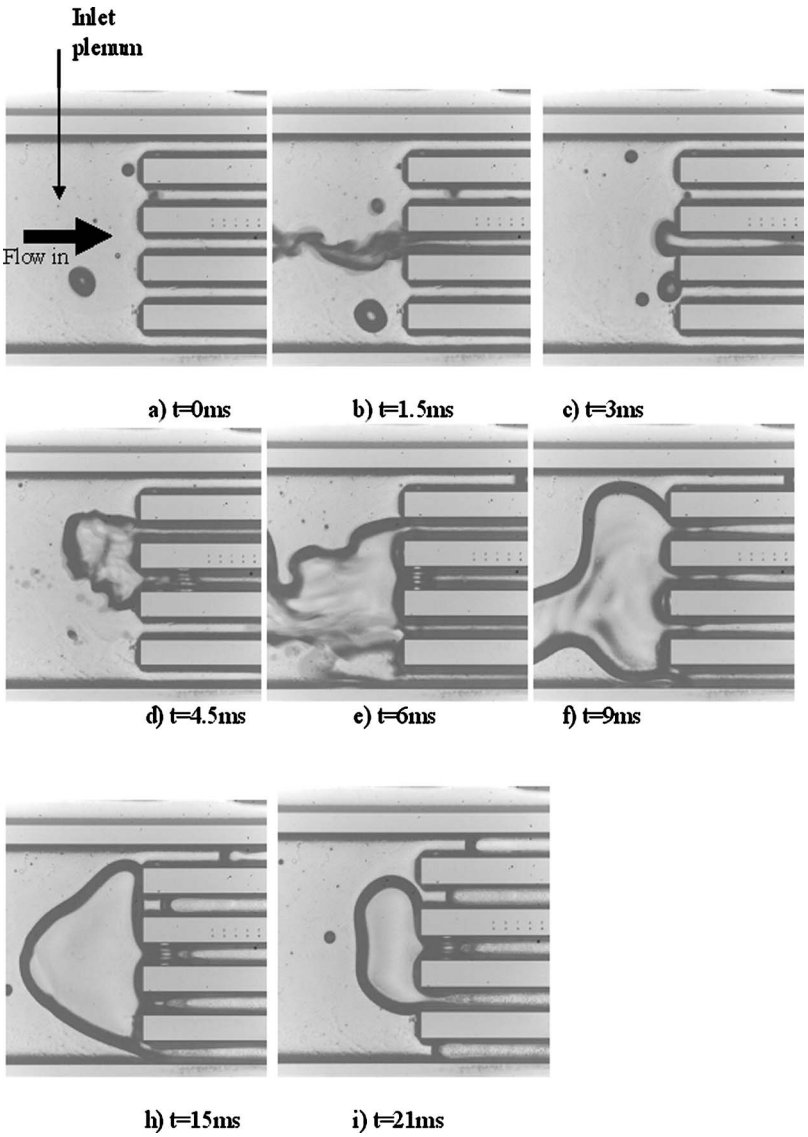

Fig. 9 Time sequence of images at OUB ($G=265$ kg/m^2 s) recorded for device 1NR at the inlet

sualization reveals no flow reversal in these devices at OUB. Further support for this identification is provided by the good agreement of the experimental OUB values of devices 3*R*200 and 4*R*400 with three published CHF correlations developed based on microchannels [42] as well as conventional scale channels [43,44] given in Table 2. As shown in Fig. 10 the results of OUB for devices 3*R*200 and 4*R*400 are well captured by the Qu and Mudawar [42] correlation (MAE=15.1% for the device 3*R*200, MAE=17.5% for the device 4*R*400). Similar to the critical heat flux condition [45], q''_{oub} linearly increases with mass velocity, and seemingly has a linear increasing profile for all the devices.

Figure 11 depicts the ratio $q''_{\text{oub}}/q''_{\text{oub,400 }\mu\text{m}}$ as a function of the pressure drop multiplier M. A sharp increase in the heat flux at onset of unstable boiling conditions in device 1NR in comparison to device 2*NR*50 is perceptible. Continuing to elevate M (device 3*R*200 and 4*R*400) results in a meager increase in q''_{oub}, which suggests an asymptotic q''_{oub}-M curve characteristic. Therefore, an exponent-type correlation can seemingly provide an adequate prediction formula to relate q''_{oub} with M.

Another important parameter controlling flow oscillations is the void fraction, α. However, the knowledge of α is not always readily available and in many cases cannot be accurately estimated (due to limited availability of correlations relevant to microsystems). A substitute parameter is therefore sought. Since α is closely related to the mass quality, the exit quality, x_e, can provide a simple measure capturing the void fraction effect on q''_{oub}. It is to be noted that under homogenous boiling assumption α can be directly obtained from the knowledge of mass quality. In an attempt to relate the onset of unstable boiling with the pressure drop multiplier and exit quality, the following correlation was obtained:

$$\frac{q''_{\text{oub}}}{q''_{\text{oub,400 }\mu\text{m}}} = [1 - \exp(-1.005\,\text{Re}^{-0.37}M^{0.82})]x_{e,400\ \mu\text{m}}^{-0.32}. \quad (12)$$

The predictions of the above correlation are included in Fig. 11. As argued previously, q''_{oub} in the 400 μm long inlet orifice device can be directly related to the CHF conditions, and therefore can be expressed in a functional form similar to CHF correlations [42]. That is:

$$q''_{\text{oub,400 }\mu\text{m}} = k_1 G h_{\text{FG}} We^{-k_2} \quad (13)$$

The least squares method has been employed to provide the best fit of the experimental data for device 4*R*400, and the corresponding constants in the above equation were derived. With k_1

Table 2 CHF correlation

Reference	Recommended channel size and fluid	Correlation
Bowring [43]	Circular, conventional channels	$q''_{CHF} = \frac{A' + d_h G(h_F - h_i)/4}{C' + L}$ $A' = \frac{0.579 F_{B1} d_h G h_{FG}}{1.0 + 0.0143 F_{B2} d_h^{1/2} G}$ $C' = \frac{0.077 F_{B3} d_h G}{1.0 + 0.347 F_{B4} (G/1356)^n}$ $n = 2.0 - 0.00725p$
Katto and Ohne [44]	Circular, conventional channels	$q''_{CHF} = XG(h_{FG} + K(\Delta h_{sub})_i)$ where $X = \frac{0.098(\rho_G/\rho_F)^{0.133}\left(\frac{\sigma\rho_F}{G^2 L}\right)^{0.433}(L/d_h)^{0.27}}{1.0 + 0.0031(L/d_h)}$ $K = \frac{0.261}{0.25\left(\frac{\sigma\rho_F}{G^2 L}\right)^{0.0433}}$
Qu and Mudawar [42]	Rectangular, $d_b = 0.38$–2.54 mm $R-113$, Water	$q''_{CHF} = 33.43 G h_{FG}\, \mathrm{We}^{-0.21}\left(\frac{\rho_G}{\rho_L}\right)^{1.1}\left(\frac{L}{d_h}\right)^{-0.36}$

$=0.00375$ and $k_2=0.06$, a MAE of 1.2% to the experimental results was obtained. If the above correlation is substituted into Eq. (12), the following correlation for q''_{oub} can be derived:

$$q''_{oub} = 0.00375 G h_{FG} We^{-0.06} x_{e,400\ \mu m}^{-0.32} \times [1 - \exp(-1.005\,\mathrm{Re}^{-0.37} M^{0.82})] \quad (14)$$

Correlation (14) predicts the experimental results well (83% of the data fall within 20% of the correlation).

6 Conclusions

Geometrical effects of inlet orifices on the suppression of boiling flow instabilities in parallel microchannels have been experimentally conducted. Friction factors for both microchannels and inlet restrictors have been obtained and compared to existing theory. The suppression of flow instabilities as a result of introducing flow restrictors has been quantified and a dimensionless parameter, the pressure drop multiplier (M), has been successfully employed to correlate the flow oscillation suppression. Severe flow oscillations causing large surface temperature fluctuations were initiated in plain microchannel devices without inlet restrictors once boiling incepts. With the introduction of flow restrictors, the heat fluxes corresponding to the onset of unstable boiling (q''_{oub}) increases asymptotically with M. For large M (longer orifices), q''_{oub} is well correlated with available archival correlations for the critical heat flux conditions.

Acknowledgment

This work was supported by the Office of Naval Research (Program Officer, Dr. Mark Spector) through the Young Investigator

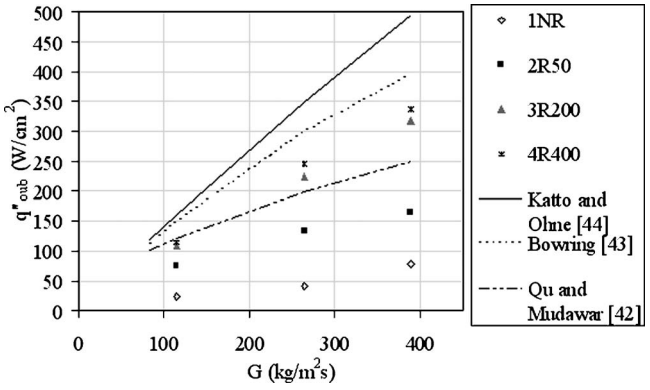

Fig. 10 Comparison of q''_{oub} data with CHF correlations

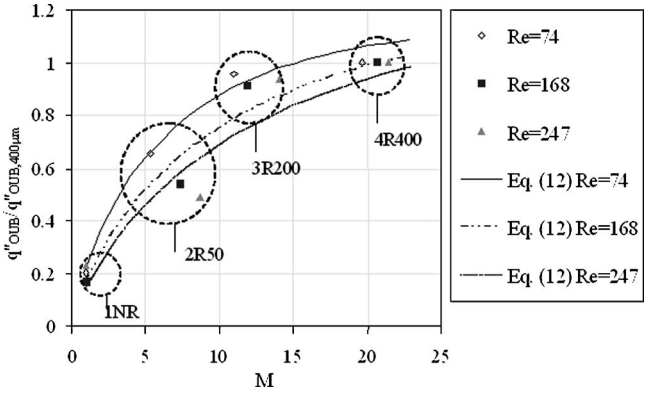

Fig. 11 $q''_{oub}/q''_{oub,400\ \mu m}$ as a function of M

Program (Yoav Peles) under Contract No. N00014-05-1-0582. Graduate student support from Rensselaer Polytechnic Institute is also gratefully appreciated.

Nomenclature

A' = parameter in the CHF correlation in Table 2
A_p = planform area (m^2)
C = parameter in Eq. (10)
C' = parameter in the CHF correlation in Table 2
C_c = vena contracta coefficient
CHF = critical heat flux ($W\,cm^{-2}$)
c_p = specific heat at constant pressure ($kJ\,kg^{-1}\,°C^{-1}$)
d_h = channel hydraulic diameter (m)
$d_{h,or}$ = orifice hydraulic diameter (m)
$d_{h,plenum}$ = inlet or exit plenum hydraulic diameter (m)
D = pin fin diameter (m)
f = friction factor across microchannels
F_{B1}, F_{B2}, F_{B3}, F_{B4} = parameter in the CHF correlation in Table 2
f_{cross} = friction factor across flow distributors
$f_{developing}$ = friction factor for developing flows
f_{or} = friction factor across orifices
G = mass velocity ($kg\,m^{-2}\,s^{-1}$)
h = enthalpy ($kJ\,kg^{-1}$)
h_{FG} = latent heat of vaporization ($kJ\,kg^{-1}$)
I = current (A)
K = parameter in the CHF correlation in Table 2
k_d = momentum correction factor
k_s = thermal conductivity of the surface (silicon) ($W\,m\,°C^{-1}$)
k_1, k_2 = constants
K_1, K_2 = constants
L = channel length (m)
$L_{e,plenum}$ = length of exit plenum (m)
L_{ent} = hydrodynamic entrance length (m)
$L_{i,plenum}$ = length of inlet plenum (m)
L_{or} = orifice length (m)
m = number of data points
$\dot{m}$ = mass flow rate ($kg\,s^{-1}$)
M = dimensionless parameter in Eq. (11)
MAE = mean absolute error
n = parameter in the CHF correlation in Table 2
N = number of pin fins in a single row of flow distributors
OUB = onset of unstable boiling
p = pressure (kPa)
P = electrical power (W)
q'' = heat flux ($W\,cm^{-2}$)
q''_{eff} = effective heat flux ($W\,cm^{-2}$)
$\dot{Q}_{loss}$ = heat loss (W)
R = electrical resistance (Ω)
Re = Reynolds number based on the channel hydraulic diameter
Re_{or} = Reynolds number based on the orifice hydraulic diameter
Re_{plenum} = Reynolds number based on the plenum hydraulic diameter
S_T = transverse pitch (m)
t = thickness of the silicon block (m)
T = temperature (°C)
$\overline{T}$ = average temperature (°C)
$\overline{T}_{heater}$ = average temperature at the heater (°C)
$\overline{u}$ = average velocity ($m\,s^{-1}$)
U = parameter being evaluated
V = voltage (V)
w = width (m)
w_{or} = orifice width (m)
We = Weber number
X = parameter in the CHF correlation in Table 2
x^+ = parameter in Eq. (10)
x_e = exit quality

Greek

β = aspect ratio
Δp = pressure drop (kPa)
$\Delta p_{distributor}$ = pressure drop across flow distributor (kPa)
Δp_e = pressure losses at the exit of microchannels (kPa)
$\Delta p_{e,or}$ = pressure losses at the exit of orifices (kPa)
Δp_i = pressure losses at the inlet of microchannels (kPa)
$\Delta p_{i,or}$ = pressure losses at the inlet of orifices (kPa)
Δp_{losses} = total pressure losses (kPa)
$\Delta p_{microchannels}$ = pressure drop across microchannels (kPa)
Δp_{or} = pressure drop across orifices (kPa)
ρ = density ($kg\,m^{-3}$)
σ = surface tension (N/m)
τ = flow area contraction ratio

Subscript

CHF = critical heat flux
cross = cross flow
developing = developing
distributor = distributor
e = exit
exp = experimental
f = fluid
fin = fin
G = gas
i = inlet
j = index in Eq. (9)
losses = losses
oub = onset of unstable boiling
or = orifice
plenum = plenum
sat = saturation
sub = subcooled
tot = total

References

[1] Jiang, L., Wong, M., and Zohar, Y., 2001, "Forced Convection Boiling in Microchannel Heat Sink," J. Microelectromech. Syst., **10**(1), pp. 80–87.
[2] Kandlikar, S. G., 2002, "Fundamental Issues Related to Flow Boiling in Minichannels and Microchannels," Exp. Therm. Fluid Sci., **26**, pp. 389–407.
[3] Qu, W., and Mudawar, I., 2003, "Flow Boiling Heat Transfer in Two-Phase Micro-Channel Heat Sink—I. Experimental Investigation and Assessment of Correlation Methods," Int. J. Heat Mass Transfer, **46**(15), pp. 2755–2771.
[4] Yun, R., Kim, Y., and Kim, M.-S., 2005, "Convective Boiling Heat Transfer Characteristics of CO_2 in Microchannels," Int. J. Heat Mass Transfer, **48**(2), pp. 235–242.
[5] Koşar, A., Kuo, C. J., and Peles, Y., 2005, "Boiling Heat Transfer in Rectangular Microchannels With Reentrant Cavities," Int. J. Heat Mass Transfer, **48**(23), pp. 4867–4886.
[6] Dupont, V., and Thome, J. R., 2005, "Evaporation in Microchannels: Influence of the Channel Diameter on Heat Transfer," Microfluidic Nanofluidic, **1**, pp. 119–127.

[7] Koşar, A., Kuo, C. J., and Peles, Y., 2005, "Reduced Pressure Boiling Heat Transfer in Rectangular Microchannels With Interconnected Reentrant Cavities," ASME J. Heat Transfer, **127**(10), pp. 1106–1114.
[8] Hapke, I., Boye, H., Schmidt, J., and Staate, Y., 2000, "Evaporation in Micro Heat Exchangers," Chem. Eng. Technol., **23**(6), pp. 496–500.
[9] Li, H. Y., Lee, P. C., Tseng, F. G., and Pan, C., 2004, "Two-Phase Phenomena for Boiling in Two Parallel Microchannels," in Proceedings of Second International Conference on Microchannels and Minichannels (ICMM2004), pp. 581–587.
[10] Steinke, M. E., and Kandlikar, S. G., 2004, "An Experimental Investigation of Flow Boiling Characteristics of Water in Parallel Microchannels," J. Heat Transfer, **126**(4), pp. 518–526.
[11] Kandlikar, S. G., 2004, "Heat Transfer Mechanisms During Flow Boiling in Microchannels," J. Heat Transfer, **126**(1), pp. 8–16.
[12] Kuo, C. J., Koşar, A., Peles, Y., Virost, S., Mishra, C., and Jensen, M. K., "Bubble Dynamics During Boiling in Enhanced Surface Microchannels," J. Microelectromechanical Systems (submitted).
[13] Zhang, L., Wang, E. N., Goodson, K. E., and Kenny, T. W., 2005, "Phase Change Phenomena in Silicon Microchannels," Int. J. Heat Mass Transfer, **40**(8), pp. 1572–1582.
[14] Fu, B. R., and Pan, C., 2005, "Flow Pattern Transition Instability in a Microchannel With CO_2 Bubbles Produced by Chemical Reaction," Int. J. Heat Mass Transfer, **48**(21–22), pp. 4397–4409.
[15] Kennedy, J. E., Roach, G. M., Dowling, M. F., Abdel-Khalik, S. I., Ghiaasiaan, S. M., Jeter, S. S., and Quershi, Z. H., 2000, "The Onset of Flow Instability in Uniformly Heated Horizontal Microchannels," J. Heat Transfer, **122**(1), pp. 118–125.
[16] Wu, H. Y., and Cheng, P., 2003, "Visualization and Measurements of Periodic Boiling in Silicon Microchannels," Int. J. Heat Mass Transfer, **46**(14), pp. 2603–2614.
[17] Stromberger, J. H., Abdel-Khalik, S. I., Ghiaasiaan, S. M., and Jeter, S. S., 2003, "The Onset of Flow Instability in Uniformly Heated Horizontal Microchannels," in Proceedings of the ASME Summer Heat Transfer Conference, v 2003, pp. 413–414.
[18] Wu, H. Y., and Cheng, P., 2004, "Boiling Instability in Parallel Silicon Microchannels at Different Heat Flux," Int. J. Heat Mass Transfer, **47**, pp. 3631–3641.
[19] Bergles, A. E., and Kandlikar, S. G., 2005, "On the Nature of Critical Heat Flux in Microchannels," J. Heat Transfer, **127**, pp. 101–107.
[20] Balasubramanian, P., and Kandlikar, S. G., 2005, "Experimental Study of Flow Patterns, Pressure Drop, and Flow Instabilities in Parallel Rectangular Minichannels," Heat Transfer Eng., **26**(3), pp. 20–27.
[21] Cornwell, K., and Kew, P. A., 1992, "Boiling in Small Parallel Channels," Proceedings of CEC Conference Energy Efficiency in Process Technology, Athens, October 1992, Elsevier Applied Sciences, pp. 624–638.
[22] Mertz, R., Wein, A., and Groll, M., 1996, "Experimental Investigation of Flow Boiling Heat Transfer in Narrow Channels," Int. J. Heat Technol., **14**(2), pp. 47–54.
[23] Jiang, L., Wong, M., and Zohar, Y., 1999, "Phase Change in Microchannel Heat Sinks With Integrated Temperature Sensors," J. Microelectromech. Syst., **8**(4), pp. 358–365.
[24] Kandlikar, S. G., 2001, "Critical Heat Flux in Subcooled Flow Boiling-an Assessment of Current Understanding and Future Directions for Research," Multiphase Sci. Technol., **13**(3), pp. 207–232.
[25] Qu, W., and Mudawar, I., 2003, "Measurement and Prediction of Pressure Drop in Two-Phase Microchannel Heat Sinks," Int. J. Heat Mass Transfer, **46**(15), pp. 2737–2753.
[26] Bergles, A. E., and Kandlikar, S. G., 2003, "Critical Heat Flux in Microchannels: Experimental Issues and Guidelines for Measurement," First International Conference on Microchannels and Minichannels, Rochester, New York, April 24–25, pp. 141–147.
[27] Kandlikar, S. G., 2002, "Two-Phase Flow Patterns, Pressure Drop, and Heat Transfer During Boiling in Minichannels Flow Passages of Compact Evaporators," Heat Transfer Eng., **23**(1), pp. 5–23.
[28] Bergles, A. E., Lopina, R. F., and Fiori, M. P., 1967, "Critical-Heat-Flux and Flow-Pattern Observations for Low-pressure Water Flowing in Tubes," J. Heat Transfer, **89**(1), pp. 69–74.
[29] Bergles, A. E., 1962, "Forced Convection Surface Boiling Heat Transfer and Burnout in Tubes of Small Diameter," Doctoral dissertation, Massachusetts Institute of Technology, Cambridge, Massachusetts.
[30] Ruan, S. W., Bartsch, G., and Yang, S. M., 1993, "Characteristics of the Critical Heat Flux for Downward Flow in a Vertical Tube at Low Flow Rate and Low Pressure Conditions," Exp. Therm. Fluid Sci., **7**, pp. 296–306.
[31] Ozawa, M., Umekawa, H., Mishima, K., Hibiki, T., and Saito, Y., 2001, "CHF in Oscillatory Flow Boiling Channels," Inst. Chem. Eng. Symp. Ser., **79**, pp. 389–401.
[32] Bouré, J. A., Bergles, A. E., and Tong, L. S., 1973, "Review of Two-Phase Flow Instability," Nucl. Eng. Des., **25**, pp. 165–192.
[33] Daleas, R. S., and Bergles, A. E., 1965, "Effects of Upstream Compressibility on Subcooled Critical Heat Flux," ASME Paper No. 65-HT 67, ASME, New York.
[34] Maulbetsch, J. S., and Griffith, P., 1966, "A Study of System-Induced Instabilities in Forced-Convection Flows With Subcooled Boiling," MIT Engineering Projects Lab Report No. 5382-35.
[35] Podowski, M. Z., *Instabilities in Two-Phase Systems: Modern Development and Advances*, Elsevier Science, Amsterdam, 1992, pp. 271–315.
[36] Kandlikar, S. G., Willistein, D. A., and Borrelli, J., 2005, "Experimental Evaluation of Pressure Drop Elements and Fabricated Nucleation Sites for Stabilizing Flow Boiling in Minichannels and Microchannels," Third International Conference on Microchannels and Minichannels, Toronto, Ontario, June 13–15, ICMM2005–75197.
[37] Geiger, G. E., "Sudden Contraction Losses in Single and Two-Phase Flow," PhD. thesis, University of Pittsburgh, 1964.
[38] Shah, R. K., and London, A. L., 1978, "Laminar Flow Forced Convection in Ducts," in *Advances in Heat Transfer*, Academic, New York, Suppl. 1.
[39] Gunther, A. Y., and Shaw, W. A., 1945, "A General Correlation of Friction Factors for Various Types of Surfaces in Cross Flow," Trans. ASME, **67**, pp. 643–660.
[40] Abdelall, F. F., Hahn, G., Ghiaasiaan, S. M., Abdel-Khalik, S. I., Jeter, S. S., Yoda, M., and Sadowski, D. L., 2005, "Pressure Drop Caused by Abrupt Flow Area Changes in Smalll Channels," Exp. Therm. Fluid Sci., **29**, pp. 425–434.
[41] Kline, S., and McClintock, F. A., 1953, "Describing Uncertainties in Single-Sample Experiments," Mech. Eng. (Am. Soc. Mech. Eng.), **75**(1), pp. 3–8.
[42] Qu, W., and Mudawar, I., 2004, "Measurement and Correlation of Critical Heat Flux in Two-Phase Micro-Channel Heat Sinks," Int. J. Heat Mass Transfer, **47**, pp. 5749–5763.
[43] Bowring, R. W., 1972, "A Simple but Accurate Round Tube Uniform Heat Flux," Dryout Correlation Over the Pressure Range $0.7-17\ MN/m^2$ (100–2500 psia), AEEW-R 789.
[44] Katto, Y., and Ohne, H., 1984, "An Improved Version of the Generalized Correlation of Critical Heat Flux for Convection Boiling in Uniformly Heated Vertical Tubes," Int. J. Heat Mass Transfer, **27**(9), pp. 1641–1648.
[45] Celata, G. P., and Mariani, A., "CHF and Post-CHF (Post-Dryout) Heat Transfer-Handbook of Phase Change: Boiling and Condensation," Taylor and Francis, Philadelphia, 1999, pp. 443–493.

Radiative Characteristic of Spherical Cavities With Specular Reflectivity Component

F. Kowsary
Mechanical Engineering Department,
Faculty of Engineering,
University of Tehran,
Tehran, Iran
e-mail: fkowsary@chamran.ut.ac.ir

J. R. Mahan
Mechanical Engineering Department,
Georgia Tech Lorraine,
Technopôle Metz 2000, 2-3, rue Marconi,
57070 Metz, France
e-mail: mahan@georgiatech-metz.fr

An exact analytical method is presented for determination of emissive as well as absorptive performance of spherical cavities having diffuse-specular reflective walls. The method presented utilizes a novel coordinate transformation technique, which provides convenient means for setting up the governing radiant exchange integral equations. These equations are then solved by the usual iterative method devized for the Fredholm integral equation of the second kind. The suggested coordinate transformation is also utilized for determination of directional absorptivity of a fully specular spherical cavity when collimated radiation enters through its mouth from a specified direction. Results show that for a spherical cavity the dependence of the apparent emissivity on the degree of specularity is high when the emissivity of the cavity wall is low, but this dependence decreases as the emissivity of the cavity wall increases. Also there are situations, unlike cases of cylindrical and conical cavities, for which the purely diffuse spherical cavity is a more efficient emitter than the purely specular cavity having an identical geometry and wall emissivity. Moreover, it is shown that the apparent directional absorptivity of specular spherical cavities having small openings becomes highly fluctuating as the direction of the incident radiation changes [DOI: 10.1115/1.2151196]

Introduction

When thermal radiation enters a cavity it has a better chance of being absorbed than when it strikes a flat surface having the same area as the cavity opening. This is because of the possibility of multiple reflections within the cavity. Of course, it is this behavior of cavities that permits the radiant heat transfer between a surface and its surroundings to be enhanced by drilling, stamping, etching, or otherwise deforming the surface. Moreover, the main component of the sensing device in instruments such as pyrometers or radiometers is a blackbody cavity.

The performance of a cavity may be described by its apparent radiative properties. For example, the apparent emissivity is defined as the ratio of the energy emitted through the opening of an isothermal cavity to the energy emitted by an imaginary black surface stretched across the cavity opening that is at the same temperature as the cavity wall. The most accepted method for predicting radiative behavior of cavities is the one based on radiant exchange calculations, although approximate methods of Gouffé [1] and De Vos [2] are occasionally referred to in applied optics literature. Analytical radiant exchange calculations for various cavity configurations were reported by Sparrow and his coworkers in a series of papers published during early to mid-1960. A summary of their findings appears in most radiation heat transfer textbooks (for example, [3]). They considered cylindrical, conical, rectangular groove, V-groove, and circular groove cavity configurations. With the exception of spherical cavities, they were able to perform radiant exchange calculations for both diffuse and specular cavities. In general, results of their studies show that, under identical conditions, cavities having specularly reflecting walls are more efficient emitters or absorbers of thermal radiation than those having diffusely reflecting walls.

Limited attempts have been made to study specular or diffuse-specular spherical cavities. Campanaro and Ricolfi [4] calculated the apparent emissivity of diffuse-specular cavities by using a modified form of the approximate method of De Vos. They showed that apparent emissivity decreases with increasing degree of specularity, which was in contrast to the behavior of other cavity configurations. Absorptive behavior of hemispherical cavities having diffuse-specular walls were analyzed by Safwatt [5] using the radiant exchange method. However, the exchange factor he derived is based on an incorrect assumption; therefore, his results must be held suspect. Tsi et al. [6] and Tsi and Streider [7] derived the emissivity factor for radiant heat transport across a spherical void with specular and diffuse-specular surface. Although useful for radiant transport calculations in porous media, their analysis does not accommodate cavities with opening on their walls. Steinfeld [8] calculated the apparent absorptance for specularly reflecting spherical cavities using the Monte Carlo method.

In the current work, a new exact analytical method is used to predict the apparent radiative behavior of spherical cavities whose walls have a specular reflectivity component. Although in their popular textbook Sparrow and Cess [3] make it clear that the solution of this problem would be a welcome contribution to the heat transfer literature, our own interest in the problem, however, was stimulated by the possibility of using spherical cavities as field-of-view limiting baffles in earth-observing radiometric instrumentation applications.

Analysis

The Apparent Emissivity. For the spherical cavity shown in Fig. 1, the irradiance H to element dA_1 located on the cavity wall is given by

$$H(\theta_1) = \int_{A'} B dE_{dA_1} - dA' \tag{1}$$

where the radiosity B is given by

$$B(\theta_1) = \varepsilon\sigma T^4 + \rho^d H(\theta_1) \tag{2}$$

The differential transfer factor $dE_{dA_1-dA'}$ is the *exchange factor*, which replaces the view or angle factor in diffuse-specular enclosures. It is defined as the sum of fractions of diffuse radiation leaving dA_1 that arrives at dA' both directly and by all possible

Contributed by the Heat Transfer Division of ASME for publication in the JOURNAL OF HEAT TRANSFER. Manuscript received March 23, 2005; final manuscript received July 28, 2005. Review conducted by Walter W. Yuen.

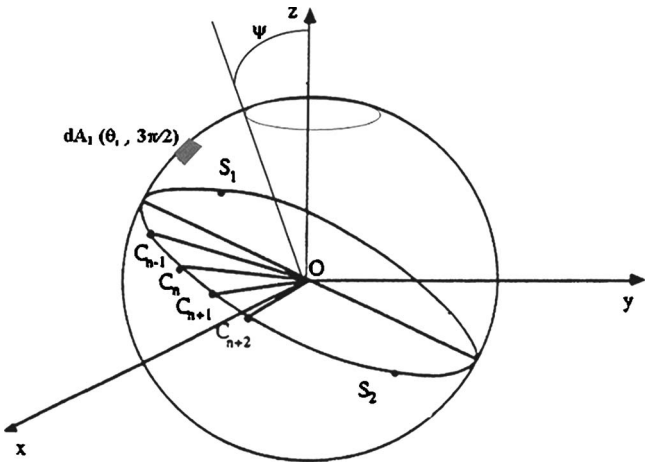

Fig. 1 Geometry for a specular spherical cavity

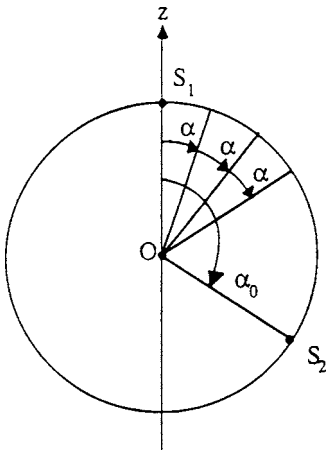

Fig. 2 Great circle for rays traveling between two arbitrary points by specular reflections

specular reflections. In evaluating the exchange factor it is necessary that, for every number of reflections n, the area element dA_n which is the area were the first reflection for the rays traveling from dA_1 to dA' occurs to be identified and located. The fraction of diffuse radiation leaving dA_1 that arrives at dA' is thus $(\rho^s)^n dF_{dA_1-dA_n}$, where $dF_{dA_1-dA_n}$ is the view factor between dA_1 and dA_n.

Equation (1) is a Fredholm integral equation that must be solved iteratively for the unknown H function. Once the irradiance H is calculated to the desired accuracy, the net heat flux supplied to the cavity surface is calculated from

$$q(\theta_1) = \varepsilon(\sigma T^4 - H) \tag{3}$$

where in Eq. (3) it is assumed that the cavity wall is gray. The apparent emissivity of the cavity ε_a is then by definition given by

$$\varepsilon_a = \frac{\int_{A'} q dA'}{A_o \sigma T^4} \tag{4}$$

The radiant exchange formulation presented above is standard for all enclosures. As is observed from the foregoing development, and particularly Eq. (1), the major task in this problem is an analytical determination of the exchange factor between the source element, located at θ_1 and other area elements of the cavity surface. For axisymmetric problems such as the present case, it has been customary to use axisymmetric differential ring elements as basic surface area elements for determination of the exchange factor used in the integration of Eq. (1). In the case of specular spherical cavities, this approach will lead to a highly discontinuous and intractable problem. This undesirable behavior is mainly due to presence of the opening (a discontinuous region) in the spherical cavity surface. To overcome this difficulty we proceed with a different approach. But first we give a brief introduction on the manner by which specular reflections occur in a spherical cavity.

Radiative Exchange by Specular Reflections in a Sphere. By referring to Fig. 1, and noting the fact that the normal to surface of a sphere is always directed toward its center O, it is easy to demonstrate that *all specular reflections of an arbitrary ray from walls of a spherical enclosure occur entirely in the single plane that passes through O*. Thus, rays that leave a point S_1 (Fig. 1) on the sphere, which arrive at S_2 by specular reflections, will stay in the plane formed by S_1, S_2, and O. The intersection of such a plane with surface of the sphere is a *great circle*. Figure 2 shows the great circle for rays traveling from S_1 to S_2 by specular reflections from the wall of the sphere. To specify locations in this great circle we use polar angles defined with respect to S_1. From Fig. 2 it can be seen that if the point of first reflection for a ray leaving S_1 is at α, the point of second reflection would be at 2α, and, in general, the point of the nth reflection would be located at $n\alpha$. This means that if rays are to travel from S_1 to S_2, which is separated from S_1 by α_o, by n specular reflections, the points of first reflection can be determined from

$$\alpha_{nk} = \frac{\alpha_o + 2k\pi}{n+1} \tag{5}$$

where $k = 0, 1, 2, \ldots$.

Although first look at Eq. (5) may suggest that there exists an infinite number of points of reflection, further examination shows that for $k > n$ points obtained from this equation are repeats. Therefore, it can be inferred that there exist $n+1$ distinct points of first reflection (or $n+1$ distinct routes) if rays leaving S_1 are to reach S_2 by n specular reflections (see Fig. 3).

The foregoing observations were utilized in evaluation of the exchange factor, which appears in Eq. (1). Furthermore, introducing a new coordinate system $x'y'z'$ as shown in Fig. 4 will greatly facilitate evaluation of the exchange factors as well. This coordinate system is oriented so that the z'-axis always passes through the element like dA_1 for which the irradiance H is being calculated. To obtain this coordinate system, the y,z plane of the main

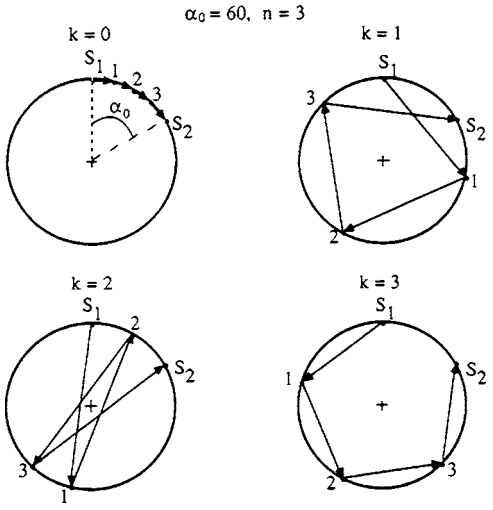

Fig. 3 Four possible specular routes for a ray leaving S_1 to reach S_2

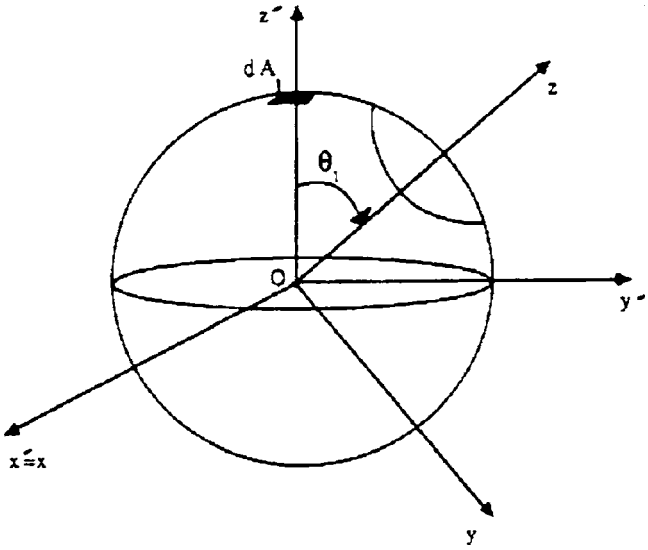

Fig. 4 Defining a new (source-oriented) coordinate system that is suitable for analysis of radiant exchange by specular reflections

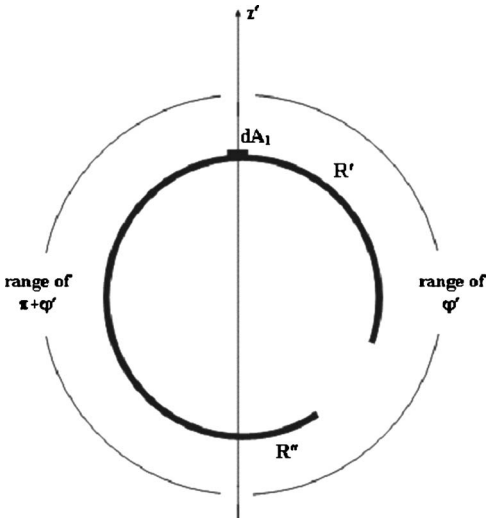

Fig. 5 A great circle that has intersected the opening

coordinate system (xyz in Fig. 1) is rotated about the x-axis by amount θ_1, the zenith angle of element dA_1. Using the spherical coordinates (θ',φ') of the new coordinate system, planes (or the great circles) in which exchange of radiation by specular reflections between dA_1 and other elements of the cavity surface occurs are identified simply by azimuthal angles such as φ'. Moreover, relation between the polar angle α of a great circle at φ' and (θ',φ') of the $x'y'z'$-coordinate system is given simply by

$$\theta'(\alpha) = \pi - |\pi - \alpha|$$

$$\varphi'(\alpha) = \begin{cases} \varphi', & \alpha \leqslant \pi \\ \pi + \varphi', & \alpha \geqslant \pi \end{cases} \tag{6}$$

The relation between spherical coordinates (θ,φ) of the xyz-coordinate system and (θ',φ') of the $x'y'z'$-coordinate system is determined from the coordinate transformation matrix for the rotation described above. That is,

$$\begin{bmatrix} 1 & 0 & 0 \\ 0 & \cos\theta_1 & -\sin\theta_1 \\ 0 & \sin\theta_1 & \cos\theta_1 \end{bmatrix} \begin{bmatrix} \sin\theta'\cos\phi' \\ \sin\theta'\sin\phi' \\ \cos\theta' \end{bmatrix} = \begin{bmatrix} \sin\theta\cos\phi \\ \sin\theta\sin\phi \\ \cos\theta \end{bmatrix} \tag{7}$$

The equation for the boundary of the cavity opening in terms of (θ',φ') can be obtained by substituting the opening angle ψ (shown in Fig. 1) for θ in Eq. (7). After multiplying out the third row of the left-hand side and performing some algebraic manipulations, we will have

$$\cos\theta' + (\tan\theta_1 \sin\phi')\sin\theta' = \frac{\cos\psi}{\cos\theta_1} \tag{8}$$

At this point we are prepared to solve Eq. (1) by the customary iterative method of solving the Fredholm integral equation of the second kind. First, initial values (guessed) are assigned to the irradiance H at discrete but uniformly spaced values of θ, the zenith angle of xyz-coordinate system. Using these initial values, the integration on the right-hand side of the equation is carried out to obtain new values for H. This procedure is repeated until results converge to a certain predetermined convergence criteria. As mentioned previously, for convenience, integration over the cavity surface area A' is performed using the spherical coordinates (θ',φ') of the $x'y'z'$-coordinate system for which the source is always located at the *north pole* of the sphere. Since the integration is over the entire cavity surface area A', limits of integration for φ' are 0 and 2π; or using the symmetry as shown in Fig. 4, one may use $\pi/2$ and $3\pi/2$ as lower and upper limits, respectively, and then multiply the results by 2.

As mentioned previously, a given φ' defines a great circle. When performing integration in φ' direction, such a great circle may or may not intersect the cavity opening. If former occurs, there will be a discontinuity or a hole in the great circle as shown in Fig. 5. For generality this situation will be focused on as the other situation would simply be a special case of this analysis. Take note of the fact that the region defined by the great circle at a given φ' is actually a spherical sector having a differential thickness of $d\phi'$. For the great circle shown in Fig. 5, the integration of θ' must be performed over two disconnected regions of R' and R'' defined, respectively, by $[\theta'=0,\ \theta'=\beta']$ and $[\theta'=\beta'',\ \theta'=\pi]$ where β' and β'', polar angles corresponding to the intersection points of the great circle with cavity opening, can be calculated using Eqs. (8) and (6).

Consider integration over the region R''. Using the definition for exchange factor, this integral may be written as sum of infinite number of integrals, each one representing exchange of radiation between dA_1 and R'' by a number of specular reflections n, plus an integral for direct exchange (i.e., no reflections). By using the simple view factor formula between two elements on the surface of a sphere [9], the integral for direct exchange is simply given by

$$I_o(\phi') = \frac{1}{4\pi}\int_{\theta'(\beta'')}^{\pi} B(\theta^*,\phi')\sin\theta^* d\theta^* \tag{9}$$

where θ^* is just a dummy variable of integration. Take note of the fact that as values of irradiance H and, hence, radiosity B are known and expressed in terms of θ, the zenith angle of the xyz-coordinate system, Eq. (7) must be used to convert them in terms of the variables of the rotated coordinate system.

For other components of the exchange factor, an argument similar to that which resulted in derivation of Eq. (4) is used. That is, it can be shown that radiation exchange by n specular reflections between dA_1 and R'' may occur through $n+1$ possible specular routes corresponding to $k=0,1,2,3,\ldots,n$. Based on the definition of exchange factor, the region on the great circle from which the first reflection occurs must be determined for all number of reflections n and all routes k corresponding to it. The limits (i.e., the polar angles) that define this region can be determined by substituting limits of R'' into Eq. (5). If the great circle was complete, that is, no discontinuity as a result of a hole existed within

it, the integral representing exchange by n number of specular reflections through the kth route would have been given by

$$I_{nk}(\phi') = \frac{(\rho^s)^n}{4\pi} \int_{\theta'(\beta''_{nk})}^{\pi_{nk}} B(\theta^*, \phi') \sin\theta^* d\theta^* \tag{10}$$

where β''_{nk} and π_{nk} are determined from substituting β'' and π, respectively, into Eq. (5).

When there exists a hole within the great circle, as is the case in Fig. 5, the regions of first reflection must be modified. This is because some parts or even all of the rays traveling from dA_1 to R'' through a certain specular path (i.e., a certain n and k) may encounter the hole as a result of reflections from the wall and, therefore, escape from the cavity. This modification is accomplished by successively comparing regions of the great circle that are illuminated by rays traveling from dA_1 to R'' with the region that defines the hole. This comparison is made after every specular reflection up until the last reflection before rays arrive at R''. Although it is difficult to present this procedure by a closed-form formulation, it is easy to implement it using a computer routine; all that is needed is the laws of specular reflection in a sphere and Eq. (5) (for additional details refer to [10]).

Based on the outline given above, a computer program was developed to perform the iterations and numerical integrations necessary for solving Eq. (1). The variables in Eq. (1) were made dimensionless by dividing both sides of the equation by σT^4.

The Romberg method in conjunction with trapezoidal rule was used for the numerical integrations. The tolerance for terminating the successive integrations in Romberg method was set at 10^{-6}. The nodal points for evaluation of H were separated by 3 deg. The convergence criteria for terminating the iterations of the integral equation was based on the square root of sum of squares of the differences between results of new and previous calculations at each node. If this value is <0.001, iterations were stopped. Reducing this convergence criterion by factor of ten changed the results only at the fourth significant figure and beyond. The number of reflections N considered in calculations was determined from criterion

$$(\rho^s)^N \leqslant 0.001 \tag{11}$$

This yields $N=3$, 6, 10, 20, and 66 for $\rho^s=0.1$, 0.3, 0.5, 0.7, and 0.9, respectively.

Apparent Directional Absorptivity. Now consider the case in which the collimated beam of radiation of flux $q_{o,n}$ (watts per unit normal area) enters a spherical cavity of unit radius having completely specular walls. The yz plane of the xyz-coordinate system shown in Fig. 6(a) is oriented parallel to the direction of the incoming radiation. The direction of incoming radiation can then be identified by the angle γ it makes with respect to the z-axis.

To begin the developments, one more time it is convenient to use $x'y'z'$ coordinate system shown in Fig. 6(b) in which the z'-axis is parallel to the incoming radiation. Once again the rays entering the cavity in the plane defined by the azimuthal φ' (measured from the positive x'-axis) undergo specular reflections as a group within that same plane. The intersection of this plane with the cavity surface is, once again, a great circle. Hence, by referring to Fig. 6(b), the total energy absorbed by the cavity can be calculated by finding the portion of the energy that enters the cavity through a longitudinal band $d\varphi'$ at φ' that is absorbed and then integrating over the appropriate limits of the cavity opening in the φ' direction.

For our developments, a typical great circle (or the spherical sector of width $d\varphi'$) in which collimated rays enter parallel to the z'-axis are shown in Fig. 7. Angles that define limits of cavity opening in the rotated coordinate system (ψ^a, ψ^b in Fig. 7) are solutions of Eq. (8) for the given φ'. Some of the rays that enter the cavity through the opening of this great circle may be reflected

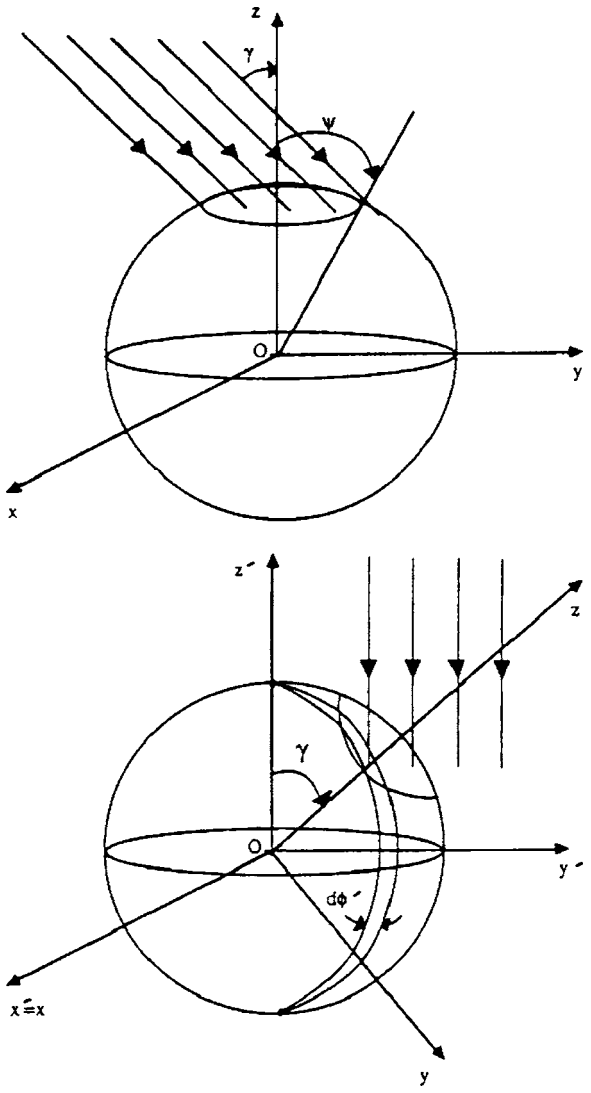

Fig. 6 (*a*) A collimated beam of flux q_0 entering a spherical cavity at angle γ; and (*b*) the same cavity as in (*a*) rotated through angle γ about the *z*-axis

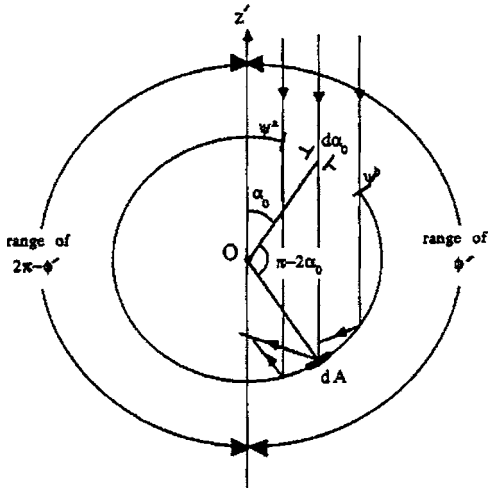

Fig. 7 Parallel rays entering a great circle (i.e., a spherical sector)

into the arc $[\psi^a, \psi^b]$ and escape through it.

Consider an amount of energy $dQ(\psi^a - \psi^b)$ that enters the cavity through a differential slit of angular width $d\varphi'$ and circular arc $[\psi^a, \psi^b]$. Now suppose that the cavity walls are perfectly reflecting ($\rho^s = 1$). After n number of specular reflections, some of this energy will have escaped through the opening. In general, there may exist some m number of circular arcs $[\psi_1^L, \psi_1^U]$, $[\psi_2^L, \psi_2^U]$,..., $[\psi_i^L, \psi_i^U]$,..., $[\psi_m^L, \psi_m^U]$ within $[\psi^a, \psi^b]$ for which incident radiation has not yet escaped through the opening after n reflections. This collection of circular arcs is identified by the symbol C_n. The procedure for finding the collection C_n can be implemented on a digital computer in a straightforward manner provided that the formula for the reflection points of a given ray entering the circle of reflection is known. The procedure involves finding the illuminated region of the circle of reflection after each reflection and subtracting from it the circular arc that defines the opening.

To obtain the illuminated region, the reflection points of a given ray entering the great circle must be determined. It is elementary to show that the polar angle between two consecutive reflection points for a ray entering the great circle through the polar angle β_o is given by $\pi - 2\beta_o$. Hence, β_n polar angle of the nth reflection point is given by

$$\beta_n = n\pi - (2n-1)\beta_o \tag{12}$$

Through each circular arc $[\psi_i^L, \psi_i^U]$ in collection C_n enters an amount of energy that is identified by the symbol $dQ_{n,i}$. The portion of this energy that is absorbed during the nth reflection is given by

$$(1-\rho^s)(\rho^s)^{n-1} dQ_{n,i}$$

Hence, the total energy that is absorbed due to that which entered the cavity through the longitudinal band $d\phi'$ at φ' is given by

$$(1-\rho^s)(\rho^s)^{n-1} \sum_{i=1}^{m(n)} dQ_{n,i}$$

where $m(n)$ indicates dependence of m, defined above, *on* the number of reflections n. The amount that is absorbed during all reflections is thus given by

$$dQ(\phi) = \sum_{n=1}^{\infty} dQ_n = (1-\rho^s) \sum_{n=1}^{\infty} (\rho^s)^{n-1} \sum_{i=1}^{m(n)} dQ_{n,i} \tag{13}$$

The quantity yet to be determined is $dQ_{n,i}$. By referring to Fig. 7, the incoming energy contained within a differential polar angle $d\alpha_o$ at α_o is given by

$$q_{o,n} \cos\alpha_o \sin\alpha_o d\alpha_o d\phi'$$

Therefore,

$$dQ_{n,i} = q_{o,n} \int_{\psi_i^L}^{\psi_i^U} \cos\alpha_o \sin\alpha_o d\alpha_o d\phi' = \frac{q_{o,n}}{2} (\sin^2\psi_i^U - \sin^2\psi_i^L) d\phi' \tag{14}$$

By substituting Eq. (14) into Eq. (13), the amount of energy that is absorbed due to that which enters the cavity through the longitudinal band $d\varphi'$ at ϕ' can be obtained. The amount of energy that is absorbed by the cavity can be obtained by integrating Eq. (13) over the appropriate limits of φ' that define the cavity opening. On the other hand, the amount of energy that has entered the cavity is given simply by

$$Q_o(\gamma) = \pi q_{o,n} \sin^2\psi \cos\gamma \tag{15}$$

Dividing the energy absorbed by the total energy that enters the cavity gives the apparent directional absorptivity.

Discussion of Results

Because of space limitations only the apparent emissivity results will be presented and discussed. Readers interested in details of net heat flux distribution on the cavity surface are referred to Kowsary [10]. Table 1 presents an independent validation of the calculated apparent emissivity results of this work against those obtained by the Monte Carlo method. In general, the agreement is within $<1\%$, except for small opening angles and high values of specularity ratio where the relative difference gets as high as 3%. The latter is mainly due to a drawback in averaging that can be done by the Monte Carlo results in small opening angles. It should be emphasized that this comparison was not made for the intention of establishing the accuracy of the results of this work, as results obtained here can be considered as exactly analytical. It was done merely for the purpose of verifying that no errors were made in the theoretical developments or in computer programing of formulations.

The apparent emissivity as a function of the cavity opening angle, surface emissivity, and specularity ratio ρ^s/ρ, where $\rho = \rho^s + \rho^d$, is shown in Fig. 8. The apparent emissivity approaches the wall emissivity as the cavity becomes wide open (i.e., becomes a flat plate). When the cavity opening angle approaches zero, the apparent emissivity in all cases approaches unity. This behavior is similar to the results for cavities previously studied.

There are, however, interesting differences between the apparent emissivity results for spherical cavities having specular component of reflectivity and those for cavities previously studied by Sparrow and Cess and their co-workers [3]. Variation of the apparent emissivity in spherical cavities is a weaker function of the specularity ratio than in the case of conical and cylindrical cavities. In spherical cavities, for a given surface emissivity, the apparent emissivity is not always an increasing function of the specularity ratio. This difference has also been noted by Campanaro and Ricolfi [4] using their approximate results and Steinfeld [8] who did the Monte Carlo calculations. According to the results shown in Fig. 8, specular spherical cavities may have a higher apparent emissivity when the surface emissivity is high. However, as the emissivity of the surface decreases, curves corresponding to the purely specular cavities begin to shift downward relative to the curves for the purely diffuse cavities. Eventually, as the emissivity of cavity surface becomes sufficiently small, the apparent emissivity of the diffuse cavity becomes greater than that of the specular cavity. This type of behavior in spherical cavities may perhaps be explained by the fact that some portions of the cavity surface face downward into the cavity (unlike the case of conical and cylindrical cavities).

As the wall emissivity ε is changed, the apparent emissivity curves for diffuse-specular case $\rho^s/\rho = 0.5$ also begin to shift downward relative to those for diffuse cavities. This trend is similar to the case of purely specular cavities but at a slower pace. For low emissivities, however, the diffuse cavity and the diffuse-specular cavity have essentially the same apparent emissivities for all opening angles. This suggests that for low emissivities the diffuse effect dominates the specular effects.

Another curious observation can be made regarding the apparent emissivity results for spherical cavities: the apparent emissivity for a diffuse specular cavity is not always bounded by the apparent emissivities of the corresponding purely diffuse and purely specular cavities. Although not very apparent at first sight, this behavior can be seen, for example, for the case of $\varepsilon = 0.5$ for $45 < \psi < 75$. The Monte Carlo results of Steinfeld [8] show this effect as well; although no statement was made in the paper regarding it. This is perhaps due to the degree of uncertainty that is involved in the results of Monte Carlo calculations. Nevertheless, this is an example in which purely diffuse reflection and purely specular reflection do not represent limiting cases in radiation exchange. The dependence of results on the specularity ratio becomes practically insignificant when the cavity opening angle be-

Table 1 Comparison of the apparent emissivities calculated by the exact analytical method and the Monte Carlo method: (a) ψ=60 deg, (b) ε=0.5

a) ψ = 60 deg

	ρ^s/ρ=0			ρ^s/ρ=0.5			ρ^s/ρ=1		
ε	Exact	M.C.	%Diff.	Exact	M.C.	%Diff.	Exact	M.C.	%Diff.
0.9	0.9730	0.9732	0.021	0.9798	0.9795	-0.031	0.9865	0.9813	-0.527
0.7	0.9032	0.9030	-0.022	0.9198	0.9154	-0.478	0.9315	0.9315	0.000
0.5	0.8000	0.7989	-0.138	0.8189	0.8138	-0.623	0.8213	0.8223	0.122
0.3	0.6316	0.6315	-0.016	0.6444	0.6423	-0.326	0.6228	0.6264	0.578
0.1	0.3077	0.3079	0.065	0.3101	0.3096	-0.161	0.2736	0.2770	1.243

b) ε = 0.5

	ρ^s/ρ=0			ρ^s/ρ=0.5			ρ^s/ρ=1		
ψ	Exact	M.C.	%Diff.	Exact	M.C.	%Diff.	Exact	M.C.	%Diff.
120	0.5714	0.5716	-0.035	0.5700	0.5694	0.105	0.5674	0.5663	0.194
105	0.6137	0.6128	0.147	0.6159	0.6169	-0.162	0.6162	0.6177	-0.243
90	0.6667	0.6647	0.300	0.6799	0.6746	0.780	0.6891	0.6810	1.175
75	0.7296	0.7307	-0.151	0.7499	0.7498	0.013	0.7603	0.7638	-0.460
60	0.8000	0.7989	0.138	0.8189	0.8138	0.623	0.8213	0.8223	-0.122
45	0.8723	0.8688	0.401	0.8851	0.8854	-0.034	0.8771	0.8810	-0.445
30	0.9372	0.9390	-0.192	0.9425	0.9476	-0.541	0.9266	0.9455	-2.040
15	0.9832	0.9912	-0.814	0.9860	1.0002	-1.440	0.9684	1.0011	-3.377

$$\% \text{ Diff.} = 100 \times \frac{(\text{Analytical} - \text{Monte Carlo})}{\text{Analytical}}$$

comes greater than approximately 105 deg for high and midrange values of emissivity. However, for small emissivity this is true for even smaller cavity opening angles.

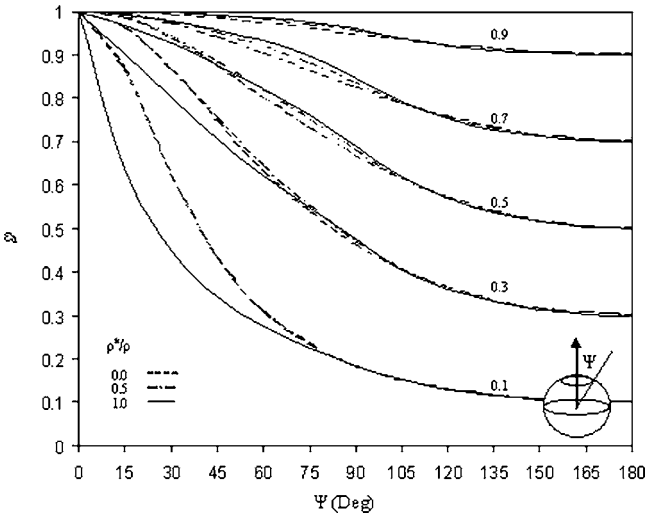

Fig. 8 Apparent emissivity of spherical cavities for various geometrical and surface conditions

Results for the directional absorptivity are shown in Fig. 9. Each plot in Fig. 9 shows the apparent directional absorptivity $\alpha_s(\gamma)$ for a different opening angle ψ as a function of the angle of incidence γ and for various surface absorptivities α. Apparent absorptivity results for the corresponding diffuse cavities, which are independent of direction [9], are also plotted for comparison. These results were also validated against those obtained by the Monte Carlo method [10].

As expected, for a given opening angle and incidence angle, as the absorptivity α of the wall increases so does the apparent directional absorptivity. Moreover, for a fixed wall absorptivity α, as the cavity opening angle increases, the apparent directional absorptivity decreases for all angles of incidence γ. The apparent absorptivity of any cavity is usually greater than the absorptivity of the cavity surface. However, for large opening angles it is possible that for some angles of incidence the radiation entering the cavity will be reflected out after only one reflection. In these cases $\alpha_s(\gamma)=\alpha$; see, for example, results for an opening angle of 150 deg.

Conclusion

An exact analytical method is developed for calculation of the apparent emissivity and apparent absorptivity of specularly reflecting spherical cavities. The results obtained using this method demonstrates a distinct specular behavior for spherical cavities. For instance, unlike other cavity configurations reported thus far,

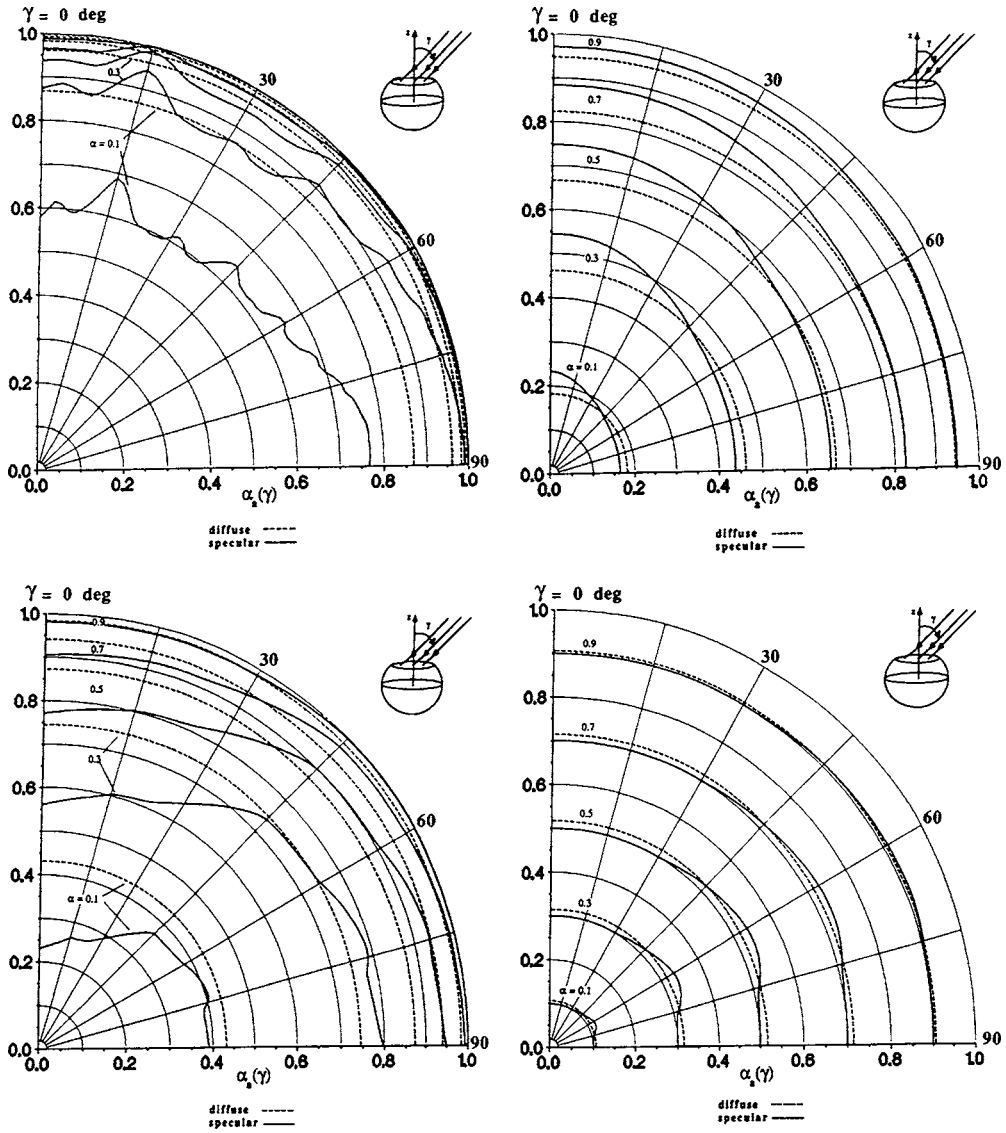

Fig. 9 (*a*) Directional apparent absorptivity of spherical cavities, opening angle=15 deg; (*b*) opening angle=45 deg; (*c*) opening angle=90 deg; and (*d*) opening angle=150 deg

there are instances where diffuse spherical cavities have a higher apparent emissivity than the identical specular cavity. Also results obtained in this work validate the approximate results obtained by previous investigators.

Nomenclature

A, dA = arbitrary area elements
A_o = area of a surface stretched across the cavity opening (m^2)
A' = area of the spherical cavity with an opening on its surface (m^2)
dA_{nk} = the fictitious area used in the definition of the specular exchange factor
A_s = surface area of the complete sphere
B = radiosity (W/m^2)
E, dE = the exchange factor
df_{nk} = factors defined in the exchange factor expression
H = irradiance (W/m^2)
$q_{o,n}$ = flux of collimated radiation (W/m^2 (normal))
q = net heat flux to the cavity surface (W/m^2)
Q_o = total radiative energy entering the cavity (W)

Greek

α = absorptivity, or polar angle
ε = emissivity
σ = Stefan Boltzmann constant
θ = zenith angle of the spherical coordinate system
θ' = zenith angle of the source-oriented coordinate system
φ = azimuthal angle of the spherical coordinate system
φ' = azimuthal angle of the source-oriented coordinate system
ρ = reflectivity
ψ = opening angle of the spherical cavity

Subscripts

k = path of reflections for a given number of reflections
n = given number of reflections
a = apparent radiative property
1 = source element

2 = receiving element

Superscripts

L = lower limit of the polar angle of the area that defines the hole
U = upper limit of the polar angle of the area that defines the hole
$'$ = directional radiative quantity
s = specular component
d = diffuse component

References

[1] Gouffé, A., 1946, "Correction d'Overture des Corps-Noirs Artificiels Compte Tenu Des Diffusions Multiples Internes," Rev. Opt., Theor. Instrum., **24**, pp. 1–10.

[2] De Vos, J. C., 1954, "Evaluation of the Quality of a Blackbody," Physica (Amsterdam), **20**, pp. 669–689.

[3] Sparrow, E. M., and Cess, R. D., 1979, *Radiation Heat Transfer*, Augmented ed., Hemisphere Publications, New York.

[4] Campanaro, P., and Ricolfi, T. J., 1966, "Effective Emissivity of a Spherical Cavity," Appl. Opt., **5**, pp. 929–932.

[5] Safwatt, H. H., 1970, "Absorption of Thermal Radiation in a Hemispherical Cavity," ASME J. Heat Transfer, **C92**, pp. 198–201.

[6] Tsai, D., Ho, F., and Strieder, W., 1984, "Specular Reflection in Radiant Heat Transfer Across a Spherical Void," Chem. Eng. Sci., **39**(4), pp. 775–779.

[7] Tsai, D., and Streider, W., 1985, "Radiation Across a Spherical Cavity Having Both Specular and Diffuse Reflectance Components," Chem. Eng. Sci., **40**(1), pp. 170–173.

[8] Steinfeld, A., 1991, "Apparent Absorptance for Diffusely and Specularly Reflecting Spherical Cavities," Int. J. Heat Mass Transfer, **34**(7), pp. 1895–1897.

[9] Sparrow, E. M., and Jonsson, V. K., 1962, "Absorption and Emission Characteristics of Diffuse Spherical Enclosures," NASA Technical Note D-128.

[10] Kowsary, F., 1989, "Radiation Characteristics of Spherical Cavities Having Partially or Completely Specular Walls," Ph.D. dissertation, Virginia Polytechnic Institute and State University, Blacksburg, VA (available from university microfilms, Ann Arbor, MI).

Kyle Daun
National Research Council of Canada,
Ottawa, Canada

Francis França
Universidade Federal do Rio Grande do Sul,
Porto Alegre, Brazil

Marvin Larsen
Sandia National Laboratories,
Albuquerque, NM

Guillaume Leduc
Laboratoire d'Energétique,
Université Paul Sabatier,
Toulouse, France

John R. Howell
University of Texas at Austin,
Austin, TX

Comparison of Methods for Inverse Design of Radiant Enclosures

A particular inverse design problem is proposed as a benchmark for comparison of five solution techniques used in design of enclosures with radiating sources. The enclosure is three-dimensional and includes some surfaces that are diffuse and others that are specular diffuse. Two aspect ratios are treated. The problem is completely described, and solutions are presented as obtained by the Tikhonov method, truncated singular value decomposition, conjugate gradient regularization, quasi-Newton minimization, and simulated annealing. All of the solutions use a common set of exchange factors computed by Monte Carlo, and smoothed by a constrained maximum likelihood estimation technique that imposes conservation, reciprocity, and non-negativity. Solutions obtained by the various methods are presented and compared, and the relative advantages and disadvantages of these methods are summarized. [DOI: 10.1115/1.2151198]

Introduction

A number of papers and reviews have been devoted to inverse design of enclosures where radiation provides the dominant mode of heat transfer [1–10]. The particular class of problems examined here is devoted to the determination of the energy input that should be supplied to a set of radiant heaters so that their output will provide a specified uniform heat flux and temperature on a given surface of the enclosure, the so-called design surface. This type of problem is encountered in the design of equipment for ovens and heaters in diverse applications, including materials processing, food production, curing and drying of coatings and bulk materials, semiconductor wafer processing, and many others. In all of these cases, the thermophysical and transport properties of the material being processed are given, the required temperature is specified, and the thermal capacity of the material sets the radiant heat flux necessary to achieve the required temperature. The designer is then left to determine the transient energy inputs into the array of heaters that heat the design surface uniformly according to the desired transient temperature profile throughout the process. Most previous papers in this area focus on steady-state radiant enclosure design problems, where the objective is to determine the energy inputs to the heaters that produce a desired heat flux and temperature distribution over the design surface [6–12]; these studies show that specifying both boundary conditions over the design surface and leaving the boundary conditions over the heater surface unspecified results in an ill-posed mathematical problem involving Fredholm integral equations of the first kind. Writing these equations in discrete form produces an ill-conditioned or singular set of equations that cannot be solved using traditional linear algebra tools. (In several of these papers [11,12] predictions were matched with experimental data, helping to validate the inverse design approach.) In the transient problem, specifying the transient temperature distribution over the design surface also causes the problem to be ill-posed, since the required heat flux is implicitly defined by the thermal capacity and rate of temperature change of the design surface.

Various approaches have been used to solve problems of this type. These can be roughly grouped into two classes, *regularization* and *optimization*. The regularization techniques work by modifying the governing relations to reduce their "ill-posedness," accepting some loss of accuracy to gain a useful solution. Optimization techniques, on the other hand, approach the design problem by casting the governing relations in the conventional form with one boundary condition on the design surface fixed, and an assumed condition (most often a heat flux distribution) on the heater surface. The assumed condition is varied in a systematic way until the second boundary condition on the design surface is satisfied within acceptable limits.

This paper shows how regularization and optimization methods are used to determine the transient heater settings of a process furnace that heats up the design surface uniformly according to a prescribed temperature history. The regularization methods used include truncated singular value decomposition, Tikhonov regularization, and conjugate gradient regularization, while the optimization methods include quasi-Newton minimization and simulated annealing. The solutions obtained by these methods are compared, and the relative performance of each method is assessed.

Solution Techniques for Inverse Radiant Enclosure Design Problems

Regularization. A direct or explicit solution of the described inverse design problem requires use of an inverse formulation. Inverse design problems are inherently ill-posed, and the corresponding discretized set of equations describing the radiative transfer is, consequently, ill-conditioned. Ordinary techniques (e.g., Gauss-Seidel, Gauss elimination, or LU decomposition) are likely to either identify nonphysical solutions with high-amplitude fluctuations and/or complex absolute temperatures, or completely fail to find a solution. To achieve an accurate and physically reasonable solution, the explicit system must instead be *regularized* by modifying the ill-conditioned system of equations.

The degree to which a system of equations is ill-conditioned can be diagnosed by carrying out a singular value decomposition (SVD) [13,14]. The SVD of an arbitrary $M \times N$ matrix $\mathbf{A}$ is $\mathbf{A} = \mathbf{USV}^T$, where $\mathbf{U}$ and $\mathbf{V}$ are orthogonal matrices and $\mathbf{S}$ is a diagonal matrix of singular values, so that $S_{1,1} > S_{2,2} > \cdots > S_{N,N} \geqslant 0$. The inverse of $\mathbf{A}$ is then given by $\mathbf{A}^{-1} = \mathbf{VS}'\mathbf{U}^T$, where $S'_{i,i} = 1/S_{i,i}$. If the condition number of this matrix $(S_{1,1}/S_{N,N})$ is large, small singular values dominate the inverse matrix and the solution becomes sensitive to small perturbations to the singular values

Contributed by the Heat Transfer Division of ASME for publication in the JOURNAL OF HEAT TRANSFER. Manuscript received March 9, 2005; final manuscript received August 3, 2005. Review conducted by Walter W. Yuen.

that are magnified by the inversion process. If **A** is rank deficient, some of the singular values equal zero and the inversion process fails completely.

To achieve an accurate and physically reasonable solution, the ill-conditioned or singular set of equations must be modified to form a related set of well-conditioned equations that have a more regular solution, but produce a residual vector when substituted back into the original ill-conditioned set of equations. It is usually left to the designer to select the degree of modification, or *regularization*. If the well-posed equations are closely related to the original ill-conditioned set, the residual vector will be very small, but the solution distribution will be highly irregular. As the degree of regularization is increased, the solution becomes more regular, but at the expense of a larger residual vector. If too much regularization is used, the character of the ill-conditioned equations is lost and the regularized solution will not produce the desired conditions over the design surface.

The most popular regularization techniques are *truncated singular value decomposition* (TSVD), *conjugate gradient regularization* (CGR) and *Tikhonov regularization* (TR). Truncated singular value decomposition is based on a singular value decomposition of **A**. The solution uses the pseudoinverse matrix that is formed by filtering or truncating small singular values; the solution using the p largest singular values becomes

$$x_n = \sum_{k=1}^{p} V_{n,k} \frac{b_m U_{m,k}}{S_{k,k}}, \quad n = 1,2, \ldots, N \tag{1}$$

where p has a value less than or equal to the rank of **A** [13]. Retaining different numbers of singular values yields alternative solutions. Those with acceptable accuracy and with physical meaning present possible alternatives to the designer.

A plot of the variation of the residual norm against the solution norm is often called the L-curve and can be used to select an appropriate solution. The residual norm represents the solution accuracy, whereas the solution norm represents the smoothness of the solution. The L-curve usually has a corner where further regularization significantly increases the norm of the residual with little improvement in solution smoothness. The optimal or desired solution often lies in the vicinity of the corner [14].

The CGR method is based on the incomplete conjugate gradient minimization of the degenerate functional $F(\boldsymbol{x}) = [\mathbf{A}(\boldsymbol{x}_{\mathbf{exact}} - \boldsymbol{x})] \cdot (\boldsymbol{x}_{\mathbf{exact}} - \boldsymbol{x})$, which is minimized when $\|\mathbf{A}\boldsymbol{x} - \boldsymbol{b}\| = 0$. For inverse problems, each minimization step corresponds to a unique solution having distinct accuracy and smoothness characteristics. These solutions can then be used to construct an L-curve to select the optimal solution. Small memory requirements, computation economy, robust convergence characteristics, and the ability to store and use the original matrix often make CGR the method of choice for regularization of large systems [4,15]. A common, stable implementation of the method consists of the following steps:

- guess: $\boldsymbol{x}_0$; determine $\boldsymbol{r}_0 = \mathbf{b} - \mathbf{A} \cdot \boldsymbol{x}_0$ and $\mathbf{p}_0 = \mathbf{A}^T \cdot \mathbf{r}_0$.
- for $k \geqslant 0$, follow the iterative steps:

$$\alpha_k = \frac{\|\mathbf{A}^{\mathbf{T}} \cdot \mathbf{r}_k\|^2}{\|\mathbf{A} \cdot \mathbf{p}_k\|^2}$$

$$\mathbf{x}_{k+1} = \mathbf{x}_k + \alpha_k \mathbf{p}_k$$

$$\mathbf{r}_{k+1} = \mathbf{r}_k - \alpha_k \mathbf{A} \cdot \mathbf{p}_k$$

$$\beta_k = \frac{\|\mathbf{A}^T \cdot \mathbf{r}_{k+1}\|^2}{\|\mathbf{A}^T \cdot \mathbf{r}_k\|^2}$$

$$\mathbf{p}_{k+1} = \mathbf{A}^T \cdot \mathbf{r}_{k+1} + \beta_k \mathbf{p}_k$$

The solution norm at each iteration $\|\mathbf{x}_k\|$ will increase monotonically with n, and the residual norm $\|\mathbf{r}_k\|$ will decrease monotonically with n if $\boldsymbol{x}_0 = 0$.

Like CGR, Tikhonov regularization [5] is based on minimizing a functional. In this method, the functional is equal to the L_2 norm of the residual vector plus an added shape constraint,

$$F(\boldsymbol{x}) = \|\mathbf{A}\boldsymbol{x} - \boldsymbol{b}\|_2 + \sum_{i=1}^{p} \lambda_i^2 [\|\mathbf{L}_i(\boldsymbol{x} - \boldsymbol{x}_0)\|]^2 \tag{2}$$

For a pth-order scheme, $\mathbf{L}_i$ approximates the discretized ith derivative operator and λ_i is the ith-order regularization parameter. Using a small regularization parameter results in an accurate solution by emphasizing minimization of the residual norm, whereas using a large regularization parameter, on the other hand, results in a solution with improved smoothness characteristics. For the standard or zeroth-order TR scheme, $p = 0$ and $\mathbf{L}_i$ becomes the identity matrix **I**, leading to the set of linear equations $(\mathbf{A}^T\mathbf{A} + \lambda_0^2\mathbf{I})\boldsymbol{x} = \mathbf{A}^T\boldsymbol{b} + \lambda_0^2\mathbf{I}\boldsymbol{x}_0$

$$(\mathbf{A}^T\mathbf{A} + \lambda_0^2\mathbf{I})\boldsymbol{x} = (\mathbf{A}^T\boldsymbol{b} + \lambda_0^2\boldsymbol{x}_0) \tag{3}$$

Using the appropriate regularization parameter results in an optimal solution that is both smooth and sufficiently accurate for the designer's needs.

Optimization. Like conventional trial-and-error design, optimization techniques use an iterative process to arrive at the final design configuration. The performance of a particular design configuration is evaluated at each iteration. If it does not satisfy the design requirements, the configuration is modified and checked again. This process is repeated until a satisfactory design configuration is identified.

The efficiency of this process and the quality of the final design depend on how much the design performance improves at each iteration. Although the trial-and-error technique relies solely on the designer's intuition and experience to improve the design, optimization techniques modify the design configuration systematically, based on sensitivity information and numerical algorithms that maximize the improvement between successive iterations. Consequently, optimization techniques require far fewer iterations than the trial-and-error approach, and the final solution is usually near optimal.

In the design optimization methodology, the design problem is converted into a multivariate minimization problem by first defining an *objective function*, $F(\boldsymbol{\Phi})$, which quantifies the "goodness" of a particular design in such a way that the minimum of $F(\boldsymbol{\Phi})$ corresponds to the desired design outcome. The objective function is dependent on a set of *design parameters* contained in the vector $\boldsymbol{\Phi}$, which specifies the design configuration. Once these quantities are defined, the design can be optimized using a multivariate minimization algorithm to find the vector $\boldsymbol{\Phi}^*$ such that $F(\boldsymbol{\Phi}^*) = \mathrm{Min}[F(\boldsymbol{\Phi})]$. Optimization methods differ on how $F(\boldsymbol{\Phi})$ is minimized and can be broadly classed as either *deterministic* or *metaheuristic*; deterministic methods work by changing $\boldsymbol{\Phi}$ at each step based on the local objection topography, whereas in metaheuristic algorithms $\boldsymbol{\Phi}^*$ is selected from a large set of candidate solutions generated by a random process. Two of the most common optimization methods are the quasi-Newton method, belonging to the deterministic class of methods, and the simulated annealing method, which is a metaheuristic method.

Deterministic (Quasi-Newton) Approach. The quasi-Newton method is a gradient-based approach, where the set of design parameters is adjusted systematically at each iteration based on the local objective function curvature; at the kth iteration, the new set of design parameters is found by

$$\mathbf{\Phi}^{k+1} = \mathbf{\Phi}^k + \alpha^k \boldsymbol{p}^k \tag{4}$$

where α^k is the step size and $\boldsymbol{p}^k$ is the search direction. The performance of gradient-based approaches is based largely on the choice of search direction (this is, in fact, how they are named). In Newton's method, the search direction at the kth iteration is set equal to Newton's direction, which is found by solving

$$\nabla^2 F(\mathbf{\Phi}^k)\boldsymbol{p}^k = -\nabla F(\mathbf{\Phi}^k) \tag{5}$$

where $\nabla F(\mathbf{\Phi}^k)$ is the gradient vector and $\nabla^2 F(\mathbf{\Phi}^k)$ is the Hessian matrix, containing the first- and second-order objective function sensitivities, respectively. Newton's method usually requires the fewest iterations to minimize the objective function and reaches $\mathbf{\Phi}^*$ in exactly one step if $F(\mathbf{\Phi})$ is quadratic.

Nevertheless, Newton's method is not always the most efficient due to the computational effort required to calculate the Hessian matrix; this is particularly true for large problems where the second-order objective function sensitivities are expensive to calculate. In such cases, it is better to use the quasi-Newton method. In this approach, the search direction is found by solving

$$\mathbf{B}^k \boldsymbol{p}^k = -\nabla F(\mathbf{\Phi}^k) \tag{6}$$

where $\mathbf{B}^k$ approximates the Hessian matrix. Most often $\mathbf{B}^0$ is initially set equal to the identity matrix and is updated at each subsequent iteration based on values of $F(\mathbf{\Phi}^k)$ and $\nabla F(\mathbf{\Phi}^k)$ from previous iterations to improve the approximation. (Various update schemes are described in [16].) Although it requires more iterations than Newton's method to find $\mathbf{\Phi}^*$, the quasi-Newton method is often more computationally efficient since second-order objective function sensitivity calculations are avoided.

Metaheuristic (Simulated Annealing) Approach. As with deterministic, gradient-based techniques, the simulated annealing approach finds $\mathbf{\Phi}^*$ iteratively, starting from an initial guess $\mathbf{\Phi}^0$. In contrast to gradient-based approaches, however, simulated annealing works by generating an alternate candidate solution at each iteration, $\mathbf{\Phi}^{k\prime}$, by randomly perturbing the elements of $\mathbf{\Phi}^k$. The Metropolis criterion [17] is then used to determine which set of design parameters should be chosen for the next iteration, i.e., whether $\mathbf{\Phi}^{k+1}=\mathbf{\Phi}^k$ or $\mathbf{\Phi}^{k\prime}$. This decision is based on the relative values of the objective function corresponding to the candidate design parameter sets, $\Delta E^k(\mathbf{\Phi}^k,\mathbf{\Phi}^{k\prime})=F(\mathbf{\Phi}^{k\prime})-F(\mathbf{\Phi}^k)$; if $\Delta E^k<0$, the new candidate improves the situation, whereas the opposite is true if $\Delta E^k>0$. A random number, $R\in(0,1)$, is generated and the perturbed solution is accepted if $R<\exp(-\Delta E^k/T)$, i.e., $\mathbf{\Phi}^{k+1}=\mathbf{\Phi}^{k\prime}$; otherwise the original solution is retained, $\mathbf{\Phi}^{k+1}=\mathbf{\Phi}^k$. Many variations are possible in the implementation of simulated annealing. The method used in this study holds the annealing temperature, T, constant for a specified number of iterations. A vector of $\delta\mathbf{\Phi}$ (neighborhood size), which controls the random disturbance of $\mathbf{\Phi}$, is also held constant (i.e., $\mathbf{\Phi}^{k+1}=\mathbf{\Phi}^k+R\delta\mathbf{\Phi}$), where R is a new random number for each parameter adjusted. At another specified interval, $\delta\mathbf{\Phi}$ is expanded or contracted based on the recent "uphill" acceptance rate to maintain approximately a 50% acceptance rate. As the annealing temperature is decreased, eventually the neighborhood has to collapse to maintain the acceptance rate. When a specified number of successive function evaluations fall within a tolerance of the best solution found, the process is stopped and the best solution realized is accepted.

A key feature of all metaheuristic methods is that there is a possibility that an uphill step will be selected, i.e., that $F(\mathbf{\Phi}^{k+1})>F(\mathbf{\Phi}^k)$. In simulated annealing, the likelihood of this outcome is determined by the annealing temperature T; the larger T is, the more likely it is that an uphill step will satisfy the Metropolis criterion. This feature enhances the performance of minimization techniques applied to solve multimodal objective functions, where the global minimum is surrounded by many local minima. In the first few iterations, T is assigned a very large value resulting in many uphill steps, preventing the minimization process from getting trapped in a relatively shallow local minimum. As the minimization progresses, it becomes increasingly likely that the algorithm has identified a deep local minimum, or possibly even the global minimum; accordingly, the annealing temperature is lowered and almost every step becomes a downhill step. The above procedure contrasts with safeguarded gradient-based methods, where every step is guaranteed to be a descent direction. Consequently, the local minimum identified by a gradient-based algorithm is dependent solely on the starting point $\mathbf{\Phi}^0$. It is therefore often necessary to restart the gradient-based algorithm to obtain a local minimum with a sufficiently small value of $F(\mathbf{\Phi}^*)$.

A further advantage of simulated annealing is that it does not require the calculation of objective function derivatives. Gradient-based methods may converge to local minima faster than metaheuristic methods, since the former class of methods updates approximations of $\mathbf{\Phi}^*$ based on the objective function topography, whereas the latter class of methods instead relies on random perturbations. A drawback of all metaheuristic methods is that the heuristic search parameters (initial annealing temperature, rate of annealing temperature decrease, and termination criteria) are not generally apparent at the onset but instead must be discovered by experience accrued from repeated experiment, hence, the name *metaheuristic*.

Problem Specification

To compare the solution methods, a design problem is proposed that incorporates some attributes of a real design for a radiant furnace. A three-dimensional geometry is considered, and the problem is to determine the radiant heater settings that will provide a prescribed transient but spatially uniform heating the design surface. The basic enclosure is three-dimensional (Fig. 1), and the design surface is inset slightly from the edges of the bottom enclosure surface. (Experience has shown that it is very difficult to attain uniform conditions on a workpiece covering the full extent of the furnace bottom.) The design surface 6a has dimensions of 0.75×1.75 m (that is, it is set in 0.125 m from each boundary). The remainder of the bottom surface around the design surface is a diffuse adiabatic surface with the same thermal properties as the sides. There is no thermal exchange between the design surface and the rest of the bottom surface (i.e., infinite contact resistance). Figure 1(*a*) shows the enclosure geometry, and Fig. 1(*b*) the computational domain, which is formed by inserting imaginary surfaces that are perfect specular reflectors along the lines of symmetry in the original enclosure. The design surface 6a is located on the bottom of the enclosure and is 0.125 m away from the edges on all sides. Since previous work has shown that the distance between the heater and design surfaces is a major factor in the accuracy of inverse solutions, we consider two different enclosure geometries with height-to-width ratios of $H/W=0.5$ m (as shown) and $H/W=0.25$ m. Table 1 gives the enclosure properties that were used in the analyses. Surface 6a is representative of a steel alloy and the remaining surfaces of a refractory brick with a glazed surface that is partially specularly reflecting. All boundaries are assumed to be lumped capacitances (i.e., no temperature profiles normal to the boundaries are included). This may introduce error into a prediction of the behavior of a real furnace, but the assumption was invoked to reduce the complexity of the analysis while still allowing comparison of the inverse methods used for treating the problem.

The computational domain is discretized into a total of 112 surface elements having equal areas. (No surface elements are located on the specularly reflecting symmetry surfaces.) Sixteen elements are located on surface 3, whereas surfaces 4, 5, and 6 each have 32 elements as shown in Fig. 2. The numbering scheme for elements on each surface is provided in the Appendix. The design surface is to be heated with a spatially uniform transient temperature following the profile shown in Fig. 3.

At any time t throughout the process, the energy applied to a given surface element i is given by

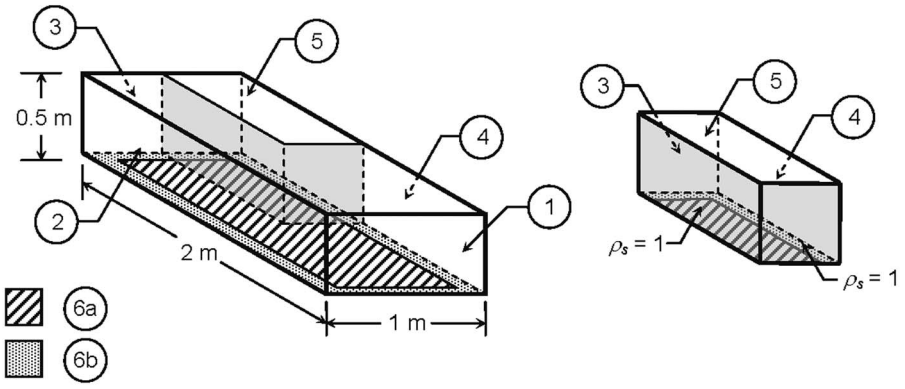

Fig. 1 Basic dimensions of three-dimensional enclosure: (*a*) enclosure geometry and (*b*) computational domain

$$(\rho c\delta)_i A_i \frac{dT_i(t)}{dt} = \sum_{j=1}^{N} E_j(t) A_j \tilde{F}_{j\to i} - E_i(t) A_i + q_{i,\mathrm{cond}}(t) \qquad (7)$$

where $E=\varepsilon\sigma T^4$ is the emissive power of a given element and $\tilde{F}_{i\to j}$ is the exchange factor, defined as the fraction of energy emitted by surface i that is absorbed by surface j, considering all possible paths of reflection among intervening surfaces. We calculated the exchange factor set using the Monte Carlo method, since this approach facilitates accommodation of partially specular reflective surfaces. The accuracy of the exchange factor set was enhanced using the smoothing algorithm presented in [18]. The numbering used for the discrete elements of the enclosure surfaces and access to the values of the exchange factors is described in the Appendix. In Eq. (7), $q_{i,\mathrm{cond}}$ accounts for the conductive heat exchanged between surface i and the surrounding elements; convection heat transfer is neglected.

Equation (7) can be placed in dimensionless form by using the reciprocity relation

$$C_i \frac{\partial\theta_i(\tau)}{d\tau} = \sum_{j=1}^{N} \theta_j^4(\tau)\tilde{F}_{i\to j} - \theta_i^4(\tau) + \frac{\psi_{i,\mathrm{cond}}}{\varepsilon_i}$$

$$\varepsilon_i A_i \tilde{F}_{i\to j} = \varepsilon_j A_j \tilde{F}_{j\to i}: \qquad (8)$$

where

$$\tau = \frac{\varepsilon_{\mathrm{DS}}\sigma T_{\mathrm{ref}}^3}{(\rho c\delta)_{\mathrm{DS}}} t;\ C_i = \left(\frac{\varepsilon_{\mathrm{DS}}}{\varepsilon_i}\right)\frac{(\rho c\delta)_i}{(\rho c\delta)_{\mathrm{DS}}};\ \theta(\tau) = \frac{T(t)}{T_{\mathrm{ref}}},\ \text{and}\ \psi_i = \frac{q_i}{\sigma T_{\mathrm{ref}}^4}.$$

In the preceding energy equation, all terms are expressed as energy flux based on area normal to the surface (though the conduction term arrives in directions parallel to the surface).

Each method of solution provided the following parts:

1. To check solutions:
   a. A uniform dimensionless temperature $\theta_5=1$ is prescribed on the top surface, $\theta_{1,3}=0.5$ on the ends, $\psi_{2,4,6b}=0$ on the sides and on the bottom around the design surface, $\theta_{6a}=0.1$ on the design surface, and $\psi_{6a}(x,y)$ is calculated on the design surface. Then, using this calculated $\psi_{6a}(x,y)$ and $\theta_{6a}=0.1$ on the design surface and the given conditions on the sides, ends, and remainder of the bottom, $\theta_5(x,y)$ on the top is found by the inverse methodology, and checked for agreement with the originally imposed condition of $\theta_5=1.0$. (This is a steady-state inverse problem that should not be ill-posed.)
   b. For a uniform heat flux input on the heaters $\psi_5=1.0$, calculate $\theta_{6b}(x,y)$ on the adiabatic design surface. Then use the computed $\theta_{6b}(x,y)$ and $\psi_{6b}=0$ on the design surface and, by inverse analysis, calculate the heat flux ψ_5 on the heaters and see if the input value is recovered to test that the inverse methodology has been correctly formulated
2. Find the heater energy input distribution $\psi_5(x,y,\tau)$ at each time that most closely gives the linear uniform temperature on the design surface $\theta_{6a}(\tau)$ versus time prescribed in Fig. 3. A reference temperature of $T_{\mathrm{ref}}=1000$ K is used for calculating and presenting the results in dimensionless form.
3. Provide the maximum error found in $\theta_{6b}(x,y,\tau)$ at any time during the transient, and the maximum error in $\theta_{6b}(\tau)$ relative to $\theta_{6b}^{\mathrm{target}}(\tau)$ found at any time, again using $T_{\mathrm{ref}}=1000$ K. Also, calculate the error in the overall energy bal-

Table 1 Enclosure properties and specifications

Surface	1 Brick	2 Brick	3 Brick	4 Brick	5 Brick	6a Steel	6b Brick
Emissivity, ε	0.3	0.3	0.3	0.3	0.9	0.6	0.3
Diffuse reflectivity, ρ_d	0.2	0.2	0.2	0.2	0.1	0.3	0.2
Specular reflectivity, ρ_s	0.5	0.5	0.5	0.5	0.0	0.1	0.5
k [W/m K]	1.0	1.0	1.0	1.0	1.0	63.9	1.0
ρ [kg/m^3]	2645	2645	2645	2645	2645	7832	2645
c [J/kg K]	960	960	960	960	960	487	960
δ [m]	0.1	0.1	0.1	0.1	0.1	0.02	0.1

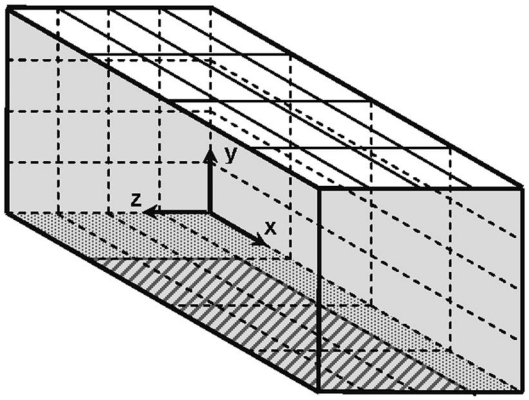

Fig. 2 Discretization of the computational domain for calculation of exchange factors

Table 2 Calculated dimensionless heat flux $\psi_{DS}(x,y)$ on the design surface for uniform heater temperatures $[\theta_5(x,y)=1.0]$ for the element distribution of Fig. 13

			$H/W=0.25$				
			$\psi_{DS}(x,z)$				
z	$x\rightarrow$						
$\downarrow$	−0.5279	−0.5434	−0.5505	−0.5539	−0.5556	−0.5565	−0.5570
	−0.5302	−0.5460	−0.5531	−0.5565	−0.5583	−0.5592	−0.5597
	−0.5308	−0.5466	−0.5537	−0.5571	−0.5589	−0.5598	−0.5602
			$H/W=0.5$				
			$\psi_{DS}(x,z)$				
z	$x\rightarrow$						
$\downarrow$	−0.4848	−0.5010	−0.5119	−0.5191	−0.5234	−0.5261	−0.5273
	−0.4880	−0.5045	−0.5159	−0.5232	−0.5278	−0.5305	−0.5317
	−0.4897	−0.5064	−0.5179	−0.5253	−0.5301	−0.5327	−0.5340

ance to the furnace. The solutions should have no negative values for the heater energy flux, $\psi_5(x,y,\tau)$.

Prior to solution of part 2, we expected that significant differences might occur between the calculated and imposed transient temperatures on the design surface, because we have imposed a temperature distribution that is physically difficult to obtain (it is expected to take a very large heater energy input near $t=0$ to get the discontinuous temperature change on the design surface). However, rather than change the temperature-time profile to an easier-to-meet S-shaped profile, we elected to see how closely we could approach the more challenging case of Fig. 3, which might be prescribed by a design customer.

It would be useful to vary other parameters than the heater-to-design surface spacing to determine the effect of these parameters on the solutions. This has been done for the individual solution methods, and some of these results are in Refs. [6–8].

Solution Techniques and Results

All of the methods were able to complete part 1a of the prescribed problem and exactly recover the prescribed uniform heater dimensionless temperature except for the simulated annealing formulation, which approached the solution but did not exactly reproduce it. In part 1b all of the methods recovered the condition of uniform heat flux. This is typical of inverse problems where the input to the inverse problem is generated by solution of a prescribed forward problem; although the problem is ill-posed, the input conditions can still be recovered. This part of the problem serves chiefly to verify that the inverse methodology has been correctly formulated. The predicted heat flux on the design surface obtained from the prescribed uniform temperature on the heaters was then used as a boundary condition for the inverse problem is shown in Table 2. As would be expected, spacing the isothermal heater and design surface more closely together ($H/W=0.25$) provides a more uniform heat flux on the design surface.

TSVD

Design Surface Elements. The energy balance in each design surface element is given by Eq. (9), assuming that conduction occurs between adjacent surface elements (but not around enclosure corners where the walls were assumed to have only edge contact), and convection is neglected

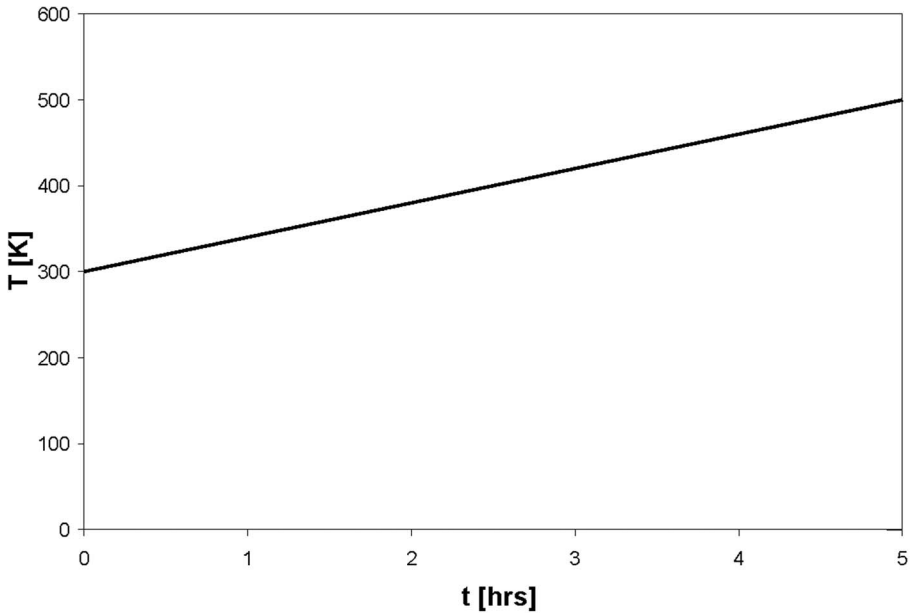

Fig. 3 Required transient spatially uniform temperature profile imposed on the design problem

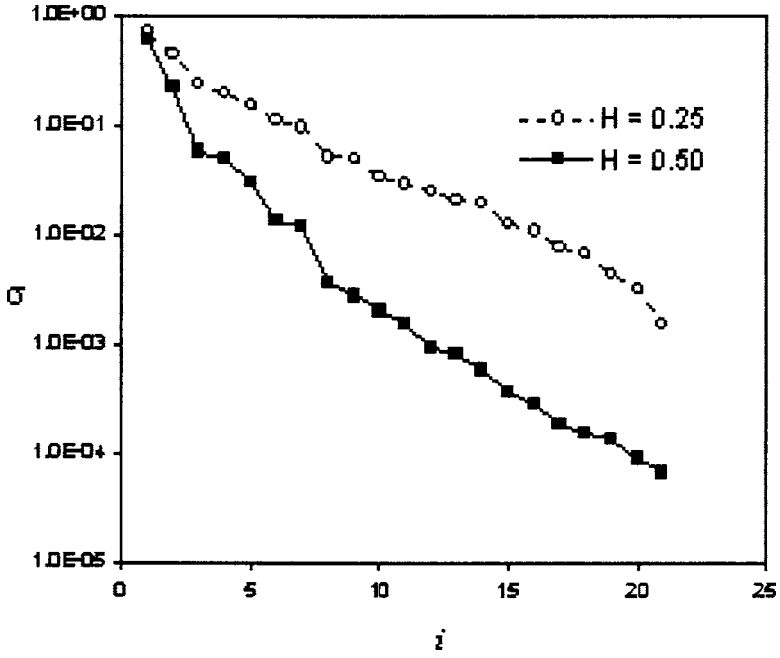

Fig. 4 Singular values of matrix A for $H/W=0.25$ and 0.50

$$\frac{\partial\theta_{\mathrm{DS},i}(\tau)}{d\tau}=\sum_{j=N_{\mathrm{DS}}+1}^{N}\theta_j^4(\tau)\tilde{F}_{i\to j}+\sum_{j=1}^{N_{\mathrm{DS}}}\theta_j^4(\tau)\tilde{F}_{i\to j}-\theta_{\mathrm{DS},i}^4(\tau)+\frac{\psi_{\mathrm{DS},i,\mathrm{cond}}(\tau)}{\varepsilon_{\mathrm{DS}}} \tag{9}$$

where the lumped capacitance model is used to account for the storage of energy in each design surface element. The DS subscript is used to denote design surface elements. These elements are also identified with the 6a subscript in the general numbering scheme used in the Appendix. From the linear temperature history prescribed in Fig. 3 for the design surface, the left-hand side of Eq. (9) is known in each instant of time.

Equation (9) can also be rearranged to provide the equations for the emissive powers of the heater elements

$$\sum_{\substack{\text{heater}\\ \text{elements}}}\theta_{\mathrm{HS},j}^4(\tau)\tilde{F}_{i-\mathrm{HS},j}=C_{\mathrm{DS}}\frac{\partial\theta_{\mathrm{DS},i}(\tau)}{\partial\tau}-\sum_{j=1}^{N_{\mathrm{DS}}}\theta_{\mathrm{DS},j}^4(\tau)\tilde{F}_{i-\mathrm{DS},j}-\sum_{\substack{\text{wall}\\ \text{elements}}}\theta_{\mathrm{WS},j}^4(\tau)\tilde{F}_{i-\mathrm{WS},j}+\theta_{\mathrm{DS},i}^4(\tau)-\frac{\psi_{\mathrm{HS},i,\mathrm{cond}}(\tau)}{\varepsilon_{\mathrm{HS},i}} \tag{10}$$

Wall Elements. The energy balance in each wall element j is given by

$$C_{\mathrm{WS},j}\frac{d\theta_{\mathrm{WS},j}}{d\tau}=\frac{\psi_{\mathrm{WS},j,\mathrm{rad}}(\tau)}{\varepsilon_{\mathrm{WS}}}+\frac{\psi_{\mathrm{WS},j,\mathrm{cond}}(\tau)}{\varepsilon_{\mathrm{WS}}} \tag{11}$$

where $C_{\mathrm{WS}}=(\varepsilon_{\mathrm{DS}}/\varepsilon_{\mathrm{WS}})[(\rho\delta c)_{\mathrm{WS}}/(\rho\delta c)_{\mathrm{DS}}]$ and $\Psi_{\mathrm{WS,rad}}$ is defined in Eq. (11).

Solution Procedure

- At $\tau=0$ (time step $k=0$), the dimensionless temperatures on the design surface and wall elements are all assumed to be at $\theta(k=0)$.
- Equation (9) is applied to find $\theta_{\mathrm{HS},j}^4(k=0)$ for the heater elements. Writing Eq. (9) for each design surface element i leads to a system having 21 equations and 32 unknowns (the emissive powers in the 32 heating elements). The TSVD method is now applied. First, the coefficient matrix $\mathbf{A}^{m\times n}$ ($m=21$, $n=32$) is SVD decomposed—the singular values are shown in Fig. 4 for $H/W=0.25$ and 0.50. Since the number of columns of matrix **A** is 32, there are 32 singular values, but only the first 21 nonzero singular values are shown in the figure. The TSVD is applied so that only the terms related to the p largest singular values are kept in the solution, where p is limited to the SVD terms $p\leqslant 21$. The solution thus obtained provides the emissive powers of the heating elements in time step k, $\theta_{\mathrm{HS},j}^{4(k)}$.

At this time step k, the temperature (and thus the emissive power) in each element of the enclosure is known. The radiative heat flux in each element, in time step k, is

$$\psi_{\mathrm{DS},i,\mathrm{rad}}^{(k)}=\varepsilon_{\mathrm{DS}}\left[\sum_{\substack{\text{design}\\ \text{elements}}}\tilde{F}_{\mathrm{DS},i-\mathrm{DS},j}\theta_{\mathrm{DS},j}^{4(k)}+\sum_{\substack{\text{heater}\\ \text{elements}}}\tilde{F}_{\mathrm{DS},i-\mathrm{HS},j}\theta_{\mathrm{HS},j}^{4(k)}+\sum_{\substack{\text{wall}\\ \text{elements}}}\tilde{F}_{\mathrm{DS},i-\mathrm{WS},j}\theta_{\mathrm{WS},j}^{4(k)}-\theta_{\mathrm{DS},i}^{4(k)}\right] \tag{12a}$$

$$\psi_{\mathrm{WS},i,\mathrm{rad}}^{(k)}=\varepsilon_{\mathrm{WS}}\left[\sum_{\substack{\text{design}\\ \text{elements}}}\tilde{F}_{\mathrm{WS},i-\mathrm{DS},j}\theta_{\mathrm{DS},j}^{4(k)}+\sum_{\substack{\text{heater}\\ \text{elements}}}\tilde{\tilde{F}}_{\mathrm{WS},i-\mathrm{HS},j}\theta_{\mathrm{HS},j}^{4(k)}+\sum_{\substack{\text{wall}\\ \text{elements}}}\tilde{F}_{\mathrm{WS},i-\mathrm{WS},j}\theta_{\mathrm{WS},j}^{4(k)}-\theta_{\mathrm{WS},i}^{4(k)}\right] \tag{12b}$$

$$\psi_{\mathrm{HS},i,\mathrm{rad}}^{(k)} = \varepsilon_{\mathrm{HS}}\left[\sum_{\substack{\text{design}\\ \text{elements}}} \tilde{F}_{\mathrm{HS},i-\mathrm{DS},j}\theta_{\mathrm{DS},j}^{4(k)} + \sum_{\substack{\text{heater}\\ \text{elements}}} \tilde{\tilde{F}}_{\mathrm{HS},i-\mathrm{HS},j}\theta_{\mathrm{HS},j}^{4(k)} + \sum_{\substack{\text{wall}\\ \text{elements}}} \tilde{F}_{\mathrm{HS},i-\mathrm{WS},j}\theta_{\mathrm{WS},j}^{4(k)} - \theta_{\mathrm{HS},i}^{4(k)}\right] \tag{12c}$$

- The increase in the temperature of the elements in the design surface and walls can be found from a finite-difference approximation. For elements in the design surface, discretizing Eq. (9) leads to

$$\theta_{\mathrm{DS},j}^{(k+1)} = \theta_{\mathrm{DS},j}^{(k)} + \frac{\psi_{\mathrm{DS},j,\mathrm{rad}}^{(k)} + \psi_{\mathrm{DS},j,\mathrm{cond}}^{(k)}}{\varepsilon_{\mathrm{DS}}}\Delta\tau \tag{13}$$

For the elements in the walls, the discretization of Eq. (10) gives

$$\theta_{\mathrm{WS},j}^{(k+1)} = \theta_{\mathrm{WS},j}^{(k)} + \frac{\psi_{\mathrm{WS},j,\mathrm{rad}}^{(k)} + \psi_{\mathrm{WS},j,\mathrm{cond}}^{(k)}}{\varepsilon_{\mathrm{WS}}C_{\mathrm{WS}}}\Delta\tau \tag{14}$$

The application of Eqs. (13) and (14) provides the temperatures in the design surface and the wall elements in the new time step $(k+1)$, and the process is repeated.

Heater Elements. Up to this point, no global energy balance was applied to the heating elements. However, based on the inverse solution, it is possible to find $\theta_{\mathrm{HS},j}^4$, the radiative power $\psi_{\mathrm{HS},j,\mathrm{rad}}$, and the conductive heat transfer $\psi_{\mathrm{HS},j,\mathrm{cond}}$ at every time step k. The power input in the heater can then be found from

$$C_{\mathrm{HS}}\frac{d\theta_{\mathrm{HS},i}}{d\tau} = \frac{1}{\varepsilon_{\mathrm{HS}}}(P_{\mathrm{HS},i} + \psi_{\mathrm{HS},i,\mathrm{rad}} + \psi_{\mathrm{HS},i,\mathrm{cond}}) \tag{15}$$

where $P_{\mathrm{HS},i} = p''_{\mathrm{HS},i}/\varepsilon_{\mathrm{DS}}\sigma T_{\mathrm{ref}}^4$, and $p''_{\mathrm{HS},i}$ is the power input in the heating element i, in watts per square meters. Applying a finite-difference approximation for the transient derivative term of Eq. (14) leads to

$$P_{\mathrm{HS},i}^{(k)} = -\frac{\psi_{\mathrm{HS},i,\mathrm{rad}}^{(k)} + \psi_{\mathrm{HS},i,\mathrm{cond}}^{(k)}}{\varepsilon_{\mathrm{HS}}} + \frac{C_{\mathrm{HS}}}{\Delta\tau}(\theta_{\mathrm{HS},i}^{(k+1)} - \theta_{\mathrm{HS},i}^{(k)}) \tag{16}$$

which gives the power input in the heating element i in time step k. Note that, to find $P_{\mathrm{HS},i}^{(k)}$, it is necessary to know $\theta_{\mathrm{HS},i}^{(k+1)}$, the temperature of the heating element in time step $(k+1)$. This does not impose a major difficulty since this term is found from the procedure outlined above, which is independent of the power input $P_{\mathrm{HS},i}$ in the heater.

Tikhonov Method. The Tikhonov method followed the procedure of the TSVD method in deriving the ill-posed equations for elements on the design surface (Eq. (10)) and found the unknown temperatures of the heaters through Eq. (3). These were then used to find the energy input to the heaters. Both solutions (TSVD and Tikhonov) found the identical set of singular values. For the case of $H/W=0.25$, the singular values were large enough and the condition number of the coefficient matrix was small enough that direct inversion was possible without truncation in TSVD and without use of a smoothing function (i.e., $\lambda_0=0$) in the Tikhonov solution.

For the case of $H/W=0.5$, truncation was necessary in TSVD, and only 3 of 21 singular values were retained to obtain a solution with all positive energy inputs to the heaters. For the Tikhonov solution, a first-order smoothing function with various values of λ_0 were computed. The appropriate regularization parameter λ_0 needs to be chosen with a view to controlling the influence of the regularization term relative to the residual term in Eq. (2). In the present problem, for $\lambda_0 \leqslant 0.004$ the solutions predicted negative heater inputs, and for $\lambda_0 \geqslant 1$, the solutions for heater input were oversmoothed and errors on the design surface temperatures became large. After some experimentation, setting $\lambda_0=0.2$ provided the best results.

CGR. The CG method followed the procedure used by the TSVD and Tikhonov methods in deriving the equations for elements on the design surface. The system of equations was then solved by the CG algorithm. For the case where $H/W=0.25$, for which a solution can be found without regularization, the CGR solution converged to the same solution obtained using TSVD and Tikhonov regularization. For the case $H/W=0.50$, the best solution provided by the CGR method was found in two iterative steps. It was possible to obtain solutions that were physically acceptable (that is, positive emissive powers and net powers in all heating elements) for as many as ten CGR steps, leading to solutions that were much more accurate. However, for such cases, it was found that in some heaters the net radiative heat flux was negative. This is because the net power is being computed from the sum of the net radiative heat flux and the increase in the temperature of the adjacent wall, so the power can be positive even if the net radiative heat flux is negative.

Optimization Techniques

As discussed above, all optimization techniques work by first casting the design problem as a constrained multivariate minimization problem, which is then solved iteratively. There are many different ways to define the objective function and design parameters; however, and many different mathematical tools can be applied to solve the resulting problem.

Quasi-Newton Method. In this implementation, the objective function is set equal to the variance of the design surface temperature from the desired temperature at a given process time, integrated throughout the entire process. If the process time is discretized into N_t discrete time steps, this is equivalent to

$$F(\mathbf{\Phi}) = \frac{1}{N_t N_{\mathrm{DS}}}\sum_{k=1}^{N_t}\sum_{i=1}^{N_{\mathrm{DS}}}[\theta_i(\mathbf{\Phi},\tau_k) - \theta^{\mathrm{target}}(\tau_k)]^2. \tag{17}$$

The design surface temperature is dependent on the transient heater inputs on the heater surface, which, in turn, are controlled by $\mathbf{\Phi}$ using cubic splines having the form

$$\psi_h(\mathbf{\Phi}) = C[\mathbf{\Phi}_{4h}\tau^3 + \mathbf{\Phi}_{4h+1}3\tau^2(1-\tau) + \mathbf{\Phi}_{4h+2}3\tau(1-\tau)^2 + \mathbf{\Phi}_{4h+1}(1-\tau)^3] \tag{18}$$

where C is a scaling factor and $\mathbf{\Phi}_h = \{\mathbf{\Phi}_{4h}, \mathbf{\Phi}_{4h+1}, \mathbf{\Phi}_{4h+2}, \mathbf{\Phi}_{4h+3}\}^T$ is the subset of $\mathbf{\Phi}$ corresponding to the hth heater, assuming that the heaters are numbered starting from $h=0$. This approach reduces the dimensionality of the problem (compared to controlling each heater setting with a corresponding design parameter at every time step) and also regularizes the transient heater inputs with respect to time, which helps ensure that the optimized transient heater settings can be implemented in a practical industrial setting.

Introducing constraints considerably complicates gradient-based minimization. In this problem, the optimized heater settings must remain strictly nonnegative for the solution to be practical. A previous work [19] satisfied this requirement by constraining $\mathbf{\Phi}_i \geqslant 0$, $i=1,2,\ldots,n$, which, in turn, ensures non-negative heater settings by virtue of the B-spline convex hull property. This is a sufficient but not necessary condition to guarantee non-negative heater settings, and indeed, it was found in this problem that this constraint was overly harsh, impairing the quality of the optimized solution.

Instead, the best results were found by simply setting the heater outputs equal to zero if Eq. (18) predicted a negative value. The drawback to this approach is that the objective function is usually only C^0 continuous when $\psi_h(\mathbf{\Phi})=0$. To account for this, minimization was carried out using an unconstrained quasi-Newton algo-

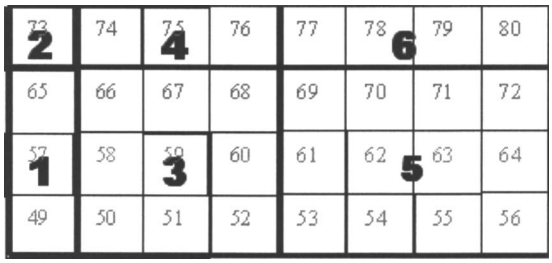

Fig. 5 Partitioning of the heater surface into six regions for simulated annealing

rithm modified so that $\mathbf{p}^k$ was set equal to the steepest descent direction if the quasi-Newton search direction failed and α^k was found using an exact line search at each step.

Optimization was started from $\mathbf{\Phi}_h^0=\{1,2/3,1/3,0\}^T$. The quasi-Newton search direction failed after only a few iterations, after which convergence became sublinear. Because of this, the algorithm did not converge to a local minimum and was instead terminated after 1000 iterations. As previously mentioned, the difficulties associated with minimizing this objective function are primarily due to the fact that $F(\mathbf{\Phi})$ is not C^2 continuous over the domain of $\mathbf{\Phi}$. Also, heater settings at time steps near the end of the process (and their corresponding design parameters) have very little effect on the design surface temperature and the objective function due to the thermal inertia of the heater surface, and several heaters likely affect the design surface temperature in a similar way; both of these factors make the objective function semidefinite in the vicinity of $\mathbf{\Phi}^*$. These difficulties may be overcome either by using a different functional representation for $\psi_h(\mathbf{\Phi})$ or by employing a more sophisticated minimization technique.

Simulated Annealing. In contrast to the quasi-Newton implementation, the optimal heater settings using the simulated annealing approach were found at each time step by minimizing

$$F(\mathbf{\Phi},\tau)=\frac{1}{N_{\mathrm{DS}}}\sum_{j=1}^{N_{\mathrm{DS}}}[\psi_j(\mathbf{\Phi},\tau)-\psi_j^{\mathrm{target}}(\tau)]^2 \tag{19}$$

where $\psi_j^{\mathrm{target}}(\tau)$ is the net radiant heat flux needed by each element on the design surface to satisfy the increase in sensible energy during that timestep, as defined in Eq. (9). As previously noted, if each heater element were controlled by a single design parameter, the resulting optimization problem (or sequence of optimization problems in this case) would be too large to be computationally tractible. Instead, the heater surface is divided into six regions, as shown in Fig. 5, and a uniform heat flux over each region (at each timestep) is specified by a corresponding $\mathbf{\Phi}_i$; thus, $\mathbf{\Phi}$ has a dimension of 6 instead of 32.

The simulated annealing algorithm used here was a modification of the one presented in [20,21]. Unlike gradient-based methods, it is comparatively easy to impose bounds on the heater settings in simulated annealing by restricting the domain of possible values that $\mathbf{\Phi}_i$ can assume; in this problem, $\mathbf{\Phi}_i$ was constrained to be non-negative. At each time step, optimization was started from the optimal heater settings of the previous time step, with the exception of the second time step. This is because a large amount of energy must be applied by the heaters during the first time step relative to the second time step to overcome the thermal inertia of the enclosure surfaces, since the heating process starts from thermal equilibrium; thus, the optimized heater settings from the first time step would not provide a good starting point for optimizing the heater settings in the second time step. Simulated annealing was then applied at each successive time step, using the state of the heaters from the previous step as a good approximation for the current step.

The parameters of the search method are the heat fluxes of six regions of the heater surface (See Appendix). Figure 5 shows the six regions chosen. The zones are numbered as zone 1(49,57,65); zone 2 (73); zone 3 (50–52,58–60,66–68); zone 4 (74–76); zone 5 (53–56,61–64,69–72); and zone 6 (77–80).

Figures 6 and 7 show the dimensionless heater fluxes for the six regions for $H/W=0.5$ and 0.25 cases after the initial time increment. Although the method appears to have delivered uniform design surface conditions, the lack of smoothness of heater operation for the $H/W=0.5$ case (Fig. 6) would be problematic if the solution were to be implemented in an actual furnace. In particular, note that the heaters experience a sudden power input at about 15 min, as the third bank of heaters takes a precipitous drop and the first bank picks up the slack; a similar event occurs just after 2.5 hr.

In contrast, the system behaves well throughout the transient for $H/W=0.25$ (Fig. 7) and all of the heater zones exhibit smooth, monotonically increasing power fluxes. The maximum differences between predicted and desired dimensionless temperatures were

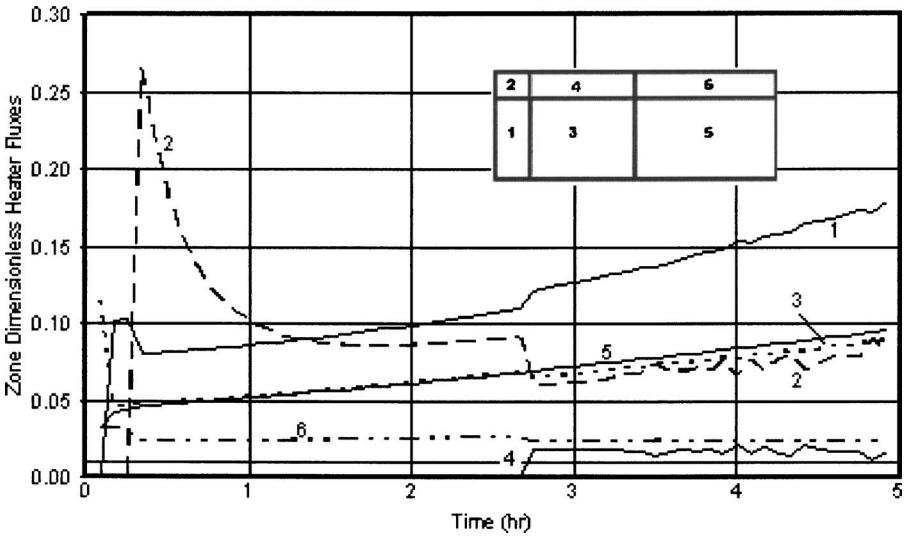

Fig. 6 Predicted power to heater zones using simulated annealing: $H/W=0.5$; $T_{\mathrm{ref}}=1000$ K

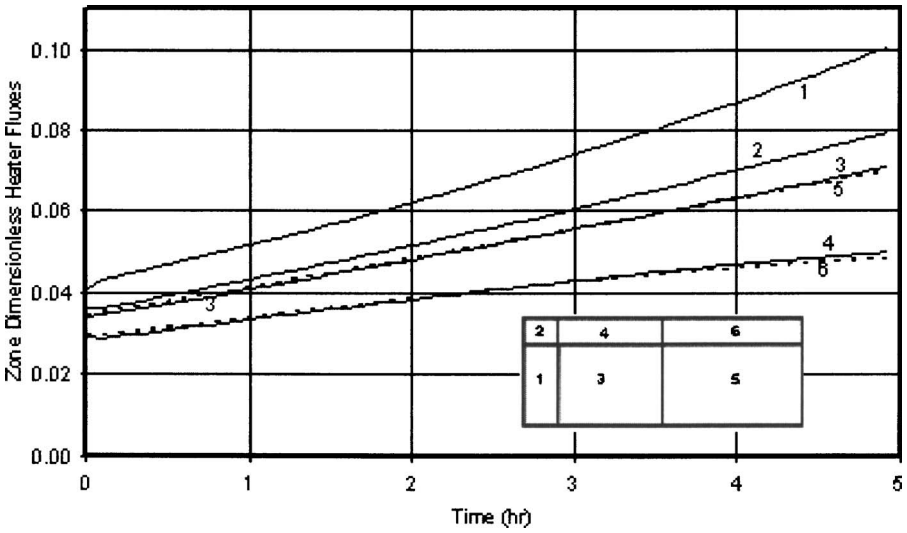

Fig. 7 Predicted power to heater zones using simulated annealing: $H/W=0.25$; $T_{ref}=1000$ K

<0.0005 throughout the transient for both values of H/W.

Combining the stated objective function, finite difference scheme, and neglecting temperature gradients through the heater surface thickness results in a large power specification for the first time step. A constraint on maximum power could be imposed, but would result in early deviation from the target path.

Furthermore, although the desired temperature distribution over the design surface was satisfied, the "fluttering" heater settings are an undesirable feature of this solution. The solution to the $H/W=0.25$ problem is less prone to this phenomenon.

Comparison of Selected Computed Results

For comparison of the predictions of the various methods for the transient case, results for the design surface at hourly intervals are presented in Tables 3 and 4. The mean value and standard deviation of the dimensionless temperatures on the design surface elements $\theta_{DS}(t)$ are given for the two chosen values of H/W.

Each of the methods gives quite good agreement with the target uniform design surface temperatures of Fig. 3. For the case of $H/W=0.25$, the TSVD, Tikhonov, and CGR methods give identical results and are in exact agreement with the target temperatures. The methods based on optimization (quasi-Newton minimization and simulated annealing) have minor differences from the target temperatures for this case, but are certainly within any reasonable design standard.

For $H/W=0.5$ (Table 4), the results of all of the methods are still within excellent agreement with the target values at all times; unlike the previous case, however, the three direct inversion methods (TSVD, Tikhonov, and CGR) now show some variation in the surface temperatures around the target value.

Although each of the methods finds solutions that closely satisfy the desired conditions over the design surface throughout the process, there are significant differences in the predicted heater energy distributions. To illustrate this, the dimensionless heater power distributions at $t=4$ hr are shown in Figs. 8–12.

In Figs. 8–12 the predicted power distributions of the heated surface are displayed at 4 hr into the process. Figures 8–10 show the heater power distributions for the three methods based on direct inversion (TSVD, TR, and CGR). Each of these methods invokes smoothing on the solutions, as reflected by the heater

Table 3 Mean temperature $\theta_{DS}(t)=T(t)/T_{ref}$ and standard deviation on design surface at various times for $H/W=0.25$, $T_{ref}=1000$ K

	$t=1$ h	$t=2$ h	$t=3$ h	$t=4$ h	$t=5$ h
Target	0.340	0.380	0.420	0.460	0.500
TSVD	0.340±0	0.380±0	0.420±0	0.460±0	0.500±0
Tikhonov	0.340±0	0.380±0	0.420±0	0.460±0	0.500±0
CGR	0.340±0	0.380±0	0.420±0	0.460±0	0.500±0
Quasi-Newton	0.3397±0.0028	0.3806±0.0012	0.4194±0.0010	0.4603±0.0022	0.4994±0.0028
Simulated annealing	0.3400±0.0000	0.3800±0.0000	0.4201±0.0000	0.4601±0.0001	0.5001±0.0001

Table 4 Mean temperature $\theta_{DS}(t)=T(t)/T_{ref}$ and standard deviation on design surface at various times for $H/W=0.50$, $T_{ref}=1000$ K

	$t=1$ h	$t=2$ h	$t=3$ h	$t=4$ h	$t=5$ h
Target	0.340	0.380	0.420	0.460	0.500
TSVD $p=3$	0.3400±0.0003	0.3799±0.0004	0.4199±0.0004	0.4598±0.0005	0.4998±0.0006
Tikhonov $L=L_1, \lambda=0.2$	0.3400±0.0002	0.3800±0.0004	0.4199±0.0005	0.4599±0.0006	0.4999±0.0007
CGR ($I=2$)	0.3399±0.0004	0.3797±0.0005	0.4199±0.0004	0.4599±0.0007	0.4999±0.0008
Quasi-Newton	0.3408±0.0033	0.3799±0.0052	0.4199±0.0008	0.4600±0.0018	0.5003±0.0019
Simulated annealing	0.3400±0.0000	0.3801±0.0000	0.4201±0.0001	0.4602±0.0001	0.5003±0.0001

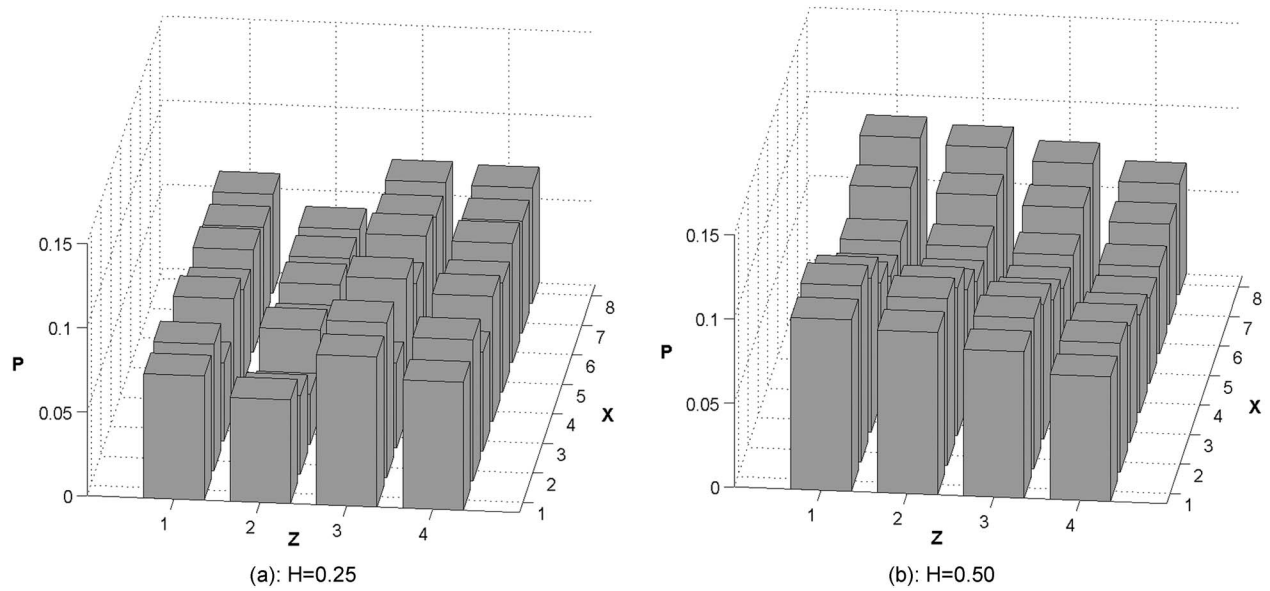

Fig. 8 Heater power distribution at $t=4$ hr, TSVD method: truncation parameter $p=3$; $T_{ref}=1000$ K; average design surface dimensionless temperature: (*a*) $\bar{\theta}=0.460$ and (*b*) $\bar{\theta}=0.4598\pm0.0005$

power distributions. For the $H/W=0.25$ case, the three solutions are identical, since the equations describing the heater power are not ill-conditioned for this particular case and accordingly all three methods provide exact solutions. For $H/W=0.5$, however, the three methods provide smooth but different distributions. The Tikhonov method, in particular, predicts a less uniform heater power distribution, which results in a more accurate temperature on the design surface (Table 4).

The optimization methods do not encourage spatially smooth solutions, but do guarantee non-negative heater settings throughout the process. Thus, the solutions for heater power are much less uniform, but allow elimination of heaters that require no power input throughout the process. Note the scale change for power on the quasi-Newton results of Fig. 11; fewer heaters with greater power input are needed to provide the design surface energy input and temperature.

The simulated annealing results of Fig. 12 show another approach to regularization, in that the heat flux distribution is smoothed a priori by aggregating the heaters into six regions as shown in Fig. 5. This provides a simpler heater array for control, and the method gives excellent agreement with the target design temperature profile. The solution for $H/W=0.5$ has discontinuities with time in the power input to the heaters as shown in Fig. 6, and it is not clear how this solution could be implemented in practice. Similar discontinuities have been observed in using the CGR method [22] when the most accurate solution at a given time step

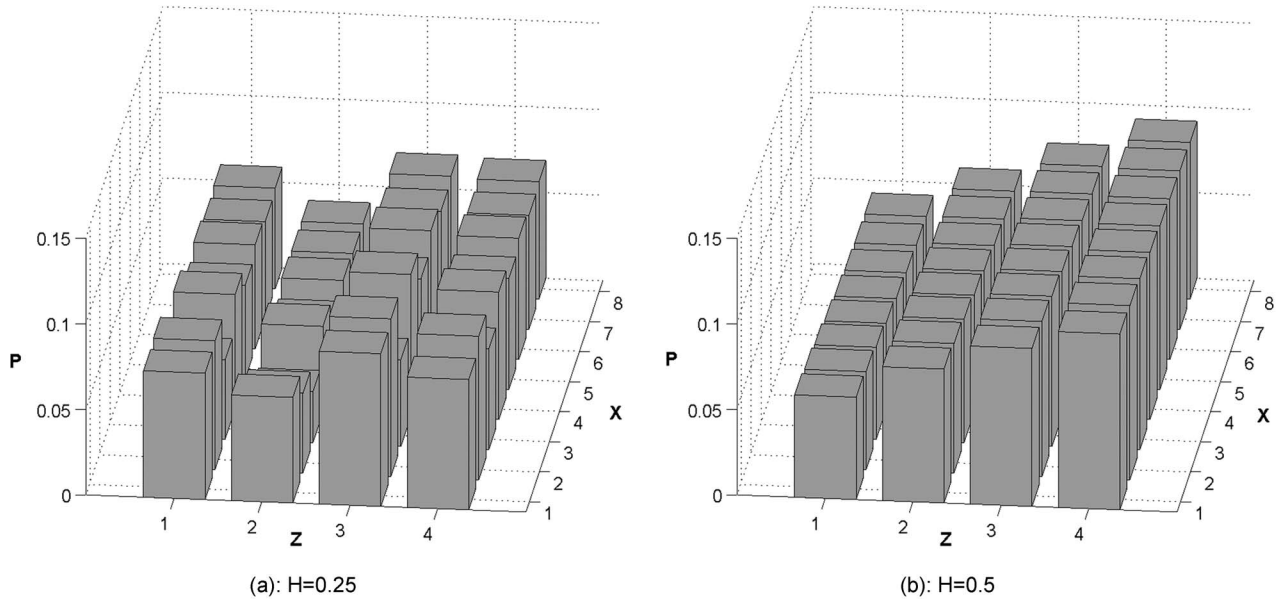

Fig. 9 Heater power distribution at $t=4$ hr, Tikhonov order 1: regularization parameters $\lambda=0.2$; $L=L_1$; $T_{ref}=1000$ K; average design surface dimensionless temperature: (*a*) $\bar{\theta}=0.460$ and (*b*) $\bar{\theta}=0.4599\pm0.0006$

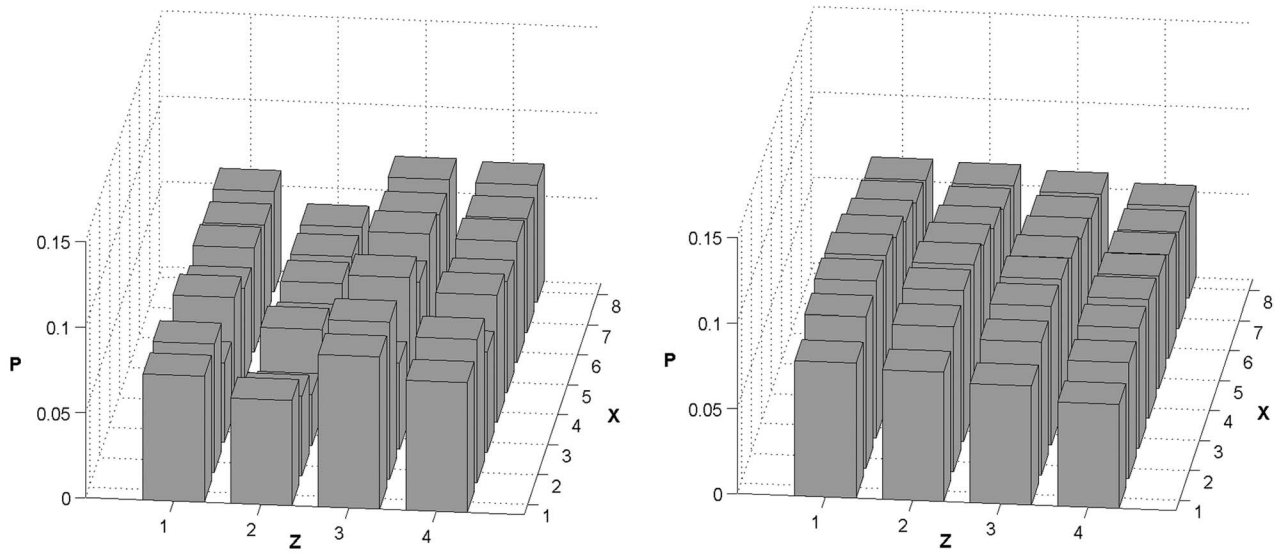

(*a*) H=0.25 (*b*) H=0.5

Fig. 10 Heater power distribution at t=4 hr, CG Method: iterative step: I=2; T_{ref}=1000 K; average design surface dimensionless temperature: (*a*) $\bar{\theta}$=0.460 and (*b*) $\bar{\theta}$=0.4599±0.0007

requires a different number of CGR steps from the previous time step, causing a major change in the heater power input distribution.

Concluding Remarks

This paper presented five techniques for solving the ill-posed problems that arises from the inverse design of radiant enclosures. Three of these techniques are based on regularization methods, which solve the ill-posed problem explicitly, whereas the remaining two are optimization-based methods, which solve the ill-posed problem in its implicit form. All of these techniques predicted solutions that are within acceptable accuracy. Each solution was verified by taking the predicted heater inputs from the inverse solution, using this distribution as a boundary condition in the forward solution and verifying that the predicted temperatures on the uniform-flux design surface matched the required temperature. The average temperature values on the design surface were within an average of <6 K from the target temperatures at all times throughout the process, and the standard deviation of the temperatures on the design surface around the average were within 8 K, which is an acceptable tolerance for most applications. However, the characteristics of the methods used for predicting the required heater power inputs in some cases provide widely different distributions that achieve the same final result, which is characteristic of solutions to inverse problems.

It was found that the regularization methods provided smooth distributions of heater inputs across the heater surface, whereas the optimization techniques gave uneven distributions. The optimization methods lend themselves to predictions that allow a reduction in the number of required heaters, however, in that some heaters were not active at any time throughout the process; on the other hand, the solutions obtained using the regularization meth-

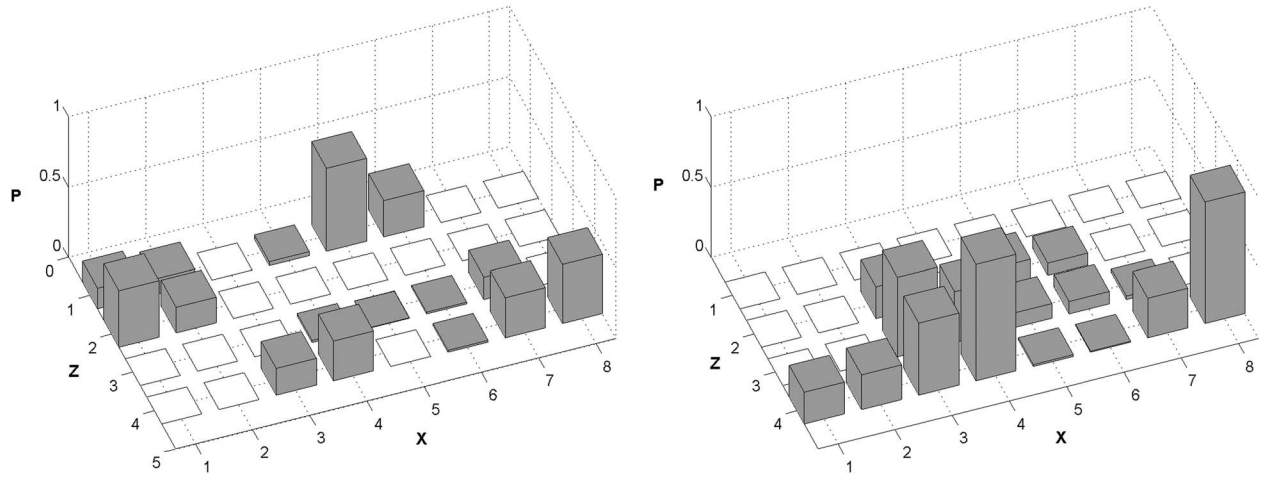

(*a*) H=0.25 (*b*) H=0.5

Fig. 11 Heater power distribution at t=4 hr, quasi-Newton minimization: T_{ref}=1000 K; average design surface dimensionless temperature: (*a*) $\bar{\theta}$=0.4603±0.0022 and (*b*) $\bar{\theta}$=0.4600±0.0018

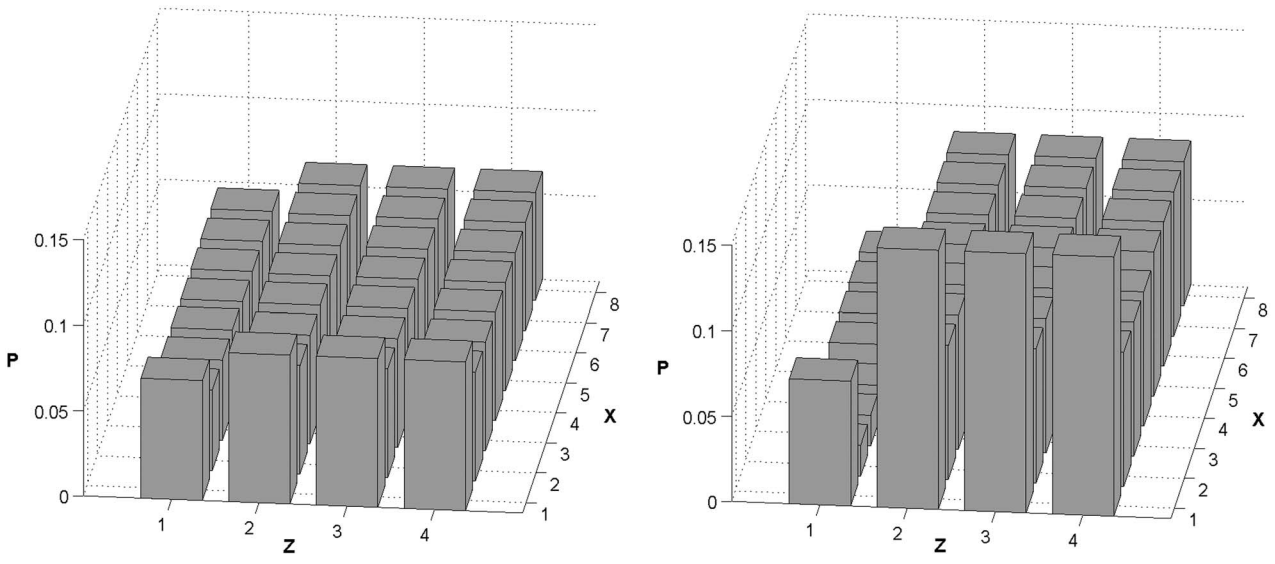

Fig. 12 Heater power distribution at $t=4$ hr, simulated annealing method: $T_{ref}=1000$ K; average design surface dimensionless temperature: (*a*) $\bar{\theta}=0.4601\pm0.0001$ and (*b*) $\bar{\theta}=0.4602\pm0.0001$

ods generally had all heaters active at lower power levels. Control of the heaters with time during the transient could be quite challenging, in that each heater requires different continually varying energy inputs.

The regularization methods gave very similar results. The conjugate gradient regularization method usually gives good results in less computer time and with less storage requirements than TSVD or the Tikhonov method, whereas the TSVD approach can be time consuming when large arrays (many heaters) are treated. However, the singular values obtained by the TSVD approach provide good insight into whether a particular design will be easy to attain or potentially will have large errors or erratic solutions. The designer has more control over the degree of regularization in the Tikhonov approach compared to TSVD and conjugate gradient since the regularization parameter in the former can be varied continuously, whereas those of the other two methods can only assume integer values. The drawback, unfortunately, is that some experience is required on the part of the designer to choose the correct Tikhonov smoothing function and regularization parameter to attain an acceptable solution.

The optimization methods also gave good results and have the advantage that constraints such as limiting heater inputs to nonnegative values can be imposed a priori. However, the resulting solutions can be quite irregular in the predicted heater inputs. Although these solutions are physically correct in that they provide accurate design surface conditions, the heater inputs may be difficult to implement in a practical system.

Although the obvious application of these methods is to size heaters when designing a furnace for a particular application, they can also be incorporated into feedback algorithms, which control the heaters during furnace operation. Active control of the heaters is usually necessary because some assumptions used in the radiative transfer model deviate from physical reality, and accordingly the actual conditions achieved over the design surface will differ from those predicted by the model. For example, although some directional characteristics of the surface reflectivities are included in the model, real surfaces will have more complex directional characteristics that will usually be unavailable to the designer. In Ref. [23], an artificial neural network was used with the conjugate gradient regularization to demonstrate applications to feedback control, and this approach could be used with any of the predictive techniques. Furthermore, an initial inverse design using the methods described here can greatly reduce the complexity and increase the reliability of the necessary control system, as the design should produce characteristics close to those for the final system.

Nomenclature

$\mathbf{A}$ = matrix of coefficients
A = area, m^2
$\boldsymbol{b}$ = vector of known coefficients
$\mathbf{B}$ = approximate Hessian matrix
c = specific heat, J/kg K
$c_j(\mathbf{\Phi},t)$ = design constraints
C_S = $(\varepsilon_{DS}/\varepsilon_S)(\rho c\delta)_S/(\rho c\delta)_{DS}$
E = emissive power, $\varepsilon\sigma T^4$, W/m^2
$F(\mathbf{\Phi})$ = objective function to be minimized
$\tilde{F}$ = exchange factor, fraction of emitted energy from a surface that is absorbed by another surface considering all possible intermediate reflection paths
H = height of enclosure, m
k = thermal conductivity, W/m K
$\mathbf{L}$ = derivative operator, Eq. (3)
N = number of points or increments
$\boldsymbol{p}$ = search direction
p = number of retained singular values
p'' = heater input power per unit surface area, W/m^2
P = heater power, $p''/\sigma T_{ref}^4$
q = energy flux normal to surface element, W/m^2
$\boldsymbol{r}$ = residual vector
$\mathbf{S}$ = matrix of singular values
T = absolute temperature, K
t = time, s
u = location along enclosure boundary, m
$\mathbf{U},\mathbf{V}$ = orthogonal matrices
W = width of enclosure, m
$\boldsymbol{x}$ = solution vector
x = location along design surface, m

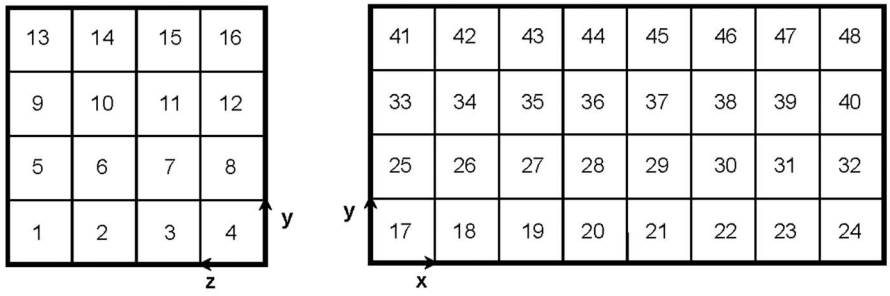

(*a*) Surface 3 (End surface)

(*b*) Surface 4 (Long adiabatic side)

(*c*) Surface 5 (Heaters, top surface)

(*d*) Surfaces 6*a* (gray, design surface) and 6*b* (unshaded, adiabatic portion of bottom surface

Fig. 13 Element numbering on enclosure surfaces

Greek Symbols

α = optimization step size, Eq. (3)
δ = thickness of surface element, m
ε = surface emissivity
θ = T/T_{ref}
$\mathbf{\Phi}$ = set of design parameters
λ = Tikhonov regularization parameter
ρ = density, kg/m^3
ρ_d = diffuse component of reflectivity
ρ_s = specular component of reflectivity
σ = Stefan-Boltzmann constant; $5.67\times10^{-8}\ \text{W/m}^2\,\text{K}$
τ = dimensionless time, $\varepsilon_{\text{DS}}\sigma T_{\text{ref}}^3/(\rho c\delta)_{\text{DS}}t$
ψ = $q/\sigma T_{\text{ref}}^4$

Superscripts and Subscripts

b = blackbody
cond = conduction
DS = design surface
HS = heater surface
WS = adiabatic wall surface
i,j = surface element index
k = iteration number, time increment index
rad = radiation
ref = reference value

Appendix

The element numbering system is given in Fig. 13. The exchange factors were computed using 10^7 Monte Carlo bundles per emitting surface and are accurate to within 0.00005, which is a conservative error estimate based on the difference between the smoothed and unsmoothed set.

The complete file can be downloaded from http://www.me.utexas.edu/~me339/Exchangefactors.xls. Exchange factors are provided for both the $1\times0.5\times2$ and $1\times0.25\times2$ enclosures. Both the raw factors and factors smoothed using the smoothing algorithm of [18] are provided.

References

[1] Alifanov, O. M., 1994, *Inverse Heat Transfer Problems*, Springer, Berlin.
[2] Alifanov, O. M., Artyukhin, E. A., and Rumyantsev, S. V., 1995, *Extreme Methods for Solving Ill-Posed Problems with Applications to Inverse Heat Transfer Problems*, Begell House, New York.

[3] Beck, J. V., Blackwell, B., and St. Clair, Jr., C. R., 1995, *Inverse Heat Conduction: Ill-Posed Problems*, Wiley, New York.
[4] Özişik, M. N., and Orlande, H. R. B., 2000, *Inverse Heat Transfer: Fundamentals and Applications*, Taylor and Francis, New York.
[5] Tikhonov, A. N., 1963, "Solution of Incorrectly Formulated Problems and the Regularization Method," Sov. Math. Dokl., **4**, pp. 1035–1038 (Engl. trans., Dokl. Akad. Nauk SSSR, **151**, pp. 501–504, 1963).
[6] França, F. H. R., Howell, J. R., Ezekoye, O. A., and Morales, J. C., 2002, "Inverse Design of Thermal Systems," *Advances in Heat Transfer*, J. P. Hartnett and T. F. Irvine, eds., Elsevier, New York, Vol. 36, Chap. 1, pp. 1–110.
[7] Daun, K. J., Ertürk, H., and Howell, J. R., 2003, "Inverse Design Methods for High-Temperature Systems," Arabian J. Sci. Tech., **27**(2C), pp. 3–48.
[8] França, F. H. R., Ezekoye, O. A., and Howell, J. R., 2001, "Inverse Boundary Design Combining Radiation and Convection Heat Transfer," ASME J. Heat Transfer, **123**(5), pp. 884–891.
[9] Daun, K. J., Ertürk, H., Gamba, M., Hosseini Sarvari, M., and Howell, J. R., 2003, "The Use of Inverse Methods for the Design and Control of Radiant Sources," JSME Int. J., Ser. B, **46**(4), pp. 470–478.
[10] Daun, K. J., and Howell, J. R., 2005, "Inverse Design Methods for Radiative Transfer Systems," J. Quant. Spectrosc. Radiat. Transf., **93**, pp. 43–60.
[11] Gamba, M., Pavy, T., and Howell, J. R., 2003, "Inverse Methods for Design and Control of Thermal Systems: Validation in a 2-D Visible Light Enclosure," *Proc. 2003 IMECE*, Washington, DC, ASME, New York, Paper IMECE-42987.
[12] Gamba, M., Erturk, H., Ezekoye, O. A., and Howell, J. R., 2002, "Modeling of a Radiative RTP-Type Production Furnace Through Inverse Design: Mathematical Model and Experimental Results," *Proc. 2002 IMECE*, New Orleans, ASME, New York, Vol. 1.
[13] Press, W. H., Teukolsky, S. A., Vetterling, W. T., and Flannery, B. P., 1992, *Numerical Recipes*, Cambridge University Press, Cambridge, England.
[14] Hansen, P. C., 1998, *Rank-Deficient and Discrete Ill-Posed Problems: Numerical Aspects of Linear Inversion*, SIAM, Philadelphia.
[15] Beckman, F. S., 1960, "The Solution of Linear Equations by the Conjugate Gradient Method," *Mathematical Methods For Digital Computers*, A. Ralston and H. S. Wilf, eds., Wiley, New York, pp. 62–72.
[16] Bertsekas, D. P., 1999, *Nonlinear Programming*, 2nd ed., Athena Scientific, Belmont, MA.
[17] Metropolis, N., Rosenbluth, A., Rosenbluth, M., Teller, A., and Teller, E., 1953, "Equation of State Calculations by Fast Computing Machines," J. Chem. Phys., **21**, pp. 1087–1090.
[18] Daun, K. J., Morton, D. P., and Howell, J. R., 2005, "Smoothing Monte Carlo Exchange Factors Through Constrained Maximum Likelihood Estimation," ASME J. Heat Transfer, **127**(10), pp. 1124–1128.
[19] Howell, J. R., and Daun, K. J., 2004, "Inverse Design in Thermal Radiation Problems," Proc. Inverse Problems, Design, and Optimization Symposium, Rio de Janeiro, Brazil, March.
[20] Corana, A., Marchesi, M., Martini, C., and Ridella, S., 1987, "Minimizing Multimodal Functions of Continuous Variables With the 'Simulated Annealing Algorithm'," ACM Trans. Math. Softw., **13**, pp. 262–280.
[21] Goffe, W. L., Ferrier, G., and Rogers, J., 1994, "Global Optimization of Statistical Functions With Simulated Annealing," J. Econometr., **60**(1/2), pp. 65–100.
[22] Ertürk, H., Ezekoye, O. A., and Howell, J. R., 2002, "The Application of an Inverse Formulation in the Design of Boundary Conditions for Transient Radiating Enclosures," ASME J. Heat Transfer, **124**(6), pp. 1095–1102.
[23] Ertürk, H., Ezekoye, O. A., and Howell, J. R., 2002, "The Use of Inverse Formulation in Design and Control of Transient Thermal Systems," *Heat Transfer 2002: Proc. International Heat Transfer Conf.*, Grenoble, Taine, J., ed. (CDRom Version), pp. 729–734.

Heat Transfer Augmentation by Ion Injection in an Annular Duct

Walter Grassi
e-mail: w.grassi@ing.unipi.it

Daniele Testi
e-mail: d.testi@ing.unipi.it

LOTHAR (LOw gravity and THermal Advanced Research Laboratory),
Department of Energetics,
"L. Poggi," University of Pisa,
via Diotisalvi 2, 56126 Pisa, Italy

The thermofluid-dynamic effects of ion injection from sharp metallic points added perpendicularly to the inner wire of a short horizontal annulus were experimentally investigated. A dielectric liquid (FC-72 by 3M) was weakly forced to flow in the duct, which was uniformly heated on the outer wall. A dc voltage as high as 22 kV *was applied to the inner electrode, while the heated wall was grounded. Both the laminar and the turbulent mixed-convection regimes were obtained, varying the imposed flow rate. Once an electric field is applied, the flow is dramatically modified by the jets of charged particles, which transfer their momentum to the neutral adjacent ones. Different injection strengths were obtained on the emitters, because the shape of the point tips was not controlled at the microscale. Nusselt number distributions were obtained azimuthally and longitudinally, monitoring the wall temperatures. In all cases, heat transfer turned out greatly enhanced in the proximity of the emitters, without a significant increase in pressure drop through the test section and with a negligible Joule heating, making this technique very attractive for application in compact heat exchangers.* [DOI: 10.1115/1.2150838]

Keywords: EHD, heat transfer enhancement, ion injection, mixed convection

Background

The work presented herein is part of a broader research aimed at the design of an electrohydrodynamic (EHD) high efficiency cold plate for space applications. Cold plates are contact-type compact heat exchangers, developed for electronic equipment and payload thermal control, which remove the generated heat by a fluid cooling loop. Typically, a weakly forced flow ($\mathrm{Re} \approx 10^3$) is needed to provide the necessary heat sink performance [1]. EHD enhanced heat transfer rates would result in a diminished pumping power or in a more compact structure for the cold plate.

Theoretical Aspects. For the sake of clarity, we briefly summarize the main theoretical aspects related to the matter dealt with in the following. In the presence of an electric field, a body force arises in a dielectric medium, given by:

$$\boldsymbol{f}_E = \rho_E \boldsymbol{E} - \frac{1}{2} E^2 \nabla \varepsilon + \frac{1}{2} \nabla \left[\rho E^2 \left(\frac{\partial \varepsilon}{\partial \rho} \right)_T \right] \tag{1}$$

We generally refer to the first RHS term as the electrophoretic component, which is the Coulomb force exerted by an electric field upon the free charge present in the medium, with density ρ_E. The second term represents the dielectrophoretic body force, which is related to a local change of fluid permittivity in an electric field. The third term, called electrostriction, acts on the dielectric in a nonuniform electric field. The last two forces act on polarization charges. In order to solve an EHD problem, one needs to insert $\boldsymbol{f}_E$ in the momentum equation among the external forces. Besides, the complete set of Maxwell equations, together with free charge continuity, is required in addition to the mass, momentum, and energy balances.

Taking the curl of the momentum equation, one obtains the vorticity ($\boldsymbol{\omega} = \nabla \wedge \boldsymbol{u}$) balance. This relation is particularly useful, since it clearly shows which conditions lead to a rotational, convective motion. In the Boussinesq approximation [2], we have calculated [3]:

$$\frac{d\boldsymbol{\omega}}{dt} = \boldsymbol{\omega} \cdot \nabla \boldsymbol{u} + \nu \nabla^2 \boldsymbol{\omega} + \left(\beta \boldsymbol{g} + \frac{\varepsilon \beta_\varepsilon \nabla E^2}{2\rho} \right) \wedge \nabla T + \frac{\nabla \rho_E \wedge \boldsymbol{E}}{\rho} \tag{2}$$

where

$$\frac{d}{dt} = \frac{\partial}{\partial t} + \boldsymbol{u} \cdot \nabla$$

is the Lagrange derivative, calculated on the path of the fluid particle, and

$$\beta_\varepsilon = -\frac{1}{\varepsilon} \left(\frac{\partial \varepsilon}{\partial T} \right)_p$$

is the temperature coefficient of electrical permittivity.

The electrostrictive component in Eq. (1) cannot produce a vortical flow, while dielectrophoresis needs both a temperature gradient and a non-uniform electric field. A free charge gradient instead is necessary for the Coulomb force to generate vorticity. Although free charge can be created in the fluid by temperature gradients, which induce electrical conductivity gradients, in the presence of a sharp electrode and at dc electric fields as high as 10^7 V/m, the main mechanism responsible for free charge building up in a liquid is ion injection at the electrode/liquid interface via electrochemical reactions [4,5].

The injected charges are homocharges [6], i.e., of the same polarity as the injecting electrode, to which we generally refer as the emitter. This phenomenon most often occurs at the sharper electrode and is mainly controlled by the high field electrochemistry of the interface, which critically depends on the chemical nature of the dielectric fluid and on the shape (radius of curvature), composition, and polarity of the electrode.

The injected space charge is driven by the Coulomb force towards the facing electrode, while dragging the fluid neutral molecules and giving rise to a jetlike motion [7]. When this jet impinges on a heat transfer surface, heat transfer coefficients are hugely enhanced [8]. It has been shown that the thermofluid-dynamic characteristics of the EHD-induced liquid flow are analogous to those of submerged impinging jets, with the injecting electrode considered as the nozzle [9].

An order of magnitude of the velocities induced in the bulk of

Contributed by the Heat Transfer Division of ASME for publication in the JOURNAL OF HEAT TRANSFER. Manuscript received January 21, 2005; final manuscript received August 23, 2005. Review conducted by John H. Lienhard V. Paper presented at the 2004 ASME Heat Transfer/Fluids Engineering Summer Conference (HTFED2004), July 11, 2004–July 15, 2004, Charlotte, North Carolina, USA.

the fluid can be obtained assuming that the electrostatic energy present in the proximity of the sharp electrode is converted into kinetic energy of the accelerated particles:

$$\frac{1}{2}\rho u^2 \approx \frac{1}{2}\varepsilon E^2 \Rightarrow \frac{u}{E} \approx \sqrt{\frac{\varepsilon}{\rho}} \tag{3}$$

Higher heat transfer enhancements by ion injection can be obtained with fluids of low viscosity and low electrical conductivity [10]. In fact, an increased viscosity of the fluid delays the onset of the electrohydrodynamic motion and the concurrent strong charge injection. Besides, with a high electrical conductivity, the charges in the liquid cross the space between the electrodes before thoroughly transferring their momentum to the fluid. This lack of momentum transfer decreases the induced velocity and thus the heat transfer augmentation.

Brief Review of Past Results. Notable results from past studies on single-phase forced convection heat transfer enhancement by the ion-drag mechanism will be shortly listed hereafter, in chronological order. Most of them are more deeply reviewed in [11].

In 1970, Porter and Poulter [12] studied EHD laminar convection of transformer oil in an annulus, enhancing heat transfer of 1.9 times by the ion-injection process. A corresponding pressure drop increase was also reported.

In 1976, Mizushina et al. [13] obtained an increase of both heat transfer coefficients (up to 2.5 times) and friction factors, with air flowing in an annulus in the laminar regime.

In 1979, Velkoff and Godfrey [14] analyzed a low-velocity airflow along a heated flat plate, obtaining a heat transfer enhancement of 3.5 times, together with a friction factor augmentation. The injecting electrodes were an array of fine wires, positioned in parallel with the main flow.

In 1987, Fernández and Poulter [15] tested a high-Prandtl number dielectric oil (Shell Diala "B") flowing in an annular duct in the laminar regime. The result was a heat transfer enhancement up to 2000%, with a threefold pressure-drop augmentation and a Joule dissipation lower than 1 W.

In 1989, Fujino et al. [16] studied the effect of the electric field in a laminar flow of R113 within two parallel plates, reporting a sevenfold heat transfer enhancement as the maximum value achieved, when a trace amount of an electrolyte solution was added to the working fluid. The sum of pumping power and electrical power consumed in the test section was less than 1% of the imposed heat flow.

In 1991, Ohadi et al. [17] examined the turbulent flow of air in a circular duct, with two high-voltage thin wire electrodes placed longitudinally in the proximity of the pipe axis, obtaining a heat transfer augmentation of 2.6.

In 1997, Hasegawa et al. [18] performed a numerical analysis of EHD-enhanced forced convection in a rectangular tube with a large aspect ratio, at Re=1470 and with "Freonsolve" (in weight, 96% of R113 and 4% of ethyl alcohol) as the test fluid. The numerical results showed that the heat transfer enhancement, produced by four longitudinal high-voltage wire electrodes placed within the channel, was four times larger than the pressure drop increase.

In 2000, Molki et al. [19] documented a numerical and experimental investigation of airflow in a square duct, with the high-voltage electrode situated at the centerline along the channel axis. The heat transfer rate at most increased by a factor 2 in the entry-region and by a factor 3.4 for the fully-developed flow. Owing to the EHD-induced motion, turbulence was taken into account even at Re=500.

In 2005, Grassi et al. [20] examined the flow of a fluorocarbon (FC-72) in a vertical annulus, under the regime of turbulent aided mixed convection. Heat transfer was augmented up to five times, with a negligible power input. Ions were injected by point electrodes fixed perpendicularly to the inner wire, along its length.

Table 1 FC-72 physical properties at 25°C (by courtesy of 3 M)

chemical formula	C_6F_{14}
electrical resistivity	$10^{13}\ \Omega\,m$
dielectric strength	$1.5\times10^{7}\ V\,m^{-1}$
relative permittivity	1.75
boiling point (at 1 bar)	56°C
density	$1.68\times10^{3}\ kg\,m^{-3}$
kinematic viscosity	$3.8\times10^{-7}\ m^2\,s^{-1}$
specific heat	$1.1\times10^{3}\ J\,kg^{-1}\,K^{-1}$
thermal conductivity	$5.7\times10^{-2}\ W\,m^{-1}\,K^{-1}$
coefficient of expansion	$1.56\times10^{-3}\ K^{-1}$

Experimental Apparatus

In this work we examine the effect of a dc electric field on developing mixed convection in a heated horizontal annulus with sharp points added to the inner electrode. In the absence of the electric field, according to the map proposed by Metais and Eckert [21], the transition from the laminar to the turbulent regime occurs in the Reynolds number range 700–1000. It is reasonable to expect the transition to be anticipated even more in the EHD case, having added a cause of instability [22].

The Working Fluid. The dielectric fluid chosen for the experimental campaign is the Fluorinert™ Electronic Liquid FC-72 (manufactured by 3 M, St. Paul, MN). FC-72 is thermally and chemically stable, compatible with sensitive materials, nonflammable, nontoxic, colorless, and has no ozone depletion potential. This valuable combination of properties makes FC-72 suitable even for the strict safety specifications needed in space applications. The physical properties of the fluid at 25°C are reported in Table 1.

Polar molecules either have a high intrinsic conductivity due to self-dissociation or are very sensitive to impurities, being good solvents. In fact, for a small increase of relative electrical permittivity around the value of 2, the resistivity can drop of many orders of magnitude [23] and Joule heating losses in the dielectric could become relevant at high applied voltages. For this reason we chose a nonpolar fluid as FC-72, with extremely low electrical conductivity.

Furthermore, the low viscosity of FC-72 is very attractive for an EHD heat exchanger, not only because of the already mentioned high efficiency of the ion-injection process, but also from a purely hydraulic point of view. In fact, in a pipe of length L and cross section area A, the pumping power needed to compensate for pressure drop can be expressed as:

$$\Pi_P = \dot{V}\Delta p = \frac{1}{2}\rho A u^3 f\frac{L}{D_h} \tag{4}$$

At a given Reynolds number, Eq. (4) can be replaced by:

$$\Pi_P = \frac{1}{2}\rho A\frac{\mathrm{Re}^3\,\nu^3}{D_h^3}f\frac{L}{D_h} = \chi\rho\nu^3 \tag{5}$$

being χ dependent only on geometrical parameters and on the Reynolds number. Thus, it must be taken into account that a reduction in viscosity can greatly diminish the pumping power needed for the fluid loop of the heat exchanger.

Description of the Apparatus. A test loop was built as shown in the schematic of Fig. 1. The fluid, moved by a gear pump, circulated through the test specimen at volumetric flow rates in the range 0.10–2.25 l/min. A flowmeter measured the flow rate with an accuracy of ±0.0086 l/min. The fluid, uniformly heated in its flow along the test section, was cooled to the desired inlet temperature by means of a shell-tube heat exchanger, with countercurrent chilled water flowing in the shell. The annular test specimen was connected with a 0–30 kV dc reversible polarity high

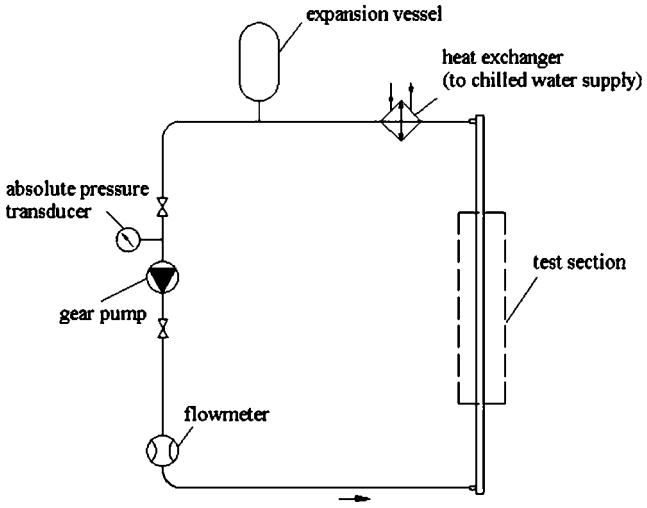

Fig. 1 Schematic of the test loop

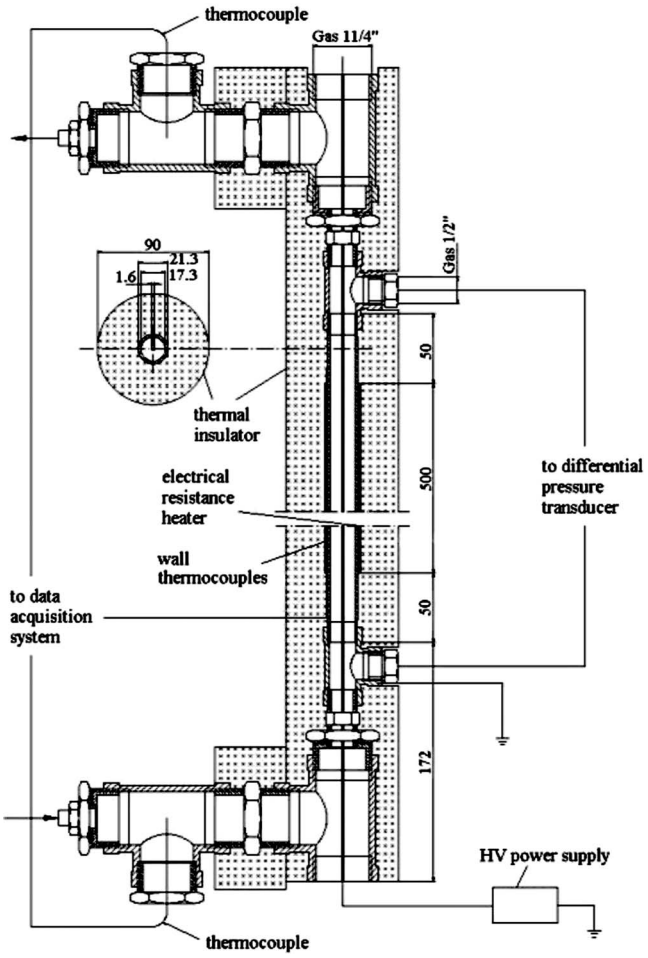

Fig. 2 Detail of the EHD test section

voltage power supply. An expansion vessel was used to compensate the volume increase in the loop due to temperature variations and to set the pressure of the position it was mounted on. An absolute pressure transducer was placed right upstream of the gear pump, in order to check that the lowest pressure of the loop was above the room pressure, thus avoiding air from being sucked in by the pump. All the tests were performed at an absolute pressure of about 2 bars.

A detailed schematic of the test section is shown in Fig. 2. The inner wire, of diameter $d=1.6$ mm, was made of stainless steel. The outer electrode, also made of stainless steel, had an inner diameter $D=17$ mm and a wall thickness $s=2$ mm. The fluid was warmed up by an electrical resistance heater applied to the outer wall for a length $L_h=50$ cm. 20 thermocouples were placed on the outer wall, under the heater, at five cross sections, 12.5 cm apart along the heated length. Each section had four thermocouples, one every 90 deg. To minimize heat losses, the entire specimen was covered with a 34 mm thick thermal insulator ($\lambda=0.038$ W m^{-1} K^{-1}). Two more thermocouples were placed at the fluid inlet and outlet, to evaluate the heat flow supplied to the test section in steady state through the energy balance:

$$\Pi_h = \dot{m} c_p (T_{\text{out}} - T_{\text{in}}) \tag{6}$$

having assumed that the electrically generated heat within the fluid is negligible, since the currents measured in the experimental campaign were in the order of 10^{-7} A.

All the thermocouples were type-T and used a zero-point reference cell, whose temperature was controlled by a reference resistance thermometer. The overall accuracy of each thermocouple after calibration in the 15–60°C range was ±0.2 K.

A differential pressure transducer measured the pressure drop through the test section. At the application of the electric field, we could not appreciate order of magnitude variations in the pressure drop, with measured values below 10 Pa.

Metallic points were welded perpendicularly to the inner electrode by means of a silver alloy. The points were simply tin-coated copper wires, of diameter 0.6 mm and length 4 mm, cut at the tip. The shapes and the radii of curvature of the point tips were not controlled at the microscale and may have differed from each other significantly.

In a first series of tests, to which we shall refer as configuration 1, two opposite points were fixed in the horizontal direction and moved from 11 cm upstream to 6 cm downstream of the midway section, which we will call Sec. C. Further tests (configuration 2) were conducted with two opposite points positioned in the vertical direction at one quarter of the heated length (Sec. B) and four points, one every 90 deg, at three quarters of L_h (Sec. D), as illustrated in Fig. 3.

Test Procedure and Data Analysis. In a preliminary operation, we tested the dielectric strength of the medium. Slowly increasing the applied voltage, we observed that electrical breakdown occurred at 24 kV. Therefore, we decided to safely operate at $HV=22$ kV and chose to use the positive polarity, which gave stable ionic currents.

Every test was run under constant volumetric flow rate and heat flow and a steady state condition in the presence of the electric field was awaited. The thermocouples' signals were acquired every 6 s by a scanner mounted on a digital multimeter (Model 2000, manufactured by *Keithley*, Cleveland, OH); then the data were sent to a PC in order to be recorded and processed by the software Labview™ (a trademark of National Instruments, Austin, TX), using Matlab® (a registered product of The MathWorks,

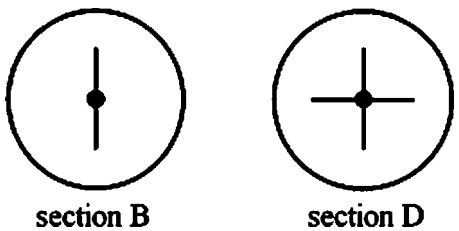

Fig. 3 Position of the points in configuration 2

Natick, MA) as the interface for mathematical calculations.

The bulk temperature of the fluid at a given axial position was calculated considering a temperature of adiabatic mixing for the examined cross section, assuming a linear trend, from the inlet to the outlet temperature, on the heated length. The temperatures of the inner side of the wall were obtained from the ones measured on the outer side, properly accounting for one-dimensional heat conduction within the wall thickness:

$$T_{w\_in} = T_{w\_out} - \frac{\Pi_h}{2\pi\Lambda L_h} \ln\left(\frac{D+2s}{D}\right) \tag{7}$$

The dimensionless numbers describing mixed convection in uniform heat flux conditions (i.e., Nu, Re, and Gr_h) were calculated as:

$$\begin{cases} \mathrm{Nu} = \dfrac{\alpha D_h}{\lambda_f} = \dfrac{qD_h}{\lambda_f(T_{w\_in} - T_b)} = \dfrac{\Pi_h}{\lambda_f(T_{w\_in} - T_b)\pi L_h} \\ \mathrm{Re} = \dfrac{u\rho_{in}D_h}{\eta_{in}} = \dfrac{4\dot{V}}{\pi(D+d)\nu_{in}} \\ \mathrm{Gr}_h = \mathrm{Gr\,Nu} = \dfrac{\beta_f g q D_h^4}{\lambda_f \nu_f^2} = \dfrac{\beta_f g \Pi_h D_h^3}{\lambda_f \nu_f^2 \pi L_h} \end{cases} \tag{8}$$

The relative errors on the derived parameters, er_F, were evaluated by the propagation law:

$$\mathrm{er}_F = \sqrt{\sum_i \left[\frac{x_i}{F(x_i)} \cdot \frac{\partial F(x_i)}{\partial x_i} \cdot \mathrm{er}_{x_i}\right]^2} \tag{9}$$

where F is the parameter depending on the variables x_i, which are measured with a known relative error, er_{x_i}, calculated by means of the above-mentioned accuracies.

The maximum relative error on the Nusselt number, corresponding to the highest heat transfer rate and the lowest heat flow, was 10.5%, while the maximum error on the Reynolds number, obtained at the lowest flow rate, was 8.6%. As for Gr_h, the highest error was 16.8%, obtained at the lowest temperature increase through the test specimen, which means at the highest flow rate and the lowest heat flow.

In any case, the fluid temperatures in correspondence of the inner side of the heated wall were fairly below the boiling point, never exceeding 50°C.

Discussion of Heat Transfer Results

The Nusselt number values reported hereafter represent the average of 20 measurements, recorded consecutively once a steady state condition at $HV=22$ kV was reached.

In configuration 1, the Nusselt number was monitored by the thermocouples positioned in Sec. C and the two opposite, horizontal points were moved from 11 cm upstream to 6 cm downstream. The same results could reasonably be obtained by keeping the points fixed in Sec. C and moving the thermocouples along the wall in the axial direction. Thus, a surface distribution of the Nusselt number was obtained, interpreting the coordinate ξ as the thermocouple's position on the heated wall with respect to the point, made dimensionless by means of the hydraulic diameter.

From the distribution of Fig. 4, obtained at $Re=2220$ and $Gr_h = 1.40\times10^8$, we deduce that the point directed towards the left side of the pipe works much better than the one on the right-hand side. This is not surprising, because the strength of the ion injection depends critically on the curvature of the point tip, which was not controlled at the microscale. A schematic drawing of the asperities generated by the cut at the point tip, as observed under the microscope, is shown in Fig. 5.

As a confirmation that the higher Nusselt numbers on the left side are due to a sharper point, we rotated the inner electrode of 180 deg and we observed symmetrically high Nu on the opposite side.

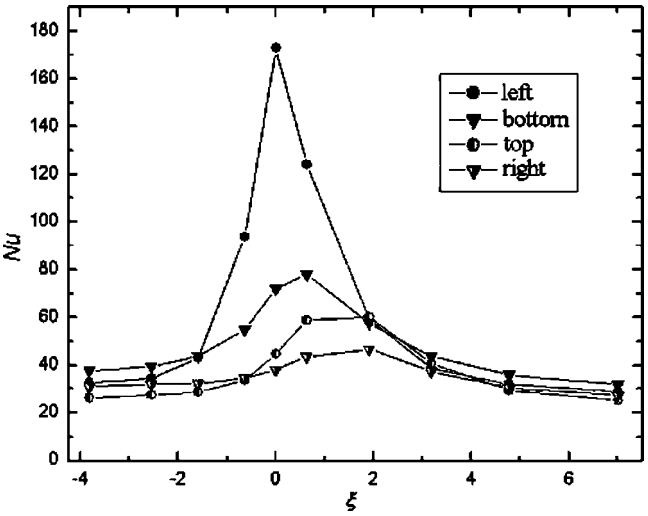

Fig. 4 Nu distribution at Re=2220 and $Gr_h=1.40\times10^8$

Figure 4 also shows that heat transfer on the bottom of the heated surface is higher than on the top, which is coherent with the fact that the bottom is helped by buoyancy forces in removing hot fluid from its surface. The heat transfer enhancement effect fades while going away from Sec. C and almost vanishes at about 5 hydraulic diameters downstream and 2 D_h upstream of the emitters.

In Fig. 4, as well as in the following figures reporting the experimental results as a function of the longitudinal coordinate, the values obtained in the absence of the electric field can be read at $\xi=7$. In fact, at this downstream dimensionless distance from the point, ion injection is no more effective in the examined Reynolds number range.

The maximum values of the Nusselt number move downstream, from $\xi=0$ on the left-hand side to $\xi\approx2$ on the right-hand side. A possible fluid-dynamical explanation could be the following (see Fig. 6): the strong jet directed on the left side turns around the circular wall while being moved downstream by the main forced flow, reaching the farther sides with weakened intensity (the dynamics of a jet under the effect of a cross-flow is analyzed, for instance, in [24]).

Coherently with the above interpretation, as Fig. 7 shows, at a lower Reynolds number ($Re=740$), the maxima lie closer to Sec. C, from $\xi=0$ on the left-hand side to less than $\xi=1$ on the opposite one.

Fig. 5 Drawing of the microasperities at the point tip

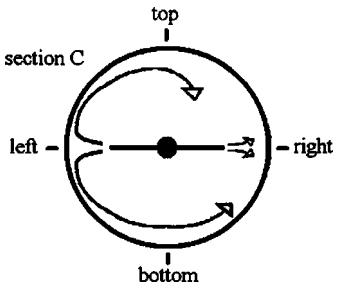

Fig. 6 Presumed dynamics of the jets from the points in configuration 1

Again, heat transfer is higher on the bottom than on the top. The enhancement effect, with a weaker main flow, almost vanishes more upstream ($\xi \approx -3$) and less downstream ($\xi \approx 4$) than before.

The Nusselt number distribution appears slightly influenced by a change in the wall heat flux. Figure 8 shows negligible Nu variations passing from $Gr_h = 1.40 \times 10^8$ to $Gr_h = 2.47 \times 10^8$.

The Nusselt number was azimuthally averaged and its distribution was plotted in Fig. 9 at three different Re. In this range, higher Reynolds numbers entail higher heat transfer rates.

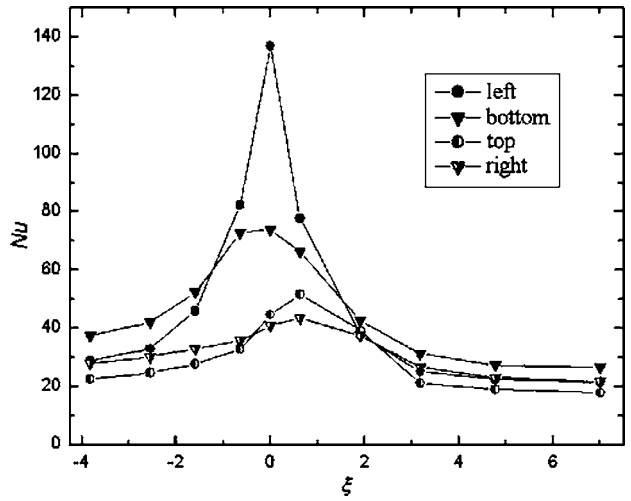

Fig. 7 Nu distribution at Re=740 and $Gr_h = 1.40 \times 10^8$

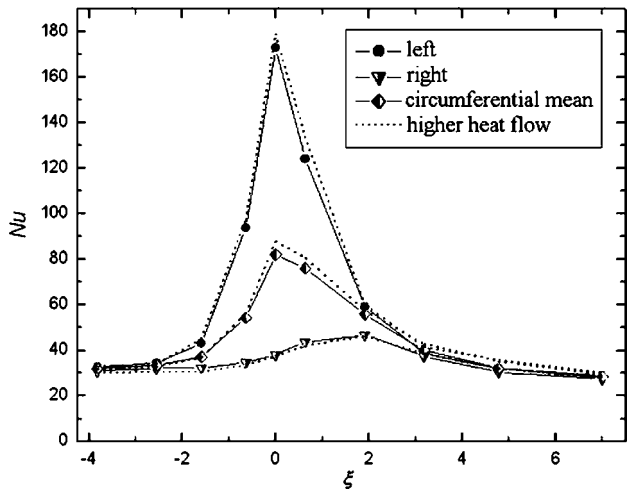

Fig. 8 Nu vs ξ at Re=2220 and $Gr_h = 1.40 \times 10^8$ and $Gr_h = 2.47 \times 10^8$ (dotted curves)

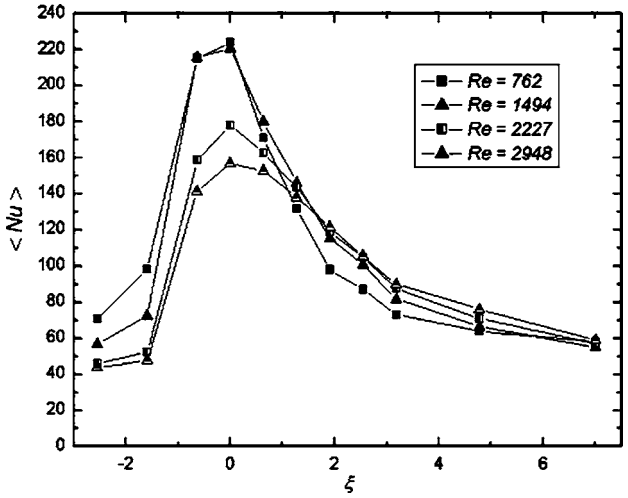

Fig. 10 $\langle Nu \rangle$ vs ξ in vertical aiding flow at $Gr_h = 3.89 \times 10^8$ [3]

This trend seems in contradiction with the Nusselt number distribution illustrated in Fig. 10, obtained in a previous experimental campaign with a heated vertical annulus [3]. In fact, Fig. 10 shows that the area under the Nusselt curve has almost the same value independently of Re. In other words, the longitudinal average of the Nusselt number does not vary much with the main flow velocity. This latter parameter only affects the wall uniformity of $\langle Nu \rangle$, which is larger at the highest flow rates.

However, the results obtained at a certain Reynolds number in a vertical configuration with aiding flow are not comparable with the horizontal ones at the same Re, as buoyancy forces play different roles. Even the transition from laminar to turbulent flow is anticipated in the vertical case: in the absence of the electric field, the flow is already turbulent at Re=400 [21].

Besides, in aiding flow, gravity helps taking hot fluid away from the heated surface. Instead, in a horizontal arrangement, a minimum main flow velocity is needed to move downstream the hot fluid, especially on the top, and reach high Nusselt numbers.

The large $\langle Nu \rangle$ increase in Fig. 9 from Re=295 to Re=740 could also be due to the transition from laminar to turbulent EHD flow.

Over a certain Re, the $\langle Nu \rangle$ in correspondence of the cross section of the emitters is supposed to decrease, as observed in the

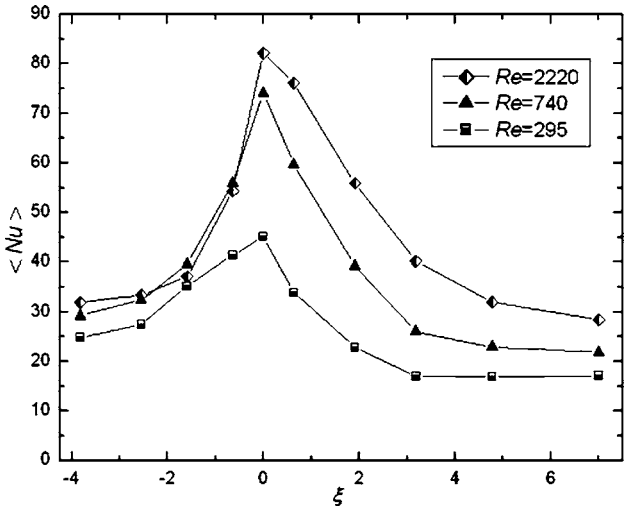

Fig. 9 $\langle Nu \rangle$ vs ξ at $Gr_h = 1.40 \times 10^8$

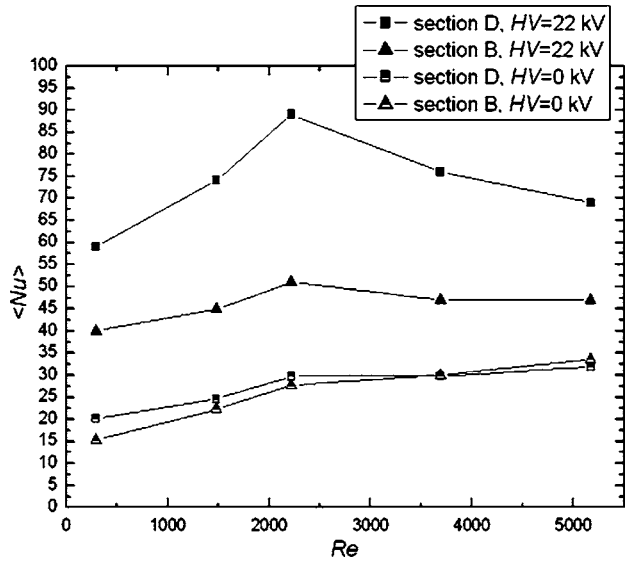

Fig. 11 ⟨Nu⟩ vs Re (Secs. B and D) at $Gr_h = 1.40 \times 10^8$

vertical upward flow. In fact, the effect of the induced jets should spread longitudinally, being carried downstream by the main forced flow.

Figure 11 actually shows this trend in configuration 2 at Secs. B and D (the points are mounted as in Fig. 3), in the Reynolds number range 295–5170. The points of configuration 2 were more accurately cut at their tips, at a repeatable angle of 45 deg. In this way, the Nusselt numbers turned out more uniformly distributed along the azimuthal coordinate.

In the absence of the electric field, ⟨Nu⟩ increases with Re. As for the dependence on the longitudinal coordinate, two opposing effects have to be taken into account: the steeper wall temperature gradient in the entry-zone, typical of pure forced convection, and the development of the buoyancy-driven secondary flow. The overall result is higher heat transfer coefficients in Sec. D for the lower Reynolds numbers and, inversely, higher ⟨Nu⟩ in Sec. B for the higher Re, owing to the diminished weight of the buoyant forces with respect to the inertial ones. Similar trends for mixed convection in a horizontal duct are documented in [25].

At the application of the electric field, the higher Nusselt numbers were obtained in Sec. D, due to the presence of four injecting points. In particular, heat transfer was enhanced by three times, with ⟨Nu⟩=59 at Re=295. In order to obtain this value in pure forced convection, without EHD effects, one needs a turbulent flow at Reynolds numbers around 5000, according to the Dittus-Bölter correlation [26].

Conclusions

Electrohydrodynamic heat transfer augmentation by ion injection may yield large reductions in pumping power of compact heat exchangers, showing remarkable heat transfer rates even at very low Reynolds numbers, without significant penalties associated with the pressure drop (in any case, less than 10 Pa) and with a negligible Joule heating. Then, the additional power input introduced by the technique can be disregarded, being in the order of 10^{-3} W. The phenomenon is localized in the proximity of the emitters, decaying more rapidly upstream than downstream of the points. Different injection strengths were observed from points apparently of the same dimensions. A more accurate control of the shape of the point tip is therefore required, in order to guarantee strong injection from each emitter.

As buoyancy forces play a significant role in differentiating the results of the horizontal configuration from the ones obtained in upward aided flow [3], experimentation in microgravity conditions will be helpful to assess the heat transfer behavior in the space environment. This is needed for designing a compact cold plate for space applications with the optimum longitudinal and azimuthal position of the emitters. As far as the presented results are concerned, to place the points at intervals of about one half of the hydraulic diameter in the axial direction, with four points per cross section, seems a good compromise (see Figs. 9 and 11).

Acknowledgment

This work was performed within the ESA Microgravity Application Program, Project No. AO-099-045. Funding by the Italian Space Agency, ASI (Grant No. I/R/061/01), is gratefully acknowledged. The authors would also like to thank Dr. Mario Saputelli for his valuable contribution to the experimental part of this work and Mr. Roberto Manetti for the essential collaboration in setting up the electronic devices.

Nomenclature

A = pipe cross-section area [m^2]
c_p = specific heat [$J\,kg^{-1}\,K^{-1}$]
D = inner diameter of the heated wall [m]
D_h = $=D-d$, hydraulic diameter [m]
d = diameter of the inner wire [m]
$\boldsymbol{E}$ = electric field [$V\,m^{-1}$]
er_F = relative error on the derived parameter
er_x = relative error on the measured parameter
f = Darcy-Weisbach friction factor
$\boldsymbol{f}_E$ = electric body force [$N\,m^{-3}$]
Gr = $=\beta_f g(T_{w\_in}-T_b)D_h^3/\nu_f^2$, Grashof number
Gr_h = Grashof number based on the wall heat flux
HV = applied high voltage [V]
L = pipe length [m]
L_h = heated length [m]
$\dot{m}$ = $=\rho\dot{V}$, mass flow rate [$kg\,s^{-1}$]
Nu = local Nusselt number
⟨Nu⟩ = azimuthal average of the Nusselt number
p = pressure [Pa]
q = heat flux [$W\,m^{-2}$]
Re = Reynolds number
s = heated wall thickness [m]
T = temperature [K]
t = time [s]
$\boldsymbol{u}$ = fluid velocity ($m\,s^{-1}$)
$\dot{V}$ = volumetric flow rate [$m^3\,s^{-1}$]

Greek

α = convective heat transfer coefficient ($W\,m^{-2}\,K^{-1}$)
β = coefficient of cubic expansion (K^{-1})
β_ε = temperature coefficient of permittivity (K^{-1})
χ = $=A\,Re^3\,Lf/2D_h^4$, parameter defined in Eq. (11) (m^{-1})
ε = electrical permittivity ($F\,m^{-1}$)
η = dynamic viscosity [Pa s]
Λ = heated wall thermal conductivity ($W\,m^{-1}\,K^{-1}$)
λ = fluid thermal conductivity ($W\,m^{-1}\,K^{-1}$)
ν = $=\eta/\rho$, kinematic viscosity ($m^2\,s^{-1}$)
Π_h = heat flow [W]
Π_P = pumping power [W]
ρ = mass density ($kg\,m^{-3}$)
ρ_E = free charge density ($C\,m^{-3}$)
ω = vorticity (s^{-1})
ξ = dimensionless longitudinal coordinate

Subscripts

b = bulk
f = calculated at film temperature
in = inlet

out = outlet
w_in = inner side of the heated wall
w_out = outer side of the heated wall

References

[1] Miedza, B., and Behrens, B., 1997, "Cold Plate Development for Space Station Application," ESA SP-400, 6th European Symposium on Space Environmental Control Systems, Noordwijk, The Netherlands 1, pp. 299–304.

[2] Tritton, D. J., 1988, *Physical Fluid Dynamics*, Oxford University Press, Oxford, UK.

[3] Grassi, W., Testi, D., and Saputelli, M., 2005, "EHD Enhanced Heat Transfer in a Vertical Annulus," Int. Commun. Heat Mass Transfer, **32**(6), pp. 748–757.

[4] Felici, N., 1971, "dc Conduction in Liquid Dielectrics: A Survey of Recent Progress (Part I)," Direct Current, **2**(3), pp. 90–99.

[5] Richter, A., Plettner, A., Hotmann, K. A., and Sandmaier, H., 1991, "A Micromachined Electrohydrodynamic (EHD) Pump," Sens. Actuators, A, **29**(2), pp. 159–168.

[6] Atten, P., 1996, "Electrohydrodynamic Instability and Motion Induced by Injected Space Charge in Insulating Liquids," IEEE Trans. Dielectr. Electr. Insul., **3**(1), pp. 1–17.

[7] Atten, P., Malraison, B., and Zahn, M., 1997, "Electrohydrodynamic Plumes in Point-Plane Geometry," IEEE Trans. Dielectr. Electr. Insul., **4**(6), pp. 710–718.

[8] Grassi, W., Testi, D., Della Vista, D., and Torelli, G., 2005, "Augmentation of Heat Transfer on the Downward Surface of a Heated Plate by Ion Injection," ECI-ITP-05-03, in *Proceedings of the Interdisciplinary Transport Phenomena in Microgravity and Space Sciences IV*, Tomar, Portugal.

[9] Grassi, W., Testi, D., and Della Vista, D., 2005, "Heat Transfer Enhancement on the Upper Surface of a Horizontal Heated Plate in a Pool by Ion Injection from a Metallic Point," Journal of Electrostatics (in press).

[10] Paschkewitz, J. S., and Pratt, D. M., 2000, "The Influence of Fluid Properties on Electrohydrodynamic Heat Transfer Enhancement in Liquids under Viscous and Electrically Dominated Flow Conditions," Exp. Therm. Fluid Sci., **21**, pp. 187–197.

[11] Ohadi, M. M., Darabi, J., and Roget, B., 2001, "Electrode Design, Fabrication, and Materials Science for EHD-Enhanced Heat and Mass Transport," *Annual Review of Heat Transfer*, C. L. Tien, ed., Begell House, New York, Vol. 11, Chap. 9, pp. 563–632.

[12] Porter, J. E., and Poulter, R., 1970, "Electrothermal Convection Effects With Laminar Flow Heat Transfer in an Annulus," in *Proceedings of the 4th International Heat Transfer Conference*, Paris, France, Vol. 2.

[13] Mizushina, T., Ueda, H., Matsumoto, T., and Waga, K., 1976, "Effect of Electrically Induced Convection on Heat Transfer of Air Flow in an Annulus," J. Chem. Eng. Jpn., **9**(2), pp. 97–102.

[14] Velkoff, H. R., and Godfrey, R., 1979, "Low-Velocity Heat Transfer to a Flat Plate in the Presence of a Corona Discharge in Air," ASME J. Heat Transfer, **101**, pp. 157–163.

[15] Fernández, J. L., and Poulter, R., 1987, "Radial Mass Flow in Electrohydrodynamically-Enhanced Forced Heat Transfer in Tubes," Int. J. Heat Mass Transfer, **30**(10), pp. 2125–2136.

[16] Fujino, T., Yokohama, Y., and Mori, H. R., 1989, "Augmentation of Laminar Forced-Convective Heat Transfer by the Application of a Transverse Electric Field," ASME J. Heat Transfer, **111**, pp. 345–351.

[17] Ohadi, M. M., Nelson, D. A., and Zia, S., 1991, "Heat Transfer Enhancement of Laminar and Turbulent Pipe Flow via Corona Discharge," Int. J. Heat Mass Transfer, **34**(4–5), pp. 1175–1187.

[18] Hasegawa, M., Yabe, A., and Nariai, H., 1997, "Numerical Analysis of Electro-Hydrodynamical Enhancement Mechanism of Forced Convection Heat Transfer in Duct Flow," *ASME Proceedings of the 32nd National Heat Transfer Conference*, Vol. 10, pp. 11–15.

[19] Molki, M., Ohadi, M. M., Baumgarten, B., Hasegawa, M., and Yabe, A., 2000, "Heat Transfer Characteristics of Airflow in a Channel Using Corona Discharge," J. Enhanced Heat Transfer, **7**, pp. 411–425.

[20] Grassi, W., Testi, D., and Saputelli, M., 2005, "Heat Transfer Enhancement in a Vertical Annulus by Electrophoretic Forces Acting on a Dielectric Liquid," Int. J. Therm. Sci., **44**(11), pp. 1072–1077.

[21] Metais, B., and Eckert, E. R. G., 1964, "Forced, Mixed, and Free Convection Regimes," ASME J. Heat Transfer, **86**, pp. 295–296.

[22] Metais, B., 1963, "Criteria for Mixed Convection," Technical Report No. 51, Heat Transfer Laboratory, University of Minnesota, Minneapolis, MN.

[23] Felici, N., Gosse, B., and Gosse, J.-P., 1976, "La Conduction dans les Liquides Diélectriques—Idées Modernes et Progrès Récents—Aspects Électrochimiques et Électrohydrodynamiques," Rev. Gen. Electr., **85**(11), pp. 861–874 (in French).

[24] Abramovich, G. N., 1963, *The Theory of Turbulent Jets*, MIT Press, Cambridge, MA.

[25] Petukhov, B. S., and Polyakov, A. F., 1988, *Heat Transfer in Turbulent Mixed Convection*, Hemisphere Publishing, New York.

[26] Kakaç, S., Shah, R. K., and Aung, W., 1987, *Handbook of Single-Phase Convective Heat Transfer*, Wiley, New York.

Journal of Heat Transfer

Technical Briefs

A Film-Theory-Based Model for a Multicomponent Droplet Evaporation at Both Low- and High-Pressure Environments

Guangfa Yao
Simulatech, LLC,
7624 William Moyers NE,
Albuquerque, NM 87122
e-mail: yao@simulatechs.com

Modeling of a multicomponent droplet evaporation is investigated based on the film theory in both low- and high-pressure environments. Unlike the classical film theory, effects of blowing due to evaporation on gas-side heat and mass transfer are included through the film thicknesses. The corresponding gas-side heat and mass transfer equations are derived in terms of film thicknesses. In a high-pressure situation, the real gas behavior is considered. Based on the derived equations, a new model for multicomponent droplet evaporation is formulated and validated against the published data. [DOI: 10.1115/1.2151197]

Introduction

Liquid spray has various applications. To make a simulation of spray processes using computational fluid dynamics (CFD) codes, simple evaporation models are needed. A comprehensive review of these models can be found in [1]. In these models, the gas-side heat and mass transfer are usually simulated based on the simple correlations [2,3] and important physical processes, such as blowing due to evaporation and droplet heating, are not included. As an improvement to these models, Abramzon and Sirignano [4] developed a model based on the film theory introduced in [5]. They derived some new relationships for Nusselt and Sherwood numbers (called "modified" Nusselt and Sherwood numbers). Using them as well as a correction factor to film thicknesses, the effects of blowing (Stefan flow) and droplet heating are accounted for.

With a similar motivation behind the Abramzon and Sirignano's film model, Yao et al. [6] presented a film model for a single-component droplet evaporation based on the film theory introduced in [7]. They presented a unified derivation of simple evaporation models and also showed that Abramzon and Sirignano's model can be alternatively derived. In the model of Yao et al. [6], the effects of Stefan flow on heat and mass transfer are accounted for through the calculation of film thicknesses that are determined from advanced and accurate correlations [8]. In these correlations, the Nusselt number correlation includes heat transfer number (B_T), which depends on the mass flux ($\dot{m}''$) and droplet heating rate ($\dot{q}''$). Both of them are variables that need to be solved for in the models. Therefore, in these correlations, the Nusselt number is implicitly represented and cannot be directly used. To this end, the model of Yao et al. [6] presented a methodology to take advantage of these correlations.

The film theory itself is not new and has been documented in textbooks, such as in [5,7]. Even though the film theory introduced in [7] was attempted to account for the high mass flux effect, the theory assumes that the film thicknesses are the same as those when low or no interfacial mass flux is considered. What are new in both the Abramzon and Sirignano's model [4] and the model of Yao et al. [6] are approaches developed to account for effect of high mass flux on heat and mass transfer film thicknesses (thereby, on heat and mass transfer). Both the film-theory-based models of Abramzon and Sirignano [4] and Yao et al. [6] were derived for a single-component droplet evaporation. The present work focuses on a multicomponent droplet evaporation with high-pressure effect.

Model Derivations

For the convenience of presentation, a multicomponent fuel droplet containing n components and evaporating into hot air or nitrogen gas is considered in the following derivations.

Referring to [7], the evaporation mass flux of fuel species i can be expressed by

$$\Gamma_i = -\rho \mathcal{D}_{im} \frac{dY_i}{dr} + Y_i \sum_{j=1}^{n+1} \Gamma_j \tag{1}$$

with the assumptions of neglecting Soret effect. Furthermore, with the mass transfer process assumed to be steady, the rate of mass transfer of species i through any spherical surface around a droplet will be constant, leading to $\Gamma_i = (r_d^2/r^2)\dot{m}_i''$ for the mass flux of species i at an arbitrary radial location, where $\dot{m}_i''$ stands for the mass flux of species i at the droplet surface. With this mass flux and Eq. (1), one gets

$$\dot{m}_i'' - Y_i \sum_{j=1}^{n+1} \dot{m}_j'' = -\frac{\rho \mathcal{D}_{im}}{r_d^2} r^2 \frac{dY_i}{dr} \tag{2}$$

Solving Eq. (2) for mass fraction of species i with the boundary condition of $Y_i = Y_{i,\infty}$ at $r = r_d + \delta_{M,i}$, an equation for mass fraction distribution of species i throughout a film thickness is derived

Contributed by the Heat Transfer Division of ASME for publication in the JOURNAL OF HEAT TRANSFER. Manuscript received February 3, 2005; final manuscript received August 31, 2005. Review conducted by Chang Oh.

$$\frac{Y_{i,s}-\dfrac{\dot{m}_i''}{\dot{m}''}}{Y_{i,\infty}-\dfrac{\dot{m}_i''}{\dot{m}''}}=\exp\left[\Lambda_i r_d\left(\frac{1}{r_d+\dot{\delta}_{M,i}}-\frac{1}{r}\right)\right] \tag{3}$$

where $\Lambda_i=\dot{m}''r_d/\rho\mathcal{D}_{im}$. Noting the condition of $Y_i=Y_{i,s}$ at the droplet surface, an equation for mass flux of species i at the droplet surface can be written as

$$\dot{m}''=\frac{\rho\mathcal{D}_{im}}{r_d}\left(\frac{r_d+\dot{\delta}_{M,i}}{\dot{\delta}_{M,i}}\right)\ln(1+B_M) \tag{4}$$

according to Eq. (3), where $B_M=(Y_{i,\infty}-Y_{i,s})/(Y_{i,s}-\dot{m}_i''/\dot{m}'')$. Calculating the Sherwood number using Eq. (3) and eliminating $\dot{m}_i''$ with the help of Eq. (4) in the resulting equation, the equation for Sherwood number of species i is given by

$$\mathrm{Sh}_i=\frac{2\Lambda_i}{\exp\left(\dfrac{\Lambda_i\dot{\delta}_{M,i}}{r_d+\dot{\delta}_{M,i}}\right)-1} \tag{5}$$

To find an equation for calculating total mass flux at the droplet surface from a given Sherwood number, from Eq. (1) and the definition of Sherwood number, the following equation for mass flux of species i is obtained:

$$\dot{m}_i''=\frac{\rho\mathcal{D}_{im}}{2r_d}B_M\mathrm{Sh}_{i,f} \tag{6}$$

Casting this equation to get an expression for $\dot{m}_i''$ and furthermore summing the resulting equation over i, the following equation for total mass flux yields:

$$\dot{m}''=\sum_{i=1}^{n}\frac{\mathrm{Sh}_{i,f}(\rho\mathcal{D}_{im})(Y_{i,s}-Y_{i,\infty})}{2r_d\left(1-\sum_{j=1}^{n}Y_{j,s}\right)} \tag{7}$$

where the insolubility of ambient gas on the droplet surface was adopted. This equation will be used to calculate a total mass flux in the new evaporation model.

Again, referring to [7], the total energy flux at an arbitrary radial location is expressed as

$$\phi=-K_g\frac{dT}{dr}+\sum_{i=1}^{n+1}\dot{m}_i''h_i \tag{8}$$

with assumptions of neglecting Dufour effect. Similar to mass transfer, the total energy flux at an arbitrary radial location (ϕ) is represented in terms of total energy flux at the droplet surface ($\mathcal{E}$), leading to $\phi=(r_d^2/r^2)\mathcal{E}$. With this expression for ϕ and Eq. (8), and representing enthalpy in terms of temperature, the following equation is obtained:

$$\mathcal{E}-\sum_{i=1}^{n}\dot{m}_i''C_{PF,i}T=-K_g\frac{r^2}{r_d^2}\frac{dT}{dr} \tag{9}$$

Integrating Eq. (9) with the boundary condition of $T=T_\infty$ at $r=r_d+\dot{\delta}_T$, the following equation for temperature distribution through a film thickness is derived:

$$\frac{T-T_s}{T_\infty-T_s}=\frac{1-\exp\left[\Omega\left(1-\dfrac{r_d}{r}\right)\right]}{1-\exp\left(\dfrac{\Omega\dot{\delta}_T}{r_d+\dot{\delta}_T}\right)} \tag{10}$$

where $\Omega=(r_d\Sigma_{i=1}^{n}\dot{m}_i''C_{PF,i})/K_g$. Noting $T=T_s$ at $r=r_d$ and from Eq. (10), an equation for Nusselt number is obtained. It is

$$\mathrm{Nu}=\frac{2\Omega}{\exp\left(\dfrac{\Omega\dot{\delta}_T}{\dot{\delta}_T+r_d}\right)-1} \tag{11}$$

From an energy balance at the droplet surface, one gets

$$\dot{m}''=\frac{K_g}{r_d\sum_{i=1}^{n}\left(\dfrac{\dot{m}_i''}{\dot{m}''}C_{PF,i}\right)}\frac{\dot{\delta}_T+r_d}{\dot{\delta}_T}\ln(1+B_T) \tag{12}$$

where B_T is defined by

$$B_T=\frac{(T_\infty-T_s)\sum_{i=1}^{n}\left(\dfrac{\dot{m}_i''}{\dot{m}''}C_{PF,i}\right)}{\dfrac{q_l''}{\dot{m}''}+\sum_{i=1}^{n}\left(\dfrac{\dot{m}_i''}{\dot{m}''}L_i\right)} \tag{13}$$

With the definition of Ω above, Eq. (12) is cast into

$$B_T=\exp\left(\frac{\Omega\dot{\delta}_T}{\dot{\delta}_T+r_d}\right)-1 \tag{14}$$

From this equation and Eq. (11), one ends up

$$\mathrm{Nu}=\frac{2\Omega}{B_T} \tag{15}$$

This equation will be used to calculate the heat transfer number, B_T. Equations (4), (5), (7), and (15) provide the gas-side transport equations of the new evaporation model to be presented later.

Comparison of Present Derivation With the Classical Film Model. To make a comparison with the classical film model used in single-droplet evaporation models, let us consider Eq. (11) in its single component form. That is,

$$\mathrm{Nu}=\frac{2r_d\dot{m}''C_{PF}/K_g}{\exp\left(\dfrac{r_d\dot{m}''C_{PF}}{K_g}\dfrac{\dot{\delta}_T}{r_d+\dot{\delta}_T}\right)-1} \tag{16}$$

When $\dot{m}''\to 0$, Nu and $\dot{\delta}_T$ converge to Nu_0 and δ_T respectively. Thus, Eq. (16) becomes

$$\delta_T=\frac{2r_d}{\mathrm{Nu}_0-2}\ \text{or}\ r_{f,T_0}=r_d\frac{\mathrm{Nu}_0}{\mathrm{Nu}_0-2} \tag{17}$$

where $r_{f,T_0}=r_d+\delta_T$. Similarly, from the single-component form of Eq. (5), one gets

$$\delta_M=\frac{2r_d}{\mathrm{Sh}_0-2}\quad\text{or}\quad r_{f,M}=r_d\frac{\mathrm{Sh}_0}{\mathrm{Sh}_0-2} \tag{18}$$

when $\dot{m}''\to 0$. Here $r_{f,M}=r_d+\delta_M$. Equations (17) and (18) are film thicknesses and equivalent radii used in simple evaporation models [3]. Derivation of simple evaporation models based on the classic film theory starts from these fixed film thicknesses or equivalent radii. In these models, Stefan flow effect is neglected.

Comparison With the Abramon and Sirignano's Model [4]. As we saw above, in the simple evaporation models based on the classic film theory, the film thicknesses do not include effect of Stefan flow, which has been found to be important. To improve this, Abramzon and Sirignano [4] developed a new film model. They started from the following assumptions:

$$r_{f,T}=r_d\frac{\mathrm{Nu}^*}{\mathrm{Nu}^*-2}\quad\text{or}\quad r_{f,M}=r_d\frac{\mathrm{Sh}^*}{\mathrm{Sh}^*-2} \tag{19}$$

by mimicking Eqs. (17) and (18), where Nu^* and Sh^* are called "modified" Nusselt and Sherwood numbers, respectively. The film thicknesses are determined by

$$\frac{\dot{\delta_T}}{\delta_T} = F(B_T) \quad \text{and} \quad \frac{\dot{\delta_M}}{\delta_M} = F(B_M) \tag{20}$$

based on boundary layer theory and with function F defined by $F(x)=(1+x)^{0.7}\ln(1+x)/x$. Thus, leading to

$$\mathrm{Nu}^* = 2 + \frac{\mathrm{Nu}_0 - 2}{F(B_T)}; \quad \mathrm{Sh}^* = 2 + \frac{\mathrm{Sh}_0 - 2}{F(B_M)} \tag{21}$$

Their model consists of the following equations derived based on the film theory introduced in [5]:

$$\mathrm{Nu} = \mathrm{Nu}^* \frac{\ln(1+B_T)}{B_T}; \quad \mathrm{Sh} = \mathrm{Sh}^* \frac{\ln(1+B_M)}{B_M} \tag{22}$$

$$\dot{m}'' = \frac{K_g}{2C_{PF}r_d}\mathrm{Nu}^* \ln(1+B_T); \quad \dot{m}'' = \frac{\rho\mathcal{D}}{2r_d}\mathrm{Sh}^* \ln(1+B_M) \tag{23}$$

Recently, we developed a film-theory-based model for a single-component droplet evaporation [6], started from the film theory introduced in [7]. The major equations in our model are

$$\dot{m}'' = \frac{K_g}{C_{PF}r_d}\left(1 + \frac{r_d}{\dot{\delta_T}}\right)\ln(1+B_T) \tag{24}$$

$$\dot{m}'' = \frac{\rho\mathcal{D}}{r_d}\left(1 + \frac{r_d}{\dot{\delta_m}}\right)\ln(1+B_M) \tag{25}$$

$$\mathrm{Nu} = 2\left(1 + \frac{r_d}{\dot{\delta_T}}\right)\frac{\ln(1+B_T)}{B_T} \tag{26}$$

$$\mathrm{Sh} = 2\left(1 + \frac{r_d}{\dot{\delta_M}}\right)\frac{\ln(1+B_M)}{B_M} \tag{27}$$

Equations (24)–(27) can be directly derived from the corresponding equations for a multicomponent droplet evaporation described above (Eqs. (4)–(6), (12), and (15)). We have shown that most equations for simple droplet evaporation models can be directly derived from Eqs. (24)–(27) [6]. In this sense, a unified model derivation was presented. By plugging Eq. (20) into Eqs. (24)–(27), Eqs. (21)–(23) are alternatively derived.

Formulation of Evaporation Model

Using the equations derived above for the gas-side heat and mass transfer processes, an evaporation model is formulated below. The model formulation is presented through its solution procedure.

1. From a given droplet surface temperature T_s and liquid mass fraction of species at droplet surface $Y_{i,l,s}$, the mole fraction of specie i at droplet surface is obtained by using the Raoult's law; that is, $X_{i,s}=X_{i,l,s}[P_i(T_s)/P]$ with the corresponding mass fraction calculated by $Y_{i,s}=X_{i,s}M_i/\Sigma_{j=1}^{n+1}X_{j,s}M_j$.
2. From Eq. (7), the total mass flux is calculated where the Sherwood number of species i is calculated based on the advanced and accurate correlations, for example, these derived from the detailed numerical simulation [9]. Then using Eq. (5), film thicknesses $\dot{\delta}_{M,i}$ are solved for. Furthermore, from Eq. (4), the mass flux for species i is obtained.
3. The left side of Eq. (15) is now replaced by a heat transfer correlation derived from the fully numerical solution [9], and B_T is solved for, followed by the calculation of q_l'' using Eq. (13).
4. Solve the one-dimensional energy and species conservation equations for a multicomponent droplet with variable property effects to get a new droplet surface temperature, species mass/mole fractions, and a new droplet radius. Equations and the corresponding solution procedures are the same as described in [10].

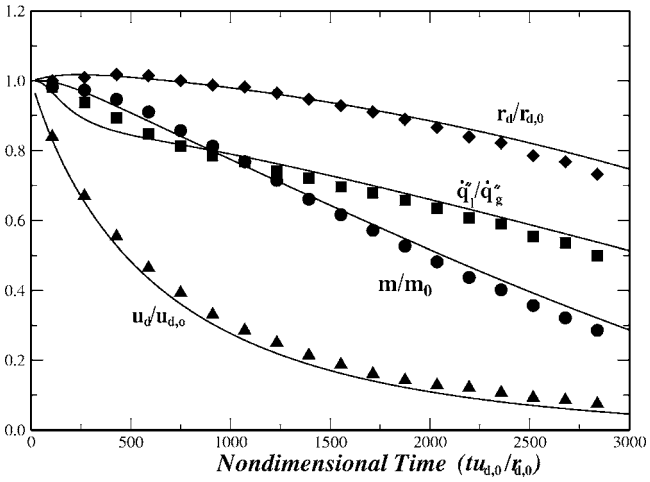

Fig. 1 The history of droplet radius, mass, velocity, and ratio of liquid heating to gas side heat transfer rate. Symbols: fully numerical date; Lines: model predictions.

For a high-pressure situation, a simplified high-pressure model presented in [11] was adopted here for phase equilibrium at the droplet surface based on the Clausius-Clapeyron relation for each fuel component. Therefore, for a high-pressure environment, the above-mentioned Raoult's law is replaced by

$$X_{i,s} = X_{i,l,s}\left\{\frac{L_i M_i}{R}\left(\frac{1}{T_{bi}} - \frac{1}{T_s}\right)\right\} \tag{28}$$

The calculation of boiling temperature T_{bi} and heat of vaporization of species i, L_i, can be found in the related reference. The real gas behavior is represented by using the Peng-Robinson equation of state [12] in the calculation of thermophysical properties. Needed thermal properties at high-pressure mixture are calculated using the models or correlations in [12] except for viscosity, which was found by the one-parameter friction theory (f-theory) [13].

Model Validation

To validate present model, the model predictions are compared to the fully numerical solution and experimental measurements in both low- and high-pressure environments. For a moving droplet, the droplet movement is tracked by solving the following equation:

$$\frac{du_d}{dt} = -\frac{3}{8}\left(\frac{\rho_{g,\infty}}{\rho_d}\right)\frac{u_d^2}{r_d}C_D + \left(1 - \frac{\rho_{g,\infty}}{\rho_d}\right)g \tag{29}$$

The drag coefficient (C_D) as well as Nusselt and Sherwood numbers needed in the model are calculated using the correlations in [9] with blowing effect due to evaporation accounted for.

The model predictions are compared with the fully numerical solution for evaporation of a binary hydrocarbon droplet (decane-hexadecane) moving in still air at 1000 K and at a pressure of 10 atm [9]. The droplet initial temperature, velocity, and diameter are 300 K, 10 m/s, and 100 μm, respectively while initial composition is 50% decane–50% hexadecane by mass. Figure 1 shows the history of droplet radius, mass, velocity, and rate of liquid heating to gas-side heat transfer rate. The average deviation compared to the data is within 5%. Thermophysical properties used in the present simulation are the same as these used in the fully numerical solutions and were given in [8].

To validate present model against experiments, we first compare to the experimental results of Daif et al. [14,15]. In their experiments, a binary droplet (heptane-decane) is suspended by a 0.2–0.3 mm dia glass capillaries, subjected to an external airflow. The model predictions along with corresponding experimental

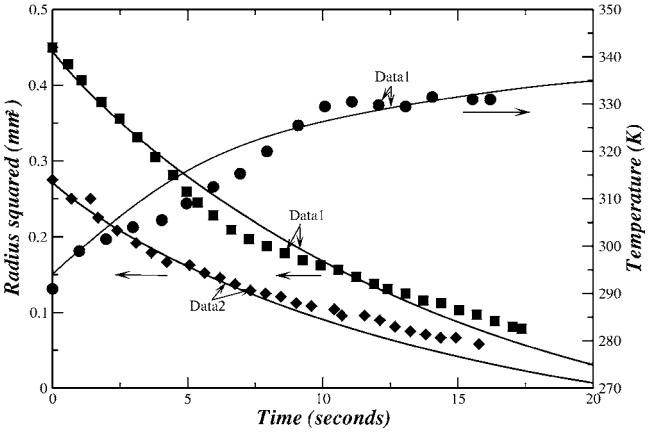

Fig. 2 Comparison with experimental measurements of Daif et al. [14,15] for droplet radius and surface temperature. Symbols: experimental data; Lines: model predictions.

data for squared droplet radius and surface temperature are presented in Fig. 2. The initial mass fractions of heptane and decane, droplet radius, temperature, ambient air temperature, and ambient air velocity are 0.74, 0.26, 0.671 mm, 348 K, 294 K, and 3.1 m/s for data1 and 0.635, 0.365, 0.521 mm, 341 K, 292 K, and 3.36 m/s for data2, respectively. Average deviations of droplet radius are within 11%, while deviations for temperature are within 3% for all data sets. Because of space limitation, only two data sets are presented here. The performance of the present model in a high-pressure environment was investigated by comparing to the experiments of Stengle et al. [16]. In their experimental study, freely falling binary hydrocarbon droplets (pentane-nonane) released with an initial velocity and in a stagnant high-pressure and high-temperature nitrogen gas environment were considered. Figure 3 presents the comparison of the predicted and measured droplet velocity and diameter data. The low-left part shows droplet diameter change versus distance, while droplet velocity versus distance is given in the top-right part of the same figure. The average deviations of droplet diameters for all data sets are within 12%. Again, only two data sets were presented here due to space limitations. The initial droplet velocity, temperature, diameter, mass fractions of pentane and nonane, ambient air temperature,

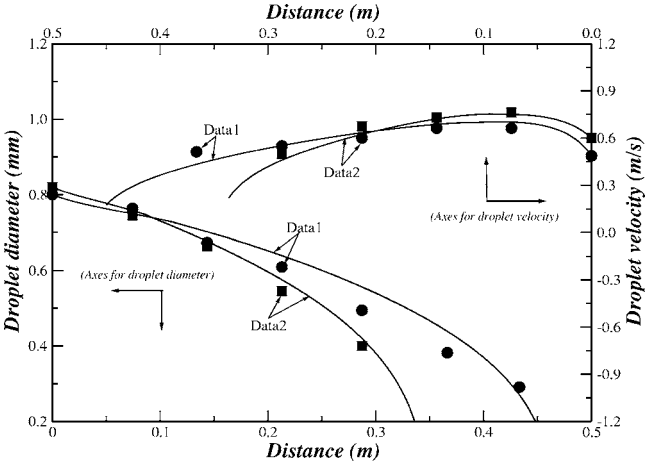

Fig. 3 Comparison with the experiments of Stengle et al. [16] for predicted and measured droplet velocity and diameter along the droplet trajectory in a high-pressure environment. Symbols: experimental data; Lines: model predictions.

and ambient pressure are 0.49 m/s; 370 K; 0.8 mm; 0.7, 0.3, 550 K; and 30 bar for data1 and 0.6 m/s; 380 K; 0.82 mm; 0.7, 0.3, 650 K; and 30 bar for data2, respectively.

Conclusions

A simple model for a multicomponent droplet evaporation is developed based on the film theory. The gas-side heat and mass transfer are expressed in terms of heat and mass transfer film thicknesses. The effects of blowing due to evaporation are included. Derived equations are compared to these from the classical film model where effects of blowing on film thicknesses are ignored. For evaporation into a high-pressure gas, a simplified relation for gas-liquid equilibrium on a droplet surface was adopted. Effects of high pressure on liquid- and gas-phase thermophysical properties were also considered. Model performance was validated against the published data in both low- and high-pressure environments. Overall, a good match between model predictions and benchmark data was achieved.

Nomenclature

C_P = specific heat, ($J\,kg^{-1}\,K^{-1}$)
$\mathcal{D}$ = species mass diffusion coefficient, ($m^2\,s^{-1}$)
h = heat transfer coefficient, ($J\,m^{-2}\,s^{-1}\,K^{-1}$); enthalpy, ($J\,kg^{-1}$)
K = thermal conductivity, ($W\,m^{-1}\,K^{-1}$)
L = latent heat of vaporization, ($J\,kg^{-1}$)
$\dot{m}''$ = mass flux at droplet surface, ($kg\,m^{-2}\,s^{-1}$)
Nu = Nusselt number, ($2r_d h/\mathrm{Kg}$)
P = ambient gas pressure, (Pa)
Pr = Prandtl number, ($\mu_g C_{pg}/\mathrm{Kg}$)
q'' = heat flux, ($J\,m^{-2}\,s^{-1}$)
r = droplet radius, (m)
Sc = Schmidt number, ($\mu_g/(\rho_g \mathcal{D})$)
Sh = Sherwood number, ($2r_d K_g/(\rho_g \mathcal{D})$)
T = temperature, (K)
u_d = relative velocity between a droplet and its ambient gas, ($m\,s^{-1}$)

Greek Symbols

δ = film thickness, (m)
Λ_i = variable in Eqs. (3) and (5), ($\dot{m}'' r_d/(\rho \mathcal{D}_{im})$)
μ = molecular viscosity, ($kg\,m^{-1}\,s^{-1}$)
ρ = density, ($kg\,m^{-3}$)

Subscripts

d = droplet
f = film condition
F = fuel
g = gas
M = mass transfer
m = mixture
s = saturated; droplet surface
T = heat transfer
0 = initial condition; with low mass transfer rate
∞ = free stream condition

Superscripts

$\cdot$ = with high mass transfer rate

References

[1] Sirignano, W. A., 1999, *Fluid Dynamics and Transport of Droplets and Sprays*, Cambridge University Press, Cambridge, England.
[2] Ranz, W. E., and Marshall, W. R., 1952, "Evaporation From Drops," Comments Condens. Matter Phys., **48**, pp. 141–173.
[3] Faeth, G. M., 1977, "Current Status of Droplet and Liquid Combustion," Prog. Energy Combust. Sci., **3**, pp. 191–224.
[4] Abramzon, B., and Sirignano, W. A., 1989, "Droplet Vaporization Model for Spray Combustion Calculation," Int. J. Heat Mass Transfer, **32**, pp. 1605–1618.

[5] Frank-Kamenetskii, D. A., 1969, *Diffusion and Heat Transfer in Chemical Kinetics*, 2nd ed., Plenum Press, New York.
[6] Yao, G. F., Abdel-Khalik, S. I., and Ghiaasiaan, S. M., 2003, "An Investigation of Simple Evaporation Models Used in Spray Simulations," ASME J. Heat Transfer, **125**, pp. 179–182.
[7] Bird, R. B., Stewart, W. E., and Lightfoot, E. M., 1960, *Transport Phenomena*, Wiley, New York.
[8] Bussmann, M., 1990, "Studies on Convective Droplet Evaporation," MS thesis, University of Waterloo, Waterloo, Canada.
[9] Renksizbulut, M., and Bussmann, M., 1993, "Multicomponent Droplet Evaporation at Intermediate Reynolds Numbers," Int. J. Heat Mass Transfer, **36**, pp. 2287–2835.
[10] Kneer, R., Schneider, M., Noll, B., and Wittig, S., 1993, "Diffusion Controlled Evaporation of a Multicomponent Droplet: Theoretical Studies on the Importance of Variable Liquid Properties," Int. J. Heat Mass Transfer, **36**, pp. 2402–2415.
[11] Aggarwal, S. K., and Mongia, H. C., 2002, "Multicomponent and High-Pressure Effects on Droplet Vaporization," ASME J. Eng. Gas Turbines Power, **124**, pp. 248–255.
[12] Poling, B. E., Prausnitz, J. M., and O'Connell, J. P., 2001, *The Properties of Gases and Liquids*, 5th ed., McGraw-Hill, New York.
[13] Quinones-Cisneros, S. E., Zeberg-Mikkelsen, C. K., and Stenby, E. H., 2001, "One Parameter Friction Theory Models for Viscosity," Fluid Phase Equilib., **178**, pp. 1–16.
[14] Daif, A., Bouaziz, M., Chesneau, X., and Alicherif, A., 1999, "Comparison of Multicomponent Fuel Droplet Vaporization Experiments in Forced Convection with the Sirignano Model," Exp. Therm. Fluid Sci., **18**, pp. 282–290.
[15] Daif, A., Bouaziz, M., and Grisenti, M., 1998, "Vaporization of Binary Fuel Mixture Droplets in a Thermal Wind Tunnel," J. Thermophys. Heat Transfer, **12**, pp. 107–113.
[16] Stengle, J., Prommersberger, K., Willmann, M., and Wittig, S., 1999, "Experimental and Theoretical Study of One- and Two-Component Droplet Vaporization in a High Pressure Environment," Int. J. Heat Mass Transfer, **42**, pp. 2683–2694.

Effectiveness of a Spiral-Plate Heat Exchanger With Equal Capacitance Rates

Louis C. Burmeister
ASME Member 160366
Department of Mechanical Engineering,
University of Kansas,
Lawrence, KS 66045
e-mail: mrub@ku.edu

A formula is derived for the dependence of heat exchanger effectiveness on the number of transfer units for a spiral-plate heat exchanger with equal capacitance rates. The difference-differential equations that describe the temperature distributions of the two counter-flowing fluids, neglecting the effects of thermal radiation, are solved symbolically to close approximation. Provision is made for the offset inlet and exit of the hot and cold fluids at the outer periphery and for large heat transfer coefficients in the entrance regions. The peak effectiveness and the number of transfer units at which it occurs are linear functions of the maximum angle of the Archimedean spiral that describes the ducts; entrance region effects reduce both. [DOI: 10.1115/1.2150839]

Keywords: spiral-plate, heat exchanger, optimal, number of transfer units

Introduction

The spiral-plate heat exchanger proposed late in the 19th century (Boothroyd [1]) was reinvented in Sweden in the 1930s. Fraas [2] gives cost correlations, Alfa Laval [3] gives geometries, overall heat transfer coefficients, and pressure drops while Molloy [4], Taborek et al. [5], and Gupta [6] cite ease of maintenance, compactness, resistance to fouling, and high heat transfer coefficients due to swirling flow.

Egner and Burmeister [7] showed that the laminar, fully-developed local heat transfer coefficient for a spiral duct of rectangular cross section is close to that for a constant-radius-of-curvature rectangular duct, either in a plane or in a helical spiral. Except for the two entrance regions, the combination of inward- and outward-spiraling fluids results in the overall heat transfer coefficient being nearly constant.

The analysis of the spiral-plate heat exchanger by Baird et al. [8] sparked interest in others [9–22] (see Zaleski and Krajewski [9] for German, Polish and Russian literature; Zhang et al. [14] for Chinese literature). Buonapane and Troupe [22] solved the describing equations with a finite-difference method to obtain curves of effectiveness ε versus number of transfer units NTU for several capacitance ratios $C=C_{\min}/C_{\max}$. Although not remarked upon, a maximum ε is shown at NTU$\approx$30 for $C=1$. Jones et al. [23] considered a spiral-plate heat exchanger for regeneration to enable combustion with very lean mixtures but did not remark upon a maximum ε. Later, Bes [16] reported a maximum ε at a large NTU value.

Cieslinski and Bes [10] constructed a symbolic solution to the describing equations as a series of Hermite polynomials for outer entrance and exit of the two fluids on opposite sides. Their solution is too complex to give much more guidance than a purely numerical solution regarding functional forms and correlation of solutions. Bes and Roetzel [16] ingeniously found an approximate symbolic solution that provides simple relationships between the maximum ε, the NTU at which it occurs, and the number of turns. These two solutions account for neither various offsets of the inlets and outlets of the two fluids nor entrance-region effects. Strenger et al. [24] applied a finite-difference method to obtain a curve of the maximum ε and the NTU at which it occurs versus the number of turns with $C=1$ for up to 18 turns.

In the following, a more general approximate symbolic solution is obtained for ε versus NTU of a spiral-plate heat exchanger with equal capacitance rates. Various offsets between the outer entrance and exit of the two fluids and entrance-region effects are taken into account.

Geometry

The geometry of a spiral-plate heat exchanger is illustrated in Fig. 1 with the inner inlet offset by 180 deg from the inner outlet. Spiral channel 1 has a center line whose radius r from the origin varies with angle θ, a is a constant, and θ_i is the angle at which the minimum radius $r_{\min}$ is achieved, as

$$r = a(\theta - \theta_i) + r_{\min} \tag{1}$$

The width W of each channel is related to a as

$$2W = r(\theta + 2\pi) - r(\theta) = 2\pi a \tag{2}$$

Heat Exchange Area. The length L_1 along the spiral center line is closely approximated by

$$L_1(\theta_1 \to \theta_2) = \int_{\theta_1}^{\theta_2} r\,d\theta = a[(\theta_2 - \theta_i + r_{\min}/a)^2 - (\theta_1 - \theta_i + r_{\min}/a)^2]/2 \tag{3}$$

The area A_1 available for heat transfer from channel 1 is given by the length of the channel multiplied by the number of sides of the channel across which heat flows to the other fluid. Thus,

$$A_1 = L_1(\theta_i \to \theta_i + \pi) + 2L_1(\theta_i + \pi \to \theta_m - \phi) + L_1(\theta_m - \phi \to \theta_m)$$

Equation (3) used in this formulation gives, $z=r/2\pi a=(\theta-\theta_i+r_{\min}/a)/2\pi$ and $z_\phi=\phi/2\pi$,

$$\frac{A_1}{4\pi^2 a} = \left(z_m - \frac{z_\phi}{2}\right)^2 - \left(z_i + \frac{1}{4}\right)^2 - \frac{1-4z_\phi^2}{16} \tag{4}$$

It is common to display ε versus NTU$=\Sigma U_j A_j/C_{\min}$, U_j being the overall heat transfer coefficient for surface area A_j. For channel 1, heat is transferred on only the outer side in the innermost half turn ($\theta_i<\theta<\theta_i+\pi$), an entrance region, and on only the inner side in the last partial turn ($\theta_m-\phi<\theta<\theta_m$); for the penultimate region ($\theta_m-2\pi<\theta<\theta_m-\phi$) the outer side abuts the entrance region of channel 2. In the midregion, heat is transferred from both sides and U is nearly constant. Thus,

$$C_{\min} = [U_i A_i + 2UA_{\text{mid}} + (U_o + U)A_{\text{pen}}]/\text{NTU}$$

Generally, $U_i > U$ and $U_o > U$. In terms of the center-line length L,

$$C_{\min}\text{NTU}/U = R_i L_1(\theta_i \to \theta_i + \pi) + 2L_1(\theta_i + \pi \to \theta_m - 2\pi) + (R_o + 1)L_1(\theta_m - 2\pi \to \theta_m - \phi) + L_1(\theta_m - \phi \to \theta_m)$$

in which $R_i=U_i/U$ and $R_o=U_o/U$. Use of Eq. (3) in this formulation results in

$$b = \frac{C_{\min}}{4\pi^2 aU} = \left\{\left(z_m - \frac{z_\phi}{2}\right)^2 - \left(z_i + \frac{1}{4}\right)^2 - \frac{1-4z_\phi^2}{16} - (1-R_o)\left[(1 - z_\phi)z_m + \frac{z_\phi^2}{2}\right] - \frac{(1-R_i)}{2}z_i + \frac{3+R_i-4R_o}{8}\right\} \Big/ \text{NTU} \tag{5}$$

Contributed by the Heat Transfer Division of ASME for publication in the JOURNAL OF HEAT TRANSFER. Manuscript received February 10, 2005; final manuscript received August 8, 2005. Review conducted by Anthony M. Jacobi.

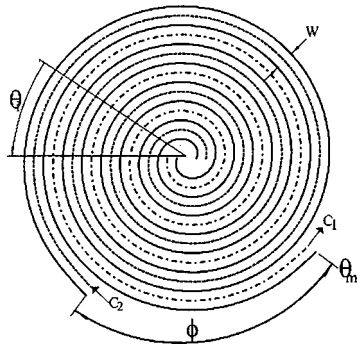

Fig. 1 Geometry of the spiral-plate heat exchanger in overview

Describing Equations. The describing equations (derivations are given by Burmeister [25]) are, for the fluid in channel 1,

$$-\frac{bC_1}{R_iC_{\min}}\frac{dT_1(z)}{dz}+\left(z+\frac{1}{4}\right)[T_2(z)-T_1(z)]=0,\quad z_i\leqslant z\leqslant z_i+\frac{1}{2} \tag{6a}$$

$$-\frac{bC_1}{C_{\min}}\frac{dT_1(z)}{dz}+\left(z+\frac{1}{4}\right)[T_2(z)-T_1(z)]+\left(z-\frac{1}{4}\right)[T_2(z-1)-T_1(z)]=0,\quad z_i+\frac{1}{2}\leqslant z\leqslant z_m-1 \tag{6b}$$

$$-\frac{bC_1}{C_{\min}}\frac{dT_1(z)}{dz}+R_o\left(z+\frac{1}{4}\right)[T_2(z)-T_1(z)]+\left(z-\frac{1}{4}\right)[T_2(z-1)-T_1(z)]=0,\quad z_m-1\leqslant z\leqslant z_m-\frac{\phi}{2\pi} \tag{6c}$$

$$-\frac{bC_1}{C_{\min}}\frac{dT_1(z)}{dz}+\left(z-\frac{1}{4}\right)[T_2(z-1)-T_1(z)]=0,\quad z_m-\frac{\phi}{2\pi}\leqslant z\leqslant z_m \tag{6d}$$

with $z=r/2\pi a=(\theta-\theta_i+r_{\min}/a)/2\pi$. For the fluid in channel 2 the equations are

$$\frac{bC_2}{R_iC_{\min}}\frac{dT_2(z)}{dz}+\left(z+\frac{3}{4}\right)[T_1(z+1)-T_2(z)]=0,\quad z_i-\frac{1}{2}\leqslant z\leqslant z_i \tag{7a}$$

$$\frac{bC_2}{C_{\min}}\frac{dT_2(z)}{dz}+\left(z+\frac{1}{4}\right)[T_1(z)-T_2(z)]+\left(z+\frac{3}{4}\right)[T_1(z+1)-T_2(z)]=0,\quad z_i\leqslant z\leqslant z_m-1 \tag{7b}$$

$$\frac{bC_2}{R_oC_{\min}}\frac{dT_2(z)}{dz}+\left(z+\frac{1}{4}\right)[T_1(z)-T_2(z)]=0,\quad z_m-1\leqslant z\leqslant z_m-\frac{\phi}{2\pi} \tag{7c}$$

The equations for inner and outer regions are similar to those for middle turns with zero overall heat transfer coefficient at either the inner or outer wall.

Solution. Coupling between adjacent channels complicates Eqs. (6) and (7), differing from those considered by others only in that radial distance is measured to a channel center line instead of to a wall, by involving $T(z\pm1)$. Two measures provide simplification. First, in view of the typical range $2\leqslant z\leqslant 40$, fractional increments of z are neglected so that $z+1/4$ is replaced by z and so forth, taking advantage of writing the equations in terms of the distance to a channel center line. Second, Taylor series are used to represent $T(z\pm1)$ in terms of $T(z)$ as done by others. Also, $C_1=C_2$ is stipulated.

Middle Turns. With the simplifications stated above, Eq. (6*b*) for the middle turns becomes

$$b\frac{dT_1(z)}{dz}+2zT_1(z)=z[T_2(z)+T_2(z-1)] \tag{8}$$

The first term of the Taylor series expansion $T_2(z)+T_2(z-1)=2T_2(z-1/2)+d^2T_2(z-1/2)/dz^2/4+\cdots$ for the right-hand side of this differential equation results in

$$\frac{dT_1(z)}{dz}+\frac{2z}{b}T_1(z)=\frac{2z}{b}T_2\left(z-\frac{1}{2}\right) \tag{9}$$

An integrating factor for Eq. (9) is $\exp(z^2/b)$, enabling it to be recast as

$$\frac{d\left[T_1(z)\exp\left(\frac{z^2}{b}\right)\right]}{dz}=\frac{2z}{b}\exp\left(\frac{z^2}{b}\right)T_2\left(z-\frac{1}{2}\right)$$

Proceeding similarly for Eq. (7*b*) gives

$$\frac{dT_2(z)}{dz}-\frac{2\left(z+\frac{1}{2}\right)}{b}T_2(z)=-\frac{z}{b}[T_1(z+1)+T_1(z)],\quad z_i+\frac{1}{2}\leqslant z_m-1$$

An integrating factor for this equation is $\exp(-(z+1/2)^2/b)$, enabling it to be recast as

$$\frac{d\left[\exp\left(-\frac{z^2}{b}\right)T_2\left(z-\frac{1}{2}\right)\right]}{dz}=-\frac{z}{b}\exp\left(-\frac{z^2}{b}\right)\left[T_1\left(z+\frac{1}{2}\right)+T_1\left(z-\frac{1}{2}\right)\right] \tag{10}$$

Differentiation of Eq. (9) with respect to z results in

$$\frac{d\left\{\left[\frac{b}{2z}\frac{dT_1(z)}{dz}+T_1(z)\right]\exp\left(-\frac{z^2}{b}\right)\right\}}{dz}=\frac{d\left[T_2\left(z-\frac{1}{2}\right)\exp\left(-\frac{z^2}{2b}\right)\right]}{dz} \tag{11}$$

Drawing on Eq. (9) for the right-hand side of Eq. (11) puts it into the form

$$\frac{d\left\{\left[\frac{b}{2z}\frac{dT_1(z)}{dz}+T_1(z)\right]\exp\left(-\frac{z^2}{b}\right)\right\}}{dz}=-\frac{z}{b}\exp\left(-\frac{z^2}{b}\right)\left[T_1\left(z+\frac{1}{2}\right)+T_1\left(z-\frac{1}{2}\right)\right]$$

Two terms of the Taylor series expansion $T_1(z+1/2)+T_1(z-1/2)\approx 2T_1(z)+d^2T_1(z)/dz^2/4+\cdots$ then give

$$z(z^2+2b^2)\frac{d^2T_1(z)}{dz^2}=2b^2\frac{dT_1(z)}{dz}$$

whose solution is found, aided by Maple [26] described by Heck [27], to be

$$T_2(z) = K_2 + K_1(z^2 + 2b^2)^{1/2}, \quad z_i + \frac{1}{2} \leqslant z \leqslant z_m - \frac{\phi}{2\pi} \quad (12a)$$

Equations (12*a*) and (12*b*) predict the linear temperature variation in the middle turns found by Strenger et al. [24] with finite difference solutions for large NTU. With $T_1(z)$ in hand, $T_2(z)$ is available from Eq. (8) as

$$T_2(z) = K_2 + K_1\left\{\left[\left(z+\frac{1}{2}\right)^2 + 2b^2\right]^{1/2} + \frac{b}{2\left[\left(z+\frac{1}{2}\right)^2 + 2b^2\right]^{1/2}}\right\} \quad (12b)$$

Innermost Segment. The temperature variation in the innermost segment of channel 1 is described by Eq. (6*a*) as

$$\frac{dT_1(z)}{dz} + R_i\frac{z+\frac{1}{2}}{b}T_1(z) = R_i\frac{z+\frac{1}{2}}{b}T_2(z), \quad z_i \leqslant z \leqslant z_i + \frac{1}{2}$$

Here, $(z+1/4)$ has been replaced with $(z+1/2)$ for convenience in accounting, imprecisely, for the effect of $R_i \neq 1$ because $T_2(z)$ is expressed in terms of the latter in Eq. (12*b*). With the aid of an integrating factor and Eq. (12*b*), this equation is rewritten as

$$\frac{d\left\{\exp\left[R_i\frac{\left(z+\frac{1}{2}\right)^2}{2b}\right]T_1(z)\right\}}{dz} = R_i\frac{z+\frac{1}{2}}{b}\exp\left[R_i\frac{\left(z+\frac{1}{2}\right)^2}{2b}\right]\left(K_2 + K_1\left\{\left[\left(z+\frac{1}{2}\right)^2 + 2b^2\right]^{1/2} + \frac{b}{2\left[\left(z+\frac{1}{2}\right)^2 + 2b^2\right]^{1/2}}\right\}\right)$$

After integration by parts and the transformation $x^2 = R_i[(z+1/2)^2 + 2b^2]/2b$, the solution is found to be

$$T_1(z) = K_3\exp\left[-R_i\frac{\left(z+\frac{1}{2}\right)^2}{2b}\right] + K_2 + K_1\left(\left[\left(z+\frac{1}{2}\right)^2 + 2b^2\right]^{1/2} - \left(\frac{b}{2R_i}\right)^{1/2}(2-R_i)D\left(\left\{R_i\frac{\left[\left(z+\frac{1}{2}\right)^2 + 2b^2\right]}{2b}\right\}^{1/2}\right)\right) \quad (13a)$$

Penultimate Segment. The temperature of the fluid in channel 2 in the penultimate section is described by Eq. (7*c*) as

$$\frac{dT_2(z)}{dz} - R_o\frac{z}{b}T_2(z) = -R_o\frac{z}{b}T_1(z), \quad z_m - 1 \leqslant z \leqslant z_m - \frac{\phi}{2\pi}$$

Use of an integrating factor and the solution for $T_1(z)$ given by Eq. (12*a*) enables recasting as

$$\frac{d\left[\exp\left(R_o\frac{z^2}{2b}\right)T_2(z)\right]}{dz} = -R_o\frac{z}{b}\exp\left(-R_o\frac{z^2}{2b}\right)[K_2 + K_1(z^2+2b^2)^{1/2}]$$

Here, fractional increments of z have been neglected and the effect of $R_o \neq 1$ is approximated. Integration by parts after use of the transformation $X^2 = R_o(z^2+2b^2)/2b$ leads to the solution

$$T_2(z) = K_4\exp\left(R_o\frac{z^2}{2b}\right) + K_2 + K_1\left\{\left(z+\frac{1}{2}\right)^{1/2} - \left(\frac{\pi b}{2R_o}\right)^{1/2}\exp\left(R_o\frac{z^2+2b^2}{2b}\right)\mathrm{erf}\left[\left(R_o\frac{z^2+2b^2}{2b}\right)^{1/2}\right]\right\} \quad (13b)$$

Outermost Segment. The temperature of the fluid in channel 1in the outermost segment is described by Eq. (6*d*) as

$$\frac{dT_1(z)}{dz} + \frac{z-\frac{1}{2}}{b}T_1(z) = \frac{z-\frac{1}{2}}{b}T_2(z-1), \quad z_m - \frac{\phi}{2\pi} \leqslant z \leqslant z_m$$

Here, $(z+1/4)$ has been replaced with $(z+1/2)$ for convenience. With the aid of an integrating factor and Eq. (12*b*), this equation is rewritten as

$$\frac{d\left\{\exp\left[\frac{\left(z-\frac{1}{2}\right)^2}{2b}\right]T_1(z)\right\}}{dz} = \frac{z-\frac{1}{2}}{b}\exp\left[\frac{\left(z-\frac{1}{2}\right)^2}{2b}\right]\left[K_2 + K_1\left\{\left[\left(z-\frac{1}{2}\right)^2 + 2b^2\right]^{1/2} + \frac{b}{2\left[\left(z-\frac{1}{2}\right)^2 + 2b^2\right]^{1/2}}\right\}\right]$$

After integration by parts and the transformation $y^2 = [(z-1/2)^2 + 2b^2]/2b$ the solution is obtained as

$$T_1(z) = K_5\exp\left[-\frac{\left(z-\frac{1}{2}\right)^2}{2b}\right] + K_2 + K_1\left\{\left[\left(z-\frac{1}{2}\right)^2 + 2b^2\right]^{1/2} - \left(\frac{b}{2}\right)^{1/2}D\left(\left[\frac{\left(z+\frac{1}{2}\right)^2 + 2b^2}{2b}\right]^{1/2}\right)\right\} \quad (14)$$

Boundary Condition Application. The five constants are evaluated by applying the conditions of two known inlet temperatures

$$T_1(z_i) = T_{1i}, \quad T_2(z_m - z_\phi) = T_{2i}$$

and three matching temperatures at the common boundaries of adjacent regions

$$T_1\left(z_i + \frac{1^-}{2}\right) + T_1\left(z_i + \frac{1^+}{2}\right), \quad T_2(z_m - 1^-) = T_2(z_m - 1^+),$$

$$T_1(z_m - z_\phi^-) = T_1(z_m - z_\phi^+)$$

Discussion. The effectiveness ε of the spiral-plate heat exchanger can be expressed in terms of these solutions. By definition

$$\varepsilon = \frac{q_{\text{actual}}}{q_m} = \frac{C_1(T_{1o} - T_{1i})}{C_{\min}(T_{1i} - T_{2i})} = \frac{\text{Num}}{\text{Den}} \quad (15)$$

Incorporation of the stipulation of equal capacitance rates and Eq. (13*a*) for $T_1(z_m) = T_{1o}$ gives, the length mainly due to the description of events in the innermost and outmost turns,

$$\text{Num} = \left[\left(z_m - \frac{1}{2}\right)^2 + 2b^2\right]^{1/2} - \left[\left(z_i + \frac{1}{2}\right)^2 + 2b^2\right]^{1/2} + \frac{z_m - z_\phi - \frac{1}{4}}{2[(z_m - z_\phi)^2 + 2b^2]^{1/2}} \exp\left[-\frac{z_\phi(2z_m - 1 - z_\phi)}{2b}\right] + \frac{z_i + \frac{3}{4}}{2\left[\left(z_i + \frac{1}{2}\right)^2 + 2b^2\right]^{1/2}} \exp\left[\frac{R_i\left(z_i + \frac{3}{4}\right)}{2b}\right] + \frac{b}{2}\left\{\frac{\exp[-z_\phi(2z_m - 1 - z_\phi)/2b]}{\left[\left(z_m - \frac{1}{2} - z_\phi\right)^2 + 2b^2\right]^{1/2}} - \frac{1}{\left[\left(z_m - \frac{1}{2}\right)^2 + 2b^2\right]^{1/2}}\right\} + \frac{b(2 - R_i)}{2R_i}\left\{-\frac{\exp\left[R_i\left(z_i + \frac{3}{4}\right)\Big/ 2b\right]}{[(z_i + 1)^2 + 2b^2]^{1/2}} + \frac{1}{\left[\left(z_i + \frac{1}{2}\right)^2 + 2b^2\right]^{1/2}}\right\} \tag{16a}$$

$$\text{Den} = [(z_m - z_\phi)^2 + 2b^2]^{1/2} - \left[\left(z_i + \frac{1}{2}\right)^2 + 2b^2\right]^{1/2} + \frac{z_m - \frac{3}{4} + b}{2\left[\left(z_m - \frac{1}{2}\right)^2 + 2b^2\right]^{1/2}} \exp\left[\frac{R_o(1 - z_\phi)(2z_m - 1 - z_\phi)}{2b}\right] + \frac{z_i + \frac{3}{4}}{2\left[\left(z_i + \frac{1}{2}\right)^2 + 2b^2\right]^{1/2}} \exp\left[\frac{\left[R_i\left(z_i + \frac{3}{4}\right)\right]}{2b}\right] - \frac{b}{R_o}\left\{\frac{\exp[R_o(1 - z_\phi)(2z_m - 1 - z_\phi)/2b]}{[(z_m - 1)^2 + 2b^2]^{1/2}} - \frac{1}{[(z_m - z_\phi)^2 + 2b^2]^{1/2}}\right\} - \frac{b(2 - R_i)}{2R_i}\left\{\frac{\exp\left[R_i\left(z_i + \frac{3}{4}\right)\Big/ 2b\right]}{[(z_i + 1)^2 + 2b^2]^{1/2}} - \frac{1}{\left[\left(z_i + \frac{1}{2}\right)^2 + 2b^2\right]^{1/2}}\right\} \tag{16b}$$

Numerical evaluations have been eased by use of asymptotic forms [27] $D(\zeta) \approx 1/2\zeta$ for the Dawson function and $\text{erf}(\zeta) \approx 1 - \exp(-\zeta^2)/\zeta\sqrt{\pi}$ for the error function into Eq. (16). Since the minimum argument of Eq. (16) is $z\sqrt{2}$ and $z_i \approx 2$ gives a least numerical value exceeding 3, the asymptotic forms are accurate.

Effectiveness versus NTU without entrance-region effects ($R_i = 1 = R_o$) is shown in Fig. 2 for $z_i = 2$ and $\phi = \pi$. For $z_m > z_c$, the critical value z_c is discussed later, there is a globally maximum ε, ε_m, and a decrease to zero as NTU becomes large. For $z_m = z_c$, there is a globally maximum ε and a decrease to a nonzero value as NTU becomes large. For $z_m < z_c$, ε approaches unity as NTU becomes large.

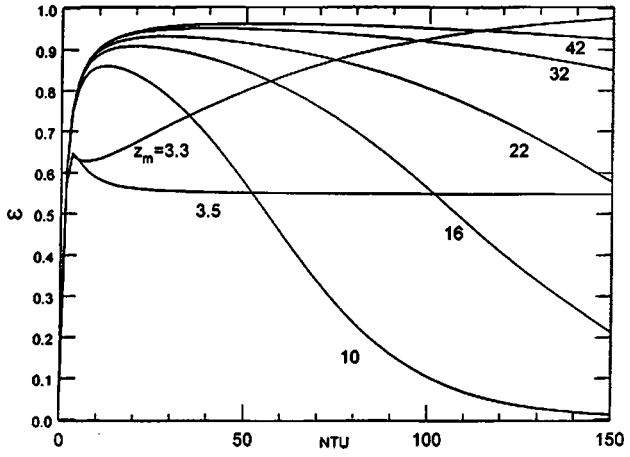

Fig. 2 Effectiveness ε versus number of transfer units NTU From Eq. (16) for $z_i = 2$, $\varphi = \pi/2$, $R_o = 1 = R_i$ and several values of z_m

The present predictions are compared in Fig. 3 with the finite-difference solution for $\phi = \pi$ of Strenger et al. [24] and the symbolic solution for $\phi = 0$ of Bes and Roetzel [16]. Agreement is good for all NTU below and in the vicinity of ε_m, the most important range. For NTU substantially above the value, NTU_m, at which ε_m occurs, the results of the other two investigations are higher. Bes and Roetzel [16] give ε_m, n is the number of double turns, and r_i is the innermost radius, as

$$1/\varepsilon_m - 1 = \frac{2.485}{[(n-1)(n+2r_i)]^{1/2}} = \frac{1.243}{\left[\left(z_m - \frac{1}{2} - z_i\right)(z_m + z_i)\right]^{1/2}} \tag{17}$$

and

$$\text{NTU} = 0.99013[(n-1)n + 2r_i]^{1/2} = 1.98026[(z_m - \tfrac{1}{2} - z_i)(z_m + z_i)]^{1/2}, \quad n \geq 6 \tag{18}$$

Their prediction for ε in terms of variables of the present study is

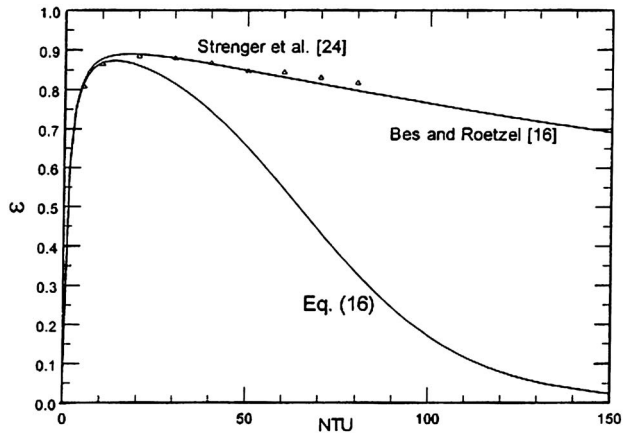

Fig. 3 Comparison of predicted effectiveness versus number of transfer units for $z_i = 2.5$, $\varphi = \pi$, $R_o = 1 = R_i$, and $z_m = 11.25$

$$\frac{1}{\varepsilon}-1=\frac{\mathrm{NTU}/[(z_m-1/2)^2-z_i^2]}{\ln\left(\dfrac{1+\{(z_m-1/4)\mathrm{NTU}/[(z_m-1/2)^2-z_i^2]\}^2}{1+\{(z_i-1/4)\mathrm{NTU}/[(z_m-1/2)^2-z_i^2]\}^2}\right)}$$

Although the special conditions at the inlet and outlet are not taken into account, there is agreement with the present prediction that $\varepsilon\to 0$ as $\mathrm{NTU}\to\infty$, although more slowly.

The finite-difference results of Strenger et al. [24] were obtained with five nodes for each half turn, each of constant (not spiral) radius as also for the numerical study of Bes and Roetzel [17], too few nodes to capture the rapid temperature variation near inlets and outlets, given by Eqs. (13*a*) and (14) as $\exp[-(z\pm 1/2)^2/2b]$, when NTU becomes large. Since the results of Bes and Roetzel [16] and Strenger et al. [24] are close to each other and the former do not accurately account for the entrance and exit conditions that are the major cause of the peak in ε, it is believed that their agreement signifies mutual inability to represent the effects of the innermost and outermost segments for large NTU values. The discrepancy becomes significant at increasingly large NTU values as z_m increases. For z_m in excess of about 20, the discrepancy is not significant until NTU attains values far above that of maximum effectiveness.

In agreement for small NTU, Strenger et al. [24] have $\varepsilon/\mathrm{NTU}=1$, Bes and Roetzel [16] have

$$\frac{\varepsilon}{\mathrm{NTU}}=1+\frac{2z_m+\dfrac{1}{8}}{z_m^2-3\dfrac{z_m}{2}-z_i^2-\dfrac{1}{2}\left(z_i+\dfrac{1}{4}\right)}$$

which gives $\varepsilon/\mathrm{NTU}=1.222$ for the conditions of Strenger et al. [24], and the present prediction is

$$\frac{\varepsilon}{\mathrm{NTU}}=1+\frac{6\left(1-\dfrac{\phi}{2\pi}\right)z_m-\dfrac{\phi}{\pi}+\left(\dfrac{\phi}{2\pi}\right)^2(3-R_o)+R_i+R_o-1}{4\left\{z_m^2-\left(3-\dfrac{\phi}{2\pi}\right)\dfrac{z_m}{2}-z_i^2-\left(1-\dfrac{R_i}{2}\right)\left(z_i+\dfrac{1}{4}\right)+\dfrac{1-R_o}{4}\left[1-\left(\dfrac{\phi}{2\pi}\right)^2\right]\right\}}$$

which gives $\varepsilon/\mathrm{NTU}=1.082$ for the conditions of Strenger et al. [24].

The prediction for ε_m of Eq. (17) can be rearranged into the form

$$\frac{1}{1-\varepsilon_m}=1+0.8048[\,z_m-z_i-1/2)(z_m+z_i)]^{1/2} \tag{19}$$

This suggests a linear relationship between $1/(1-\varepsilon_m)$ and z_m that is seen in Fig. 4. The prediction of Bes and Roetzel [16] for $\phi=0$ has a smaller slope than the numerical predictions of Strenger et al. [24] for $\varepsilon=\pi$. The present predictions are intermediate with the slope for $\phi=\pi$ exceeding that for $\phi=0$.

As can be seen in Figs. 4 and 5, the prediction of Eq. (16) agrees well with the NTU_m obtained by Strenger et al. [24] and with the prediction of Eq. (18) by Bes and Roetzel [16].

Bes and Roetzel [16] predict that there is no maximum in ε for $n\leqslant 4$. Strenger et al. [24] remark that they could not establish $\varepsilon(\mathrm{NTU}\to\infty)$ by their finite-difference solutions, although stating that $\varepsilon_\infty=0$ for entrances at the core and the outside on the same side and $\varepsilon_\infty>0$ when those entrances are on opposite sides. Information on this is available from the present results. In the limit as $b\to 0$, $b\sim 1/\mathrm{NTU}$ according to Eq. (5) and then the solution for ε in Eq. (16) has the form

$$\varepsilon(b\to 0)=1\Bigg/\left\{1+\frac{\left(z_m-\dfrac{3}{4}\right)\left(z_i+\dfrac{1}{2}\right)}{\left(z_m-\dfrac{1}{2}\right)\left(z_i+\dfrac{3}{4}\right)}\exp\left[\frac{R_o(1-z_\phi)(2z_m-1-z_\phi)}{2b}-\frac{R_i\left(z_i+\dfrac{3}{4}\right)}{2b}\right]\right\}$$

whose behavior is controlled by the exponential term. Thus, there is a critical z_m, z_c, given by

$$z_c=\frac{1-z_\phi^2+\left(z_i+\dfrac{3}{4}\right)\dfrac{R_i}{R_o}}{2(1-z_\phi)} \tag{20}$$

Since the critical number of turns $N_c=z_m-z_i$, $z_c>z_i$. The accompanying limiting effectiveness is

$$\varepsilon(\mathrm{NTU}\to\infty)=\begin{cases}0, z_m\rangle z_c\\ 1\Big/\left\{1+\left(z_m-\dfrac{3}{4}\right)\left(z_i+\dfrac{1}{2}\right)\Big/\left[\,z_m-\dfrac{1}{2}\right)\left(z_i+\dfrac{3}{4}\right)\right]\right\}, z_m=z_c\\ 1, z_m\langle z_c\end{cases}$$

For $z_i=2$, $z_\phi=1/2$, and $R_i=2R_o$, Eq. (20) gives the critical number of turns as $N_c=6.25$. Although the parameter values used by Bes

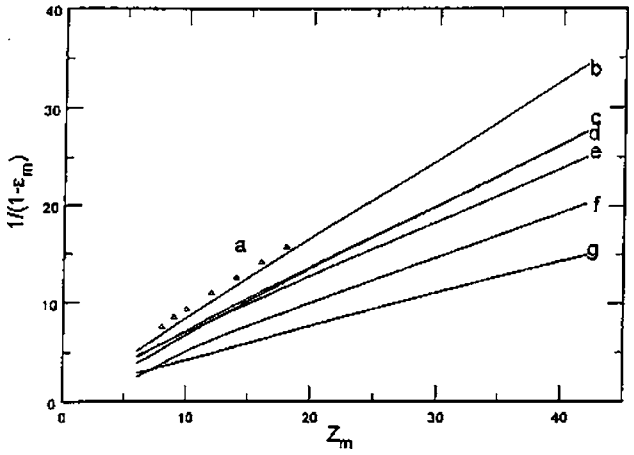

Fig. 4 Inverse maximum effectiveness deficit versus maximum dimensionless angle: (*a*) [24] for $z_i=2.5$, $\phi=\pi$, $R_o=1=R_i$; (*b*) [16] for $z_i=2$, $\phi=\pi$, $R_o=1=R_i$; (*c*) Eq. (16) for $z_i=2$, $\phi=\pi$, $R_o=1=R_i$; (*d*) Eq. (16) for $z_i=3$, $\phi=\pi$, $R_o=1=R_i$; (*e*) Eq. (16) for $z_i=2$, $\phi=0$, $R_o=1=R_i$; (*f*) Eq. (16) for $z_i=2$, $\phi=0$, $R_o=2=R_i$; (*g*) Eq. (16) for $z_i=2$, $\phi=\pi$, $R_o=2=R_i$

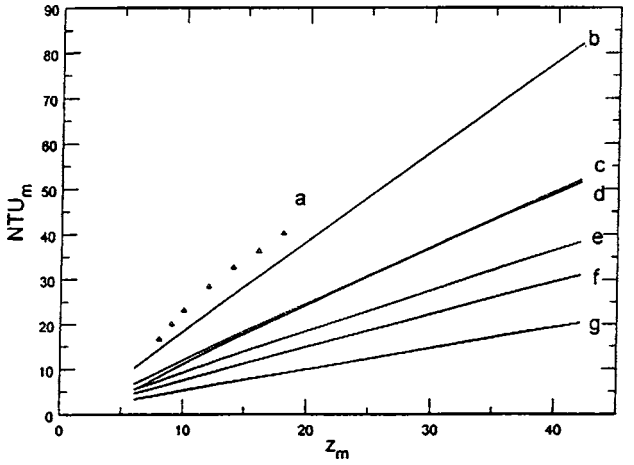

Fig. 5 Maximal number of transfer units NTU_m at which the maximum effectiveness ε_m occurs versus maximum dimensionless angle z_m: (*a*) Strenger et al. [24] for $z_i=2.5$, $\phi=\pi$, $R_o=1=R_i$; (*b*) Bes and Roetzel [16] for $z_i=2$, $\phi=0$, $R_o=1=R_i$; (*c*) Eq. (16) for $z_i=2$, $\phi=\pi$, $R_o=1=R_i$; (*d*) Eq. (16) for $z_i=3$, $\phi=\pi$, $R_o=1=R_i$; (*e*) Eq. (16) for $z_i=2$, $\phi=0$, $R_o=1=R_i$; (*f*) Eq. (16) for $z_i=2$, $\phi=\pi$, $R_o=2=R_i$; (*g*) Eq. (16) for $z_i=2$, $\phi=0$, $R_o=2=R_i$

and Roetzel [16] are unknown, this is in fair agreement with their prediction that no maximum in ε occurs for n, the number of double turns, less than 4. Strenger et al. [24] have $z_\phi=1/2, z_i=2.5$, and $R_o=1=R_i$ for which Eq. (20) gives $N_c=4$. This is of the same size as their $8\leqslant N\leqslant 18$, partly explaining why they were unable to resolve the limiting value of ε at large NTU, a difficulty also remarked upon by Bes and Roetzel [16].

The effects of parameters on ε are shown in Fig. 6 for $z_m=10$. Case (b) differs from case (a) for which $z_i=2, \phi=\pi$, $R_o=1=R_i$ only in that the inner dimensionless angle z_i is increased to $4-\varepsilon$ is reduced only in the high NTU region with a slight reduction in ε_m and NTU_m. The reduced ε is due to a reduction in the heat transfer area which is roughly proportional to $z_m^2-z_i^2$ [see Eq. (4)] and the slightness is due to the fact that most of the heat transfer area is near the outer periphery. Case (c) differs from case (a) only in that the offset angle ϕ is decreased to 0. There is considerable reduction of ε in the high-NTU region, but ε_m is barely reduced while NTU_m is noticeably reduced. The entrance region effects are shown in cases (d) and (e) in which the limiting value of 2 is used for the ratio R to be reduction in both ε_m and NTU_m and, generally, in ε for all NTU in the near- and above-optimal regions.

Nomenclature

a = constant for the Archimedean spiral, see Eq. (1) (m)
A = area $(m)^2$
b = parameter, $=C_{min}/4\pi^2 aU$
C = ratio of capacitance rates, $=C_{min}/C_{max}$
C_p = specific heat (kJ/kg K)
C_1 = capacitance rate in channel 1, $=\dot{m}C_p$(kJ/sK)
$D(z)$ = Dawson's integral, $=\exp(-z^2)\int_0^z \exp(t^2)dt$
e = natural number, $=2.71828\ldots$
$\mathrm{erf}(x)$ = error function, $=2/\sqrt{\pi}\int_0^x \exp(-t^2)dt$
$\exp(x)$ = exponential function, $=e^x$
L = length along channel center line (m)
n = number of double turns, $=2N$
N = number of turns of a single channel, $=z_m-z_i$
q = heat flow rate
r = radial distance to channel 1 center line (m)
r_i = innermost radius of Ref. [16] (m)
R = ratio of local to average overall heat transfer coefficient
T = temperature (K)
U = overall heat transfer coefficient $(W/m^2 K)$
W = channel width, $m=\pi a$
x = transformed coordinate, $=\{R_i[(z+1/2)^2+2b^2]/2b\}^{1/2}$
X = transformed coordinate, $=[R_o(z^2+2b^2)/2b]^{1/2}$
y = transformed coordinate, $=\{[(z-1/2)^2+2b^2]/2b\}^{1/2}$
z = dimensionless coordinate, $=r/2\pi a=(\theta-\theta_i+r_{min}/a)/2\pi$
z_i = $r_{min}/2\pi a$
z_ϕ = $\phi/2\pi$

Greek Symbols

ε = effectiveness, $=q_{actual}/q_m$
θ = angular coordinate
π = natural number, $\pi=3.1415\cdots$
ϕ = offset angle for channel 2 inlet from channel 1 outlet

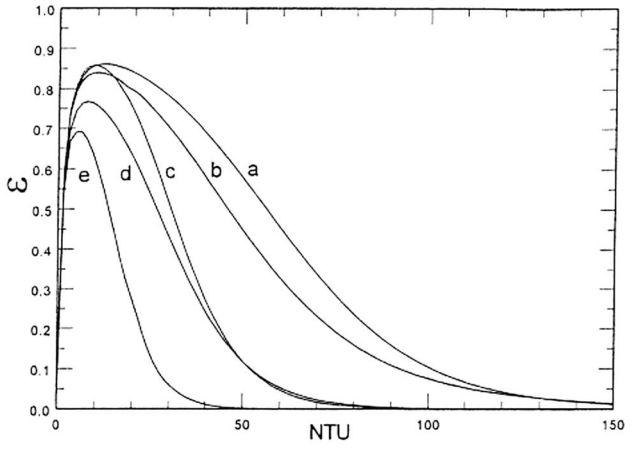

Fig. 6 The effect of parameters on effectiveness ε versus number of transfer units NTU from Eq. (16) for $z_m=10$: (*a*) $z_i=2$, $\phi=\pi$, $R_o=1=R_i$; (*b*) $z_i=4$, $\phi=\pi$, $R_o=1=R_i$; (*c*) $z_i=2$, $\phi=0$, $R_o=1=R_i$; (*d*) $z_i=2$, $\phi=\pi$, $R_o=2=R_i$; (*e*) $z_i=2$, $\phi=0$, $R_o=2=R_i$

Subscripts

c = critical
i = inner, inlet
j = index
m = maximum
mid = middle
min = minimum
o = outer
pen = penultimate
1 = channel 1
2 = channel 2
∞ = value at large argument

References

[1] Boothroyd, A., 1997, "Spiral Heat Exchangers," *International Encyclopedia of Heat and Mass Transfer*, G. Hewitt, G. Shires, and Y. Polezhaev, eds., CRC Press, New York, 1997, p. 1044.

[2] Fraas, A., *Heat Exchanger Design*, 1989, Wiley-Interscience, New York, p. 226.

[3] *Thermal Handbook*, Alfa Laval, Sweden.

[4] *Chemical Engineering Processes and Equipment*, 1955, E. Molloy, ed., George Newnes Ltd., London, United Kingdom, pp. 185–188.

[5] *Heat Exchangers, Theory and Practice*, 1983, J. Taborek, G. Hewitt, and N. Afgan, eds., Hemisphere, New York, p. 683.

[6] Gupta, J., 1986, *Fundamentals of Heat Exchanger and Pressure Vessel Technology*, Hemisphere, New York, pp. 317–320.

[7] Egner, M., and Burmeister, L., 2005, "Laminar Flow and Heat Transfer in Spiral Ducts," J. Heat Transfer, **127**, pp. 352–356.

[8] Baird, M., McCrae, W., Rumford, F., and Slesser, C., 1957, "Some Considerations on Heat Transfer in Spiral Plate Heat Exchangers," Chem. Eng. Sci., **7**, pp. 112–115.

[9] Zaleski, T., and Krajewski, W., 1972, "Meted Obliczania Wymienników Spiralnych," Inżynieria Chemiczna, **2**, pp. 35–51 (in Polish).

[10] Ciéslinski, P., and Bes, T., 1983, "Analytical Heat-Transfer Studies in a Spiral Plate Exchanger," in *Proceedings of the XVth International Congress Refrigeration (Paris)*, V. II, paper B. 1-198, pp. 449–454.

[11] Jarzebski, A., 1984, "Dimensioning of Spiral Heat Exchangers to Give Minimum Costs," Int. J. Heat Mass Transfer, **106**, pp. 633–637.

[12] Chowdhury, K., Linkmeyer, H., Bassiouny, M., and Martin, H., 1985, "Analytical Studies on the Temperature Distribution in Spiral Plate Heat Exchangers: Straightforward Design Formulae for Efficiency and Mean Temperature Difference," Chem. Eng. Process., **19**, pp. 183–190.

[13] Zaleski, T., and Lachowski, A., 1987, "Unsteady Temperature Profiles in Parallel-Flow Spiral Heat Exchangers," Int. Chem. Eng., **27**, pp. 556–565.

[14] Zhang, N., Jiao, Z., Ni, Z., and Kung, H.-C., 1988, "A Computational Method for Thermal Design of Spiral Plate Heat Exchanger," in *Proceedings of the 1988 Heat Transfer Conference* (July 24–27, Houston, TX, ASME HTD-96, Vol. 1, pp. 445–449.

[15] Morimoto, E., and Hotta, K., 1988, "Study of the Geometric Structure and Heat Transfer Characteristics of a Spiral Plate Heat Exchanger," Heat Transfer-Jpn. Res., **17**, pp. 54–71.

[16] Bes, T., and Roetzel, W., 1991, "Approximate Theory of Spiral Heat Exchanger," *Design And Operation of Heat Exchangers*, in *Proceedings of the EUROTHERM Seminar No. 18, Feb. 17–March 1, 1991, Hamburg, Germany*, W. Roetzel, P. Heggs, and D. Butterworth, eds., Springer-Verlag, Berlin, pp. 223–232.

[17] Bes, T., and Roetzel, W., 1992, "Distribution of Heat Flux Density in Spiral Heat Exchangers," Int. J. Heat Mass Transfer, **35**, pp. 1331–1347.

[18] Bes, T., and Roetzel, W., 1993, "Thermal Theory of the Spiral Heat Exchanger," Int. J. Heat Mass Transfer, **36**, pp. 765–773.

[19] Yang, W.-J., and Rundle, D., 1994, "Optimized Thermal Design of Plate and Spiral Type Heat Exchangers," in *Proceedings of the 1994 International Mechanical Engineering Congress and Exp., Chicago, Illinois, Nov. 6–11*, ASME HTD-Vol. 282, pp. 15–21.

[20] Devois, J., and Durastanti, J., 1996, "Modeling of a Spiral Plate Heat Exchanger by a Finite Difference Method," *New Developments in Heat Exchangers*, N. Afgan, M. Carvalho, A. Bar-Cohen, D. Butterworth, W. Roetzel, eds., Gordon and Breach, New York, pp. 377–401.

[21] Bes, T., 1987, "Eine Methode der thermische Berechnung von Gegen-und Gleichstrom-Spiralwärmeaustauschern," Wärme-und Stuffübertragung, **21**, pp. 301–309.

[22] Buonopane, R., and Troupe, R., 1970, "Analytical and Experimental Heat Transfer Studies in a Spiral Plate Heat Exchanger," *Heat Transfer 1970, Preprints of Papers Presented at the Fourth Int. Heat Transfer Conf., Paris-Versailles, France*, Verein Deutscher Ingenieure, Düsseldorf, Germany, **I**, Paper No. HE 2.5.

[23] Jones, A., Lloyd, S., and Weinberg, F., 1978, "Combustion in Heat Exchangers," Proc. R. Soc. London, Ser. A, **360**, pp. 97–115.

[24] Strenger, M., Churchill, S., and Retallick, W., 1990, "Operational Characteristics of a Double-Spiral Heat Exchanger for the Catalytic Incineration of Contaminated Air," Ind. Eng. Chem. Res., **29**, pp. 1977–1984.

[25] Burmeister, L., 2005, "Spiral-Plate Heat Exchanger Effectiveness With Equal Capacitance Rates," in *Proceedings of the 2005 ASME Summer Heat Transfer Conference*, July 17–22, San Francisco, CA, Paper No. HT2005-72041.

[26] *Maple 9 Getting Started*, 2003, Maplesoft, Waterloo Maple Inc., Waterloo, Canada.

[27] Heck, A., 2003, *Introduction To Maple*, 3rd ed., Springer-Verlag, New York.

[28] Abramowitz, A., and Stegun, I., 1965, *Handbook of Mathematical Functions*, National Bureau of Standards, Applied Mathematics Series No. 55, Superintendent of Documents, U.S. Government Printing Office, Washington, D.C. 20402, pp. 298 and 319.

Measurement of Total Hemispherical Emittance and Specific Heat of Aluminum and Inconel 718 by a Calorimetric Technique

Giovanni Tanda
Full Professor
e-mail: giovanni.tanda@unige.it

Mario Misale
Full Professor
e-mail: mario.misale@unige.it

Dipartimento di Ingegneria della Produzione,
Termoenergetica e Modelli Matematici (DIPTEM),
Università degli Studi di Genova,
via all'Opera Pia 15a,
I-16145 Genova, Italy

An apparatus for the measurement of the total hemispherical emittance and specific heat of metals has been developed. The measurement principle is based on the calorimetric technique: the sample, heated by Joule effect and placed in a vacuum chamber, exchanges radiative heat transfer with the walls of the container, kept at a relatively low temperature. Emittance is deduced from the radiative heat transfer laws at the steady state. When the heating power is switched off, the specific heat of the sample can be recovered from the time history of the sample temperature during the cooling transient. Measurements have been performed on samples of aluminum Anticorodal alloy and Inconel 718 alloy under different surface conditions in the 350–635 K *range.*
[DOI: 10.1115/1.2150840]

Keywords: emittance, specific heat, aluminum, Inconel 718, thermophysical properties

1 Introduction

Data on the thermophysical properties of metallic substances are very important in numerous engineering devices. Among these properties, emittance and specific heat play a crucial role in high-vacuum and/or high temperature conditions, which has encouraged the development of techniques for their precise and, when possible, simultaneous measurements.

Sasaki et al. [1] proposed a new principle for the simultaneous measurement of the total hemispherical emittance and specific heat of metals. The technique is based on the transient calorimetric method, usually employed only for measuring radiative properties (see, for instance [2–4]). Two types of samples were required: one type is made only of the test material and the other is a compound type made of the test material and of a standard material (of known emittance and specific heat). The processing of data recorded during a thermal transient of the samples inside a vacuum chamber allowed the simultaneous reconstruction of emittance and specific heat of the test material.

In this paper, a device for the measurements of the total hemispherical emittance and specific heat of metals is presented. The measurement principle is the steady-state calorimetric technique for the evaluation of total hemispherical emittance, while the specific heat is determined in transient conditions. The device has been applied to the measurement of thermal properties of commercial aluminum (Anticorodal 6063) and Inconel 718. These two materials are very popular in most heavy industries. Aluminum alloys found intense applications in transportation (aircraft and automotive structural parts), packaging (foils and cans), and construction (domes, bridges, sidings) owing to their favorable strength-to-weight ratio, corrosion resistance and full recyclability. Inconel 718 is a high-strength, high-temperature resistant and corrosion resistant nickel-chromium alloy. It is suitable for use at cryogenic temperatures and also for use in air up to 1000 K, and applications include gas turbine hot section components and cryogenic storage tanks.

Despite the widespread use of these two materials, there is still a lack of thermal properties in the technical literature, with special reference to radiative properties, markedly affected by surface conditions (microgeometry induced by a particular surface treatment, presence of oxide layers, etc.). In the present paper, total hemispherical emittance of aluminum and Inconel 718, measured under different surface conditions for both materials (including the presence of oxide layers) is reported, together with the specific heat versus temperature of both materials.

2 Theory

Consider a body (the sample), with isothermal, plane surfaces, suspended inside an isothermal cavity. The thermal radiation emitted, absorbed and reflected in the system is diffuse; sample and cavity surfaces are gray.

Under these assumptions, the net radiative heat transfer rate q between the body and the cavity surfaces is:

$$q = \sigma(T_s^4 - T_\infty^4)/[(1-\varepsilon_s)/\varepsilon_s A_s + 1/A_s F_{s,\infty} + (1-\varepsilon_\infty)/\varepsilon_\infty A_\infty] \quad (1)$$

where the subscripts s and ∞ denote sample and cavity properties, respectively, T is the surface temperature, A the surface area, ε the total hemispherical emittance, σ the Stefan-Boltzmann constant, and $F_{s,\infty}$ the sample-to-cavity view factor, equal to 1. The emittance ε_s of the sample surface can be easily obtained from Eq. (1):

$$\varepsilon_s = [\sigma A_s (T_s^4 - T_\infty^4)/q - C_\infty]^{-1} \quad (2)$$

where $C_\infty = (1-\varepsilon_\infty)A_s/(\varepsilon_\infty A_\infty)$ is a constant that can be neglected since A_s is typically much smaller than A_∞.

In the presence of high vacuum in the cavity, the heat dissipated by the sample (for instance by Joule effect, through a heater fitted inside) is almost totally transferred to the cavity by thermal radiation, provided that the cavity surfaces are maintained at a temperature lower than that of the internal body. Therefore, the heat transfer rate q can be evaluated as follows:

$$q = q_{\text{el}} - q_{\text{gas}} - q_k \quad (3)$$

where q_{el} is the heat transfer rate dissipated into the sample by Joule effect, q_{gas} is the conductive heat transfer rate through the residual gas in the evacuated cavity, and q_k is the conduction/radiation heat transfer rate through the wires suspending the sample. The measurements of q, properly corrected to take into account heat losses through the wires, as well as the sample and cavity surface temperatures (on several spots, to assess the required surface temperature uniformity) allow the evaluation of the emittance ε_s of the sample to be performed through Eq. (2).

As the heating power is turned off, the temperature T_s of the sample begins to decay, owing to the heat exchange with the cavity wall, taken at a lower temperature (T_∞). According to the lumped capacitance model, the cooling rate of the sample can be written as:

Contributed by the Heat Transfer Division of ASME for publication in the JOURNAL OF HEAT TRANSFER. Manuscript received December 21, 2004; final manuscript received June 15, 2005. Review conducted by Ashley F. Emery.

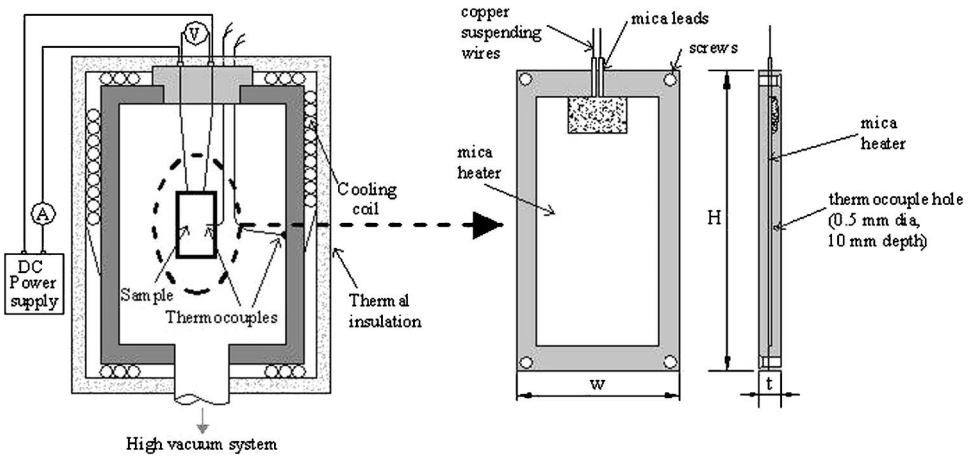

Fig. 1 Schematic drawing of the apparatus and sketch of the sample/heater assembly (*H* =0.09 m, *W*=0.05 m, *t*=0.007 m)

$$dT_s/d\tau = -[\sigma A_s(T_s^4 - T_\infty^4)/(1/\varepsilon_s + C_\infty) + q_k + q_{\text{gas}}]/(m_s c_{p,s} + m_h c_{p,h}) \tag{4}$$

where m_s and m_h denote the masses of the sample and heater, respectively, while $c_{p,s}$ and $c_{p,h}$ are the relevant specific heats and ε_s is the total hemispherical emittance at the actual temperature T_s. The values of m_h, m_s, and $c_{p,h}$ are typically known parameters; therefore the following expression for $c_{p,s}$ can be deduced,

$$c_{p,s} = -[\sigma A_s(T_s^4 - T_\infty^4)/(1/\varepsilon_s + C_\infty) + q_k + q_{\text{gas}}]/(m_s dT_s/d\tau) - m_h c_{p,h}/m_s \tag{5}$$

with $m_h \ll m_s$ in order to minimize the value of the term $m_h c_{p,h}/m_s$.

Equation (5) enables the specific heat of the sample (and its variation with temperature) to be determined from the measurements of the instantaneous values of T_s and its time history and from the previously calculated (by Eq. (2)) total hemispherical emittance.

3 Experiment

Figure 1 depicts the schematic layout of the experimental apparatus. A large stainless-steel chamber, cylindrical in shape (inner diameter=0.15 m, inner height=0.34 m) is connected to a high vacuum pump (able to attain air pressures as low as 10^{-4} Pa) and equipped with a cold cathode-pirani low pressure transducer. The inner surface of the chamber is black painted in order to minimize the value of constant C_∞ in Eq. (2), equal to 0.0143 in the present experiment. A copper coil, for the circulation of a fluid (water) coming from a thermostatic bath (typically programmed to maintain a container temperature of about 285 K), is wrapped around the outer surface of the chamber.

The sample consisted of two rectangular plates ($50\times90\times7$ mm) arranged as a sandwich structure, i.e., two identical thin plates with a plane electrical resistance (heater) sandwiched in between, as shown in Fig. 1 (right-hand side). Extra care was taken to mill the plates on the inner sides to accommodate the heater inside the material. The heater, made of mica in order to achieve temperatures up to 870 K, had the following dimensions: length 78 mm, width 40 mm, thickness 1 mm. The facing plates were blocked by four screws, whose area exposed to the chamber wall was less than 1% of the total sample area. The plate/heater assembly was suspended in the chamber by the electric wire of the heater, connected to a dc power supply. The electric wires were made of 0.5 mm diam copper, mechanically polished (expected emittance lower than 0.1).

According to Eq. (2), the total hemispherical emittance ε_s of the sample can be deduced by performing the temperature and heat transfer rate measurements at the steady state (typically after several hours from the beginning of each test). The thermal power dissipated into the resistance was measured by a voltmeter and an amperometer. Owing to the low Biot number of the plate, the temperature T_s of the sample, measured by means of a thin (0.5 mm diam), metal-sheathed, type K thermocouple, was expected to be fairly uniform over the sample surface. Preliminary tests, conducted placing two 0.5 mm diam thermocouples into small holes drilled into the material at different positions, confirmed this assumption. Five type K thermocouples were employed to measure the temperature T_∞ of the container in different spots at the inner wall, in order to check the degree of temperature uniformity. A digital data logger was employed to record all temperature data and to control the achievement of the steady state condition.

In order to evaluate ε_s with the desired accuracy, a reliable estimation of terms q_{gas} and q_k has to be performed. If the pressure of the container is in the low 10^{-4} Pa range, the term q_{gas} can be neglected as stated in previous papers [2,5]. The term q_k is associated with the thermal conduction along the sample thermocouple wire and the leads of the resistance and with radiation from the outside surface of the thermocouple and resistance leads to the container; it has been calculated by numerically solving the steady-state conduction equation for each wire

$$d^2T/dx^2 = c_0(T^4 - T_\infty^4) \tag{6}$$

where x is the spatial coordinate along the wire of length L, T is the wire temperature (equal to T_s and T_∞ at the two extremities $x=0$ and $x=L$, respectively) and c_0 is a constant depending on known parameters (diameter, thermal conductivity, and emittance of wire). The calculated heat loss from the wires has been taken into account in Eqs. (2) and (3); the role played by q_k for expected emittance of 0.3 and T_s equal to 400 K (T_∞ fixed at 300 K) is about 2.7% of q_{el} and about 1.9% of q_{el} when T_s is raised to 700 K. For emittances higher than 0.5, q_k/q_{el} is in the 0.7–1.8% range when T_s is between 300 and 700 K (and $T_\infty=300$ K).

After the total hemispherical emittance has been determined, the specific heat of the sample material can be deduced from the cooling curve through Eq. (5). The cooling transient that follows the interruption of power supply is recorded by the data logger at intervals of 15–60 s. To obtain the value of the derivative $dT_s/d\tau$ at a specific instant value, the recorded time history of temperature $T_s(\tau)$ is expressed by an exponential function

$$T_s(\tau) = a_i \exp[-b_i(\tau - \tau_0)] \quad (7)$$

where τ_0 is an arbitrarily fixed time and the constants a_i and b_i are locally determined by using a least-squares method with a set of five adjacent experimental data, as done by Masuda and Higano [3]. After fitting the measured response with Eq. (7), the residuals of the fit were of the order of 0.05–0.15 K. After the constants a_i and b_i have been determined, the local time-derivative of sample temperature is easily calculated.

The uncertainty analysis at the 95% confidence level has been performed according to the procedure described by Moffat [6]. It takes into account the errors associated with voltage, current, and temperature measurements and with the calculation of heat losses from electric and thermocouple wires. The uncertainty (in terms of percent) in ε_s turned out to be in the 8–12% range for ε_s of about 0.05, in the 4–6% range for ε_s of about 0.1, and in the 2–3% range for for ε_s higher than 0.3, while the uncertainty (in percentage) in $c_{p,s}$, for the employed samples, was found to be in the 4.1–4.9% range.

4 Experimental Results

A commercial aluminum alloy and Inconel 718 alloy were chosen as the sample materials.

The aluminum alloy, namely Anticorodal 6063, is 98–99% pure aluminum. The other constituents (% of weight) are the following: Si 0.3–0.6%, Fe 0.1–0.3%, Cu 0.1%, Mn 0.1%, Mg 0.35–0.6%, Cr 0.05%, Zn 0.15%, and Ti 0.1%. The samples were prepared by successively rolling bar stocks to the desired shape and thickness. Experiments were conducted using the following samples: (1) as-rolled and -received conditions; (2) rolled and sandblasted; (3) rolled and black anodized.

Sample (1), tested as received, presented ordinarily polished surfaces. Sample (2), previously rolled like sample (1), was sandblasted. The surface mechanical average roughness *Ra*, measured by means of a Taylor-Hobson Talysurf 10 instrument, turned out to be 1.14 μm (average value among 5 individual measurements performed varying both the direction and the length of the tracer point). Sample (3), previously rolled like sample (1), was anodized using an electrolyte solution of sulfuric acid (190 g per l). The current density was approximately 0.5 amp per dm^2, the sample remained in the solution for 40–45 min and the oxide thickness was about 11–15 μm.

Inconel 718 alloy has the following constituents (% of weight): Ni 52.5%, Cr 19%, Fe 18.5%, Nb 5.2%, Mo 3%, Ti 0.8%, Al 0.6%, Si 0.2%, and Mn 0.2%. The samples were prepared by electrodischarge machining (EDM) from a bar stock to the desire shape and thickness. The EDM is a metal removal process using a series of electric sparks to erode material from a workpiece. Experiments were conducted using the following samples: (4) as EDM machined conditions; (5) EDM machined and polished; (6) EDM machined, polished and thermally oxidized.

Sample (4) was tested directly after the EDM without any further surface finishing treatment. Sample (5) was mechanically polished by means of successive grinding stages with abrasive papers of finer and finer grain (from No. 80 to No. 1500 grit silicon carbide paper) and finally mirror-polished by cloth polishing with diamond paste, 6 μm and alumina powder, 1 μm. Sample (6), previously EDM prepared and polished like sample (5), was thermally oxidized in air at 1000°C and atmospheric pressure for 30 min.

All the samples were cleaned (after the surface treatment) with acetone, and then washed thoroughly with ultrasonic waves (for five minutes) in distilled water.

Figures 2 and 3 show the total hemispherical emittance results for aluminum (in the 350–635 K temperature range) and Inconel 718 (between 350–580 K), respectively.

The emittance of aluminum (Fig. 2) in as-received conditions (sample (1)) increases almost linearly with temperature; the same trend has been reported by other authors [3,7] using a transient calorimetric technique. The large differences in the emittance values appear to be mainly due to the different surface-finishing conditions of the samples: the sample employed in the present experiment probably has a different magnitude of surface damage (due to the surface treatment) and a significant alteration in surface geometry as compared with the mechanically polished [3] and the electropolished [7] samples. The sandblasted aluminum sample (2) shows emittance values 4–5 times higher than those of the ordinarily polished sample. The high emittances after sandblasting are related to surface irregularities induced by the surface treat-

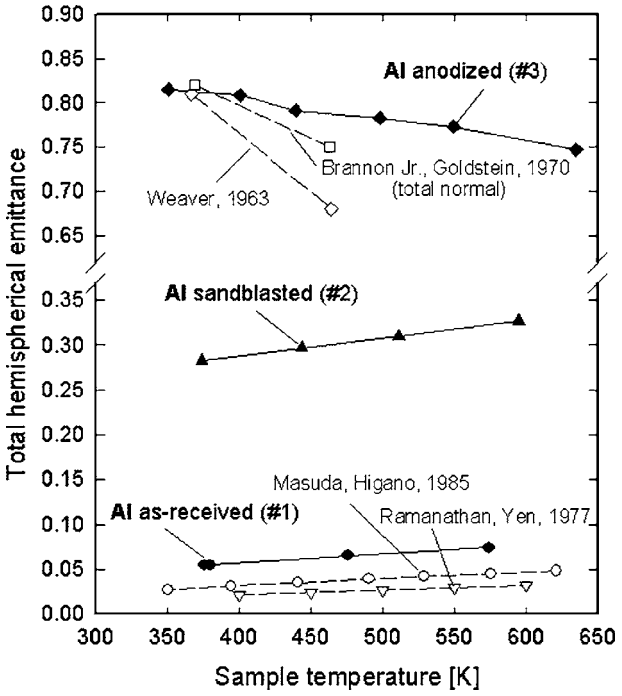

Fig. 2 Total hemispherical emittance of aluminium Anticorodal 6063 alloy, as received (1), sandblasted (2), and anodized (3)

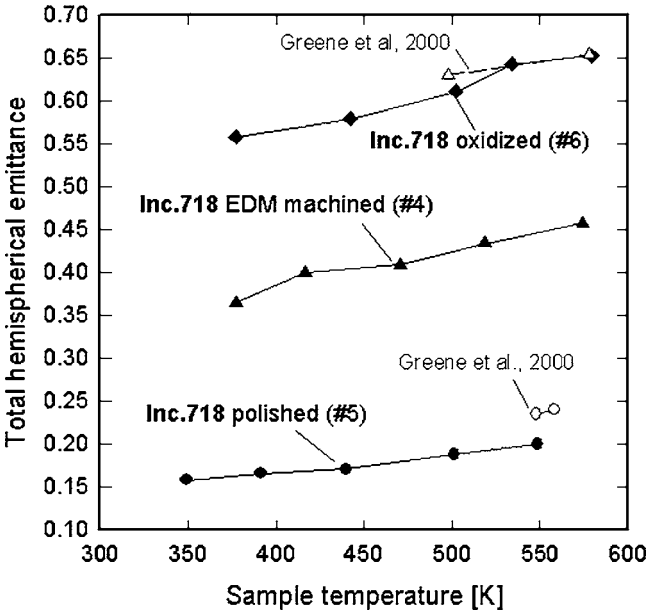

Fig. 3 Total hemispherical emittance of Inconel 718 alloy, as electrodischarge machined (4), polished (5), and thermally oxidized (6)

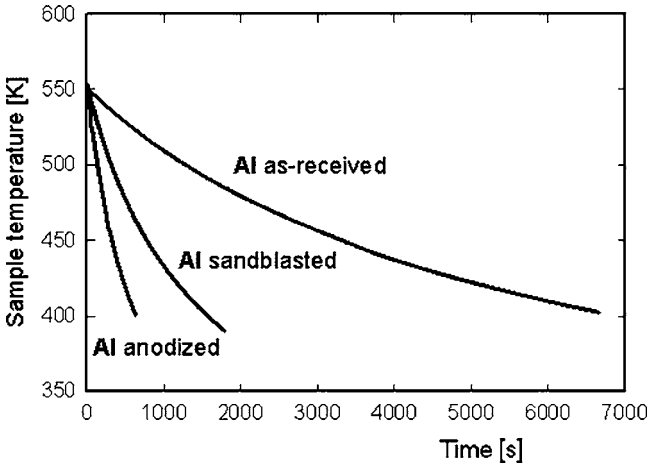

Fig. 4 Cooling curves of temperature vs time for the aluminum samples

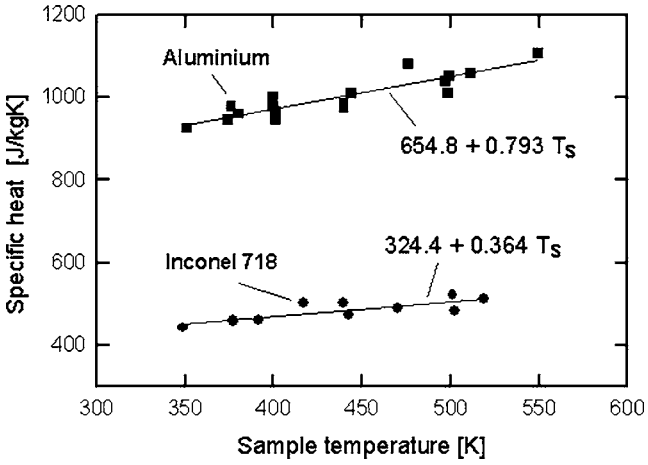

Fig. 5 Specific heat of aluminum Anticorodal 6063 and Inconel 718 alloy

ment, as found by Misale et al. in previous papers [8,9]. Emittance of the anodized aluminum sample (3) decreases with increasing sample temperature; this behavior is typical of oxides, whose absorption coefficient tends to decrease with decreasing wavelength, thereby making the oxide more transparent to radiation when the temperature increases. The same trend was found by Weaver [10] and Brannon Jr. and Goldstein [11] by means of radiometric measurements performed on anodized aluminum samples with approximately the same oxide thickness as the present experiment. Differences in emittance values may be ascribed to the nongray nature of surfaces or to the different anodizing process used.

Figure 3 shows the emittance versus temperature for Inconel 718. Samples having surfaces in as-machined (EDM) conditions (4) and after the mechanical polishing (5) are characterized by moderate increases of emittance with temperature; results indicate that the polishing treatment reduces by over 50% the emittance of the electrodischarge machined sample. Recorded data for the polished sample are in good agreement with measurements performed by Greene et al. [5] using a steady-state calorimetric technique. As expected, the thermal oxidation (at 1000°C for 30 min) of the polished sample (6) leads to a significant increase (by 300–350%) in emittance. Again, emittance was found to increase with surface temperature; the same trend was observed by Greene et al. [5] that found the same emittance levels (0.65 at 600 K) for samples with the same oxidation history but values up to 0.9 (practically unchanged with temperature) for higher time and temperature of oxidation. These considerations, together with visual observation of the sample after the oxidation, suggest that the oxide layer was not so thick to completely inhibit the role played by the substrate in the radiant exchange with the surroundings.

The specific heat of samples is recovered from the analysis of cooling curves without supply of external energy. Typical cooling curves are plotted in Fig. 4, for the three aluminum samples (from 550 K). Inspection of the figure shows faster temperature reductions for samples having higher emittance; it is worth noting that the lumped capacitance model requires that thermal gradients inside the material to be negligible. According to Cheng [2], the rate of cooling of the sample must be lower than a limiting value given by

$$|dT_s/d\tau|_{\lim} = 0.01\alpha_s A_s^2 (T_s - T_\infty)/V_s^2 \tag{8}$$

where α_s and V_s are the thermal diffusivity and the volume of the sample, respectively. In the present experiment, $|dT_s/d\tau|_{\lim}$ for aluminum samples is about 3.5 K/s, at $T_s - T_\infty = 50$ K and 21 K/s at $T_s - T_\infty = 300$ K, while for Inconel 718 is about 0.25 K/s at $T_s - T_\infty = 50$ K and 1.5 K/s at $T_s - T_\infty = 300$ K. Maximum measured values of the derivative $|dT_s/d\tau|$ for aluminum samples were 0.45 K/s at the highest T_s and 0.06 K/s at the lowest T_s (sample (3)), while for Inconel 718 samples $|dT_s/d\tau|$ was, at the most, 0.22 K/s at the highest T_s and 0.05 K/s at the lowest T_s (sample (6)); for both materials the limiting rate of cooling is never exceeded and then temperature gradients within the sample can be neglected.

Specific heat values of aluminum (between 350 and 550 K) and Inconel 718 (between 350 and 520 K) are reported in Fig. 5; the plotted results include temperature transient analysis of all samples for aluminum and Inconel 718. The scatter of data around the best fit (solid line) is mainly ascribed to the uncertainty induced by the different levels of cooling rates of individual samples. For instance, samples at high emittance are characterized by rapid cooling, with possible small errors due to residual thermal gradients in the material but, at the same time, the role played by heat losses q_k (and relative errors associated with their evaluations) is minimal; conversely, low emittance samples have a slow temperature decay with time, with no errors related to the lumped capacitance model but with a larger uncertainty due to errors in temperature measurements and in heat losses estimation. It is concluded that the lowest deviation from the best fit of data is obtained for samples with intermediate values of emittance and rate of cooling (sample (2) for aluminum and (4) for Inconel 718); these operating conditions are the most suitable for very accurate measurements of specific heat by the present calorimetric technique.

5 Conclusions

An experimental apparatus for the measurement of the total hemispherical emittance and specific heat of metals has been described. The apparatus, based on the calorimetric technique, enables measurements of emittance during a steady-state experiment, followed by a cooling transient from which the specific heat of sample is recovered. The total hemispherical emittances have been measured for ordinarily polished, sandblasted and black anodised aluminum (Anticorodal 6063) samples and for electrodischarge machined, mechanically polished and thermally oxidized Inconel 718 samples. Besides, for both materials the specific heats have been measured. Experiments proved the suitability of the method to measure emittance and specific heat of metals using the same apparatus.

Acknowledgment

The research was granted by ASI (Italian Space Agency), Contract No. I/R/274/02.

Nomenclature

A = heat transfer surface area (m^2)
a_i, b_i = constants in Eq. (7)
C_∞ = constant in Eq. (2)
c_0 = constant in Eq. (6)
c_p = specific heat (J/kg K)
$F_{s,\infty}$ = sample-to-cavity view factor
H, W, t = sample length, width and thickness (m)
m = mass (kg)
q = radiative heat transfer rate (W)
q_{el} = thermal power dissipated by Joule effect (W)
q_{gas} = conductive heat transfer rate through the residual gas (W)
q_k = heat transfer rate through the wires (W)
T = temperature (K)
V = volume (m^3)
x = longitudinal coordinate (m)

Greek Symbols

α = thermal diffusivity (m^2/s)
ε = total hemispherical emittance
σ = Stefan-Boltzmann constant ($=5.67\times10^{-8}$ W/m^2 K^4)
τ = time (s)
τ_0 = reference time in Eq. (7) (s)

Subscripts

h = heater
lim = limiting value
s = sample
∞ = cavity

References

[1] Sasaki, S., Masuda, H., Higano, M., and Hishinuma, N., 1994, "Simulataneous Measurements of Specific Heat and Total Hemispherical Emissivity of Chromel and Alumel by a Transient Calorimetric Technique," Int. J. Thermophys., **15**, pp. 547–565.
[2] Cheng, S. X., 1984, "An Accurate Transient Calorimeter for Measuring the Total Hemispherical Emissivity of Metals and Alloys," High Temp. - High Press., **16**, pp. 459–468.
[3] Masuda, H., and Higano, M., 1985, "Transient Calorimetric Technique for Measuring Total Hemispherical Emissivities of Metals with Rigorous Evaluation of Heat Loss Through Thermocouple Leads," J. Opt. Soc. Am. A, **2**, pp. 1877–1882.
[4] Masuda, H., and Higano, M., 1988, "Measurement of Total Hemispherical Emissivities of Metal Wires by Using Transient Calorimetric Technique," ASME J. Heat Transfer, **110**, pp. 166–172.
[5] Greene, G. A., Finfrock, C. C., and Irvine Jr., T. F., 2000, "Total Hemispherical Emissivity of Oxidized Inconel 718 in the Temperature Range 300–1000°C," Exp. Therm. Fluid Sci., **22**, pp. 145–153.
[6] Moffat, R. J., 1988, "Describing the Uncertainties in Experimental Results," Exp. Therm. Fluid Sci., **1**, pp. 3–7.
[7] Ramanathan, K. G., and Yen, S. H., 1977, "High-Temperature Emissivities of Copper, Aluminum, and Silver," J. Opt. Soc. Am. A, **67**, pp. 32–38.
[8] Misale, M., Pisoni, C., and Tanda, G., 1988, "Influence of Surface Finishing Operation on Total Normal Emittance of Nickel and Titanium," Int. J. Heat Technol., **6**, pp. 97–110.
[9] Misale, M., Pisoni, C., and Tanda, G., 1989, "Investigation of Total Emittance of Metals and Steels Subjected to Mechanical Surface Treatments," High Temp. - High Press., **21**, pp. 311–315.
[10] Weaver, J. H., 1963, "Anodized Aluminum Coatings for Temperature Control of Space Vehicles," Air Force Systems Command, Technical Documentary Report No. ASD-TDR-62-918.
[11] Brannon Jr., R. R., and Goldstein, R. J., 1970, "Emittance of Oxide Layers on a Metal Substrate," ASME J. Heat Transfer, **92**, pp. 257–263.

Analysis of an Impinging Two-Dimensional Jet

A. H. Beitelmal[1]
Hewlett-Packard Laboratories,
1501 Page Mill Rd.,
Palo Alto, CA 94304
e-mail: monem@hp.com

A. J. Shah
Department of Mechanical Engineering,
University of California,
Berkeley, CA 94720-1742

M. A. Saad
Department of Mechanical Engineering,
Santa Clara University,
Santa Clara, CA 95053

Heat transfer in jet impingement is a complicated phenomenon and a general analytical solution is not available. Typical jet impingement studies are conducted experimentally and best-fit correlations are proposed (Beitelmal, Saad, and Patel [2]; Beitelmal [3]; Beitelmal, Saad, and Patel [4]; Schauer and Eustis [7]; McMurray, Myers, and Uyehara [8], Gardon and Akfirat [9]). Separate solutions for the stagnation region and the wall jet region are then combined to determine the overall heat transfer solution for the impinging jet. In this paper, stagnation and wall jet region solutions for a two-dimensional jet normally impinging on a flat surface are developed using heat transfer relations available in the literature. These solutions are analyzed and compared to previous experimental results (Beitelmal, Saad, and Patel [2]; Beitelmal [3]). The potential flow assumption is used for the fluid dynamics analysis at the stagnation region. For the wall jet region, a comparison was achieved through consideration of the classical analytical solution for parallel flow over a flat plate. Analytical solutions as well as semiempirical solutions for the stagnation region and the wall jet reported by previous investigators were also considered. Predictions for heat transfer in the stagnation region using potential flow assumptions were found to be accurate to within 20%. For the wall jet region, previous correlations predicted by McMurray, Myers, and Uyehara [8] and Nizou [10] were found to be the most accurate. At large values of x/D, the heat transfer properties in the wall jet are shown to be very similar to those of a turbulent boundary layer over a flat plate. Such a simplified analysis in different regions of an impinging jet using some basic fluid dynamics assumptions can greatly facilitate a prediction of the local Nusselt number. [DOI: 10.1115/1.2150841]

Introduction

A free submerged jet issuing from a nozzle becomes turbulent at a short distance from the point of discharge for exit Reynolds number greater than 700. Turbulence occurs when the fluid jet moves past a stagnant layer of fluid where a slipline is formed. This slipline becomes unstable and the flow changes into a turbulent mixing zone due to entrainment of the surrounding fluid. Entrainment induces more fluid from the surroundings into the jet causing the flow rate to increase as the distance from the nozzle exit increases. Upon impingement over a flat surface, the flow can be divided into four main regions: an initial mixing zone, a jet core (potential core), an impinging zone and a wall jet. The center velocity within the jet core is highest; it decreases beyond the tip of the jet core and eventually is reduced to zero at the point of impact with the target surface (the stagnation point). At this point the static pressure is higher than the ambient pressure, resulting in a favorable pressure gradient that turns the flow to a direction parallel to the target surface, forming the wall jet region. The jet adheres to the surface as it flows over the plate. The heat transfer from the surface is a maximum at the stagnation point and tapers off as the parallel flow picks up heat from the surface and its velocity is reduced away from the stagnation region.

At the impingement surface, the flow is divided into two distinct regions: a stagnation region and a wall jet region. These regions are illustrated in Fig. 1. The factors affecting these two regions are very different. The stagnation region is affected by the external flow just outside the boundary layer and the maximum free jet velocity arriving at the stagnation region (arrival velocity). The maximum pressure is at the stagnation point, and decreases to the ambient pressure at a distance y_0 from the stagnation point in the direction of impingement. Along the wall, the pressure also decreases until it recovers to the ambient pressure at a distance x_0 from the stagnation point. The boundary layer flow in the immediate vicinity of the stagnation point will almost certainly be laminar in view of the low local Reynolds number and it is safe to assume that the flow remains laminar for the entire stagnation region [1]. The positive pressure gradient in the region accelerates the flow, stabilizes the boundary layer and helps laminarize the flow. The maximum velocity just outside the stagnation region recovers to the maximum approach velocity as the stagnation flow develops into a wall jet.

The resulting wall jet is a turbulent boundary layer with zero pressure-gradient in the flow direction. It is divided into two layers: an inner layer and an outer layer. For a long enough wall, the maximum wall jet velocity decreases with x due to entrainment and viscous effects. The maximum velocity just outside the inner layer affects the heat transfer from the wall. The overall heat transfer from the wall is also affected by the turbulent intensity in the outer layer that might propagate into the inner layer.

Stagnation and wall jet region solutions for a two-dimensional jet impinging normally on a flat surface are developed using heat transfer relations available in the literature. These solutions are analyzed and compared to experimental results [2,3] using a slot nozzle, 70 mm long and 5.5×50 mm^2 exit area. The nozzle is attached to a plenum chamber with inner dimensions of $55\times 50\times 25$ mm^3. The experiments were conducted for a practical Reynolds number range of interest to the electronic industry between 4000 and 12 000, vertical nozzle-exit to target surface distance between 4D and 12D, and horizontal distance from the stagnation point between 0 and 8D, where D is the hydraulic diameter and is approximated as $(\sim 2w)$. This approximation is valid for the nozzle aspect ratio used in the experiments. The reader is referred to [2] or [3] for more details on the experimental apparatus.

Beitelmal et al. [4] investigated the effect of surface roughness of a uniformly heated plate on the average heat transfer characteristics of an impinging air jet. Miyazaki and Silberman [5] approximated the stagnation region to extend up to half the width of the slot nozzle (w) and found this region to be independent of the vertical distance between the nozzle exit and the target surface, z. Beltaos and Rajaratnam [6] concluded that it is safe to apply the potential flow solution within the vicinity of the stagnation point. In this analysis, the potential flow assumption is used for the entire stagnation region flow. For the wall jet region, a comparison was achieved through consideration of the classical analytical solution for the stagnation point and for parallel flow over a flat

[1]Corresponding author.

Contributed by the Heat Transfer Division of ASME for publication in the JOURNAL OF HEAT TRANSFER. Manuscript received January 13, 2005; final manuscript received August 17, 2005. Review conducted by Yogendra Joshi.

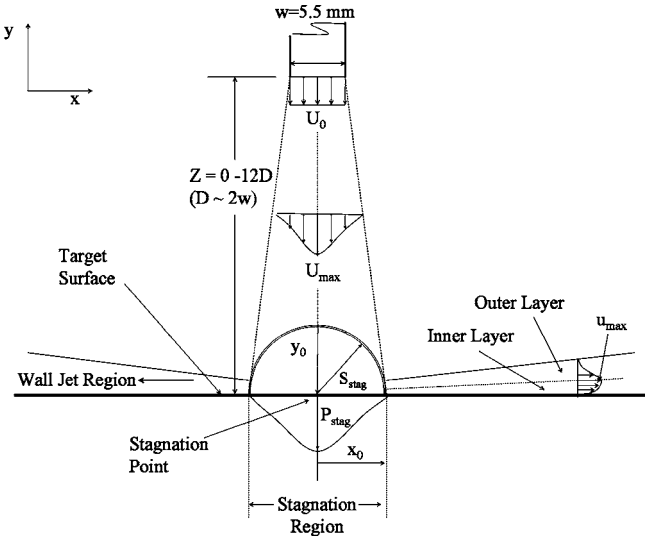

Fig. 1 Impinging jet nomenclature

plate. Analytical solutions as well as semiempirical solutions for the stagnation region and the wall jet reported by previous investigators [7–10] were also considered.

Many attempts have been published in the literature, highlighting numerical recipes for solving jet impingement heat transfer [11–14]. However the interaction between the jet impingement regions is complicated and there is no general CFD code that can be applied for all different types of jet impingement. For example, a recent publication [11] used Large-Eddy Simulation (LES) techniques for jet Reynolds number between 500 and 3000. The LES method is a compromise between Direct Numerical Simulation (DNS) and Reynolds-Averaged Navier-Stokes (RANS), where DNS is the most accurate method of predicting turbulent flow while RANS only solves for the average flow properties. With sufficient grids, LES behaves similarly to DNS; however, LES can be worse than RANS if the grid resolution is not high enough. The dynamic model employed in this case would require a very fine meshing near the wall, which would result in a high computational cost. The authors [11] used 21 cells along the impinging direction and less along the other two directions. However, for higher Reynolds number flow, it is questionable whether the effects of turbulence generation due to free shear and entrainment in the free jet can be captured by this grid resolution. At higher Reynolds number, as energy begins to populate the cells at a smaller scale, the accuracy of the LES method would diminish significantly.

Stagnation Region Analysis

The stagnation flow model chosen here is based on the following assumptions: the fluid is incompressible and has no viscous effects, and fluid properties are constant. For the normally impinging two-dimensional jet, the stagnation region is assumed to extend a distance S_{stag} from the stagnation point. It is further assumed that the velocity arriving at this region is equal to the velocity leaving the region, and the maximum static pressure is at the stagnation point. The entrainment is neglected.

Based on the previous assumptions, the velocity parallel to the wall can be assumed to vary linearly with the horizontal distance x starting at the stagnation point and up to a distance S_{stag}.

Using approximations from the literature [1,5–7,15], the Nusselt number in the stagnation region for air (Pr=0.7) can be given as:

$$\mathrm{Nu}_{stag} = 0.824(\mathrm{Re}_D)^{0.5}\left(\frac{z-\kappa}{D}\right)^{-0.25} \quad (1)$$

In this study, the size of the stagnation region is assumed to be independent of z and to be only a function of the slot width. The best fit to the experimental data [2,3] is assumed to apply up to 1.2 of the slot nozzle width from the impingement point. The axial velocity then reaches the maximum arrival velocity value at $1.2w$ distance from the stagnation point, so that:

$$x_0 = 1.2w \quad (2)$$

Note that the equation reveals that the heat transfer Nusselt number is independent of x within the stagnation region. Since the thermal boundary layer thickness is also constant, potential flow theory suggests that the amount of heat transfer should not change in the stagnation region.

The approach velocity and the turbulence level of the free jet are thus the important factors in determining the extent of the stagnation region and the location of the transition region. However, as discussed by Martin [16], it would not be practical to include the turbulence level as a variable into an engineering correlation for heat and mass transfer as it cannot be a design variable.

Wall Jet Analysis

The velocity decreases to zero at the stagnation point and the flow proceeds parallel to the wall where the pressure gradient causes the axial velocity to accelerate to u_{max} at the edge of the stagnation region. The flow from the stagnation region to the wall jet takes place via a discontinuity in a transition layer. The flow becomes unstable at the edge of the stagnation region due to the presence of random turbulent fluctuations and the inertial forces becomes important [17–19]. Boundary conditions are particularly important in jet impingement heat transfer since factors affecting this region include the turbulence level at the free jet, nozzle size, exit conditions, and the free jet Reynolds number. This causes difficulty in determining the transition region location and characteristics experimentally but numerical techniques can shed light on this layer. From the point of view of heat transfer, this layer is not critical and it is not covered in this study.

As previously stated, two layers define the wall jet. The inner layer is the most important to the heat transfer from the wall surface. The outer layer is similar in properties to a free jet and will not be considered here. The inner layer exhibits similarities in structure with that of a boundary layer over a flat plate, but differs in that it is developed under the influence of an external turbulent flow. As a result of neglecting the viscous effects in the stagnation region, the maximum velocity at the start of the wall jet will be equal to the maximum free jet velocity arriving at the stagnation region. It is also assumed that the virtual origin of the wall jet (the point where the turbulent boundary layer would originate if it were not preceded by the stagnation region) coincides with the stagnation point. It is further assumed that the flow is incompressible with constant properties, entrainment is negligible and the surface heat flux is constant.

The maximum wall jet velocity depends on several factors including the arrival velocity at the stagnation region, the turbulent level from the outer layer, and the viscous effects at the wall that cause the wall jet to decelerate. In the present analysis, it is assumed that the maximum free jet velocity arriving to the stagnation region is decaying based on the approximation by Schauer and Eustis [7]:

$$\frac{U_{max}}{U_0} = \frac{2.35}{\sqrt{(z-\kappa)/(D/2)}} \quad (3)$$

The maximum wall jet velocity (just outside the boundary layer) is equal to the velocity arriving at the stagnation region and is used to calculate the wall heat transfer coefficient.

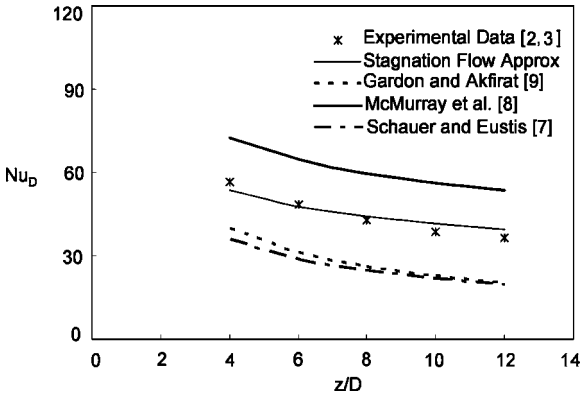

Fig. 2 A comparison between the present results and previous investigations for the stagnation point (Re=7900)

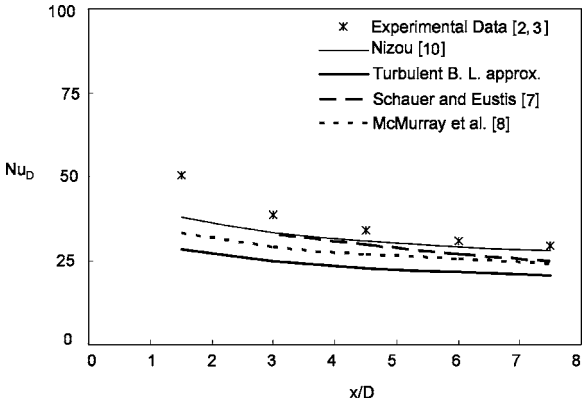

Fig. 3 A comparison between the present results and previous investigations for the wall jet (z/D=10, Re=12 000)

$$u_{\max} = U_{\max} \tag{4}$$

The classical analytical approximation for the effect of a constant wall heat flux on turbulent boundary layers over a flat surface [20] can be rewritten as follows:

$$\mathrm{Nu}_D = \frac{0.0308(\mathrm{Pr})^{0.333}(u_{\max}x/\nu)^{0.8}}{x/D} \tag{5}$$

Substituting Eq. (3) and Eq. (4) into Eq. (5) with Pr=0.7 for air, we obtain:

$$\mathrm{Nu}_D = 0.0410(\mathrm{Re}_D)^{0.8}\left(\frac{z-\kappa}{D}\right)^{-0.4}\left(\frac{x}{D}\right)^{-0.2} \tag{6}$$

The above equation is used to calculate the Nusselt number for the wall jet region.

Results and Discussion

Stagnation Region. For the case of two-dimensional flow impinging normally on a flat plate, the stagnation region can be assumed to extend S_{stag} from the stagnation point. At the point of the jet impacting the target surface, the velocity and friction factor are assumed to be zero and the Nusselt number is maximum.

Figure 2 shows a sample comparison between predicted values for Nusselt Number in the stagnation region and the experimental results of Beitelmal et al. [2,3]. Equation (1), derived from the classical stagnation flow solution, matches the experimental values at Re_D=4000 and Re_D=7900 with a maximum deviation of 15%. The agreement weakens at Re_D=12 000 and the deviation increases to 20%. The reason may be due to the increase in turbulence intensity in the experiments. The deviations between the Nusselt number correlations from the literature [7–9] and the experimental values [2,3] ranged between 28%–50%.

In the neighborhood of the stagnation point (within the stagnation region), the heat transfer is independent of x, and since the thermal boundary layer thickness is also constant, potential flow theory suggests that the amount of heat transfer should not change in the stagnation region and is only a function of the temperature difference between the jet and the wall at that point. The Nusselt number remains nearly constant, even though the velocity along the wall increases with x. This means that a single measurement is sufficient to evaluate the stagnation region heat transfer.

The length of the stagnation region in the above analysis is based only on the size of the slot nozzle. This works for the practical z/D range in electronic industries ($4 \leqslant z/D \leqslant 12$), as seen in Fig. 2, where the stagnation point values maintain the same trend as the experimental values [2,3] as z/D increases. The temperatures measured in the experiments [2,3], taken up to x/D =1.5, are average temperatures over this range. The temperature difference between the jet and the plate over this region is constant and the heat flux is also constant. Therefore, the heat transfer coefficient and the Nusselt number are also constant. From Fig. 2, it appears that Eq. (1) derived from the classical stagnation solution gives the best fit to the experimental results. This relation can be used to estimate the stagnation Nusselt number for the range of Re and z/D values used in the experiments [2,3].

Wall Jet Region. Wall jet Nusselt number comparisons are shown in Fig. 3 for Re_D=12 000, z/D=10, and in Fig. 4 for the Re_D range from 4000 to 12 000, the z/D range from 4 to 12, and x/D from 0 to 8. The plots show that the classical boundary layer solution for flow over a flat plate underestimates the heat transfer coefficient for the wall jet over the range of this study. This is due to the increase in turbulence intensity that propagate downward from the outer layer. Furthermore, the solution neglects the turbulence intensity that gets amplified from the free jet down to the wall jet. However, the wall jet behaves very similar to a turbulent boundary layer over a flat surface for large x/D. Although Schauer and Eustis [7] predicted the heat transfer based on experimental results obtained over the range of Re>16 000, their predictions match the experimental results [2,3] to within 10%–20%. The maximum deviation, however, is as much as 40% and takes place at small x/D, which might indicate that the wall jet has not begun yet at these values. The prediction by McMurray et al. [8] for the turbulent wall jet compares well with the experimental results [2,3], except for z/D=12. This correlation matched better for higher Reynolds number. The Nusselt number expression from Nizou's relation [10] qualitatively follows the trend of the experimental results [2,3] rather closely, except for z/D=4. This could be because the Nizou relation does not include the z/D factor. Quantitatively, the plots show that his equation deviates from the experimental results [2,3] by as much as 30%, but this deviation

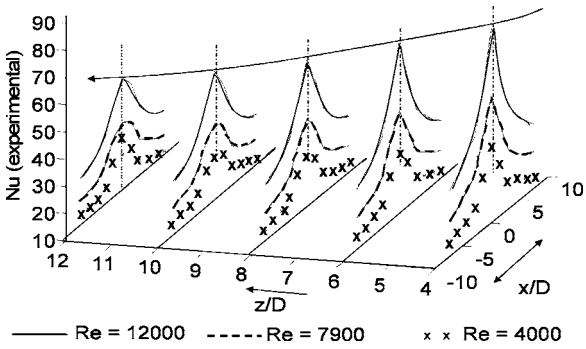

Fig. 4 Experimental trends in the Nusselt number as a function of (x/D, z/D, Re)

decreases significantly as x/D increases. This might indicate that the wall jet is affected by the stagnation region, causing the Nusselt number to be higher than the one predicted by the analysis.

In summary, the theoretical values of the Nusselt number in the wall jet are generally lower than the experimental values. This may be attributed to turbulent intensity in the free jet, which could be much higher than that expressed by the Reynolds analogy approach used in this study. The theory solves only the equations for the wall jet while the experimental heat transfer data include the effects of turbulence pregenerated in the initial free jet. The temperature profile measured experimentally depends on the conditions at the nozzle exit and the turbulent intensity of the jet and is not just a function of the mean velocity profile. The turbulence intensity appears to be uniquely determined by the jet design variables (Reynolds number and dimensionless jet length) and therefore heat transfer rates can be correlated very effectively without including turbulence characterization [9]. Predictions by McMurray et al. [8] and Nizou [10] represent the best fit to the experimental results [2,3] in the wall jet immediately downstream of the stagnation region. The classical solution for turbulent boundary layer flow over a flat plate can be used to predict the heat transfer at large x/D values.

Conclusions

(1) Approximate solutions are developed using simplified flow assumptions for both the stagnation and wall jet regions.
(2) The potential flow assumption is used for the stagnation region, while the wall jet is approximated as a turbulent boundary layer over a flat plate.
(3) Different correlations available from the literature are included in the analysis and compared to experimental results [2,3].
(4) In the stagnation region, the classical stagnation solution is found to give the best fit to the experimental results.
(5) In the wall jet regions, the correlations published by McMurray et al. [8] and Nizou [10] represented the best fit. The classical solution for turbulent boundary layer flow over a flat plate can be used to predict the heat transfer at large x/D values for the wall jet region.

Nomenclature

D = hydraulic diameter, m
Nu_D = Nusselt number ($=hD/k$)
$\mathrm{Nu}_{\mathrm{stag}}$ = Nusselt number at stagnation point
Pr = Prandtl number
P_{stag} = stagnation pressure, Pa
S_{stag} = stagnation region radius, m
Re_D = Reynolds number ($=UD/\nu_{\mathrm{air}}$)
$u_{\max}$ = maximum wall jet velocity, m/s
$U_{\max}$ = maximum free jet velocity, m/s
U_0 = mean velocity of the air jet at nozzle exit, m/s
w = width of slot nozzle, m
x = distance along the plate measured from the geometrical center, m
x_0 = axial distance between stagnation point and edge of stagnation region, m
y_0 = vertical distance between stagnation point and edge of stagnation region, m
z = vertical distance between the nozzle exit and the center of the plate, m
κ = distance between the stagnation point and the edge of the stagnation region, m
ν = kinematic viscosity, m^2/s

References

[1] Cartwright, W. G., and Russell, P. J., 1967–68, "Characteristics of a Turbulent Slot Jet Impinging on a Plane Surface," Proc. Inst. Mech. Eng., **182**, pp. 309–319.
[2] Beitelmal, A. H., Saad, M. A., and Patel, C. D., 2000, "The Effect of Inclination on the Heat Transfer Between a Flat Surface and an Impinging Two-Dimensional Air Jet," Int. J. Heat Fluid Flow, **21**, pp. 156–163.
[3] Beitelmal, A. H., 2000, "An Investigation of Heat Transfer Characteristics in Axisymmetric and Two-Dimensional Impinging Jets," Ph.D. Dissertation, Santa Clara University, Dept. of Mech. Eng.
[4] Beitelmal, A. H., Saad, M. A., and Patel, C. D., 2000, "Effects of Surface Roughness on the Average Heat Transfer of an Impinging Air Jet," Int. Commun. Heat Mass Transfer, **27**, pp. 1–12.
[5] Miyazaki, H., and Silberman, E., 1972, "Flow and Heat Transfer on a Flat Plate Normal to a Two-Dimensional Laminar Jet Issuing From a Nozzle of Finite Height," Int. J. Heat Mass Transfer, **15**, pp. 2097–2107.
[6] Beltaos, S., and Rajaratnam, N., 1973, "Plane Turbulent Impinging Jets," J. Hydraul. Res., **11**, pp. 29–59.
[7] Schauer, J. J., and Eustis, R. H., 1963, "The Flow Development and Heat Transfer Characteristics of Plane Turbulent Impinging Jets," Stanford University, Tech. Rep. No. 3, Dept. of Mech. Eng.
[8] McMurray, D. C., Myers, P. S., and Uyehara, O. A., 1966, "Influence of Impinging Jet Variables on Local Heat Transfer Coefficients Along a Flat Surface with Constant Heat Flux," *Proc. 3rd Int. Heat Transfer Conf.*, Chicago, IL, Vol. 2, pp. 292–299.
[9] Gardon, R., and Akfirat, C., 1965, "The Role of Turbulence in Determining the Heat Transfer Characteristics of Impinging Jets," Int. J. Heat Mass Transfer, **8**, pp. 1261–1272.
[10] Nizou, P. Y., 1981, "Heat and Momentum Transfer in a Plane Turbulent Wall Jet," J. Heat Transfer, **103**, pp. 138–140.
[11] Chattopadhyay, H., Biswas, G., and Mitra, N. K., 2002, "Heat Transfer From a Moving Surface Due to Impinging Slot Jets," J. Heat Transfer, **124**, pp. 433–440.
[12] Cziesla, T., Biswas, G., Chattopadhyay, H., and Mitra, N. K., 2001, "Large-Eddy Simulation of Flow and Heat Transfer in an Impinging Jet," Int. J. Heat Fluid Flow, **22**, pp. 500–508.
[13] Voke, P. R., and Gao, S., 1998, "Numerical Study of Heat Transfer From an Impinging Jet," Int. J. Heat Mass Transfer, **41**, pp. 671–680.
[14] Chen, J., Wang, T., and Zumbrunnen, D. A., 1994, "Numerical Analysis of Convective Heat Transfer From a Moving Plate Cooled by an Array of Submerged Planar Jets," Numer. Heat Transfer, Part A, **26**, pp. 141–160.
[15] Gauntner, J., Livingood, N. B., and Hrycak, P., 1970, "Survey of Literature on Flow Characteristics of a Single Turbulent Jet Impinging on a Flat Plate," Lewis Research Center, NASA TN D-5652.
[16] Martin, H., 1977, "Heat and Mass Transfer Between Impinging Gas Jets and Solid Surfaces," Adv. Heat Transfer, **13**, pp. 1–60.
[17] Antonia, R. A., Browne, L. W. B., Rajagopalan, S., and Chambers, A. J., 1983, "On the Organized Motion of a Turbulent Plane Jet," J. Fluid Mech., **134**, pp. 49–66.
[18] Antonia, R. A., Chambers, A. J., Britz, D., and Browne, L. W. B., 1986, "Organized Structures in a Turbulent Plane Jet: Topology and Contribution to Momentum and Heat Transport," J. Fluid Mech., **172**, pp. 211–229.
[19] Nishino, K., Samada, M., Kasuya, K., and Torii, K., 1996, "Turbulence Statistics in the Stagnation Region of an Axisymmetric Impinging Jet Flow," Int. J. Heat Fluid Flow, **17**, pp. 193–201.
[20] Kays, W. M., and Crawford, M. E., 1980, *Convective Heat and Mass Transfer*, 3rd ed., McGraw-Hill, New York.

Thermal Analysis on Flat-Plate-Type Divertor Based on Subcooled Flow Boiling Critical Heat Flux Data Against Inlet Subcooling in Short Vertical Tube

Koichi Hata[1]
ASME
Institute of Advanced Energy,
Kyoto University,
Gokasho, Uji,
Kyoto 611-0011, Japan
e-mail: hata@iae.kyoto-u.ac.jp

Nobuaki Noda
National Institute for Fusion Science,
322-6, Oroshi-cho, Toki,
Gifu 509-5292, Japan

The critical heat fluxes (CHFs) and the heat transfer coefficients (HTCs) in subcooled flow boiling were applied to a thermal analysis of the flat-plate-type divertor of a helical-type fusion experimental device, which is a Large Helical Device (LHD) located in the National Institute for Fusion Science (NIFS), Japan. The incident CHF, $q_{cr,inc}$, for the divertor plate with the cooling tube diameter, d, of 10 mm and the plate width, w, ranging from 16 to 30 mm were numerically analyzed based on the measured CHFs, $q_{cr,sub}$, and HTCs for the test tube inner diameter, d, of 9 mm and the heated length, L, of 48 to 149 mm. The peripheral distributions of the surface heat flux and the surface temperature in the cooling tube were obtained. Numerical solutions of $q_{cr,inc}$ become larger with a decrease in w/d at a fixed L. It is confirmed that the ratio of the one-side heat loading data, $q_{cr,inc}$, to the uniform heat loading data, $q_{cr,sub}$, can be represented as the simple equation based on the numerical solutions. The values of the $q_{cr,inc}$ for the tube length of 50, 100, and 150 mm were estimated with various w/d at a higher pressure. [DOI: 10.1115/1.2150842]

1 Introduction

The knowledge of the critical heat fluxes (CHFs) and the heat transfer coefficients (HTCs) in subcooled flow boiling is important for the design of a divertor plate in a nuclear fusion facility. Recently, the CHFs and HTCs for subcooled flow boiling of water in short vertical tubes of 22 to 150 mm in length with 2, 3, 6, 9, and 12 mm inner diameters (ID) cooled with an upward flow of subcooled water were measured for wide ranges of flow velocities (u), outlet and inlet subcoolings ($\Delta T_{\mathrm{sub,out}}$ and $\Delta T_{\mathrm{sub,in}}$) and pressures by Hata et al. [1,2,4–9] and Sato et al. [3]. It has been clarified that the $q_{\mathrm{cr,sub}}$ against $\Delta T_{\mathrm{sub,out}}$ for $\Delta T_{\mathrm{sub,out}} \geqslant 30$ K are almost proportional to $d^{-0.4}$ and $u^{0.4}$ for fixed $\Delta T_{\mathrm{sub,out}}$ and L/d, to $(\Delta T_{\mathrm{sub,out}})^{0.7}$for a fixed L/d, and to $(L/d)^{-0.1}$ for a fixed $\Delta T_{\mathrm{sub,out}}$ based on the experimental data [4–9]. And, the following CHF correlations related to outlet and inlet subcoolings [5–9] have been given based on the effects of test tube inner diameter (d), flow velocity (u), outlet and inlet subcoolings ($\Delta T_{\mathrm{sub,out}}$ and $\Delta T_{\mathrm{sub,in}}$) and the ratio of heated length to inner diameter (L/d) on CHF.

$$\mathrm{Bo} = 0.082\left\{\frac{d}{\sqrt{\sigma/g(\rho_l-\rho_g)}}\right\}^{-0.1}\mathrm{We}^{-0.3}\left(\frac{L}{d}\right)^{-0.1}\mathrm{Sc}^{0.7}$$
$$\text{for outlet subcooling } (\Delta T_{\mathrm{sub,out}} \geqslant 30\ \mathrm{K}) \quad (1)$$

$$\mathrm{Bo} = C_1\left\{\frac{d}{\sqrt{\sigma/g(\rho_l-\rho_g)}}\right\}^{-0.1}\mathrm{We}^{-0.3}\left(\frac{L}{d}\right)^{-0.1}e^{-(L/d)/C_2Re^{0.4}}\mathrm{Sc}^{*C_3}$$
$$\text{for inlet subcooling } (\Delta T_{\mathrm{sub,in}} \geqslant 40\ \mathrm{K} \quad (2)$$

where, $C_1=0.082$, $C_2=0.53$, and $C_3=0.7$ for $L/d \leqslant$ around 40 and $C_1=0.092$, $C_2=0.85$, and $C_3=0.9$ for $L/d >$ around 40. Bo, We, Sc, and Sc* are boiling number ($=q_{\mathrm{cr}}/Gh_{fg}$), Weber number ($=G^2d/\rho_l\sigma$), nondimensional outlet subcooling ($=c_{pl}\,\Delta T_{\mathrm{sub,out}}/h_{fg}$), and nondimensional inlet subcooling ($=c_{pl}\,\Delta T_{\mathrm{sub,in}}/h_{fg}$), respectively. The thermophysical properties for the saturated condition were evaluated at a saturated temperature corresponding with the outlet pressure. It has been confirmed that almost all the CHF data (1805 points) [5–9] measured by the authors for wide ranges of test tube inner diameters ($d=2$ to 12 mm), heated lengths ($L=21.5$ to 149.7 mm), $L/d=4.08$ to 74.85, outlet pressures ($P_{out}=159$ kPa to 1 MPa), and flow velocities ($u=4.0$ to 13.3 m/s) are within 15% differences of the values given by Eqs. (1) and (2) for $30\ \mathrm{K} \leqslant \Delta T_{\mathrm{sub,out}} \leqslant 140\ \mathrm{K}$ and $40\ \mathrm{K} \leqslant \Delta T_{\mathrm{sub,in}} \leqslant 151\ \mathrm{K}$. No data were discarded for this comparison.

On the other hand, the divertors are not heated uniformly but heated from one side. How the database of CHFs for uniformly heated pipes can be used to evaluate the maximum heat load for a divertor is a problem. At a Large Helical Device (LHD), which is a helical heliotron-type fusion experimental device located in the National Institute for Fusion Science (NIFS), the short pulse mode experiments will be performed with a maximum of 30 MW of heating. The heat load will be estimated to exceed 15 MW/m^2 on the divertor element where most of heating energy is concentrated. Figure 1 shows a typical photograph of the LHD divertor. LHD has two types of the divertor element. One is a flat-plate-type (rectangular one); the other is a mono-block type (cylindrical one). And, the heat load tests have been under way by the electron beam heating on a mock up of a certain divertor element, which is consisting of the carbon armors joined to the copper heatsink with a cooling tube. However, the data of CHFs for such tests are significantly dependent on the shapes of divertors and do not become general ones. If the maximum heat load for a certain divertor can be evaluated by numerical calculation based on the database of CHFs and HTCs for uniformly heated pipes, the database would become the general one for the design of divertors. For such a purpose, not only the CHFs but also the HTCs prior to and after CHFs are necessary. However, there have been few data of CHFs with HTCs for wide ranges of independent variables such as test tube inner diameter, heated length, inlet and outlet pressures, and flow velocity in highly subcooled and pressurized water.

Our purpose in this study is first is to make the thermal analysis of the flat-plate-type divertor based on the CHFs and the HTCs data for the 9 mm inner diameter with the tube length, L, of 48 to 149 mm, second, to clarify the peripheral distribution of the surface heat flux and the surface temperature in the cooling tube of the divertor by the analysis and thirdly to give the ratio of the one-side heat loading CHF, $q_{\mathrm{cr,inc}}$, to the uniform heat loading CHF, $q_{\mathrm{cr,sub}}$, as the simple equation based on the numerical solutions and establish the database for the high heat flux thermal management at the divertor.

[1]Author to whom all correspondence should be addressed.

Contributed by the Heat Transfer Division of ASME for publication in the JOURNAL OF HEAT TRANSFER. Manuscript received July 3, 2004; final manuscript received August 24, 2005. Review conducted by Chang Oh.

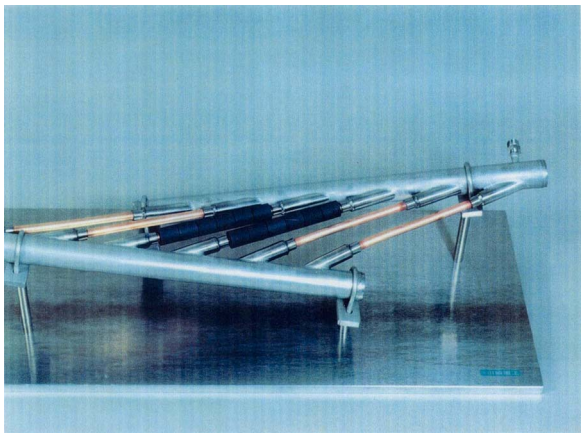

Fig. 1 Typical photograph of the LHD divertor

2 Divertor Types

The cross-sectional views of flat-plate-type and mono-block-type divertors are shown in Figs. 2(*a*) and 2(*b*). The flat-plate-type divertor is made of the oxygen-free copper block of 30 mm wide by 25 mm high and the carbon tile (CX2002U) of 30 mm wide by 10 mm high. The carbon tile is brazed to the copper block. The cooling tube with an inner diameter of 10 mm is horizontally located at a height of 17 mm from the lower surface on the central line of the copper block. On the other hand, the mono-block type one is made of the oxygen-free copper cooling tube with a 10 mm inner diameter and a 1.5 mm thickness, and the carbon armor (CX2002U) with a 33 mm outer diameter and a 10 mm thickness. The cooling tube is located in the center of the carbon armor. The carbon armor is brazed to the cooling tube. The heated lengths of the divertors are given as 48–149 mm in this work, which are equal to the heated lengths of the test tubes in the former CHF experiments [1–9]. The high heat flux heat removal is achieved in the following way; the heat induced by collecting the high heat flux flow and the high-energy particles on the carbon armor upper surface is transferred to the highly subcooled and pressurized water due to the forced convection and nucleate boiling heat transfer on the inner surface of the cooling tube. It was supposed that the right, left, and lower surfaces for the flat-plate-type diverter and the lower surface for the mono-block-type one are under the adiabatic conditions because the divertor is equipped in the plasma vessel, which will be normally operated under ultrahigh vacuum (10^{-10} atmospheres for hydrogen).

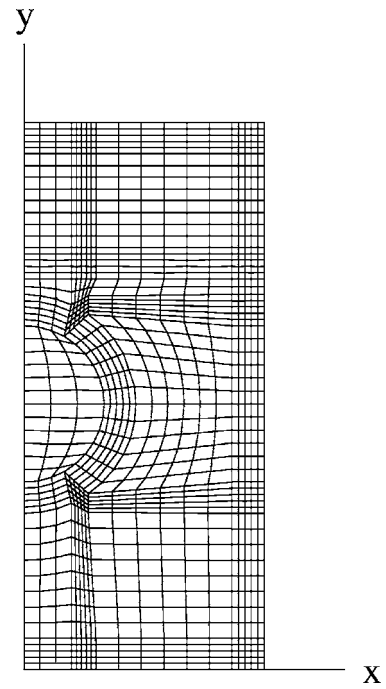

Fig. 3 Boundary fitted coordinates of the flat-plate-type divertor

3 Numerical Analysis of the Flat-Plate-Type Divertor

3.1 Fundamental Equations. The unsteady two-dimensional heat conduction equation in a boundary fitted coordinate for the flat-plate-type divertor as shown in Fig. 3 is described as follows:

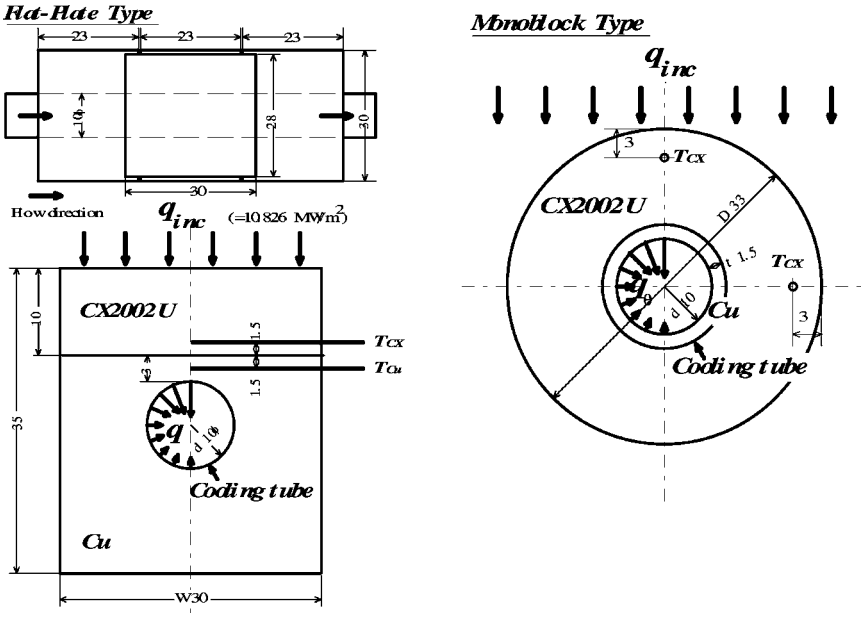

Fig. 2 Cross-sectional views of LHD divertors; (a) flat-plate type and (b) mono-block type

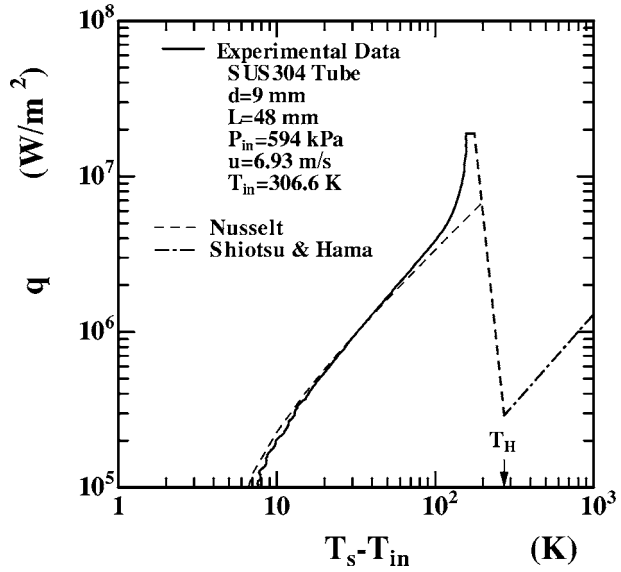

Fig. 4 Relationship between q and $(T_s - T_{in})$ for $d=9$ mm with $L=48$ mm at an inlet pressure of 594 kPa

$$\frac{\partial}{\partial t}(\rho c_p T) = \frac{\partial}{\partial x}\left(\lambda \frac{\partial T}{\partial x}\right) + \frac{\partial}{\partial y}\left(\lambda \frac{\partial T}{\partial y}\right) \quad (0 \leq x \leq w/2,\ 0 \leq y \leq 0.035), \tag{3}$$

The boundary conditions are expressed in the following forms:

$$x = 0: \quad \frac{\partial T}{\partial x} = 0 \tag{4}$$

$$x = w/2: \quad \frac{\partial T}{\partial x} = 0 \tag{5}$$

$$y = 0: \quad \frac{\partial T}{\partial y} = 0 \tag{6}$$

$$y = 0.025: \quad T_{Cu} = T_{cx2002u} \tag{7}$$

$$y = 0.035: \quad q = q_{inc} \tag{8}$$

$$x = \sqrt{\frac{d^2}{4} - (y - 0.017)^2}: \quad q = -q\theta \tag{9}$$

where the divertor plate width, w, and the cooling tube diameter, d, are in (m) and the incident heat flux, q_{inc}, and the surface heat flux, q_θ, of the cooling tube are in (W/m^2). The q_θ are given with the aid of the relation between the heat flux, q, and the surface temperature, T_s, previously measured based on the surface temperature of the cooling tube numerically analyzed at every $\pi/18$ for θ ranging from 0 to π. The effect of heated length, L, on CHF appeared in the relation between q and T_s measured.

3.2 Calculation Method. Boiling curves measured for the test tube with an inner diameter of 9 mm and with three heated lengths of 48, 99, and 149 mm at inlet pressures, P_{in}, ranged from 594 kPa to 1 MPa are used for the numerical analysis. Figure 4 shows the typical example of the heat transfer characteristics for $d=9$ mm with $P_{in}=594$ kPa, $u=6.93$ m/s, and $T_{in}=306.6$ K. The heat flux gradually becomes higher with an increase in $(T_s - T_{in})$ on the forced convection curve derived from Nusselt correlation [10] up to the point where the slope begins to increase with heat flux following the onset of nucleate boiling, and increases up to a value called CHF, where the heater surface temperature rapidly jumps from the nucleate boiling heat transfer regime to the film boiling one. The film boiling curve in the figure is given by the values derived from the Shiotsu and Hama's correlation [11]. It is assumed that the film boiling exists for the heater surface temperature, T_s, higher than the homogeneous spontaneous nucleation temperature, T_H. The transition boiling curve is given as the straight line drawn between the point for $(T_s - T_{in})$ 20 K higher than that at CHF and that at the minimum heat flux based on the experimental study on transient boiling heat transfer including the transition to film boiling on a 1.2 mm diameter horizontal cylinder in a pool of water caused by a rapid pressure reduction from an initial pressure under an initial heat input [12]. Minimum film boiling temperature or heat flux on the inner surface of a vertical tube with water flowing upward is not clearly understood, at present, experimentally or theoretically. On the other hand, Sakurai et al. [13] performed systematic experiments of minimum film boiling states on horizontal cylinders in a pool of liquids at pressures. They observed that the minimum film boiling temperature, T_{min}, in each liquid was lower than the homogeneous spontaneous nucleation temperature, T_H, at atmospheric pressure, and it increased and approached T_H with an increase in pressure. In the case of water, T_{min} almost agreed with T_H for the pressures higher than around 1 MPa. They also reported that the minimum film boiling state seemed to be characterized by the surface temperature rather than the heat flux. It was because T_{min} on different diameter cylinders under the same condition agreed with each other, although the heat flux at the point was lower for a larger diameter cylinder due to the dependence of film boiling heat transfer coefficients on the cylinder diameter. It is assumed based on these facts that T_{min} for the forced convection film boiling of water at high pressures would be around T_H.

Table 1 Constants of Eq. (10)

P (kPa)	Boiling condition	C	n	ΔT range (K)
594	Forced convection	1.4583×10^{4}	1.2136	0 to 117.552
		84.7218	2.2936	117.552 to 133.631
	Nucleate boiling	$7.440\,06\times10^{-2}$	3.7313	133.631 to 153.11
		$4.800\,59\times10^{-30}$	16.633	153.11 to 158.546
		18.901×10^{6}	0	158.546 to 178.281
	Transition boiling	$6.131\,06\times10^{29}$	−10	178.281 to 270.818
	Film boiling	441.748	1.1574	Higher than 270.818

The q_θ value for each control volume is given from the boiling curve shown in Fig. 4 as the heat flux at the surface temperature numerically obtained for each control volume. The boiling curve shown in Fig. 4 was formulated to give the surface heat flux on the cooling tube in the CFD (computational fluid dynamics) code as follows.

$$q = C\,\Delta T^{n}, \tag{10}$$

$$\Delta T = T_s - T_{in} \tag{11}$$

where all constants, C, and exponents, n, are given in Table 1. The surface heat flux, q_θ, and the surface temperature, T_s, on the cooling tube were calculated from the analyzed temperature, T_1, at the center of the first control volume on the cooling tube, by the iteration on the thermal conduction in the control volume as follows:

$$\lambda_{Cu}(T_1) = f(T_1) \tag{12}$$

$$q_{s1} = C(T_1 - T_{in})^{n} \tag{13}$$

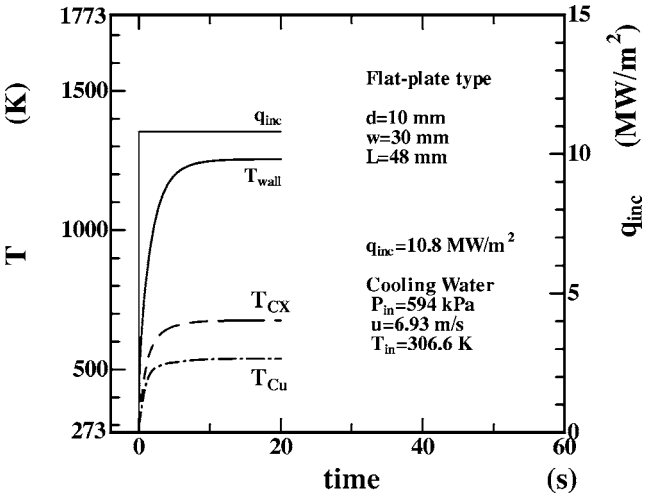

Fig. 5 Time variations in T_{wall}, T_{CX}, and T_{Cu} for q_{inc} =10.8 MW/m^2 with d=10 mm and L=48 mm

$$T_s = T_1 - q_{s1}\frac{z}{2\lambda_{Cu}}(T_1) \tag{14}$$

$$q_s = C(T_s - T_{in})^n \tag{15}$$

$$T_s = T_1 - q_s\frac{z}{2\lambda_{Cu}(T_1)} \tag{16}$$

Equations (15) and (16) were iterated 50 times in the code.

$$q_\theta = q_s \tag{17}$$

where the thermal conductivity of the oxygen-free copper, λ_{Cu}, is in (W/mK) and the depth of the first control volume on the cooling tube, z, is in (m). All the calculations were made by using the PHOENICS code [14].

4 Results and Discussion

4.1 Conditions for Calculation. Flat-plate-type divertors are numerically analyzed as follows:

• Flat-plate type divertors
Material: Oxygen-free copper and CX2002U
Width (w): 16 to 30 mm
Height (h): 35 mm
Heated length (L): 48 to 149 mm
Incident heat flux (q_{inc}): 9 to 19 MW/m^2
Cooling tube diameter (d): 10 mm
• Cooling water
Inlet pressure (P_{in}): 594 kPa to 1 MPa
Flow velocity (u): 6.9 to 13.3 m/s
Inlet liquid temperature (T_{in}): 304.6 to 315.3 K
(31.4 °C to 41.2 °C)

4.2 Incident Critical Heat Flux. Figure 5 shows the numerically obtained time variations in the surface temperature, T_{wall}, the inner temperature of the carbon tile, T_{cx}, and the inner temperature of the copper block, T_{Cu}, for q_{inc}=10.8 MW/m^2 for the divertor of 30 mm wide with the cooling tube diameter, d, of 10 mm, which is cooled with highly subcooled and pressurized water for the inlet liquid temperature, T_{in}, of 306.6 K at the inlet pressure, P_{in}, of 594 kPa with the flow velocity, u, of 6.93 m/s. In this calculation the boiling curve for the test tube inner diameter (d =9 mm) and the heated length (L=48 mm) was used. The surface temperature of the carbon tile (CX2002U) rapidly increases up to 1248.2 K after 10 s of the heating and gradually approaches the constant value of about 1273.2 K with the elapse of time. The heat transfer on the inner surface of the cooling tube stays in the nucleate boiling regime (N-B).

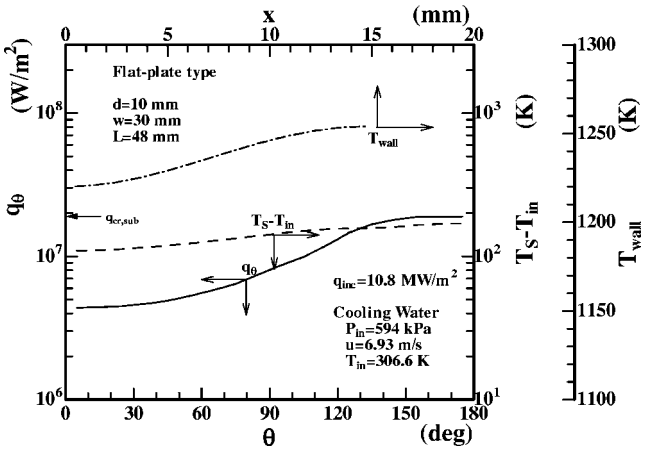

Fig. 6 Peripheral distribution of q_θ, $T_s - T_{in}$, and T_{wall} for q_{inc} =10.8 MW/m^2

The peripheral distributions of the surface heat flux, q_θ, and the inner surface temperature, T_s, on the cooling tube and the intersectional one of T_{wall} on the carbon surface after 20 s of heating are shown in Fig. 6 with the experimental data point of CHF, $q_{cr,sub}$. The line, x=0, is the central axis of the carbon tile. The q_θ values on the cooling tube are widely distributed, ranging from 4.37 MW/m^2 at θ=0° (the bottom of the cooling tube) to 18.9 MW/m^2 at θ=180° (the top of the one), which is almost the CHF value. It is assumed from this figure that the boiling phenomena on the whole surface of the cooling tube will be the nucleate boiling regime for q_{inc}=10.8 MW/m^2.

The numerical solutions of the time variations in T_{wall}, T_{cx}, and T_{Cu} for q_{inc}=11.6 MW/m^2 are shown in Fig. 7. After 6.3 s of the heating, the T_{wall} value steeply increases again because the top inner surface of the cooling tube begins to be covered with vapor, the vapor spreads downward the cooling tube surface and the surface temperature of the cooling tube jumps to that of the film boiling regime. The heat transfer on the inner surface of the cooling tube turns to film boiling regime (F-B). The incident critical heat flux, $q_{cr,inc}$, is defined as the maximum value of q_{inc} without

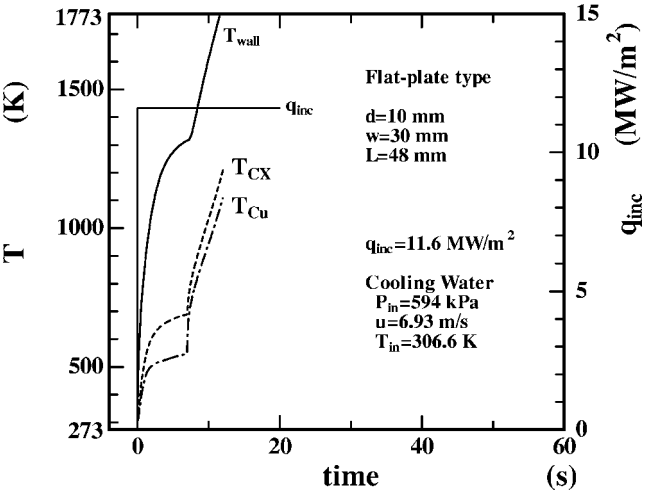

Fig. 7 Time variations in T_{wall}, T_{CX}, and T_{Cu} for q_{inc} =11.6 MW/m^2 with d=10 mm and L=48 mm

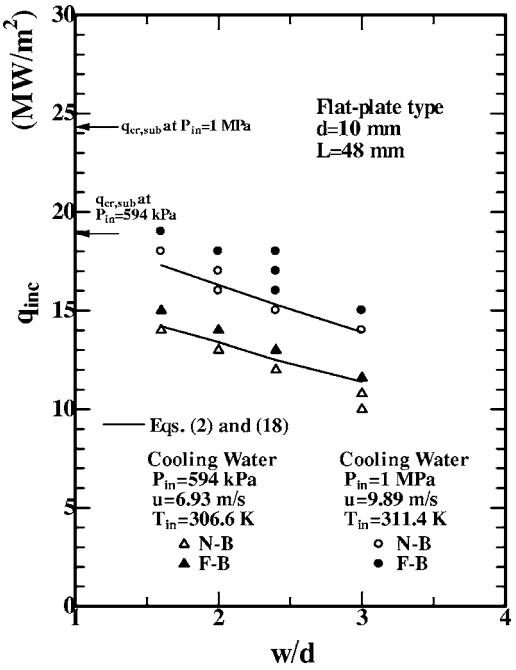

Fig. 8 Relationship between q_{inc} and w/d at a cooling tube inner diameter of 10 mm

the steep increase of T_{wall} due to the surface temperature on the cooling tube increasing to that of the film boiling regime.

4.3 Influence of Width. The numerical solutions of q_{inc} for the divertor width, w, ranging from 16 to 30 mm, are shown in Fig. 8 with the triangle symbols. The q_{inc} values with and without the transition to film boiling are shown as the solid and open symbols, respectively. The $q_{cr,inc}$ value for P_{in}=594 kPa is around 11 MW/m^2 at a w/d of 3. They become higher with a decrease in w/d and finally reach a value of about 14 MW/m^2 at a w/d of 1.6. The $q_{cr,inc}$ value becomes 27% higher with a decrease in w/d from 3 to 1.6. The numerical solutions of q_{inc} for the inlet pressure, the flow velocity, and the inlet temperature of 1 MPa, 9.89 m/s, and 311.4 K were also shown in this figure for comparison. The values of $q_{cr,inc}$ for P_{in}=1 MPa show nearly the same trends of dependence on w/d, although they are 25% higher than the corresponding values for P_{in}=594 kPa.

4.4 Comparison With Uniform Heating Data. The ratios of the calculated q_{inc} for the flat-plate-type divertor and with the cooling tube diameter of 10 mm at the inlet pressures of 594 kPa to 1 MPa to the experimental data of $q_{cr,sub}$ with the SUS304 tube of 9 mm inner diameter at the same inlet pressure condition, $q_{inc}/q_{cr,sub}$, are shown versus w/d in Fig. 9. The numerical solutions of the $q_{cr,inc}$ for the heated length of 48 to 149 mm with the flow velocity of 6.9 to 13.3 m/s at the inlet pressure of 594 kPa to 1 MPa are approximately expressed by the following correlation.

$$\frac{q_{cr,inc}}{q_{cr,sub}} = 0.97e^{-w/6.4d} \tag{18}$$

The curve derived from this correlation is independent of the flow velocity and the inlet pressure for the entire numerically solved range. On the other hand, the $q_{cr,sub}$ value in Eq. (18) for $\Delta T_{sub,in}$ higher than around 40 K is given by Eq. (2). The $q_{cr,inc}$ value for higher pressures can be predicted by using Eqs. (2) and (18). The $q_{cr,inc}$ value thus derived for the inlet pressures of 0.5, 1, and 2 MPa at the flow velocity of 10 m/s with the inlet liquid temperature of 308.2 K are shown in Fig. 10 as a curve for each value of the inlet pressure. The $q_{cr,inc}$ value for L=50 mm becomes

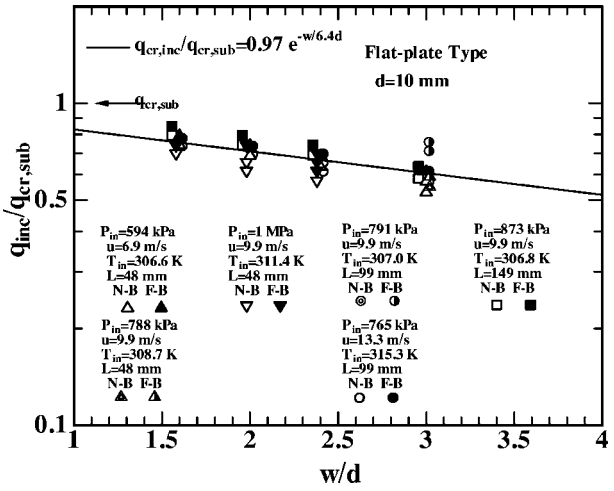

Fig. 9 Relationship between $q_{inc}/q_{cr,sub}$ and w/d for a flat-plate-type divertor

higher than 20 MW/m^2 with the decrease in the w/d smaller than 2 for the inlet pressure of 2 MPa. Those for L=100 and 150 mm become higher than 15 MW/m^2 with a decrease in w/d smaller than 3.3 and 2.6 for the inlet pressure of 2 MPa, respectively.

It is considered that the incident critical heat flux, $q_{cr,inc}$, for the divertor will be larger than the value derived from Eqs. (2) and (18). Because the divertor is made of a copper tube or copper block whose thermal conductivity is very high, and so the difference between the inlet and outlet temperatures of the divertor will become smaller than that of the experimental data by using the thin SUS304 tube. It is assumed based on this fact that Eq. (18) will give the lower limit for the ratio of the one side heat loading data to the uniform heat loading data.

5 Comparison of Our Numerical Solution With Other Worker's Experimental Data

The mock-up experiment has been performed by Kubota et al. [15,16] at the National Institute for Fusion Science (NIFS). This is the high heat flux heat removal experiment on the mock-up divertor plate heated by the electron beam facility. The cross-sectional view of this divertor plate is almost the same as shown

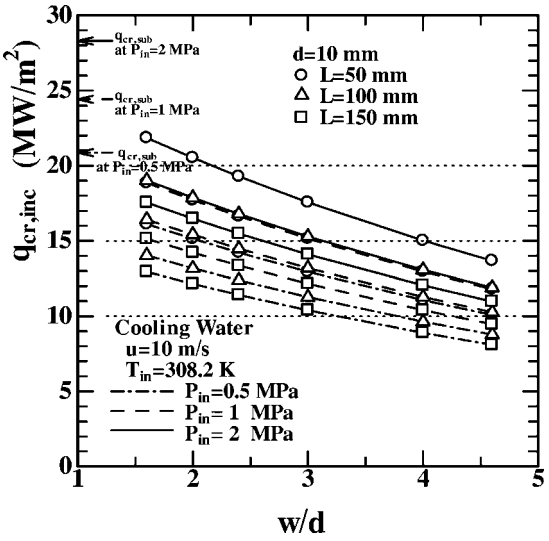

Fig. 10 Relationship between $q_{cr,inc}$ and w/d at P_{in} =0.5–2 MPa

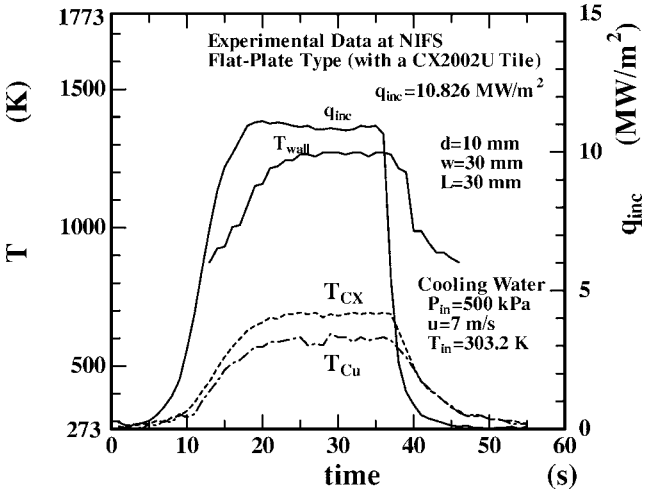

Fig. 11 Time variations in T_{wall}, T_{CX}, and T_{Cu} for q_{inc} =10.8 MW/m^2 in the heat load test (Kubota et al. [15,16])

in Fig. 1(*a*). The hatching area on the upper surface of the divertor shown in the figure is heated with the heat flux of 11.6 MW/m^2. The incident heat flux, q_{inc}, within the heated length (L =30 mm) is equivalent to 10.826 MW/m^2. The cooling water for P_{in}=500 kPa, u=7 m/s, and T_{in}=303.2 K is circulated through the divertor. The mock-up experimental results of time variations are shown in Fig. 11. The T_{wall} is measured by a pyrometer, and T_{CX} and T_{Cu} by thermocouples. Figure 12 shows the numerically obtained time variations in the surface temperature, T_{wall}, the inner temperature of the carbon tile, T_{cx}, and the inner temperature of the copper block, T_{Cu}, for q_{inc}=10.8 MW/m^2 with the divertor of 30 mm wide and the cooling tube diameter, d, of 10 mm, which is cooled with highly subcooled and pressurized water for the inlet liquid temperature, T_{in}, of 306.6 K at the inlet pressure, P_{in}, of 594 kPa with the flow velocity, u, of 6.93 m/s, which is the same with Fig. 5. The experimental data in Fig. 11 are also shown in the figure for comparison. From the comparison of the numerical solutions with the mock-up results in Fig. 12, the T_{wall}, T_{CX}, and T_{Cu} in the numerical results and those in the mock-up results are approximately the same, respectively, although their increasing rates for the experiment are a little smaller than those for the numerical solution. This fact verified that numerical analyses are reliable. It is assumed that the incident heat flux of the mock-up experiment might be just below the incident critical heat flux. The effect of difference between tube inner diameter and heated length on heat transfer and CHF are estimated as follows. In the fully developed boiling region, the tube inner diameter and the heated length, both of which have a little influence on the single-phase heat transfer [10,17,18], have little or no effect on the surface temperature [19–22]. And the $q_{cr,sub}$ are almost proportional to $d^{-0.4}$ and $(L/d)^{-0.1}$, as mentioned above, so the CHFs for the numerical solution would become 4.1% higher for the tube inner diameter and 4.6% lower for the heated length than those for the mock-up experiment, because in this calculation the boiling curve for the test tube inner diameter (d=9 mm) and the heated length (L =48 mm) was used.

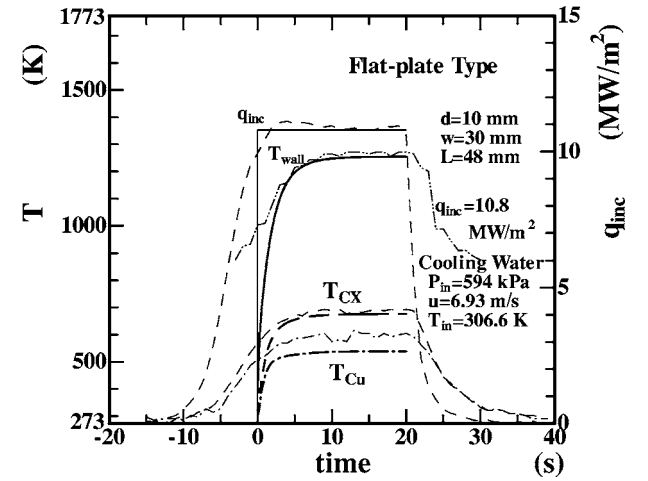

Fig. 12 A comparison of the experimental data with the numerical solution

6 Conclusions

The subcooled flow boiling critical heat fluxes (CHFs) and the heat transfer coefficients (HTCs) for the test tube inner diameters (d=9 mm) and the heated lengths (L=48 to 149 mm) were applied to thermal analysis of the flat-plate-type divertor of LHD. The incident CHFs, $q_{cr,inc}$, for the divertor with the cooling tube diameter, d, of 10 mm and the carbon armor plate width, w, ranging from 16 to 30 mm, were numerically analyzed based on the CHFs and HTCs measured. Experimental results lead to the following conclusions.

The incident critical heat flux, $q_{cr,inc}$, is defined as the maximum value of q_{inc} without the steep increase of T_{wall} due to the surface temperature on the cooling tube increasing to that of the film boiling regime.

The $q_{cr,inc}$ value becomes 27% higher with a decrease in w/d from 3 to 1.6.

The ratio of the one-side heat-loading CHF data, $q_{cr,inc}$, to the uniform heat loading CHF data, $q_{cr,sub}$, can be represented as the simple equation based on the numerical solutions.

The values of the $q_{cr,inc}$ for the tube lengths of 50, 100, and 150 mm were estimated with various w/d at higher inlet pressures.

Acknowledgment

This research was performed as a LHD joint research project of NIFS (National Institute for Fusion Science), Japan and was partially supported by the Japan Society for the Promotion of Science, Grant in Aid for Scientific Research (C), 15560180, 2004.

Nomenclature

Bo = q_{cr}/Gh_{fg}, boiling number
C = constant used in (Eq. (10))
d = test tube inner diameter, m;
= cooling tube inner diameter, m
h = height, m
L = heated length, m
n = exponent used in (Eq. (10))
P = pressure, kPa
q = heat flux, W/m^2
$q_{cr,sub}$ = critical heat flux for subcooled condition, W/m^2
$q_{cr,inc}$ = incident critical heat flux, W/m^2
q_{inc} = incident heat flux, W/m^2
q_θ = surface heat flux on the cooling tube, W/m^2
Re = Gd/μ_l, Reynolds number
Sc = $c_{pl}(\Delta T_{sub,out})_{cal}/h_{fg}$, $c_{pl}\,\Delta T_{sub,out}/h_{fg}$, nondimensional outlet subcooling
Sc* = $c_{pl}\,\Delta T_{sub,in}/h_{fg}$, nondimensional inlet subcooling
t = time, s
T_{Cu} = outer temperature of the copper cooling tube, K
T_{cx} = inner temperature of the carbon armor, K

T_H = homogeneous spontaneous nucleation temperature, K
T_{in} = inlet liquid temperature, K
T_{min} = minimum film boiling temperature, K
T_s = heater inner surface temperature, K;
= surface temperature of the cooling tube, K
T_{wall} = carbon armor surface temperature, K
u = flow velocity, m/s
We = $G^2d/\rho_l\sigma$, Weber number
w = divertor width, m
x-y = Cartesian coordinates, m-m
z = depth of the first control volume, m
ΔT = $(T_s - T_{in})$, K
$\Delta T_{sub,in}$ = $(T_{sat} - T_{in})$, liquid inlet subcooling, K
$\Delta T_{sub,out}$ = $(T_{sat} - T_{out})$, outlet liquid subcooling, K

Subscript

I = control volume number
Cu = copper
in = inlet
out = outlet

References

[1] Hata, K., Fukuda, K., Shiotsu, M., Sakurai, A., Noda, N., Motojima, O., and Iiyoshi, A., 1998, "Critical Heat Fluxes in Subcooled Boiling of Water Flowing Upward in a Vertical Tube for Wide Ranges of Liquid Velocity, Subcooling and Pressure," *Proceedings of 6th International Conference on Nuclear Engineering*, Paper No. ICONE-6362, pp. 1–16.

[2] Hata, K., Fukuda, K., Shiotsu, M., and Sakurai, A., 1999, "The Effect of Diameter on Critical Heat Flux in Vertical Heated Short Tubes of Various Inside Diameters Cooled with an Upward Flow of Subcooled Water," *Proceedings of 9th International Topical Meeting on Nuclear Reactor Thermal Hydraulics*, Paper No. NURETH9-194, pp. 1–20.

[3] Sato, G., Hata, K., Shiotsu, M., and Noda, N., 2000, "Critical Heat Fluxes on Short Vertical Tube Inner Surface in Water Flowing Upward (Effect of tube Inner Diameter and Application to Thermal Analysis of Divertor Plate)," *Proceedings of the 8th International Conference on Nuclear Engineering*, Paper No. ICONE-8126, pp. 1–12.

[4] Hata, K., Sato, T., and Shiotsu, M., 2001, "Influence of Tube Length on Critical Heat Fluxes in Water Flowing Upward," *Proceedings of the 9th International Conference on Nuclear Engineering*, Paper No. ICONE-9569, pp. 1–12.

[5] Hata, K., Sato, T., Tanimoto, T., Shiotsu, M., and Noda, N., 2002, "Critical Heat Fluxes of Subcooled Water Flow Boiling against Outlet Subcooling in Short Vertical Tube," *Proceedings of the 10th International Conference on Nuclear Engineering*, Paper No. ICONE10-22324, pp. 1–10.

[6] Hata, K., Tanimoto, T., Komori, H., Shiotsu, M., and Noda, N., 2003a, "Critical Heat Fluxes of Subcooled Water Flow Boiling against Inlet Subcooling in Short Vertical Tube," *Proceedings of the 11th International Conference on Nuclear Engineering*, Paper No. ICONE11-36116, pp. 1–11.

[7] Hata, K., Komori, H., Shiotsu, M., and Noda, N., 2003b, "Critical Heat Flux of Subcooled Water Flow Boiling for High L/d Region," *Proceedings of the 10th International Topical Meeting on Nuclear Reactor Thermal Hydraulics*, Paper No. NURETH10-C00207, pp. 1–13.

[8] Hata, K., Shiotsu, M., and Noda, N., 2004a, "Critical Heat Fluxes of Subcooled Water Flow Boiling against Outlet Subcooling in Short Vertical Tube," Trans. ASME, Ser. C: J. Heat Transfer, **126**, pp. 312–320.

[9] Hata, K., Komori, H., Shiotsu, M., and Noda, N., 2004b, "Critical Heat Fluxes of Subcooled Water Flow Boiling against Inlet Subcooling in Short Vertical Tube," JSME Int. J., Ser. B, **47**, pp. 306–315.

[10] Nusselt, W., 1931, "Der Wärmeaustausch Zweischen Wand und Wasser im Rohr," Forsch. Geb. Ingenieurwes. **2**, pp. 309.

[11] Shiotsu, M., and Hama, K., 2000, "Film Boiling Heat Transfer from a Vertical Cylinder in Forced Flow of Liquids under Saturated and Subcooled Conditions at Pressures," Nucl. Eng. Des., **200**, pp. 23–38.

[12] Sakurai, A., Shiotsu, M., and Hata, K., 1980, "Transient Boiling Caused by Rapid Depressurization From Initial Non-Boiling State," *Multiphase Transport, Fundamentals, Reactor Safety, Applications*, Hemisphere Pub. Corp., Washington, DC, Vol. II, pp. 727–747.

[13] Sakurai, A., Shiotsu, M., and Hata, K., 1990, "Effect of System Pressure on Minimum Film Boiling Temperature for Various Liquids," Exp. Therm. Fluid Sci., **3**, pp. 450–457.

[14] Spalding, D. B., 1991, "The PHOENICS Beginner's Guide," published by CHAM, UK.

[15] Kubota, Y., Noda, N., Sagara, A., Komori, A., Inoue, N., Akaishi, K., Suzuki, H., Ohyabu, N., and Motojima, O., 1995, "Development of High Heat Flux Components in Large Helical Device (LHD)," *Proceedings of the ASME Heat Transfer Division*, HTD-Vol. 317-1, 1995 IMECE, pp. 159–163.

[16] Kubota, Y., private communication, 28 December 1998.

[17] Dittus, F. W., and Boelter, L. M. K., 1930, University of California, Berkeley, Pub. Eng., Vol. 2, p. 443.

[18] Sieder, E. N., and Tate, C. E., 1936, "Heat Transfer and Pressure Drop of Liquids in Tubes," Ind. Eng. Chem., **28**, pp. 1429–1435.

[19] McAdams, W. H., Kennel, W. E., Minden, C. S. L., Carl, R., Picornell, P. M., and Dew, J. E., 1949, "Heat Transfer at High Rates to Water with Surface Boiling," Ind. Eng. Chem. **41**, pp. 1945–1953.

[20] Jens, W. H., and Lottes, P. A., 1951, "Analysis of Heat Transfer Burnout, Pressure Drop and Density Data for High Pressure Water," ANL-4627, May.

[21] Rohsenow, W. M., 1952, "A Method of Correlating Heat-Transfer Data for Surface Boiling of Liquids," Trans. ASME, **74**, pp. 969–976.

[22] Thom, J. R. S., Walker, W. M., Fallon, T. A., and Reising, G. F. S., 1965, "Boiling in Subcooled Water During Flow up Heated Tubes or Annuli," Proc. Inst. Mech. Eng., **180**, pp. 226–246.

Effect of Rotation and Surface Roughness on Heat Transfer Rate to Flow through Vertical Cylinders in Steam Condensation Process

Hany A. Mohamed
Associate Professor
Mechanical Engineering Department,
Faculty of Engineering,
Assiut University,
Assiut, Egypt
e-mail: hah@aun.edu.eg

The enhancement in the rate of the heat transfer resulting from rotating smooth and rough vertical cylinders, of 1.28 and 21.75 μm *average roughness, respectively, are experimentally studied. Experiments were carried out for cooling fluid Reynolds numbers from 3300 to 7800 with varying the rotational speed up to* 280 rpm. *Experimental runs at the stationary case showed an acceptable agreement with the theoretical values. The experimental Nusselt number values at various rotational speeds are correlated as functions of Reynolds, Weber, and Prandtl numbers for smooth and rough surfaces. The correlated equations were compared with the correlation obtained by another author. The results show that the enhancement of the heat transfer rate becomes more appreciable for low Reynolds numbers at high rotational speeds and for high Reynolds numbers at low rotational speeds. The rotation causes an enhancement in the overall heat transfer coefficient of* ~89% *at* Re=7800, We=1084, *and* Pr=1.48 *for smooth surface and of* ~13.7% *at* Re=4700, We=4891, *and* Pr=1.696 *for rough surface. Also, the enhancement in the heat transfer rates utilizing rotary surface becomes more pronounced for the smooth surface compared with the rough one, therefore the choice of the heat transfer surface is very important. The present work shows a reduction in the heat transfer rate below its peak value depending on the type of the heat transfer surface. It is shown that the enhancement in the heat transfer, i.e., enhancement in the Nusselt number, depends on the Weber number value and the surface type while the Nusselt number value mainly depends on the Reynolds and Prandtl numbers. Correlated equation have been developed to represent the Nusselt number values as functions of the Weber and Reynolds numbers within the stated ranges of the parameters.* [DOI: 10.1115/1.2098862]

1 Introduction

Condensation occurs when the temperature of vapor is reduced below its saturation temperature. In industrial equipment, the process commonly results from contact between the vapor and a cold surface. The dominant form of condensation is a way in which a liquid film covers the entire cool surface and under the action of gravity, the film flows continuously upon the surface. In the film condensation, the condensate provides a resistance to heat transfer between the vapor and the surface. Because this resistance increases with increasing condensate thickness in the flow direction, it is desirable to reduce the thickness of condensate film on the condensing surfaces. The centrifugal force obtained by utilizing rotational cold surface has been proposed to obtain a thinner condensate film for enhancing heat transfer. However, a mechanical power was consumed for the rotation, thus this enhancement represents additional running cost compared to conventional stationary heat exchanger. In spite of this additional cost, a mechanical condenser of this type is suitable where compact equipment is a must, or in outer space where gravitational force is absent.

Heat transfer enhancement resulting from the rotation of the heat transfer surfaces has received a great deal of attention in the past decades. Several previous works have been done to enhance the heat transfer rate by rotating horizontal [1–3] and vertical [4,5] heat transfer surfaces. Chandran and Watson [1] observed heat transfer coefficients in films of methanol, isopropanol, ethylacetate, *n*-butanol, and water condensing on rotating plain and pinned horizontal tubes. Singer and Preckshot [2] studied the overall heat transfer coefficient on a horizontally rotating cylinder cooled on the inside by water and enclosed in a steam chamber. They concluded that the flow and heat transfer characteristics of the system went through three regimes as the rotational speed increased. At low rotational speeds the vertical gravitational drainage force was partly opposed by the radial centrifugal force and the circumferential friction force between the fluid and the rotor, thus causing an increase in the mean film thickness and a reduction in heat transfer rate. At moderate speeds the condensate sprayed from the cylinder making the liquid film thinner and increasing the heat transfer rate. At very high speeds the droplets on the cylinder elongated into streaks and heat transfer rate fell. Hoyle and Matthews [3] investigated the effects of diameter and rotational speed of cylinder carrying cooling water on the heat transfer from steam. They did not report any decrease in heat transfer at high rotational speeds. Nicol and Gacesa [4] obtained high heat transfer coefficients for condensing steam on a vertical cylinder rotating on its axis. They attributed the increase in heat transfer to be due to the film being thrown off the wall due to the centrifugal force. Ball et al. [5] experimentally studied the heat transfer in a vertical annulus with a rotating inner heated cylinder. They concluded a qualitative description of the transition of a buoyancy dominated flow regime to one dominated by rotation. More studies were done for studying the enhancement in the heat transfer due to rotation effect (e.g., [6–13]).

All the previous studies have shown that increasing the rotational speed resulted in an enhancement of the heat transfer rate with different peak values. Some of these works show that a further increase in speed resulted in a reduction in the heat transfer coefficient below its peak value (e.g., [1,2]). Hirai et al. [14] had shown that increasing the pipe rotational speed had resulted in the change of the fully developed turbulent profile of the axial velocity into a laminar-like velocity profile and had decreased the friction factor causing the reduction in the heat transfer coefficient. They called this phenomenon "the laminarization phenomena." This phenomenon restricts the enhancement in the heat transfer coefficient and may cause the reduction in the heat transfer rate below its peak value with the increase in the rotational speed.

The aforementioned works have not studied any way for retarding of the laminarization phenomena or the effect of the cold surface roughness on the heat transfer. Therefore, an experimental test rig used in the present work was designed so that cold fluid flows between two rotating central surfaces as a way to restrict the cold fluid flow for retarding the laminarization phenomena. Also the paper investigates the effect of rotational speed and surface roughness of two heat transfer surfaces on the heat transfer rate. Experiments were conducted using saturated water vapor at atmospheric pressure as the hot fluid and liquid water as the cold fluid in counter flow. The cold fluid flows in the annular passage to obtain larger heat transfer surface compared with the flow inside the inner cylinder. The results obtained for different Reynolds numbers are presented in terms of Nusselt and Weber numbers to characterize the effect of the surface tension and centrifugal force on the rate of the heat transfer. The values of Nusselt number were

Contributed by the Heat Transfer Division of ASME for publication in the JOURNAL OF HEAT TRANSFER. Manuscript received August 30, 2004; final manuscript received April 12, 2005. Assoc. Editor: Chang Oh.

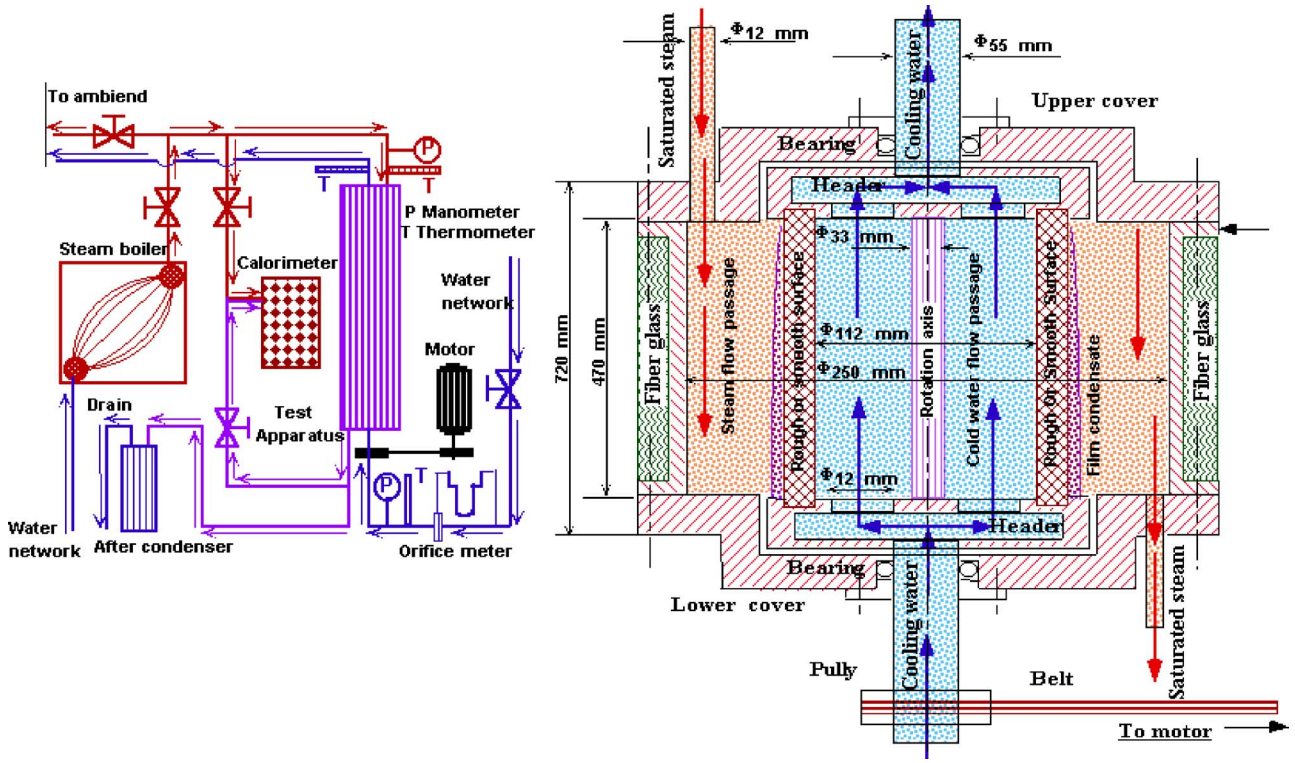

Fig. 1 Schematic drawing of the flow paths and the experimental apparatus

correlated as functions of Reynolds, Weber, and Prandtl numbers for the smooth and the rough surfaces and were compared with the correlation obtained by another author [4].

2 Experimental Work

A schematic drawing of the flow paths and the experimental apparatus which was set up in the thermal laboratory of Mechanical Engineering Department at Assiut University is shown in Fig. 1. It is mainly composed of thick brass shell and rotary part. The thick shell was made from brass cylinder of 250 ± 0.05 mm inner diameter with 10 ± 0.05 mm wall thickness and 720 ± 0.5 mm length. The two ends of the shell were bolted to thick brass covers through which the end shafts were passed. Thrust and ball bearings were installed in each cover. Two holes of 12 ± 0.05 mm diameter are opened on the top and bottom of the cover for flowing the hot fluid into and out of the shell. Precautions were made for preventing any leakage from these ends using rubber seals and glands.

The rotary part is constructed from two steel headers and a rough galvanized steel pipe of 33.4 ± 0.05 mm outer diameter, located in the center of the heat transfer cylinder (rough or smooth surface). The rough cylinder is made from brass material of 115.4 ± 0.05 mm inner diameter, 3.0 ± 0.05 mm wall thickness, and 470 ± 0.5 mm length. The smooth cylinder is made from PVC material of 112 ± 0.05 mm inner diameter, 4.0 ± 0.05 mm wall thickness, and 470 ± 0.05 mm length. The ends of the rough galvanized steel pipe and the heat transfer cylinders were fixed on the two headers by using oxygen-ethylene welding or iron chemical glue. The rotary part was balanced and tested for alignment with a dial indicator on a lathe machine for reducing the vibration as much as possible. Before housing it in the shell, the heat transfer surfaces had been carefully cleaned from any dirt or grease. The shell and the connecting pipes were insulated with fiberglass of thickness 50 mm. The apparatus was connected to the static cooling water inlet and outlet pipes by special sealed joints to prevent leakage of cooling water. The surface roughnesses were measured by a commercial surface profilometer (Surtronic 3). The average roughnesses for the smooth and rough surface are 1.28 and 21.75 μm, respectively.

A saturated vapor steam at atmospheric pressure was fed into shell of the apparatus as the hot fluid. Cooling water was admitted to the apparatus from the main laboratory network. The water flow rate was regulated by a network valve and measured by a calibrated orifice meter with maximum uncertainty of ±1%. Large-scale mercury thermometers were used to measure inlet and outlet temperatures of the saturated steam and the cooling water with an accuracy of $\pm0.5^\circ$C. The saturated steam exiting from the apparatus was condensed and its mass flow rate was measured by using a graduated glass tube mounted on a calibrated tank and stopwatch with maximum uncertainty of ±0.01 kg/s. A 3.7 kW squirrel cage variable speed electric motor is connected to the apparatus. The rotational speed was measured by a tachometer with uncertainties of ±5 rpm for speeds up to 500 rpm.

At the beginning of each experiment, the equipment was operated under the presumed test conditions for 40 min before readings were recorded to ensure steady state condition. The heat given up in condensation is compared with the heat gained by the cooling water. Only when the heat balance was within 5%, the results were accepted. Experiments were performed over a range of cooling water Reynolds numbers from 3300 to 7800 and rotational speeds up to 280 rpm. The experimental measurements were carried out at constant cooling water Reynolds number.

3 Analysis

For each experiment, measurements of all variables were recorded after steady state conditions were established. Conduction heat losses through the ends of the rotating hollow shaft were neglected due to the small temperature difference between the cooling water flowing through the shaft and the ambient. The rate of heat transfer, Q, is determined from:

$$Q = m\,C\,(T_2 - T_1) \tag{1}$$

where m and C are the mass flow rate and the specific heat of the cooling water and T_1 and T_2 are the inlet and outlet cooling water temperatures, respectively. The overall heat transfer coefficient, U, based on the outside surface of the cylinder, A_o, is calculated from

$$U = \frac{Q}{(A_o\,\Delta T)} \tag{2}$$

where ΔT is the logarithmic mean temperature difference, given by

$$\Delta T = \frac{(T_2 - T_1)}{\ln \dfrac{(T_s - T_1)}{(T_s - T_2)}} \tag{3}$$

where T_s is the steam saturation temperature. The mean heat transfer coefficient of the condensation, h_m, is calculated from

$$h_m = \frac{Q}{A_o(T_f - T_w)} \tag{4}$$

where T_f and T_w are the mean temperature of the condensate film and the outside surface temperature, respectively. Due to the small difference in temperature between the exit and inlet cooling water and the slightly subcooled condensate at the delivery as recorded by experiments, hence, T_w, can be estimated from

$$T_w = 0.5\left(T_f + \frac{T_1 + T_2}{2}\right) \tag{5}$$

where the condensate film temperature was calculated from a relation, $T_f = T_s - 0.75(T_2 - T_1)$, as it is mentioned and used by Chandran and Watson [1] for a similar work. The Nusselt number, Nu, cooling water Reynolds number, Re, and Weber number, We, were computed from the following

$$\mathrm{Nu} = \frac{h_m\,D_o}{k_f} \tag{6}$$

$$\mathrm{Re} = \frac{\rho\ V\,D_h}{\mu} \tag{7}$$

$$\mathrm{We} = \frac{\rho_f \omega^2 D_o^3}{4\sigma_f} \tag{8}$$

where k_f, ρ_f, and σ_f are the thermal conductivity, the density, and the surface tension of the condensate film, ρ and μ are the density and viscosity of the cooling water at mean temperature, $(T_1 + T_2)/2$, V is the cooling water axial velocity, ω is the rotor angular velocity, D_h is the hydraulic diameter, $D_h = D_i - d$, d is the outer diameter of the closed central pipe, and D_i and D_o are inner and outer diameter of the tested (rough or smooth) cylinder, respectively. The enhancement in the rate of the heat transfer, ε, due to the use of rotation is calculated from

$$\varepsilon = \frac{U - U_o}{U_o} \tag{9}$$

where U_o is the overall heat transfer coefficient obtained with no rotation (stationary case).

The theoretical heat transfer coefficient for the film condensation, h_o, was calculated using Nusselt equation on a vertical stationary surface, which is

$$h_o = 0.943\left[\frac{k_f^3 \rho_f(\rho_f - \rho_v)\,g h_{fg}}{L\mu_f(T_s - T_w)}\right]^{0.25} \tag{10}$$

where ρ_v is the vapor density, g is the gravity acceleration, h_{fg} is the steam latent heat, L is the length of the test cylinder.

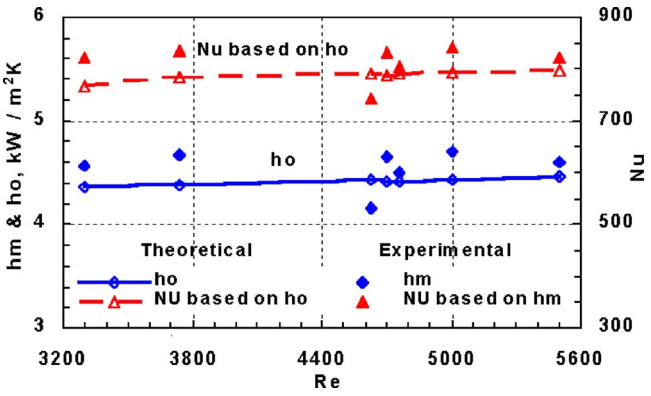

Fig. 2 Comparison between the experimental and theoretical values of the heat transfer coefficient and Nusselt number with stationary rough surface

4 Uncertainty Analysis

The uncertainty analysis presented in this section is based upon the methods discussed by Moffat [15]. Three independent measurements are required for the completion of the experimental program which are rotational speed, inlet and exit cooling water temperatures, and orifice head difference required for calculating cooling water mass flow rate.

Measurements of rotational speed were made with a tachometer with maximum uncertainty of ±5 rpm that covers full scale of 500 rpm. Individual temperature measurements were made with mercury thermometers with uncertainty of ±0.5 °C. Measurement of the cooling water flow rate, kg/s, was made using a calibrated orifice meter of correlated equation $m = 10.381\sqrt{\rho \Delta h}/3600$, where Δh is the orifice head difference in mm Hg with maximum uncertainty of ±1 mm. Fluid properties are assumed with negligible uncertainty and were taken from tables of thermophysical properties of [16].

Following the method presented by Moffat [15], then the maximum uncertainty of Q, U, h_m, Re, We, and Nu through this study were calculated as: ±0.628 kW, ±0.049 kW/m^2 K, ±0.072 kW/m^2 K, ±96, ±102 and ±8.7, respectively, which in percentage values will be: ±6.4%, ±6.4%, ±4.6%, ±1.2%, ±6.1%, and ±4.2%, respectively.

5 Experimental Results and Discussion

Comparison between the experimental and theoretical values of the heat transfer coefficient and Nusselt number at the stationary case (no rotation) for the rough surface are shown in Fig. 2. The trend of the experimental results is seen to be in agreement with the theoretical values where the deviations between the experimental and the theoretical values are small. It is observed that the heat transfer coefficient is increased with the cooling water Reynolds number. This comparison gives confidence in the accuracy of the experimental results.

Fifty-one experiments were conducted using the smooth surface at constant cooling water Reynolds numbers of 3300, 4500, 6200, and 7800 and different Prandtl numbers of the condensate film in the 1.448–1.52 and at Weber numbers up to 5025. Seventeen experiments were conducted using the rough surface at constant cooling water Reynolds number of 4700 and varying Prandtl numbers of the condensate film in the 1.667–1.696 and at Weber numbers up to 4892.

The overall heat transfer coefficients, U, and the Nusselt number, Nu, against the Weber number, We, for the rough surface at Re = 4700 are presented in Fig. 3. The figure shows that both U and Nu increase almost linearly with an increase in We. The increase in Nu means an increase in the convection heat transfer coefficient of the steam side with the rotational speed. The in-

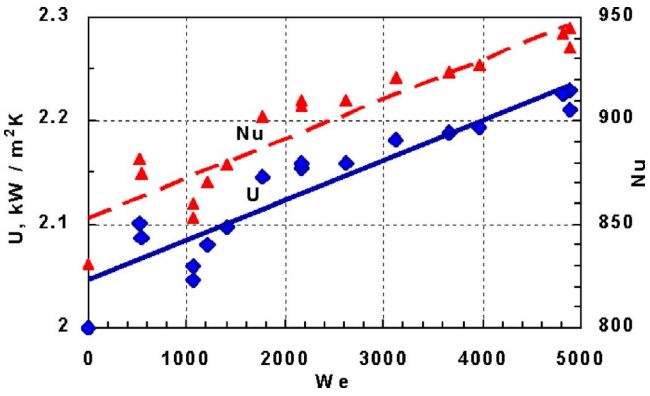

Fig. 3 Experimental results versus Weber numbers for the rough surface at Re=4700

crease in U means an increase in the convection heat transfer coefficients of either the steam side, the cold water side, or both sides, with the rotational speed. One can conclude that the rotation reduces the thickness of the condensate film causing an increase in the convection heat transfer coefficient of the steam side, as explained in [3,4], and an increase in the cold water velocity causing an increase in the convection heat transfer coefficient of the cold water side, as discussed in [14].

Values of U and Nu against We for smooth surface at Re of 3300, 4500, 6200, and 7800 are presented in Fig. 4. It is clearly shown that almost parabolic curves represent the variation of both the Nu and U values with We. It is also shown that increasing Re causes an increase in the values of both Nu and U. At Re of 3300, the heat transfer rate increases by increasing We. On the other hand for Re of 4500, 6200, and 7800, the heat transfer rate gradually increases to its peak value and gradually decreases by increasing We. Normally, the heat transfer rate would increase by increasing Re or We or both. But, the reduction in the heat transfer rate below its peak value with the increase in We can be expected as a result of either the elongation of the condensate drops into streaks form on the outside surface as discussed in [1,2] or the laminarization of the inner cold flow as concluded by [14]. From Figs. 3 and 4, it is also observed that the reduction in the heat transfer below the peak value depends on the surface roughness.

The experimental Nu results obtained for both the rough and the smooth surfaces at different rotational speeds are correlated, using the least squares method, as functions of Re, We, and Pr and are given in Eqs. (11) and (12) for rough and smooth surface, respectively. However, due to the experimental narrow range of Pr, so the $Pr^{0.333}$ term given in Eqs. (11) and (12) can be replaced

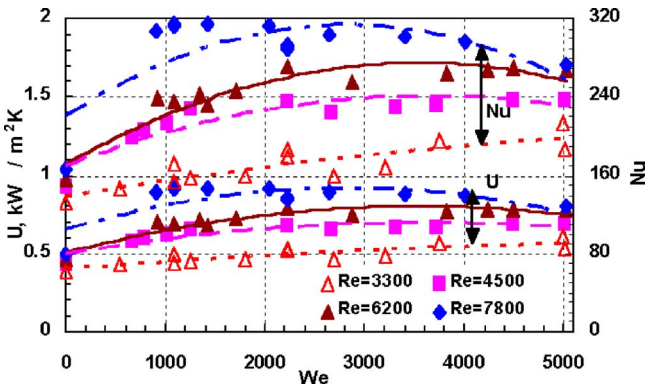

Fig. 4 Experimental results versus Weber numbers for the smooth surface at Reynolds numbers of 3300, 4500, 6200, and 7800

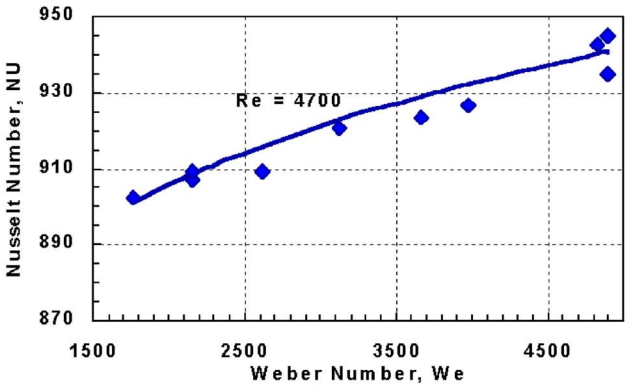

(*a*)

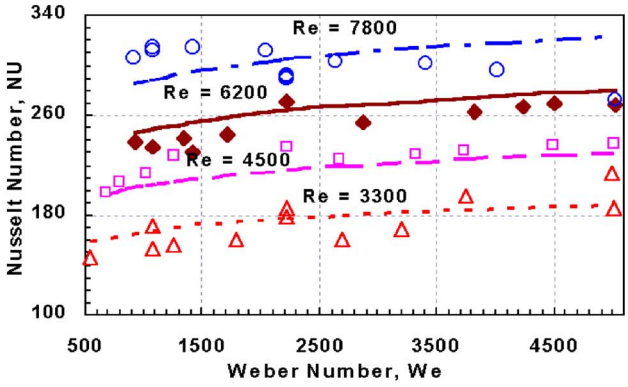

(*b*)

Fig. 5 Correlated Nu values and their corresponding experimental results at different Re and We for (*a*) rough surface, (*b*) smooth surface

with average values of 1.1915 and 1.1406, respectively. Figures 5(*a*) and 5(*b*) show both Nu numbers calculated from the correlated equation and the corresponding experimental values for the rough and the smooth surfaces, respectively. Maximum deviations of Nu calculated from Eqs. (11) and (12) from the corresponding experimental values at $1500 \leqslant We \leqslant 5000$ are 0.72% and 10%, respectively, except only one worse point obtained from Eq. (12) has a deviation of 12.5%. The maximum error in the Nusselt number values calculated from Eqs. (11) and (12) are 4.57% and 11.15%, respectively

$$Nu = 561.7We^{0.04}Pr^{0.333}$$

for rough surface (21.75 μm *roughness*)

at $1500 \leqslant We \leqslant 5000$, $1.687 \leqslant Pr \leqslant 1.696$, *and* $Re = 4700$ (11)

$$Nu = 0.511\,Re^{0.634}\,We^{0.075}Pr^{0.333}$$

for smooth surface (1.28 μm *roughness*)

at $500 \leqslant We \leqslant 4900$, $1.448 \leqslant Pr \leqslant 1.52$, *and*

$$3300 \leqslant Re \leqslant 7800 \quad (12)$$

Figures 5(*a*) and 5(*b*) show that Nu number values obtained using the rough surface are higher than those values obtained using smooth surface. This result is expected because a great amount of steam condensation was completed with the use of the rough surface compared with that quantity completed by the use of the smooth surface where the rough surface has higher thermal con-

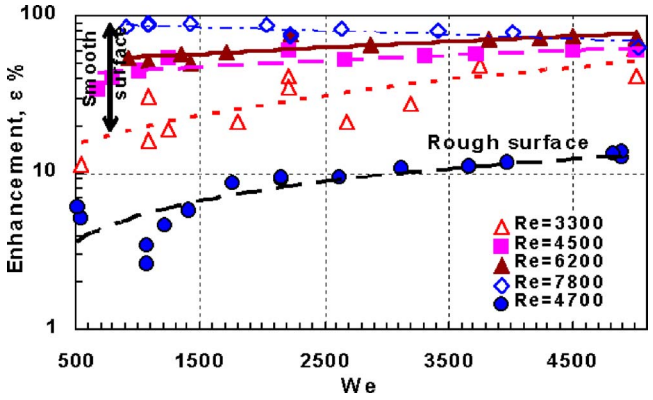

Fig. 6 Percentage enhancement in heat transfer rate against We at different Re values for both the smooth and rough surfaces

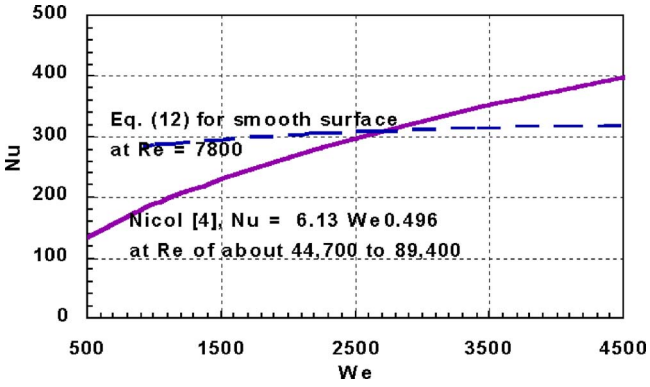

Fig. 7 Comparison of Nu versus We for correlated equation for the smooth surface at Re of 7800 with that of [4]

ductance and thinner wall thickness compared to the smooth surface. The rate of increase ε, represents the enhancement in the heat transfer rate due to rotational effect. The percentages of enhancement in the heat transfer rate against We at different Re values for both the smooth and the rough surface are presented in Fig. 6. It is shown that this enhancement becomes more appreciable for low Re at high rotational speeds and for high Re at low rotational speeds. It is also shown that the maximum enhancement in the heat transfer rate for smooth surface is about 60.6% at Re =4500 and about 13.7% for rough surface at Re=4700. This difference in the enhancement would be due to the effect of the surface tension of the condensate droplets. Therefore choice of the type of the heat transfer surface is very important in rotational cases. The maximum enhancement in heat transfer is about 89% at Re=7800, We=1084, and Pr=1.48 for the smooth surface and about 13.7% at Re=4700, We=4891, and Pr=1.696 for rough surface. This is more clear from the correlated equations, where the power of We in Eq. (12), 0.075 (smooth surface correlated equation), is almost twice the power of We in Eq. (11), 0.04 (rough surface correlated equation). Equation (12) shows that Re and Pr have the greatest effect on the Nu values compared to the We where they have the highest exponent in the equation. Therefore one can conclude that the enhancement in the heat transfer depends on We and the surface roughness while Nu mainly depends on Re and Pr.

From the available literature, Nicol and Gacesa [4] had done some experiments on steam condensation on a rotating vertical aluminum cylinder of 12.7 mm inner diameter with cooling water flow rate from 3600 to 7200 lb/h, i.e., equivalent to Reynolds number of about 44,700 to 89,400. They reported that the aluminum cylinder used in their work was cleaned using steel wool, then polished using abrasive powder and finally washed with alcohol, giving roughness of their surface almost comparable to that of the smooth surface in the present work. Therefore, comparing present correlation for the smooth surface given in Eq. (12) with that of [4] (i.e., $Nu=6.13\ We^{0.496}$), as shown in Fig. 7, shows that their correlation gives lower values of the Nu at low We and then grows to higher values with increasing We compared with the present correlation. At low We, Nicol and Gacesa [4] reported that Nu obtained from their correlation gave lower values compared with those obtained by other authors for horizontal rotating tube. Normally, the Nicol and Gacesa correlation gives higher Nu with increased Re where Re recorded through the Nicol and Gacesa experiments were much higher than those recorded through the present work. Generally, it can be stated that Nu-We correlation of [4] has an agreement with the present correlations from the point of view that Nu value is increased by increasing We, however, the present correlations show that the increasing value of Nu depend on Reynolds numbers, signifying that the present results are reasonably accepted. It should be noted that the low vibrations which have occurred during experimental test might reduce the film condensation causing an increase in the convection heat transfer coefficients with the increase of rotational speeds. This effect needs further study.

The above discussion clearly shows that the present apparatus has some potential in the enhancement in the heat transfer due to rotational effect for all cases. However, a mechanical power was consumed for the rotation, thus this enhancement represents additional running cost compared to conventional heat exchanger. In spite of this additional cost, a mechanical condenser of this type is suitable where compact equipment is a must, or in outer space where gravitational force is absent.

6 Conclusions

The experimental results for the heat transfer at the stationary case give an acceptable agreement with the theoretical values showing a confidence in the accuracy of the experimental results. The following conclusions can be drawn from the present study:

1. The rotation causes an enhancement in the overall heat transfer coefficient with percentage values of about 89% at Re=7800, We=1084, and Pr=1.48 for smooth surface and about 13.7% at Re=4700, We=4891, and Pr=1.696 for rough surface.
2. The enhancement in the heat transfer rates utilizing rotary surface becomes more pronounced for the smooth surface compared with the rough one, therefore the choice of the heat transfer surface roughness is very important. The present work shows that the occurrence of reduction in the heat transfer rate below its peak value depends on the type of the heat transfer surface.
3. The enhancement in the heat transfer, i.e., enhancement in the Nusselt number, depends on the Weber number value and the surface type while the Nusselt number value mainly depends on the Reynolds.
4. Present correlated equation could be used to represent the Nusselt number values as function of the Weber and Reynolds numbers within the stated ranges of the parameters for similar heat exchanger.
5. Effect of mechanical vibrations on the enhancement of the heat transfer rates needs further study.

Nomenclature

Alphabetic Symbols

A_o = outer heat surface area, m^2
C = specific heat of the cold fluid, kJ/kg K
Cf = specific heat of condensate, kJ/kg K
d = outer diameter of the central pipe, m

D_h = hydraulic diameter, m
D_i, D_o = inner and outer diameters of the cylindrical heat surface, m
h_{fg} = latent heat of condensation, kJ/kg
h_m = mean heat transfer coefficient, $kW/m^2 K$
h_o = theoretical heat transfer coefficient for film condensation, $kW/m^2 K$
Δh = orifice head difference, mm Hg
k_f = film thermal conductivity, kW/m K
L = length of test cylinder, m
m = cold water mass flow rate, kg/s
Nu = Nusselt number, $h_m D_o/k_f$
Pr = Prandtl number of the film condensate, $\mu C_f/k_f$
Q = heat rate gained by cold fluid, kW
Re = cold fluid Reynolds number, $\rho V D_h/\mu$
T_1 = inlet cold water temperature, K
T_2 = outlet cold water temperature, K
T_s = steam side temperature, K
T_w = steam side heat surface temperature, K
U = overall heat transfer coeff, $kW/m^2 K$
U_o = overall heat transfer coeff. at stationary case, $kW/m^2 K$
V = velocity of cold water, m/s
We = Weber number, $\rho_f \varpi^2 D_o^3/4\sigma_f$

Greek Symbols

μ = viscosity of cold water, Pa s
μ_f = viscosity of the film, Pa s
ρ = density of cold water, kg/m^3
ρ_f = density of film, kg/m^3
ρ_v = density of vapor, kg/m^3
σ_f = surface tension of the film, N/m
ω = angular velocity, rad/s
ΔT = logarithmic mean temp. difference, K
ε = enhancement in heat transfer rate

References

[1] Chandran, R., and Watson, F. A., 1976, "Condensation on Static and Rotating Pinned Tubes," Trans. Inst. Chem. Eng., **54**, pp. 65–72.
[2] Singer, R. M., and Preckshot, G. W., 1963, "The Condensation of Vapor on a Horizontal Rotating Cylinder," Proc. Inst. Heat Transfer Fluid Mech., **14**, pp. 205–211.
[3] Hoyle, R., and Matthews, D. H., 1965, "The Effect of Speed of the Condensate Layer on a Cold Cylinder Rotating in a Steam Atmosphere," J. Fluid Mech., **22**, pp. 105–113.
[4] Nicol, A. A., and Gacesa, M., 1970, "Condensation of Steam on a Rotating Vertical Cylinder," J. Heat Transfer, **92**, pp. 144–152.
[5] Ball, K. S., Farouk, B., and Dixit, V. C., 1989, "An Experimental Study of Heat Transfer in a Vertical Annulus With a Rotating Inner Cylinder," Int. J. Heat Mass Transfer, **32**, pp. 1517—1527.
[6] Sharipov, F., and Kremer, G. M., 2001, "Transport Phenomena in Rarefied Gases," Phys. Fluids, **13**, pp. 335–346.
[7] Peng, S. W., 1998, "Theoretical Analysis of Laminar Film Condensation in a Rotating Cylinder With a Scraper," Heat Mass Transfer, **34**, pp. 279–285.
[8] Willett, F. T., and Bergles, E., 2000, "Heat Transfer in Rotating Narrow Rectangular Pin-Fin Ducts," *ASME-ZSITS International Thermal Science Seminar*, Bled-Slovenia, pp. 11–14.
[9] Ishigaki, H., 1999, "Laminar Convective Heat Transfer in Rotating Curved Pipes," JSME Int. J., Ser. B, **42**, pp. 489–496.
[10] Yan, W. M., 1994, "Developing Flow and Heat Transfer in Radially Rotating Rectangular Ducts With Wall-Transpiration Effects," Int. J. Heat Mass Transfer, **37**, pp. 1465–1473.
[11] Yan, W. M., 1995, "Simultaneously Developing Mixed Convection in Radially Rotating Rectangular Ducts," Int. J. Heat Mass Transfer, **38**, pp. 665–677.
[12] Mahadevappa, M., Rao, V. R., and Sastri, V. M. K., 1995, "Numerical Study of Steady Laminar Fully Developed Fluid Flow and Heat Transfer in Rectangular and Elliptical Ducts Rotating About a Parallel Axis," Int. J. Heat Mass Transfer, **39**, pp. 867–875.
[13] Rao, M. M., and Sastri, V. M. K., 1995, "Experimental Investigation for Fluid Flow and Heat Transfer in a Rotating Tube With Twisted-Tape Inserts," Heat Transfer Eng., **16**, pp. 19–28.
[14] Hirai, S., Takagi, T., and Matsumoto, M., 1988, "Predictions of the Laminarization Phenomena in an Axially Rotating Pipe Flow," Trans. ASME, **110**, pp. 424–430.
[15] Moffat, R. J., 1988, "Describing the Uncertainties in Experimental Results," Int. J. Experimental Heat Transfer, Thermodynamics, and Fluid Mechanics, **1**, pp. 3–17.
[16] Incorpera, F. P., and Dewitt, D. P., 1996, "Introduction to Heat Transfer," 3rd ed., Wiley, New York.